Development of Al (Fuel) and nc-Ceria (Oxidizer) Nanocomposites – Sonoprocess, Crystal growth, and Energetics

By Santanu Kumar Padhi



Thesis Submitted To
UNIVERSITY OF HYDERABAD
In partial fulfilment of the requirements
For the degree of
DOCTOR OF PHILOSOPHY

In

PHYSICS

ACRHEM-School of Physics University of Hyderabad Hyderabad, 500046 INDIA June-2020

DECLARATION

I hereby declare that the content embodied in this thesis entitled "Development of Al (Fuel) and nc-Ceria (Oxidizer) Nanocomposites – Sonoprocess, Crystal growth, and Energetics" submitted to University of Hyderabad for the award of Doctor of Philosophy in Physics is a record of original research work carried out under the supervision of Prof. M. Ghanashyam Krishna, ACRHEM-School of Physics, University of Hyderabad, Hyderabad. This work has not been submitted partially or fully for any degree in any other university.

Date: 12/06/2020

Hyderabad

Santanu Kumar padhe Santanu Kumar Padhi

ACRHEM-SOP

CERTIFICATE

This is to certify that the research work presented in this thesis entitled "Development of Al (Fuel) and nc-Ceria (Oxidizer) Nanocomposites – Sonoprocess, Crystal growth, and Energetics" for the award of DOCTOR OF PHILOSOPHY is an original work carried out by Mr. Santanu Kumar Padhi under my supervision at ACRHEM-School of Physics, University of Hyderabad, and Hyderabad. This thesis research work has not been submitted to this or any other University partially or fully for the award of if any degree or diploma.

Further, these studies have the following publications before the submission of the thesis for adjudication and have produced evidence for the same in the form of acceptance letter or the reprint in the relevant area of his research.

- 1. Padhi, S.K., Gottapu, S.N., and Krishna, M.G., 2016. Electron-beam irradiation-induced transformation of Cu₂(OH)₃NO₃ nanoflakes into nanocrystalline CuO. Nanoscale, 8(21), pp.11194-11201. [Chapter-2]
- 2. S. K. Padhi and M. Ghanashyam Krishna, 2019. Non-Classical Crystal Growth Recipe using nanocrystalline ceria, a detailed review. Preprint arXiv: 1911.07454. [Chapter-3]
- 3. S. Gottapu, S.K. Padhi, M.G. Krishna, and K. Muralidharan, Poly (vinylpyrrolidone) stabilized aluminum nanoparticles obtained by the reaction of SiCl₄ with LiAlH₄. New Journal of Chemistry, 39(7), 2015, pp.5203-5207. [Chapter-5]

And has made presentations in the following conferences

- 1. Presented and participated in the two-day workshop on "HR-TEM methods: STEM, EELS and In-situ," organized by EMSI and NISER-BBSR, from 16-17th July 2018.
- 2. Participated in Frontiers in Nanoscience and Technology organized by Center for Nanotechnology, the University of Hyderabad from 6-7th April 2018.

- 3. Participated and presented on Electron Microscopy and Microanalysis of Materials (EMMM-2016) conducted by ACMS IIT Kanpur from 1st to 5th August 2016
- 4 Participated in the National Seminar on Crystallography for Material Scientists' held at Defence Metallurgical Research Laboratory, Hyderabad on 1st-2nd September 2014
 - 5. Presented ICONSAT-2014 organized by INST, Punjab.
- 6. Participated in FAEMMS-2013 at UoH during March 25-26 2013. Also, the student has passed the following courses towards the fulfillment of the

coursework required for a Ph.D.

S. No	Course code	Name of the course	Credits	Pass/Fail
1	AC805	Matlab	2	Pass
2	AC807	Research Methodology	4	Pass
3	IC475	Nanotechnology	4	Pass
4	MT715	Characterization of materials	4	Pass

Date:

Hyderabad

School of Physics, University of Hyderabad HYDERABAD-500 046. Telangana, India.

Dr. V. KAMESWARA RAO ACRHEM-UOH (ACRHEM)

Prof M. Ghanashyam Krishna | 12 6 2020.

Prof. M. GHANASHYAM KRISHNA tre for Advanced Studies in esis Science & Technology

Dean

School of Physics

DEAN School of Physics University of Myderabad HYDERABAD - 500 046.

DEDICATED.... TO

Guru

गुरुर्ब्रह्मा गुरुर्विष्णुः गुरुर्देवो महेश्वरः । गुरुः साक्षात् परं ब्रह्म तस्मै श्री गुरवे नमः ॥

The Guru is Brahma, the Guru is Vishnu, the Guru is Shiva, the God of gods, the Guru is verily the Supreme Brahman. Salutations to the adorable Guru.

Acknowledgements

I have immense pleasure to acknowledge the guidance, support and the innovative thoughtfulness ingrained to me at University of Hyderabad, and many other institutes of India; which have given me the required space to grow tremendously and standup by my own.

First and foremost, I bow my head in front of the supreme soul with his/her blessings able to work in standalone mode to achieve this.

Firstly, I wish to express my most profound sense of gratitude to Prof. M. Ghanashyam Krishna, thesis supervisor, for his constant support, guidance and help during the entire span of my doctoral research.

I thank Prof Dibakar Das at the initial stage of Ph.D. to help me in procuring and installing Ultrasonic Processor, which involves major part of this thesis work. Also, making me involve one part of his research work; which becomes my first second author publication at HCU.

Most importantly, dealing with nano-Al requires a chemistry laboratory having facility. In this context, I put forth my difficulties to Prof. K Muralidharan SOC. I can't forget the friendliness with which he allowed me to work in his lab, use his lab instrumental and SOC- facilities, and also asked me (by many telephonic) to join many instrumental demonstration and hand on operation activities. Thanks to him.

Scientific discussion with faculties; Prof. T P Radhakrishnan, Prof. C Bansal, Prof. S N Kaul, Prof. C S Sunandana, Prof. S P Tiwari, Prof. A K Chaudahary are gratefully acknowledged.

I extend my sincere thanks to Prof. K Muralidharan and Prof. Soma Venugopal Rao Sir, for their thoughtful discussions and suggestions during doctoral committee reviews.

Use of research facilities of IIT-Kanpur, IIT-madras, DMRL, IPR, Pondicherry University, NISER-BBSR, IICT-Hyderabad, and NSTDA-Thailand are acknowledged.

I want to thank present ACRHEM director Dr. V. Kameswara Rao and former directors Prof. S P Tiwari, Dr. Venkateswara Rao, for support in ACRHEM facilities and DRDO funding, without which it would have been difficult to finish this doctoral research.

I want to thank Prof. V Seshu Bai, Dean School of Physics, and all former deans and all faculty schools of physics, University of Hyderabad, for providing facilities, interaction, and enhancing my physics knowledge base.

I am deeply indebted to all my friends and seniors of SOP, SOC, and SEST-UoH from 2010 onwards for making me the person whom I am and keep me actively engaged.

Friends like Dr. K Lakshun Naidu, Dr. S Pavan Kumar Naik, Dr. Raju Botta, and also my family members' constant support throughout the Ph.D. program is sincerely appreciated.

I thank Prof K.C.James Raju for interacting and helping me as required.

I thank all faculty and scholars from the School of Physics. I acknowledge the support of Mr. T. Abraham, School of Physics, and Ms. Grace, Centre for nanotechnology. I extend thanks to all non-teaching staff from the School of Physics and NRS hostel.

I express thanks to technical staff from the school of physics and center for Nanotechnology, namely Mr. Tirumalaiah, Ms. Arundhati (FESEM), Mr. M Durga Prasad (TEM), Sunitha (AFM) and B. Sandhya for their help in obtaining data from various instruments.

I acknowledge the support of Postdoctoral fellows in thin-film laboratory Dr. Sachin D Kshirsagar and Dr. Ahmed for help in academic issues.

I acknowledge the help of my seniors Dr. Rajeeb Brahma and Dr. K. Vasu.

I feel joy in acknowledging my labmates Dr. Ummar Pasha, Mr. A Sivaramakrishna, Dr. S L D Verma, Dr. Rambabu, Dr. Anil Tumuluri, Dr. Ramakanth, Dr. S. Bashaiah, Dr. Shivnag Reddy, Dr. V. Shankernath, Dr. G. Thirupathi, Mr. Pundareekam, Mr. Andrews, Mr. Chaitanya, and Dr. Alkathy.

I express my gratitude towards my parents, Laxmidhar Padhi and Minati Padhi, for their love and encouragement, without whom I would never achieve this success. I also thank my brother Sibani, mother in law Mamata madam, and fiancé Swastika for their loving presence. Also, I thank sister Moni for her sweet presence.

Finally, I thank God almighty for giving me immense strength to achieve this.

Table of Contents

List of Figures	1
Introduction	7
1.1 Motivation and objective of the present study	8
1.2 Crystal Growth	10
1.2.1 Non-Classical Crystal Growth (NCG) Scheme	11
1.2.2 Oriented Attachment (OA) Process	13
1.2.3 In-Situ Transmission Electron Microscopy	14
1.3 Sono mechano-chemical process: feasibility for nanoscience	16
1.3.1 Process Intensification	16
1.3.2. Sonocrystallization	17
1.3.3. Sono-agglomeration	17
1.4 Energetic Materials	18
1.4.1 Nanoenergetic Materials	18
1.4.2 Metallic Aluminium as Fuel	19
1.4.3 Nanostructured Ceria as Oxidizer	20
Experimental and In-situ TEM electron beam irradiation techniques	23
2.1 Material Characterization	24
2.2 X-Ray Diffraction	24
2.3 Field Emission Scanning Electron Microscope	25
2.4 Transmission Electron Microscope	29
2.5 UV-Visible Spectroscopy	32
2.6 Photoluminescence Spectroscopy	33
2.7 Raman Spectroscopy	33
2.8 Thermal Analysis	34
2.9 In-situ TEM Studies	34
2.10 Nano- Particle Size Analyzer	36
2.11 Atomic Force Microscopy	
3.1 Introduction:	
3.2 Materials and Methods	

3.3Synthesis and Charge Transfer transition	45
3.3.1 Synthesis Protocol	45
3.3.2. Charge Transfer transition	46
3.3.3. Origin of the blue-shift	53
3.4 Characterization of Ce_SS@RT product surface attributes using Raman spec	troscopy
	63
3.5 Agglomeration of Ceria nanocrystals a boon or bane: a detailed evaluation i	in tune
with the non-classical crystal growth route	69
3.6 1D-Ceria fibers growth by OA mechanism in DI-water facilitated biominera	ılization72
3.7 Tyndall Effect	73
3.8 Validation of OA mechanism in 1D-Ceria grown fibers	74
3.9 TEM Validation of OA mechanism of Hexagonal building units to develop ceria grown fiber	
3.10 In-situ TEM e-beam facilitated studies of OA mechanism	
3.10.1 Prescribed Protocol for TEM e-beam Probe or Modification to be followed	
3.10.2 TEM e-beam devised Hammering and Amorphization (E4I20m)	
3.10.3 Probing the TEM e-beam Grown Crystalline Region (E4I16m)	
3.10.4 TEM e-beam Facilitated Aggregative Growth and Growth Kinetics:	
3.10.5 OA Crystal Growth Facilitated by TEM e-beam Irradiation	
3.10.6 TEM e-beam Un-hammered region under e-beam exposure	
3.11 Conclusions	
Viability of Ultrasonic Sonochemical processing for nanostructures: Case study Aluminum-crystal growth and Poly (vinylpyrrolidone)-graphitization	
4.1 Introduction	
4.2 Materials and Methods	
4.3 Results and Discussion	
4.3.1 PVP TEM Investigations	
4.3.1.1PVP Pristine	
4.3.1.2 PVP Sonicated	
4.3.1.3 DFM probing PVP Sono-fragmentation	
4.3.1.4 TEM probing PVP Sono-crystallization	
4.3.1.4 TEM probing Aluminum Sono-agglomeration	117

4.4 Al Characterization	119
4.4.1 Nanostructured Al Stabilization	119
4.4.2 Sonocrystallization of PVP at RT	122
4.4.3 Intercalation of metallic Al in sonocrystallized GC and PVP Matrix composite	127
4.5 Metallic Al Crystal Growth	129
4.6 Conclusions	133
Investigation of energetics of 1:1 stoichiometric Al/PVP-fuel and nc-CeO ₂ -oxidizer	
nanocomposite material	137
5.1 Introduction	140
5.2 Materials and Methods	142
5.3 Results and Discussion	143
5.3.1 NEMs Physically Mixed Reaction Investigation	143
5.3.2 Nano-Al inherent Surface oxide phase (i.e., in μ -Al, CEM) as inhibitor	145
5.3.2 Al/PVP Fuel and nc-ceria Oxidizer TG/DTA investigation	147
5.3.3 NEM and Al-PVP Ignition and Energy release investigation	148
5.4. Conclusions	153
Thesis summary, Conclusions and Scope for the future work	155
6.1 Thesis Pictorial Summary	156
6.2 Future Research activities need to be undertaken	161
References	165

List of Figures

Fig.1 1 [Aquatic biominerals]: (a) radiolarian siliceous, (b) foraminifera calcareous skelet are microstructural evolution adopted to sustain neighbouring aquatic environmen (courtesy Prof. A. C Narayana unpublished data)	t respectively
Fig.1 2 [1D-ceria Mesocrystal]: TEM (a) BF distinct core-shell region, (b) DF individual brighter dots, (c) FFT of nc-ceria crystal one from the core and other from shell region pattern with no rotation (shell crystal-1 inset in fig.1.2 (a), core crystal-2 as inset in fig.1.2 TEM-SAED spot pattern from the entire region showing lattice mismatch of core justification to OA character.	ual crystals as identical spot .2 (c)), and (d) and shell an
Fig.2 1 (a) Reflection (Bragg-Brentano geometry) schematic, (b) Corundum standard accestep width of 0.02°	
Fig. 2 2 Schematic representation of (a) functioning of the filtering grid in separating SEs different detector positions in the Gemini column of Ultra 55 FESEM.	
Fig.2 3 Acquired FESEM micrographs employing signal collected by (a) In-lens, (b) SEZ	
Fig. 2 4 (a) SDD detector schematic and operation, (b) Highlighted 0 keV noise peak in (mostly excluded in subsequent thesis EDS presentations)	•
Fig. 2 5 TEM basic operation modes schematic (a) diffraction mode, and (b) Imag reproduced from B D Williams and C B Carter TEM a text book for Material Science)	ing mode. (#
Fig.2 6 A typical CTF plotted for a 200 keV microscope at a Scherzer defocus (Δ_{fsch} =-67 1.2 mm, Cc =1.2 mm, Δ E=0.6 eV, HT ripple = 0.25 ppm, Obj. Lens Instabilities = 0.5 ppm, =1.97 nm, Convergence =0.30 mrad and K is the spatial frequency. Under these conditional planes of 2.5 Å spacing can be resolved.	nm) with Cs = , Focal Spread ons the lattice
Fig.2 7 UV-VIS-NIR spectrophotometer instrument schematic	
Fig.2 8 Filament Supervisor with emission current steps	magnification is about 0.93 le bar for the
Fig.3 1 [Hydrothermally grown 1D-ZnO validating NCG scheme]: Building units in (a)-(d respectively (courtesy Y. Rajesh et al. unpublished data)	-
Fig.3 2 [Aquatic biominerals]: (a) radiolarian siliceous, (b) foraminifera calcareous skelet are microstructural evolution adopted to sustain neighbouring aquatic environmen (courtesy Prof. A. C Narayana unpublished data).	t respectively
Fig.3 3 [1D-ceria Mesocrystal]: TEM (a) BF distinct core-shell region, (b) DF individual brighter dots, (c) FFT of nc-ceria crystal one from the core and other from shell region pattern with no rotation (shell crystal-1 inset in fig.1.2 (a), core crystal-2 as inset in fig.1.	ual crystals as identical spot

istification to OA character
Fig.3 4 [UV-Vis optical spectra of the Ce_SI@RT]: (a) The spectral transmission curves for origina (Ce_SI@RT) and interface modified (SPW H2O2) sample (b) SPW H2O2 aging stability, and (c) time dependent wavelength specific SPW H2O2 product measurements respectively
Fig.3 6 [Tauc and Urbach regions]: (a) identification of the optical transition type, and (b) linear fit for band tail width and Ee-ph strength computation respectively
is used to focus the laser to about 3-5 μ m spot), and (c) Quenching of the CT luminescence band employing λ_o =532 nm laser operated at 2.5 mW output maintained for 12 minutes demonstrating not
ceria surface oxidation respectively56
Fig.3 9 [Optical band gap Narrowed defective nc-ceria]: (a) Optical absorption spectra of cerial products i.e., Ce_SP@RT and Ce@RT, (b) and (c) are the respective Tauc plots demonstrating computed bandgap values.
Fig.3 10 [Photoluminescence spectroscopy of Ce_SP@RT]: (a) PLE spectral data acquired for 666 nm PL (inset gives schematic of sub-optical gap absorption), (b) PL emission with probable defects, and (c) occurrence of the 2 photon absorption for 532 nm sub-band gap excitation respectively for Ce_SP@RT product
Fig.3 11 [Effect of the ultrasonication and 532 nm Nd-YAG laser irradiance on Ce_SP@RT product]: (a XRD data of ultrasonic induced product size reduction; (b), (c), and (d) are the IPL observed by lase
irradiance of 5, 10, 15, 20, and 40 kW/cm ² respectively. In increasing order these set of values represent PL-recovery, steady-state, and quenching data recordings
Fig.3 13 [Dynamic changes to the phonon-modes of Ce_SS@RT brought in by neighbouring environment changes]: (a) thermal oxidation on hot plate @ 150 °C spectral traces, and (b) Ramar mapping data in which the product is maintained in continuous contact with DI-water. (c) Spectra data extracted out of the mapping data to demonstrate the appearance of 488 cm-1 mode respectively
Fig.3 14 [Classical Crystal growth stages induced by thermal processing: FESEM illustration] Nucleation: (a) monomers generation and adsorption, and (b) nucleating sites evolution; Ostwalc ripening: (c) micron-Al surface, (d)-(e) ripening, (f) final evolved grain surface with larger crystallites

ig.3 15 [Particle mediated two step non-classical crystal growth: FESEM illustration]: Building block of: (a) 2D hexagon, (b) cubes, and (c) spherical particles; Evolved morphologies: (d) flower like, (e ods, and (f) nano porous microspheres respectively
ig.3 16 [Autocatalytic regenerative feature and biomineralization]: (a) Oxidation by aging; (b) optical pectra of progressive bio-mineralized products (with inset of 12 MSM products in glass vial (1) edispersion (2), and (3) morphology with composition).
ig.3 17 [Light Scattering efficacy of Ce_SI@RT product]: Laboratory lights (a) ON, and (b) OFF state amera snaps illustrating scattering efficiency with 1year aged product. Microstructure of 3 month ged settled mass: (c) FESEM, and (d) TEM BF image respectively
ig.3 18 [GI_XRD data of 1D-Ceria fibers coated on fused silica substrates]: (a) 1D anisotropy induced ubic (CeO2) to hexagonal (Ce2O3) structural phase transition, and (b) schematic of the two lexagonal building units along (110) crystal plane OA, in accordance with the 1D-fiber obtained exture respectively.
ig.3 19 [Growth stages of 1D-ceria fibers: Schematic view]: Ceria unit cell; (a)-(c) depicts crystal face levelopment, (d) gradual elimination of $\{111\}$ planes and $<001>$ texture formation, (e) <001 extured 1D-ceria fiber observed along c-axis and away from the c-axis respectively
ig.3 21 [Schematic of TEM e-beam activity]: (a) LaB6 filament emission to probe (E2P) and emission or irradiation (E4I), (b) E4I modified region, and (c) schematic for subsequent studies respectively. 8: ig.3 22 [Micrographs of two distinct nc-ceria formulations]: Ultrasonic (a) horn, (b) cleaning bath lispersed nc-ceria HRTEM micrographs respectively
ig.3 23 [Micrographs of TEM e-beam hammered amorphized region]: (a) nc-ceria lump with distinct-beam hammered region, (b) HRTEM, and (c) comparative SAED patterns of nc-ceria and morphized region respectively
ig.3 24 [Probing e-beam grown nano-crystallite]: (a) TEM BF micrograph of the e-beam grown anocrystalline (marked as 1), and the original nc-ceria region (marked as 2) respectively. (b) α =0, (c=5, and (d) α =10 e-beam tilt series acquired SAED patterns acquired from (a) with the aperture entered on grown crystallite.
ig.3 25 [Probe region TEM e-beam irradiation hardened]: Sequential time evolved BF image lepicting a single nano-crystal growth form; (a) amorphized (t=0), (b) t=4, (c) t=8, (d) t=12, and (e=16 minutes of step-4 e-beam irradiation. Images for subsequent longer exposure snapped
nicrographs are in (f) t=20, and (g) t=24 minutes (not shown here) respectively
ig.3 27 [Probing the TEM e-beam Radiation Hardened Region]: Sequential in-situ HR-TEM time volved BF images after; (a) t=0, (b) t=4, (c) t=8, (d) t=12, and (e) t=16 minutes of step-4 e-beam luence irradiation. Evolved nano-crystallite tracked in (e), growth direction is evident in (f)

Fig.4 18 [Nano-Al Crystal growth under TEM e-beam]: (d)-(f) already exposed larger Al-crystallite is seen to undergoes OR by consuming smaller adjacent ones; (a)-(c) particle attachment illustrations respectively.
Fig.5 1 NEMs oxidation (a) TG, and (b) corresponding DTA traces respectively
procured from US Nano, and (e)-(f) Al/PVP along with its obtained NEM respectively
Fig.5 6 DSC data illustrating effect of the HR in igniting the fuel, inset indicates slow HR AI melting transition
Fig.5 7 (a) TG of Al/PVP fuel representing explosion, (b) HEM DSC recorded at varying heating rates for activation energy calculation respectively
Fig.6 1 Thesis Pictorial view of physical properties investigated and data flow

List of Tables

Table 3 1 Optical parameters extracted from the measured STC for different samples	51
Table 3 2 CT absorption band position in nm for the case of nc-ceria (reported and this work)	57
Table 3 3 : 12 MSM product bulk X-ray structural attributes extracted	76
Table 4 1 GC unit cell taken from the material project (mp) [398] and ICSD database	126
ruble 11 de unit den taken nom the material project (mp/[556] and 1655 autubuse	120
Table 5.1 Ignition and Energy release data obtained and literature	150

Chapter-I

Introduction

1.1 Motivation and objective of the present study

The motivation of the present thesis is to process, develop and investigate nano energetic materials (NEMs) prepared by the physical-mixing process. The reactive components utilized to process NEMs are Poly (vinylpyrrolidone) (PVP) embedded nano-aluminum (nm-Al) particles as the candidate fuel, and sonochemically processed 2-nm ultrafine nanocrystalline ceria (nc-ceria) constitute the oxidizer. The aim is to process stoichiometric 1:1 NEMs made out of the above fuel and oxidizer components, and then to investigate energetics.

The processing and development stages involve studies on crystal growth of fuel and oxidizer, fuel stabilization in the PVP matrix, oxidizer surface-interface characteristics illustration, and stabilization of the reactive components in the sonoprocessed graphitic carbon (GC) matrix systematically. For this, ultrasonic-sonochemistry physio-chemical viables like (1) solution-phase nanostructured material processing, (2) reaction rate enhancement also named as process intensification (i.e., strictly linked to shortened reaction time product delivery); (3) sono-fragmentation, (4) sono-agglomeration, and (5) sono-crystallization attributes are investigated. These are used for the nc-ceria and nc-Al crystal growth facilitation, composite NEM development, and for reactive component stabilization. An illustrative demonstration of the physical involvement of these sets of the sonochemical attributes is accessed and will be experimentally illustrated to extend its utility for a variety of other material solution phase processing schemes.

In the recent decade exploration of non-classical crystal growth (NCG) scheme has been an ongoing development. Use of NCG to grow microstructurally distinct variety of anisotropic morphologies is of interest for the current investigation. In brief, the "crystallization by building-units attachment" is the NCG scheme. The building units' attachment is a result of either material-specific or directed by the neighboring environment. These two are the recognized crystal growth contributing factors. Thus, specifically for inorganic crystal growth, the rule is to feasibly control

indivisual building units' attachment leading to anisotropic growth. That is, building units tailored attachment in a prescribed fashion leading to the growth and development of the tunable and novel technologically relevant morphologies having industrial scale applications.

Based on the literature reports on NCG, the aim is to formulate and illustrate by demonstration, the NCG scheme as a viable recipe. In this context, the nc-ceria is chosen as the prototypical material for evaluation as a result of its well-established unique attributes which are of special importance to the current thesis. These are, specifically (1) enhanced ceria lattice oxygen vacancy mobility, (2) nc-ceria autooxidation-reduction with regenerative surface feature the neighbouring environments changes, and (3) radiation-damage and its self-healing efficacy brought in by changes to its immediate/near-neighbor surroundings. These surface attributes are examined in the present context specifically to investigate the role of; (1) Transmission electron microscope electron beam (TEM e-beam) periodic exposure and withdrawal, (2) similarly recurring aqueous oxidized and reduced neighboring chemical environment changes and (3) the process of biomineralization is mimicked with aging employing sonochemically developed water-soluble nc-ceria transparent colloidal dispersion.

With this objective, one of the major sections is devoted to the realization of the NCG scheme. It is done to track the ongoing nanoscale physical ordering of individual building units both modified and probed under TEM e-beam. This illustrates the application of TEM e-beam as a standalone tool for probe and modification. Lastly, it is demonstrated that the TEM e-beam can be explicitly employed as an in-situ probe, while enabling NCG scheme. This specific case study of technologically relevant nc-ceria can be extended to similar other radiation-sensitive materials, also having the defect healing capability with the introduction of appropriate neighbouring gaseous environment. This will, in addition, enable the localized in-situ distinct nanostructural features design and development.

The **main objectives** of the thesis are

- 1. Investigate **biomineralization** mimicked nc-ceria individual building units utilized to grow 1D-ceria nanostructures. In this context, de-ionised water (DI-water) having transparent nc-ceria colloidal dispersion with aging leads to anisotropic 1D-ceria nanorods development. Thereby DI-water as enabler of NCG, similar to aquatic biominerals is established. In order to physically demonstrate the building units' attachment, in-situ TEM e-beam is utilized to act as a probe and also as an enabler of NCG scheme.
- 2. Apart from NCG a major section is also devoted to investigate the autocatalytic regenerative **surface feature of nc-cer**ia in delivering a tunable charge transfer (CT) visible photoluminescence (PL) emission and quenching.
- 3. The feasibility of a variety of **ultrasonic-sonochemical physio-chemical processes for nanoscience** are tracked. Their mechanistic features are accessed and also utilization in solution-phase material processing is realized.
- 4. To explore and present **ultrasonic-sonochemical process intensification** while evaluating the nucleation, growth and stabilization aspect of the ultrafine oxide-free PVP embedded Al-rich, Al/PVP composite fuel.
- 5. Lastly, to investigate physically mixed stoichiometric 1:1 NEM made out of the Al/PVP composite fuel and nc-ceria oxidizer. The NEM characteristics evaluated are oxidation, ignition, energy contained and also energetics respectively.

In the following sections introductory notes which are intended to present a general introduction of the thesis are provided.

1.2 Crystal Growth

The repeated attachment of atoms, ions, or molecules to grow into a symmetrical shaped crystalline material out of a single nucleus is the usual classical layer by layer crystal growth scheme. A detailed summary on the classical crystal growth scheme,

developed equilibrium structures, and these equilibrium structures probable surface informations mathematical formulations is reported as early as 1951, and thereafter evolved concepts till date is presented by Woodruff et al. [1]. This classical layer by layer crystal growth is an idealized shape morphological growth scheme and therefore has limited value for developing microstructures of having technological utilities. Whereas the growth and development of hollow, core-shell, and of twinned crystalline material morphologies require reversed crystal growth route (i.e., a non-classical scheme) [2]. For example, in the reversed crystal growth scheme evolved crystal morphological anisotropy is facilitated by the surfactants or polymers adsorption onto the specific surface of nucleating crystal at an early stage of the shape progression. These NCG is one of the recognised ways forward to process a variety of fine-tuned morphologies. These NCG protocol fine-tuned morphologies are having the potential to enrich the materials synthesis field and are of the specific interest of the current investigation for a detailed study.

1.2.1 Non-Classical Crystal Growth (NCG) Scheme

Non-classical crystal growth (NCG) scheme is a nature formulated enriched pathway most recently explored to process advanced hierarchical materials of complex morphologies, and is of a variety of composition [3]–[12]. Briefly, NCG is the "crystallization by building-units attachment." The building units' attachment is brought by either (1) a material-specific, or (2) the neighbouring environments direct participation facilitating the interaction. Thereby it is the identified sole-growth deciding factor. Thus, specifically for inorganic materials the objective is to feasibly control the growth directing building units' to have interaction. It will enable to realize tunable and novel technologically relevant morphologies.

There are numerous reports on (A) *building units*, (B) *growth driving force*, and (C) *the final evolved hierarchical morphologies* following the NCG protocol. Examples of *building units shape* are (1) PbSe nanocrystals [10], (2) ZnO nanocrystals [13], (3)

 α -MnO₂ nanowires [14], (4) 10-20 nm diameter PbTiO₃ fibers [15], (5) Au spherical seeds [16], (6) 1D-TiO₂ fibers [17], (7) δ -MnO₂ nanosheets [18], (8) 200-250 nm SnO₂ dodecahedrons [3].

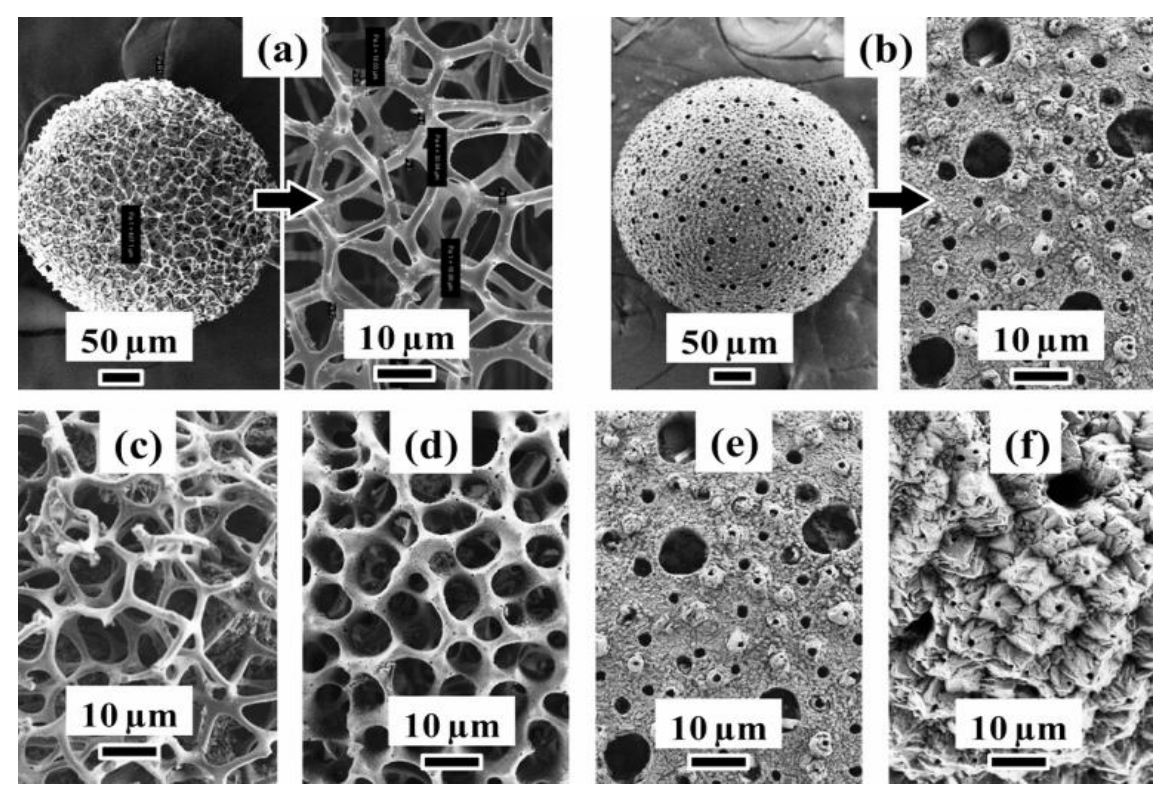


Fig.1 1 [Aquatic biominerals]: (a) radiolarian siliceous, (b) foraminifera calcareous skeleton, and (c)-(f) are microstructural evolution adopted to sustain neighbouring aquatic environment respectively (courtesy Prof. A. C Narayana unpublished data).

Similarly, examples of the *corresponding growth directing forces* are (1) dipolar-interaction [10], (2) orientation specific directional ZnO-ZnO interfacial interaction [13], (3) K^+ -stabilized ionic interaction [14], (4) surface-electrostatic force [15], (5) laser intense pulses force field [16], (6) electric-field [17], (7) hydrogen-bonding [18], (8) pressure-induced interaction [3]. These lead to the *subsequent developed hierarchical morphologies* such as (1) PbSe nanowires and nanorings [10], (2) 1D-ZnO nanorods [13], (3) tunneled α -MnO₂ nanowires [14], (4) large-sized 3D-PbTiO₃ hollow fibers [15], (5) triangular Au nanoplates [16], (6) multilevel twinned tree-like branched TiO₂

morphologies [17], (7) nanoflowers [18], and (8) μ -sized 3D-ordered SnO₂ superstructures [3], are respectively.

Importantly the unique morphology of aquatic biominerals and hierarchical motifs is the motivation and basis of the current NCG investigation [19]. Observed in fresh and salt water these μ-sized silica (spongy skeleton in soft bodies) and of the calcium carbonate (appropriate mechanical strength at the sea bed living)ubiquitous biominerals macro and microstructures are shown in figs.1.1 (a)-(f) respectively [20]. Reported recent activities of involving studies on biominerals formation and its concept exploration to mimic a variety of other inorganic materials for hierarchical morphology development is an actively engaged field [3], [10], [13]–[18], [21]–[25]. Most importantly, even the role of water as an active participant in facilitating building units' attachment is investigated. These investigations suggest the role of water in bringing localized order for inducing attachment is a prominent factor [13], [26]–[30].

1.2.2 Oriented Attachment (OA) Process

The building unit's attachment in an orderly fashion is oriented attachment (OA), to develop an intermediate structure named as the mesocrystals [31]–[34]. Penn et al. TEM illustrations [35], and ongoing continuous in-situ exploration while OA process happening is constantly under investigation to understand and develop new avenues for material growth. Besides ongoing utilization of the OA process in developing novel anisotropic materials [36]–[40], publications like "OA Revisited: does a chemical reaction occur ?"add valuable fundamental insights to the already existing concepts [41]. Although ceria in mesocrystalline structural formulation had plenty of OA illustrations [42], [43], this is not true in case of nanocrystalline ceria (nc-ceria). An investigation relating to the use of Ce³⁺ surface charge steric difference with that of the grain interior Ce⁴⁺ in aqueous medium by hydrothermal processing is of importance to the present study [44]. Specifically, nc-ceria surface charge auto-

regenerative feature with aging by storing in aqueous medium and morphological features of agglomeration of nanoparticles developed, by Transmission Electron Microscopy (TEM) microstructural investigations, will be of significance to understand OA implications. In other words, the objective is to employ nc-ceria with aging to bio-mimic the natural biominerals development for anisotropic morphological feature development.

1.2.3 In-Situ Transmission Electron Microscopy

In-situ TEM plays an essential role in tracking of ongoing NCG linked nanoscale crystalline ordering. In this context, the building units' rotation and attachment leading to a single/meso-crystalline grown unit is commonly traced as a physical observation of the NCG concept. For a general illustration of the NCG concept TEM microstructural detailing of nc-ceria particulates attachment derived single crystalline nanorods is shown in fig.1.2 (a)-(d). The grown ceria nanorod (see fig.1.2 (a), TEM BF core and shell microstructure) is reaction quenched, not as a whole crystallized entity, (differential nc-ceria particles packing density between nanorod core and shell) but an intermediate aging derived reaction product localized microstructure is presented. The nanorods particulate microstructure is shown in fig.1.2. (b) (TEM DF), and (c) (HRTEM) respectively. Clear indication of nanorods single/meso crystalline nature is the spot diffraction pattern (see fig.1.2. (d)). Even a rotational angular mismatch between core and shell crystalline arrangement exists and is schematically overlaid on fig.1.2 (d), for observation. It depicts OA of nc-ceria particles employed as building units to develop into a nanorod just by aging in aqueous solvent. In this context, it is usual ex-situ TEM observation employed to illustrate NCG validation. However, frequent dynamical tracking of the ongoing NCG process is by in-situ liquid cell TEM/STEM instruments [45]–[50]. In these case studies, TEM electron beam (TEM e-beam) is utilized just for probing. In contrast, its utilization in simultaneous material modification in a controlled fashion has also

many scientific demonstrations [51]–[53]. Most recently Asghar et al. investigated ncceria under TEM e-beam to support the argument that the instrument can be utilized as a standalone technique to probe and also for material modification [52]. The current research study is devoted to the use of TEM e-beam for both activities and also examine if DI-water behaves as a direct participant in achieving NCG growth of 1D-ceria.

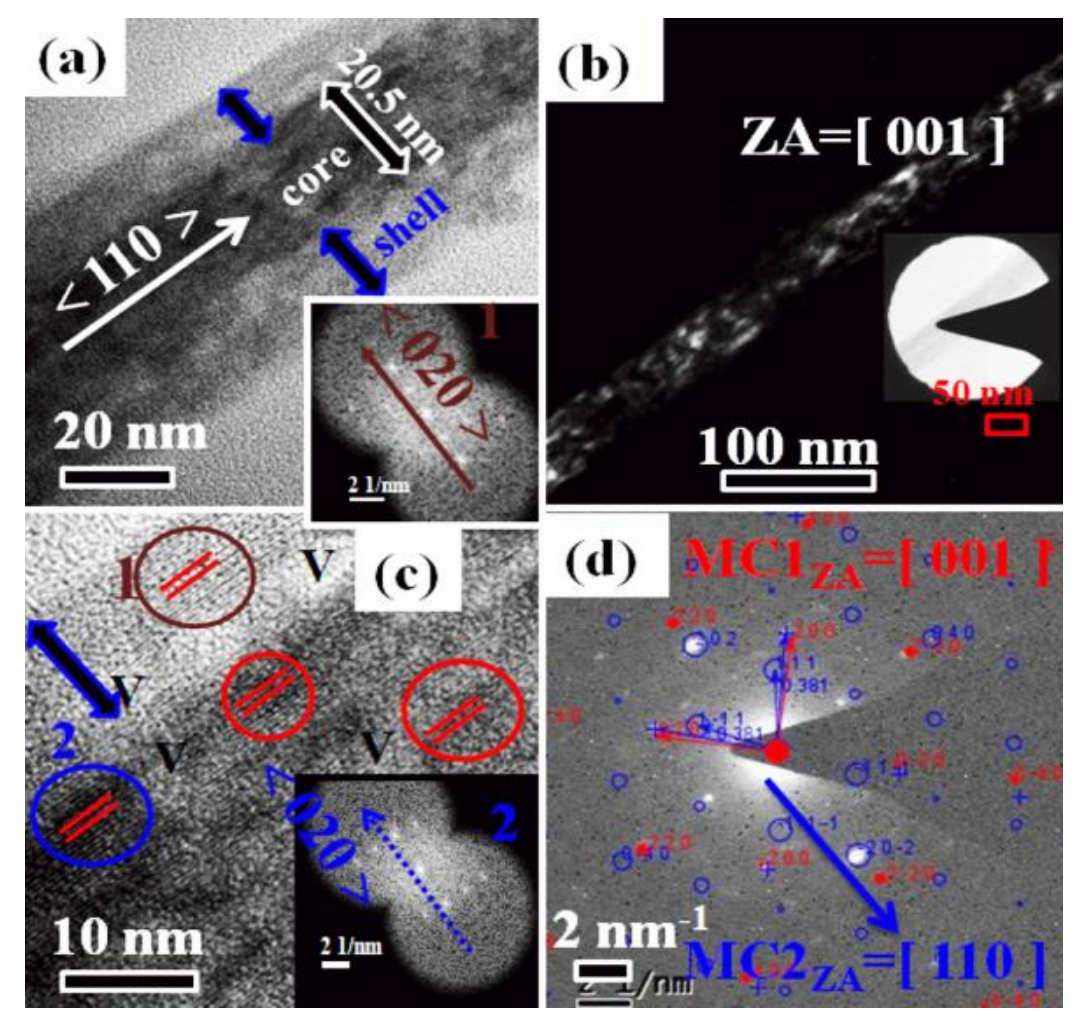


Fig.1 2 [1D-ceria Mesocrystal]: TEM (a) BF distinct core-shell region, (b) DF individual crystals as brighter dots, (c) FFT of nc-ceria crystal one from the core and other from shell region identical spot pattern with no rotation (shell crystal-1 inset in fig.1.2 (a), core crystal-2 as inset in fig.1.2 (c)), and (d) TEM-SAED spot pattern from the entire region showing lattice mismatch of core and shell an justification to OA character.

1.3 Sono mechano-chemical process: feasibility for nanoscience

Sono mechano-chemical variables like; (1) process intensification, (2) sonocrystallization, and (3) sono-agglomeration/fragmentation linked to novel nanomaterials design, growth and tailoring are briefly introduced below.

1.3.1 Process Intensification

The widespread application of ultrasound under environmentally benign conditions to deliver products at industrial scale, quality enrichment and production at a shortened duration are benefitting the society. These specific industrial applications are: (1) food sciences and its associated technologies (like processing, preservation, and extraction) related activities [54]-[60], (2) water remediation [61]-[66], (3) biomedical field [67]-[69], and also (4) the reaction process intensification achievements of variety of solution processing's [59], [70]–[73], etc respectively. This above list is non-exhaustive, but represents the most frequently engaged activities. If the "process intensification" term is repeated, then the general demonstrated fact is ultrasound-assisted protocol comes out to be more effective than that of the corresponding conventional (physical, chemical, and biological) process without ultrasound [74], [75]. The reported demonstration include, extraction of the organometallic complexes (e.g., organo-lithium, -magnesium, and -aluminum like materials) as early as 1950s [76]. Well known cases of metals linked activation by ultrasound (i.e., sonic acceleration) lead to substantial shortened reaction duration. These synthetically significant protocols are; (1) Zinc-induced Reformatsky-reaction [77], (2) Copper-induced Ullmann-couplings [78], and (3) Lithium-induced Barbierreaction [79], respectively. In addition to these, the conceptualized book chapters on the principles of ultrasound-induced activation of metals, and then its subsequent use to accelerate (process intensification) organic-synthesis are available [80]-[84]. The point being ultrasound-introduced time shortened synthetic protocols

identification/listing is a subject of ongoing interest. It is worth noting here that the ultrasound-induced cavitation and its cavitation impulsive collapse generated mechanical effects (like liquid microjets, turbulent mixing, shock waves, and acoustic streaming) and collective interplay is identified as the responsible mechanism. Therefore, for sono-acceleration of the synthetic process, separating the dominant responsible cause (material, solvent used, and process parameter) out of these intermittently connected mechanical effects require highly controllable experimentations [85].

1.3.2. Sonocrystallization

Since its introduction to scientific community in 1927, sonocrystallization is another major viable of ultrasonic-sonochemistry with many significant deliverables for nanoscience [86]–[89]. Possible mechanistic reasoning of sonocrystallization events are actively taken up for research. e.g. Whether it is ambient room temperature (RT) or mostly athermal shock wave-dominated happening is explored. In fact, the investigated sonocrystallization experimentation includes (1) aspirin as model for the molecular crystal [90], (2) organic molecules [91], (3) alkali halides as the ionic crystals [92], etc as illustrations. Such experimental studies suggest that the direct material and sonics generated shock-wave interaction as the facilitating mechanism. However, there is no generic acceptance. The conceptualization of sonocrystallization based on these few individual case studies is not practically possible. Extensive data collection by variety of experimentation leading to conclusive inferences is required. Besides, a recent detailed review highlighting all the possible mechanistic happening on sonocrystallization in the solution phase is reported [93], [94].

1.3.3. Sono-agglomeration

Sono-agglomeration as a result of a high-velocity inter-particle collision and subsequent fusion by melting delivered grain growth is also another most common

physical viable available to the material scientists. Literature on these encountered sonochemical-assisted assemblies obtained are: (1) graphene oxide (GO) with carbon nanotube (CNT) [95], (2) 2D-materials (graphene, MoS₂, h-BN etc) decoration on the polymer derived flexible substrates [96], (3) mesocrystals of TiO₂ and BaTiO₃ [97]–[100], and (4) silica-spheres [101] etc. The case of metals sono-agglomeration achieved during sonoprocess is extensively investigated by Suslick and co-authors et al [102]–[104]. Two particular outcomes of the metal sono-agglomeration studies are; if (1) particles collide head-on, it leads to agglomeration; otherwise if (2) the collision is at the glancing angle will detach inbuilt respective metals surface oxide layers by cracking. The removal of surface metal oxide will finally ramp up exposed metallic surface reactivity. Thus, a convergence exists between (1) sonocrystallization leading to the generation of the crystalline nucleus, which on the other hand is supported by, (2) the sono-agglomeration driving these evolved crystal nuclei to coalescence, thereby resulting finally in a smallest crystal building unit, and interaction of these will lead to crystal growth.

1.4 Energetic Materials

The energetic material (EM) processed out of the nano-Al as fuel and conventional metal oxide as its oxidizer of interest to the current thesis investigation, are introduced sequentially below.

1.4.1 Nanoenergetic Materials

Conventional thermitic materials made of μ -sized metals and oxide of a less reactive metal as components with low-energy release rate and long-ignition delay, has continued applications in rail road-track welding [105]–[107]. These conventional thermite reactions is diffusional, and energy release is limited by the thick alumina shell covering the μ -Aluminum (Al) fuel particles [108]–[110]. Pre-stressing of these μ -Al core- alumina shell particles is also attempted, to improve reactivity. The flame

rate investigation of such pre-stressed µ-Al fuel, illustrates an enhancement of even 68 % is recoverable, which is similar to that currently observed for the best case scenario of nano-Al particles utilized as fuel [111]. However, the advancement of chemical processing protocol to deliver, intimately mixed nanostructured composite formulations of both nano-Al and a desired metal oxide dominates the energetic applications [112]–[120]. These composites are otherwise named as the metastable intermolecular composites (MICs; also called nanoenergetic materials (NEMs)); with enhanced demonstrated thermo-physical performance is one of the materials of research interest. In these reports, one common agreed conceptualization for enhancement is ascribed to the increased interfacial contact area made available for the intended solid-state heterogeneous reaction and to the intermittent contact facilitated reduced diffusion distance. The composite metastability is ascribed to the existing inertness prior to the thermal, laser, or electrical actuation, and also to ignition by mechanical impact, spark, and frictional force respectively [121]–[127]. For example, when ignited these MICs undergo a self-sustained exothermic reaction process to generate almost twice the higher volumetric enthalpy (i.e., TNT (conventional explosive) = 7.22 kJcm^{-3} , and $\text{Al/I}_2\text{O}_5$ (MIC) = 25.7 kJ cm^{-3}), as compared to that of the conventional monomolecular high-energy explosives [128].

1.4.2 Metallic Aluminium as Fuel

Metallic Al is one of the ideal and widely experimented fuel candidates. For example in propellant NEM design, its addition brings in delivery of (a) high heat of combustion (Enthalpy = 31kJ/g), (b) increases propellant energy density, (c) lowers combustion instability, and (d) facilitates the formation of low molecular weight exhaust gases release respectively [129]. It also leads to the system specific impulse increase at an economically lower-cost. Another detailed investigation on these set of NEMs by Zachariah and group et al, on whether the gas phase oxygen generation from solid oxidizer is an essential prerequisite to initiate NEMs reaction had

interesting outcomes to be noted in the current context [120]. It is found that for specific NEMs like: (1) Al/Bi₂O₃ and (2) Al/SnO₂ ignition occur below the oxygen release temperature from its corresponding above mentioned oxidizers, where as for the second set of specific NEMs like: (3) Al/Co₃O₄ ignition results above its oxidizers oxygen release temperature. Further, where as for these other specific set (4) Al/MoO₃, (5) Al/Sb₂O₃, and (6) Al-WO₃ NEMs respectively, had oxidizers that did not release any oxygen or gas phase product. In spite of this, these last sets are seen to ignite. It demonstrates that oxygen or gas release is a necessary, but not an essential sufficient condition to determine whether or not the initiation of these NEMs reactions. NEMs reaction is thus, a result of the direct interfacial contact between Alfuel and another oxidizer of choice, facilitated by the condensed phase mobility of the reactive species named as reactive-sintering [120], [130]. Many synthetic approaches for NEMs fabrication to develop nano-architecture having nano-Al fuel and oxidizer intimately packed for safer handling are; (1) NEMs composite droplet into core-shell structure [131], (2) filling the oxidizer in protein cages (biothermite) [132], [133], (3) nanowire-based thermite membrane [134], (4) carbon nano-fibers [127], and (5) in the form of both bi-layer/multilayer nanofoil formulations [135]– [139], respectively. The one and only objective of such synthetic protocol is to achieve tunability and efficient thermo-chemical and energy release attributes.

1.4.3 Nanostructured Ceria as Oxidizer

Cerium (IV) oxide (CeO₂) is an active candidate extensively used in solid oxide fuel-cells, and in catalytic converter of toxic species of automobile exhausts, due to its exceptionality recognized reversible reduction-oxidation attribute ($2CeO_2 \leftrightarrow Ce_2O_3 +1/2 O_2$) [140]–[146]. Importantly, the performance of low-emission power generation sources such as solid- oxide fuel-cells depend on the ability of nanocrystalline-ceria (nc-ceria) to accept, store, release, and transport oxygen ionic species. In doing so, while in reducing environments the nc-ceria undergoes a series of non-stoichiometric

oxide phases leading to Ce₂O₃ as the end reduced product, this generated product in turn again easily take-up oxygen in oxidizing environment to return back to its fully oxidative state. Examined in temperature programmed reduction (TPR) experiments, the nc-ceria highlights a four-fold increase in oxygen storage capacity (OSC), and also the presence of more reactive surface superoxide (O²⁻) ions [147]–[149]. Theoretical density functional investigations on structure stabilization conducted thereafter, reaffirms this experimental evaluated increase in OSC, to fully surface adsorbed supercharged superoxide ions rather than bulk-lattice oxygen species activity [148]. This supercharging effect is particle size dependent leading thereby to largest OSC for the ultrafine nc-ceria particulate. Thus, an enhancement in the OSC is attributed to the active source of oxygen species at much lower temperatures (TPR peaks at ≈ 325 °C and 425 °C), while additional higher temperature bulk and surface lattice oxygen TPR peaks also exist [149]. The unique demonstrated fascinating properties of nc-ceria like larger OSC and its facile release are the attributes of choice, which encourages the current investigation into nc-ceria as an oxidizer candidate for NEMs design.

Page Intentionally Kept Blank

Chapter-II

Experimental and In-situ TEM electron beam irradiation techniques

Padhi, S.K., Gottapu, S.N. and Krishna, M.G., 2016. Electron-beam irradiation induced transformation of Cu₂(OH)₃NO₃ nanoflakes into nanocrystalline CuO. Nanoscale, 8(21), pp.11194-11201.

Keywords:

FESEM, XRD, TEM, UV-VIS-NIR, PL, RAMAN, TG/DTA, TG/DSC, Particle Size analyzer, TEM electron beam (e-beam)

2.1 Material Characterization

The material characterization instruments employed in the thesis are listed below with an introductory note on their physical, operational-principles, and specifics to the scientific data collection modes. The sequence of presentation is as follows.

- 1. structural (X-Ray Diffraction (XRD)),
- 2. morphological (Field Emission Scanning Electron Microscopy (FESEM), Atomic Force Microscopy (AFM)),
- 3. microstructural (TEM),
- 4. thermal (Thermo Gravimetric- Differential Thermal Analysis (TG-DTA),
 Differential Scanning Calorimetry (DSC)),
- 5. particle size (Particle Size Analyzer (PSA),
- 6. spectroscopy (UV-Vis-NIR, Raman, Photoluminescence (PL)), and
- 7. In-situ TEM standardization, respectively.

2.2 X-Ray Diffraction

Bruker D8 Advance X-ray diffraction system equipped with; θ -2 θ ° vertical Goniometer (250 mm), Cu anticathode (operated at 40 kV, 30 mA), LynxEye linear detector (3° 2 θ detector window, divergence slit 0.3 mm), and Ge (111) Johansson type monochromator is employed for phase purity and structural characterization. The diffractometer is operated by Diffracplus software in a continuous locked couple scan mode for the required 2 θ range having 0.02°, 0.4 s, and 15 rpm as increment, time per step, and sample stage rotation. The incident angle (= θ) is between an X-ray source and a sample placed. Detector angle (=2 θ) is the angle between the incident beam and detector. The incident angle is always half of the detector angle. The schematic of the sample mounted in Bragg-Brentano geometry is shown in fig. 2 1(a). The diffraction vector, which is the vector bisector of the angle between the incident and scattered beam, is always normal to the sample surface (Bragg-Brentano

geometry). X-rays are scattered in a sphere around the sample. A cone along the sphere corresponds to a single Bragg angle=2 θ . A linear diffraction pattern is formed as the detector scans through an arc that intersects each Debye cone at a single point, thus giving the appearance of a discrete diffraction peak [150]. Standard corundum sample is checked for peak shift (δ (2 θ) = 0.02°), and FWHM =0.04°) calibration and the prominent (104) peak fitted with Lorentzian peak shape is presented in fig. 2 1(b).

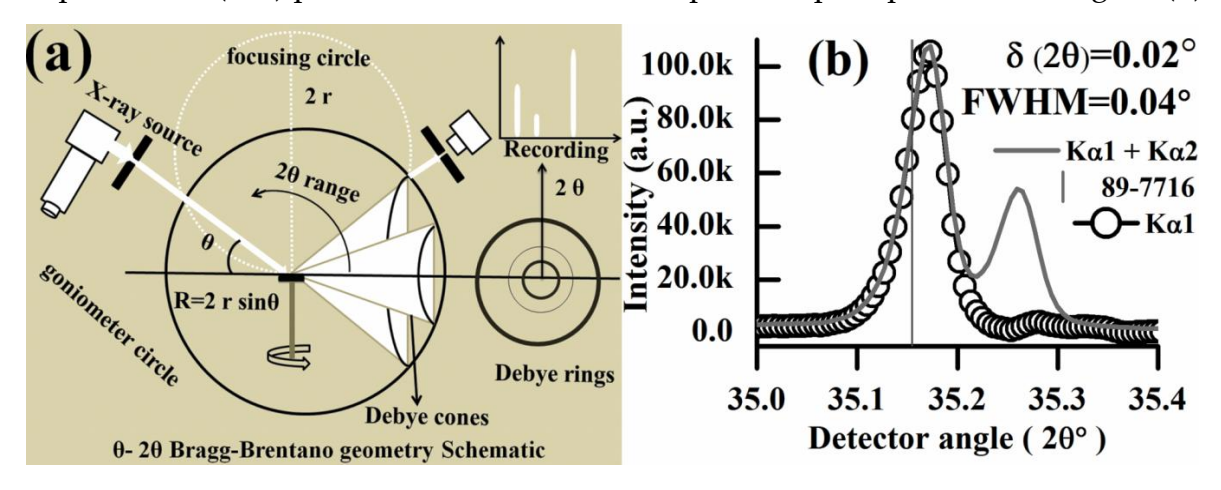


Fig.2 1 (a) Reflection (Bragg-Brentano geometry) schematic, (b) Corundum standard acquired with 2θ step width of 0.02° .

2.3 Field Emission Scanning Electron Microscope

Carl Zeiss ULTRA-55 FESEM with Oxford INCA X-Act energy dispersive spectroscopy (EDS) system is utilized to obtain samples topographical (SEs) and compositional quantification (BSEs) at magnifications levels ranging from 10 X to 1000 K X (12 X -900 K X in SE mode, 100 X- 900 K X with EsB detector). Mostly, secondary (SEs) and back scattered electrons (BSEs) are tracked. The SEs are ejected from the outer atomic shell of the sample and moves at energy less than 50 eV. SEs are categorized into SE1 (originated from primary beam impact point), SE2 (generated after multiple scattering inside interaction volume and leaves the sample surface at greater distance from primary impact point), and SE3 (generated when backscattered electrons hits chamber wall or the lens system). All the generated electrons with energy higher than 50 eV are backscattered electrons (BSEs) and

originate from much deeper range of interaction volume by elastic scattering. The backscattered electron coefficient increases with atomic number and used in providing atomic number contrast or compositional contrast images along with depth information (see fig. 2 3) [151]. The standard detectors for available are (1) Incolumn In-lens detector (termed as annular SE detector): best high resolution surface morphological information, (2) In specimen chamber ET-SE detector (Everhart-Thornley type): Optimal topographical information, (3) Annular shaped in-column EsB (Energy selective backscattered electron) detector: clear compositional contrast, and (4) In-column AsB (Angle selective backscattered electron) detector at very short working distance (~1mm) above sample respectively. A schematic of FESEM standard detectors locations are shown in fig. 2 2. The EsB detector with a filtering grid for SE is placed above In-lens detector and is typically collects BSEs in a cone angle of 15° to the primary electron beam.

The FESEM instrument is controlled by SmartSEM® software. A graphical user interface directs data acquisition and processing. For imaging and compositional analysis, electron source emitted electrons are accelerated by applied accelerating voltage (EHT) between 5 kV and 20 kV. The acquired images of this thesis are obtained employing SEs through In-lens detector, having standard aperture of 30 μ m unless otherwise stated. FESEM samples are prepared by dispersing powder samples (or sticking pressed pellet) on carbon tape and mounting it on an aluminum specimen holder. Insulating samples are gold sputter-coated (EMITECH SC7620 Mini sputter coater) in the air at 2 x 10-1 mbar pressure label for 120 s with 10 mA plasma current (sputtering rate approx. = 0.7 Å/sec at 1 kV applied voltage). The microscope operates in 0.1 kV to 30 kV range with Schottky field-emitter type electron source (W (100) tip coated with a layer of ZrO2; stability of probe current > 0.2%/h) emitting 4 pA to 10 nA. The FESEM has a stated resolution of 1.0 nm @ 15 kV, 1.7 nm @ 1 kV, and 4.0 nm @ 0.1kV along with seven integration and averaging modes for noise reduction and image processing.

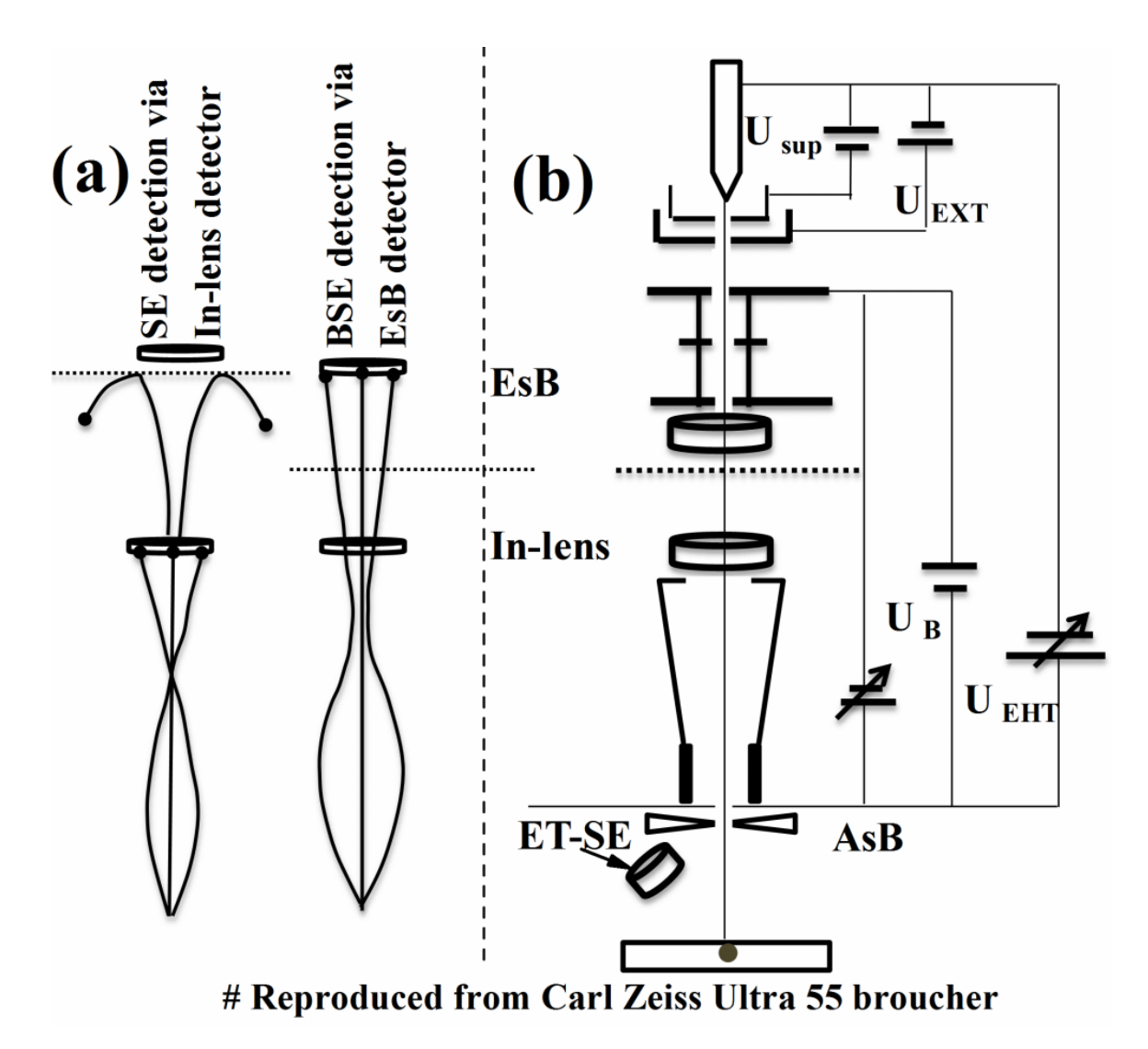


Fig.2 2 Schematic representation of (a) functioning of the filtering grid in separating SEs and BSEs, (b) different detector positions in the Gemini column of Ultra 55 FESEM.

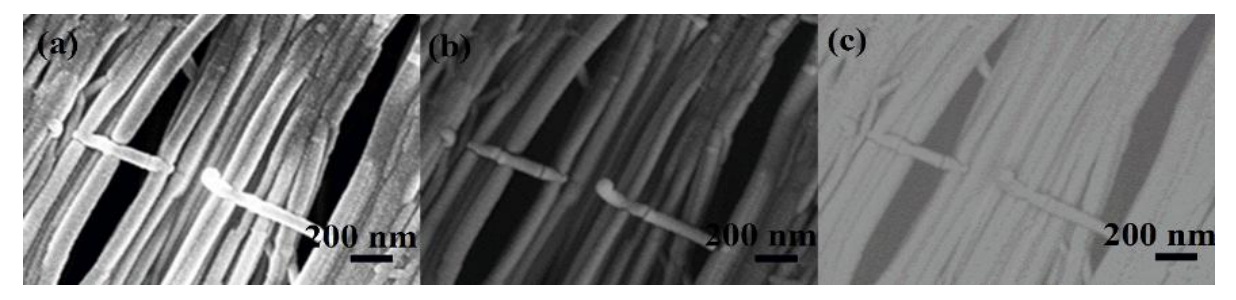


Fig.2 3 Acquired FESEM micrographs employing signal collected by (a) In-lens, (b) SE2, and (c) BsE detector.

Energy dispersive spectroscopy (EDS) analyses the generated X-ray energies from the sample placed under an electron beam to provide elemental composition. Each element in the sample has its characteristic X-ray emission energies, thereby counting the X-ray emitted photons of different energies an elemental quantification is provided. Oxford INCA X-Act EDS system uses a 10 mm² Peltier cooled silicon drift detector sensor (SDD) fabricated from high purity silicon having a large area of contact on the entrance side facing the incoming X-rays. On the opposite side, there is a small central anode, which is surrounded by a number of concentric drift electrodes. The schematic and operation of SDD are in fig. 2 4. The incoming characteristic X-rays energies are converted into a proportional amount of electron cloud with a charge by the ionization of atoms in the semiconductor (n-Si) crystal. These electrons are then collected at the anode (n*-Si) by a gradient-field applied between drift rings. Anode acquired charge is converted into a voltage signal by the FET preamplifier.

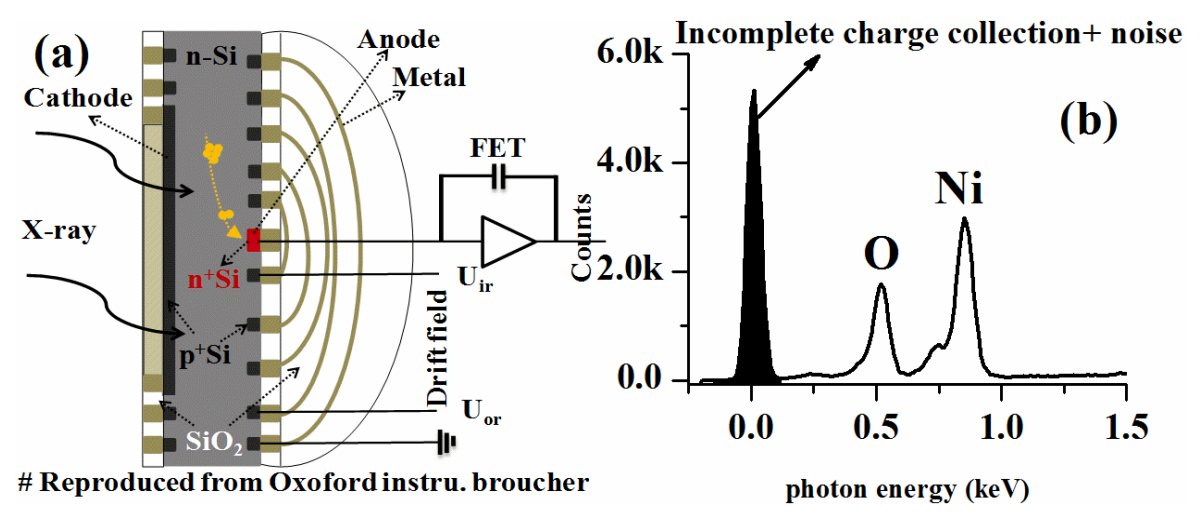


Fig.2 4 (a) SDD detector schematic and operation, (b) Highlighted 0 keV noise peak in EDS spectra (mostly excluded in subsequent thesis EDS presentations)

Lastly, the generated voltage-signal is fed into the pulse processor. The pulse processor identifies the energies of the incoming X-rays and then provides a digital count to the multichannel computer analyzer. The EDS detector manufacturers specify the resolution using the X-rays of manganese K_{α} line. At the Mn K_{α} energy

=5.9 keV, detector specified resolution is about 135 eV (MnK $_{\alpha}$ =FWHM). The EDS spectral data presented in this thesis is acquired employing EHT=20 kV, WD=8.5 mm, and with 60 μ m aperture for about 180 s. In EDS analysis, the detection limits are typically of about 0.1% by weight, and can be reduced further by increasing long counting times [152]. Line scans and X-ray maps can also be generated based on requirements.

2.4 Transmission Electron Microscope

In a TEM, a thin sample (5-100 nm) is probed with an electron beam of uniform current density. The acceleration voltage employed for these instruments is of the order of 100–200 keV. For, 100 keV electrons have wavelengths λ =0.0037 nm much smaller than the size of an atom (0.1 nm) and are capable of resolving the atomic planes in a crystal delivering high-resolution imaging [153]. This image contrast in TEM comes from the mass-thickness variation or Bragg's scattering. Lighter atoms in the sample scatter fewer electrons than heavy atoms; therefore, they generate weak contrast. Both types of scattering (elastic or inelastic scattering) are useful for material analysis, but inelastic scattering has the side-effect of being responsible for the specimen damage [154]. The common TEM modes used in the thesis as data; include bright-field (BF) imaging, dark-field (DF) imaging, selected area electron diffraction (SAED), and high-resolution imaging (HRTEM). The signals arising mainly from elastic scattering are mostly used in this work. The schematic of the imaging and diffraction operating mode of a TEM instrument is plotted in fig. 2 5. The conventional operating modes in TEM are:

(1) Bright-Field:

The objective aperture passes the transmitted beam to form the image. The SAED aperture is retracted, and the image is formed on the image plane of the objective lens. It is the most common imaging mode in TEM.

(2) Dark-Field:

Same as the BF, except the objective aperture passes only the diffracted electrons that are not in the direct beam to form an image. The specimen regions that diffract are of brighter appearance in DF imaging mode. It is mostly employed as a tool for identifying inorganic nanoparticles in biological or polymer matrices [154].

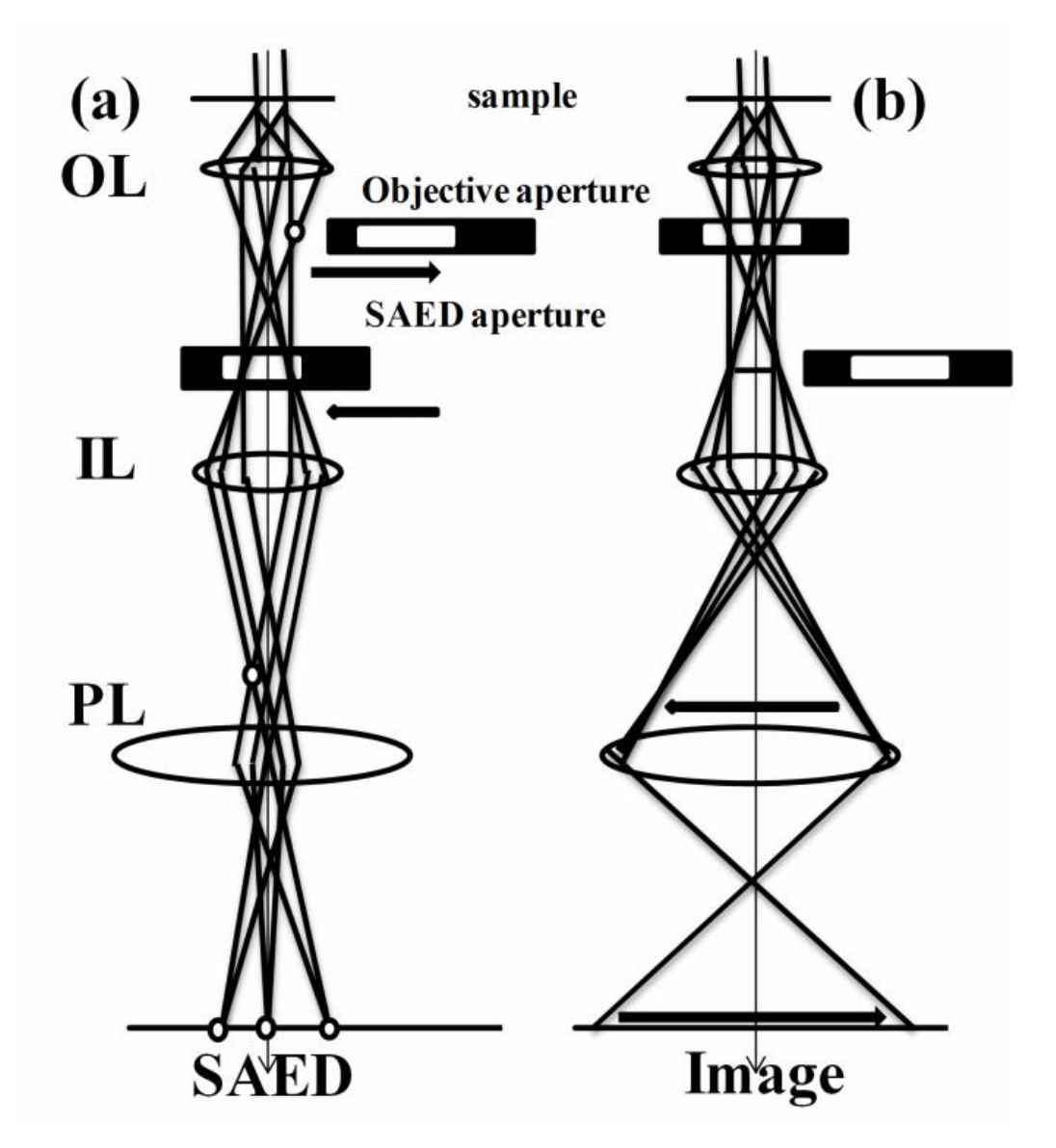


Fig.2 5 TEM basic operation modes schematic (a) diffraction mode, and (b) Imaging mode. (# reproduced from B D Williams and C B Carter TEM a text book for Material Science)

(3) Selected Area Electron Diffraction:

Objective aperture is removed, and the image is formed at the back focal plane of the objective lens. SAED aperture passes the image of the selected region. SAED contains crystal structure and orientation information.

(4) High-Resolution Transmission Electron Microscopy:

HRTEM is widely used to study the crystalline state of grains in nanometer. It's, in fact, a coherent BF image of the transmitted beam and the diffracted beams of the interested grains. Unlike BF and DF imaging, where the amplitude contrast is more important, in the high-resolution imaging phase-contrast dominates. The phase information is transformed into an image form by the contrast transfer function (CTF, see fig. 2 6). The factors that affect CTF are aperture sizes, attenuation of the wave, and aberration coefficients of the lens (spherical Cs and chromatic Cc). It is an oscillatory function with zeros (no transmission) and passbands. When CTF is nonzero (i.e., means transmission). For negative CTF, the phase contrast is positive, meaning that atoms would appear dark against a bright background. When CTF is positive, the phase contrast is negative, meaning that atoms would appear bright against the dark background. When it is zero, there is no detail in the image, and subsequently, the first zero (transmission of the CTF) defines the resolution limit, Kl at which lattice planes with $g < K_1$ show the same sign of contrast. The presence of zeros in the CTF at specific wave vectors of Ki means, gap that lattice planes with $g_{hkl}=K_i$ will not show any contrast in the phase-contrast image. For $K > K_l$, it oscillates between +1 and to -1. The CTF can be optimized by a particular negative value of defocus (Δf). It is known as Scherzer-defocus and is defined as Δf_{sch} = -1.2 (Cs λ) 1/2, where λ is the wavelength of the electron. At Scherzer-defocus all the beams with g < K₁ will have nearly constant phase and provide maximum information into the image. The first zero in the Scherzer-defocus determines microscope resolution limit. The red line on the defocus map (frequency vs. defocus vs. intensity) indicates the defocus at which 1D-CTF is calculated. The HRTEM, in general, is used to give lattice fringes or atoms down to the angstrom scale based on aberration correction. TEM is carried out on an FEI TECNAI G² S-Twin instrument at an accelerating voltage of 200 kV.

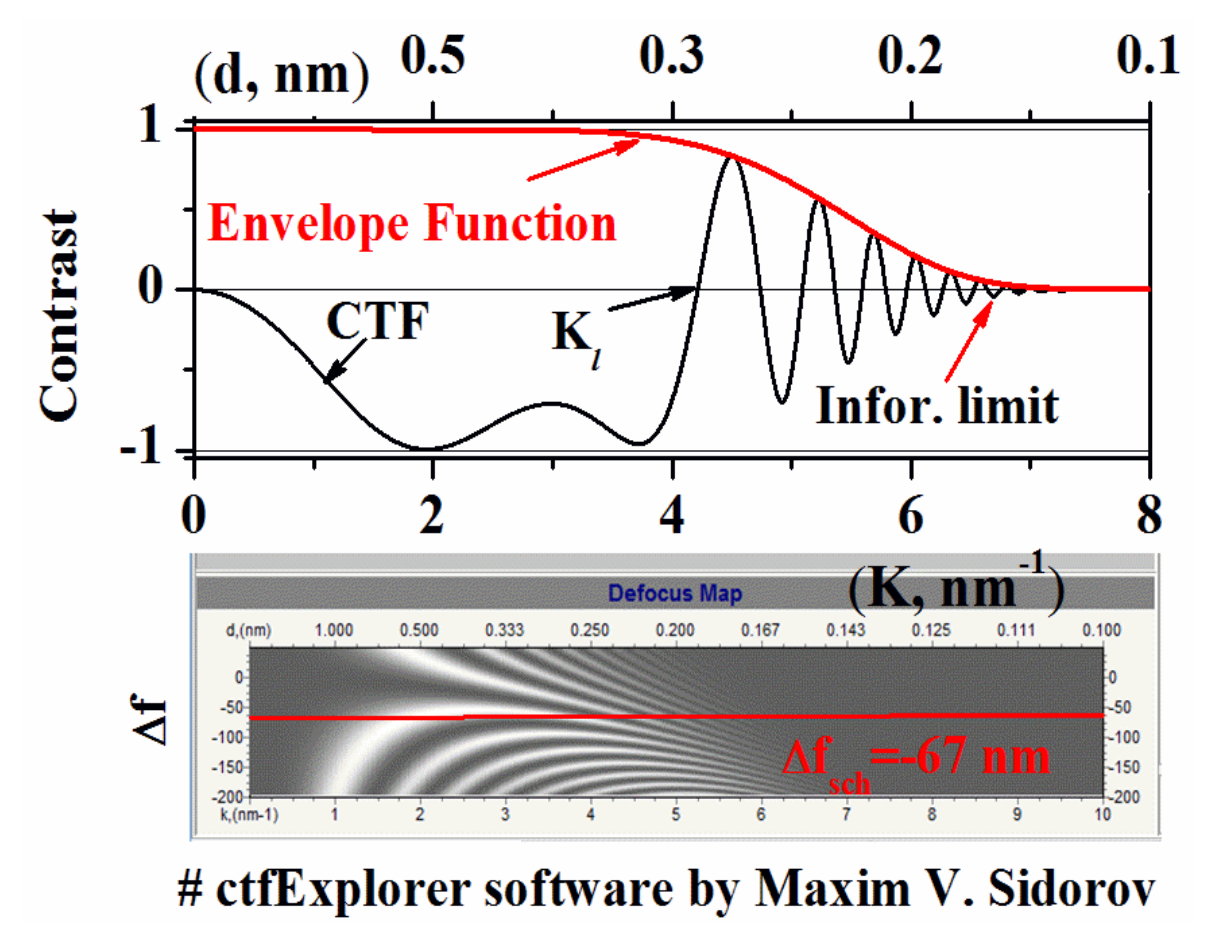


Fig.2 6 A typical CTF plotted for a 200 keV microscope at a Scherzer defocus (Δ_{fsch} =-67 nm) with Cs = 1.2 mm, Cc =1.2 mm, Δ E=0.6 eV, HT ripple = 0.25 ppm, Obj. Lens Instabilities = 0.5 ppm, Focal Spread =1.97 nm, Convergence =0.30 mrad and K is the spatial frequency. Under these conditions the lattice planes of 2.5 Å spacing can be resolved.

2.5 UV-Visible Spectroscopy

Optical properties of solution dispersed samples taken in a quartz cell are studied using the JASCO V-570 UV-VIS-NIR dual-beam spectrophotometer [155]. Two lamps are used. Usually, a deuterium lamp (λ =190-350 nm) is used for the ultraviolet region and a halogen lamp (λ =330-2500 nm) for the visible and NIR region. In this way, radiation across the whole range is scanned by the spectrometer. A reference cell containing only the solvent is used. Light passes through the sample and reference

cell simultaneously during measurement. The transmitted radiation is detected, and the spectrometer records the absorption spectrum by scanning the wavelength of light passing through the cells. A schematic diagram of the UV-Visible spectrophotometer instrument is shown in fig. 27.

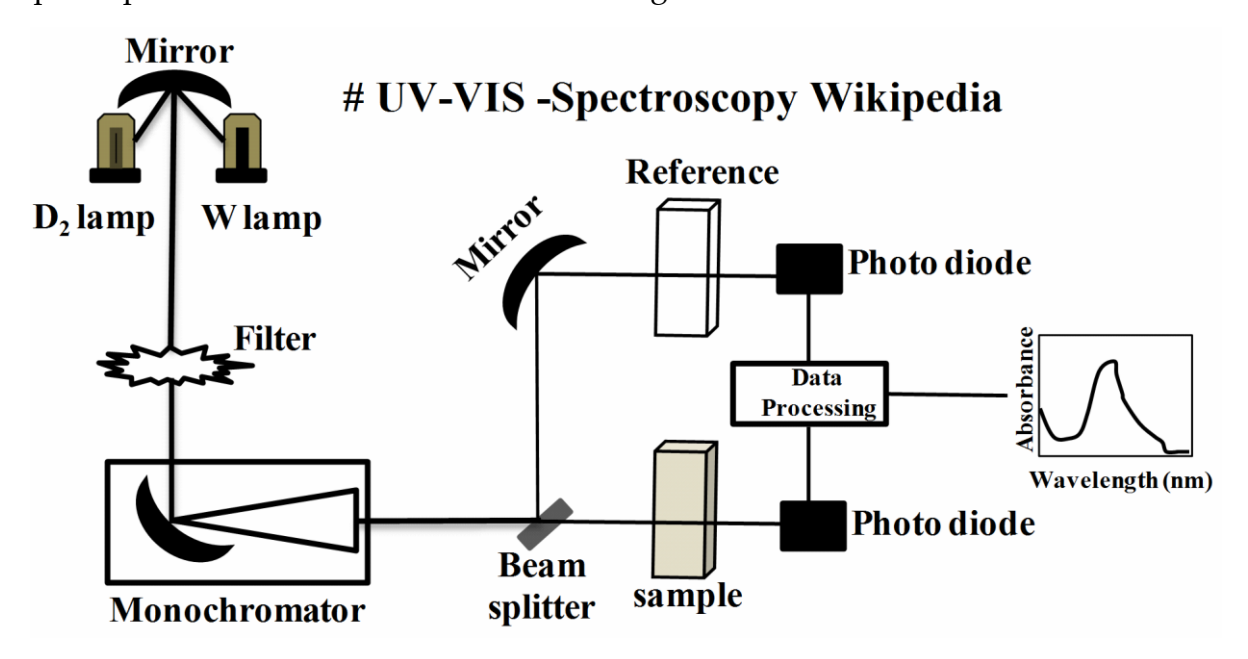


Fig.2 7 UV-VIS-NIR spectrophotometer instrument schematic

2.6 Photoluminescence Spectroscopy

The photoluminescence spectral data are acquired by using a confocal Raman spectrometer (Alpha 300, Witec Germany) attached with a piezo-driven controlled scanning stage and objective of 20X 0.4 NA AFM/SNOM at room temperature (RT). An Nd: YAG laser at 532 nm is employed as the excitation source. Also, the Horiba Jobin Yvon model FL3-22 spectrometer is employed for other excitation wavelength requirement.

2.7 Raman Spectroscopy

The basic principles and operation illustrating Raman spectroscopy utilization for nanomaterials analysis can be found in books published [156], [157]. In the thesis, Raman spectral data is acquired using Nd: YAG laser at 532 nm in the backscattering

geometry. A CRM spectrometer attached to a confocal microscope and 100X objective to the CCD detector (model alpha 300 of WiTec, Germany) is used.

2.8 Thermal Analysis

For simultaneous thermogravimetry- differential scanning calorimetry (TGA/DSC), powder samples of (3±0.2) mg are taken in alumina cups (90 μ L) with UHP nitrogen flow =100 cm³/min is maintained as the purse and protective gas. The TGA/DSC runs are carried out from ambient to 1300 °C. TGA and DTA sensitivity are 0.1 μ g and 0.001 °C, respectively.

2.9 In-situ TEM Studies

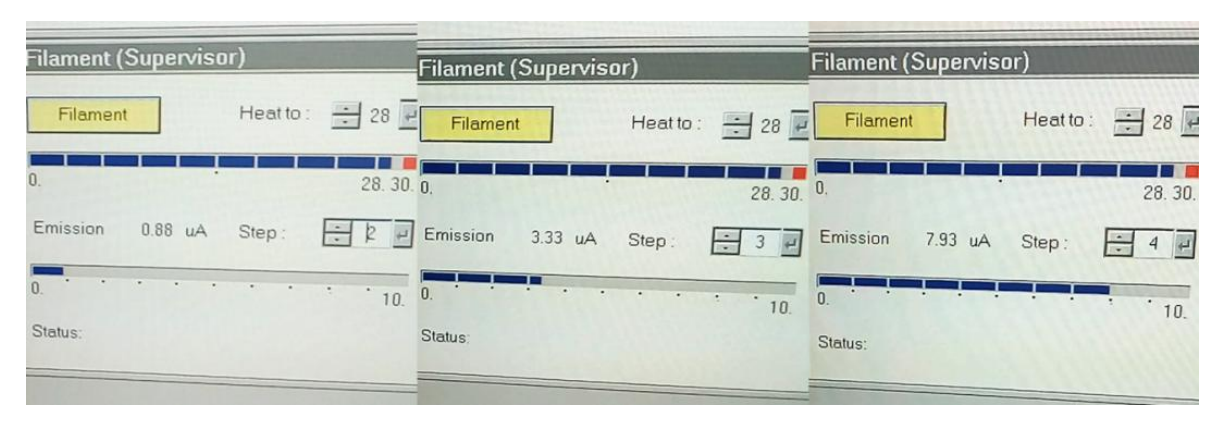


Fig.2 8 Filament Supervisor with emission current steps.

An initial attempt of in-situ TEM investigation employing TEM e-beam is adopted on a radiation-sensitive (copper hydroxy nitrate (CHN)) material nanomaterial. It is then extended to nc-ceria (which has both radiation damage and self-heating attribute) to examine and evaluate crystal growth. First a protocol to examine CHN is established, which is then extended to nc-ceria and nano-Al, materials of this thesis. These CHN samples are susceptible to damage under the TEM e-beam irradiation conditions, commonly used for HRTEM imaging [53]. The preferable way to mitigate such a problem is to use low e-beam emission current (TEM User Interface Filament Supervisor tip emission current steps). The emission (snapshot from the TEM console

screen) displayed below in fig. 2 8. Step-2 filament emission current is used for the present TEM probing. Whereas the CHN flakes micrographs with step-4 filament emission are modified.

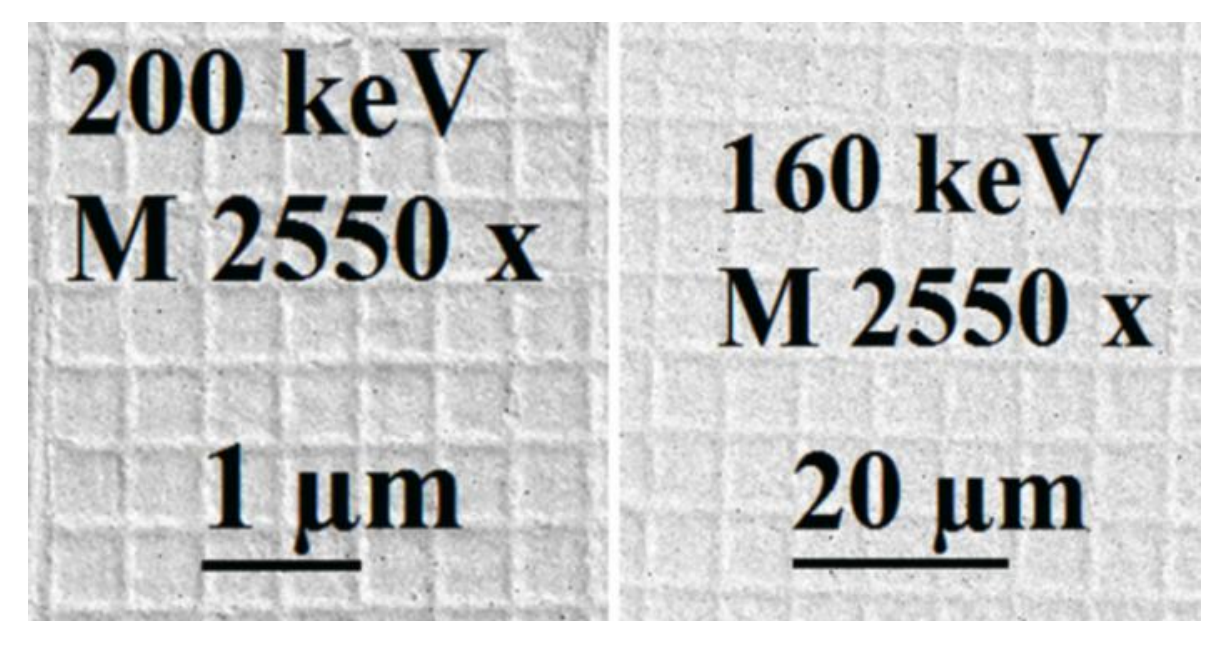


Fig.2 9 Standard grating at two different voltages demonstrating TEM instrument magnification calibration and repeatability. The actual distance of two rectangular squares at 2500 x is about 0.93 μm . The shown distance for calibrated 200 keV energy is near about 1 μm . The scale bar for the uncalibrated 160 keV should be near about 1.4 μm not 20 μm as obtained by microscope software.

Another important aspect is the TEM calibration. It can be in simply stated that once TEM is calibrated, remains accurate until a significant failure or changes take place in the microscope column. Calibration of TEM is of utmost importance since the demonstrated work will, otherwise, remain irreproducible. The primary calibrations TEM instrument require are:

- (a) Magnification Calibration (images)
- (b) Camera constant calibration (diffraction patterns)
- (c) Image/diffraction pattern rotation calibration (the relationship between the images and the diffraction patterns)

To ascertain the TEM instrument is well-calibrated, the magnification calibration part of TEM is demonstrated here:

The standard specimen used to demonstrate is diffraction grating replica product no. 607, obtained from Ted Pella, Inc. When imaged at around 2500 x the line spacing is 0.463 mm. The scale bar lengths acquired at 2550 x with two different e-beam voltages (calibrated voltage=200 kV and un-calibrated voltage= 160 keV) are shown in the fig. 2 9.

2.10 Nano- Particle Size Analyzer

Anton parr GmbH, Litesizer 500 model light-scattering instrument is used for the particle size analysis (PSA) of liquid dispersions. Laser of wavelength 658 nm is used. Samples in liquid dispersion taken in quartz cuvettes at side scattering angle of 90° are recorded.

2.11 Atomic Force Microscopy

Seiko SPA-400 Scanning probe microscope is used in the intermittent-contact DFM mode for both topography and corresponding phase image acquiring. The detailed principles and AFM modes of operation can be found elsewhere [158]. DFM standard Silicon microcantilevers (SI-DF20, Al back coated) of 225 μ m length and 10 μ m tips are used. The cantilever resonant frequency, spring constant for torsion, and elongation are 134 kHz, 100 N/m, and 13 N/m, respectively is used

Chapter-III

"Non-Classical Crystal Growth Recipe":

An investigation of near-neighbour environment on the surface/interface attributes of the nanocrystalline ceria

Cite this document as

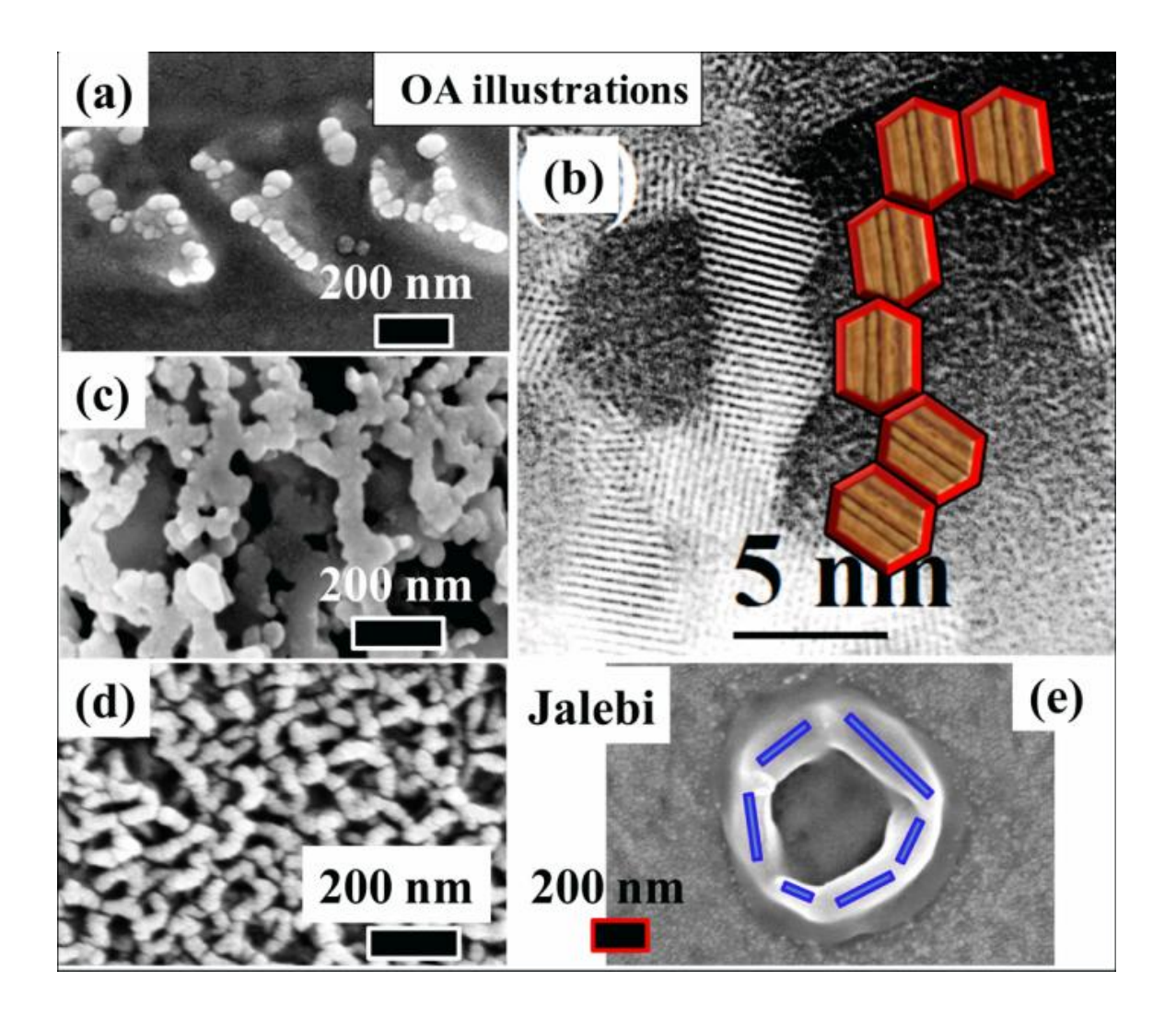
S. K. Padhi and M. Ghanashyam Krishna, 2019. Non-Classical Crystal Growth Recipe using nanocrystalline ceria a detailed review. *arXiv preprint arXiv:* 1911.07454

https://arxiv.org/abs/1911.07454

Keywords:

Non-Classical Crystal Growth, Oriented Attachment, Mesocrystals, Nanocrystalline ceria, In-situ TEM, Electron Beam Irradiation, Structural Phase Transition, 1D-ceria Fiber

Graphical Abstract



[Microstructures and morphologies of NCG]: Significantly Oriented attachment (OA) schematic and electron microscopy observations.

Abstract

In this chapter, room temperature (RT) precipitation of the nanocrystalline-ceria (ncceria) re-dispersed and subsequently size-reduced by 20 kHz probe sonication in 25 % ethylene glycol/75 % DI-water mixed media is investigated. The sonication result in three nanostructured products: (1) water-soluble supernatant nc-ceria (Ce_Sl@RT), (2) settled gelatinous nc-ceria mass (Ce_SS@RT), and (3) ambient dried nc-ceria solid powder (Ce_SP@RT) product, along with the parent RT nc-ceria (Ce@RT) precipitates. Surface/interface attributes are investigated systematically with the help of suitable spectroscopic probes. By following this synthesis protocol, the nc-ceria (Ce_SS@RT) is made to cohabit with a variety (water, ethylene glycol, air) of neighbors that lead to the distinct surface and interface termination. The physical and chemical aspects of these varieties of the specific surface terminated nc-ceria are explored coherently with respect to the Ce@RT precipitate. The second aspect of this chapter is devoted to the biomineralization for which the sonication derived Ce_Sl@RT is the candidate of choice. Aging of Ce_Sl@RT is physically tracked to mimic the natural aquatic medium crystal growth by the biomineralization process. In-situ TEM is extensively used to demonstrate the non-classical crystal growth mechanism physically. Uniquely TEM electron beam (e-beam) is exploited to aid both in the material manipulation and probing.

3.1 Introduction:

Non-classical crystal growth (NCG) is a nature formulated enriched protocol recently explored to grow advanced hierarchical materials of complex morphologies and composition [3]–[12]. NCG briefly is the "crystallization by building-units attachment." The building units' attachment is brought about by either material-specific or neighbouring environment directly contributing to the interaction and is the recognized sole growth deciding factor. Thus, in this inorganic crystal growth pathway the rule is to feasibly control interaction of growth directing building units' to realize tunable and novel technologically relevant morphologies.

There are numerous reports on (A) building units, (B) growth driving force, and (C) the final evolved hierarchical morphologies following the NCG protocol. Examples of *building units shape* are (1) PbSe nanocrystals [10], (2) ZnO nanocrystals [13], (3) α -MnO₂ nanowires [14], (4) 10-20 nm diameter PbTiO₃ fibers [15], (5) Au spherical seeds [16], (6) 1D-TiO₂ fibers [17], (7) δ-MnO₂ nanosheets [18], (8) 200-250 nm SnO₂ dodecahedrons [3]. The examples for *corresponding growth directing forces* are (1) dipolar interaction [10], (2) direction specific ZnO-ZnO interfacial interaction [13], (3) K⁺-stabilized ionic interaction [14], (4) surface electrostatic force [15], (5) intense laser pulses [16], (6) electric field [17], (7) hydrogen bonding [18], (8) pressure induced [3]. Meanwhile these interactions generated subsequent developed hierarchical morphologies are (1) PbSe nanowires and nanorings [10], (2) 1D-ZnO nanorods [13], (3) tunneled α -MnO₂ nanowires [14], (4) large-size 3D-PbTiO₃ hollowed fiber [15], (5) triangular Au nanoplates [16], (6) multilevel twinned tree-like branched TiO₂ [17], (7) nanoflowers [18], (8) µ-sized 3D-ordered SnO₂ superstructures [3], respectively. In addition, author's involvement in hydrothermal 1D-ZnO growth observations in the context of NCG protocol as a model system has been explored. The following sequence is (A) building units shape: shown as topview having (1) nanoparticles, (2) needles, (3) 3D-hexagonal discs, and (4) 2D-

hexagonal plates; whereas the (C) *corresponding evolved morphologies*: as side-view (1)-(4) of 1D- grown ZnO are illustrated in figs. 3 1 (a)-(d) respectively.

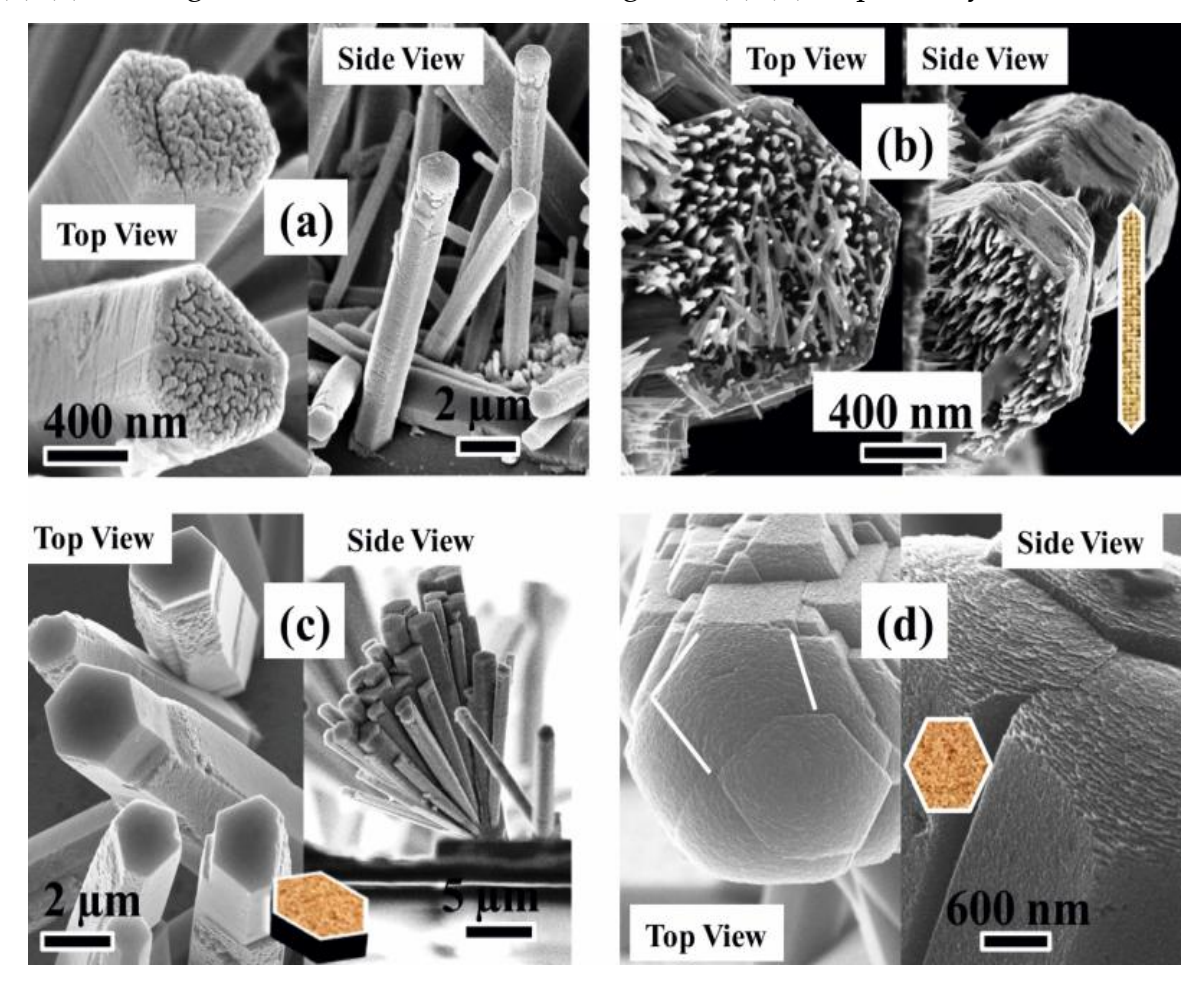


Fig.3 1 [Hydrothermally grown 1D-ZnO validating NCG scheme]: Building units in (a)-(d) as side view respectively (courtesy Y. Rajesh et al. unpublished data).

Importantly the unique morphology of aquatic biominerals and hierarchical motifs is the motivation and fundamental basis of the NCG scheme [19]. To illustrate these biominerals natural architecture two generic cases FESEM microstructure is presented below. These include fresh and salt water observed μ-sized silica (spongy skeleton in soft bodies) and calcium carbonate (appropriate mechanical strength at the sea bed living) are two ubiquitous biominerals morphology and microstructures are shown in figs. 3 2 (a)-(f) respectively [20]. The recent activities on biominerals involve, investigation on its formation and its subsequent extension to mimic other varieties of inorganic materials hierarchical growth is ongoing [3], [10], [13]–[18],

[21]–[25]. Significantly, the role of solvent water as an active participant in NCG is also investigated. The idea is to verify whether water facilitates in bringing localized order for inducing building units attachment [13], [26]–[30].

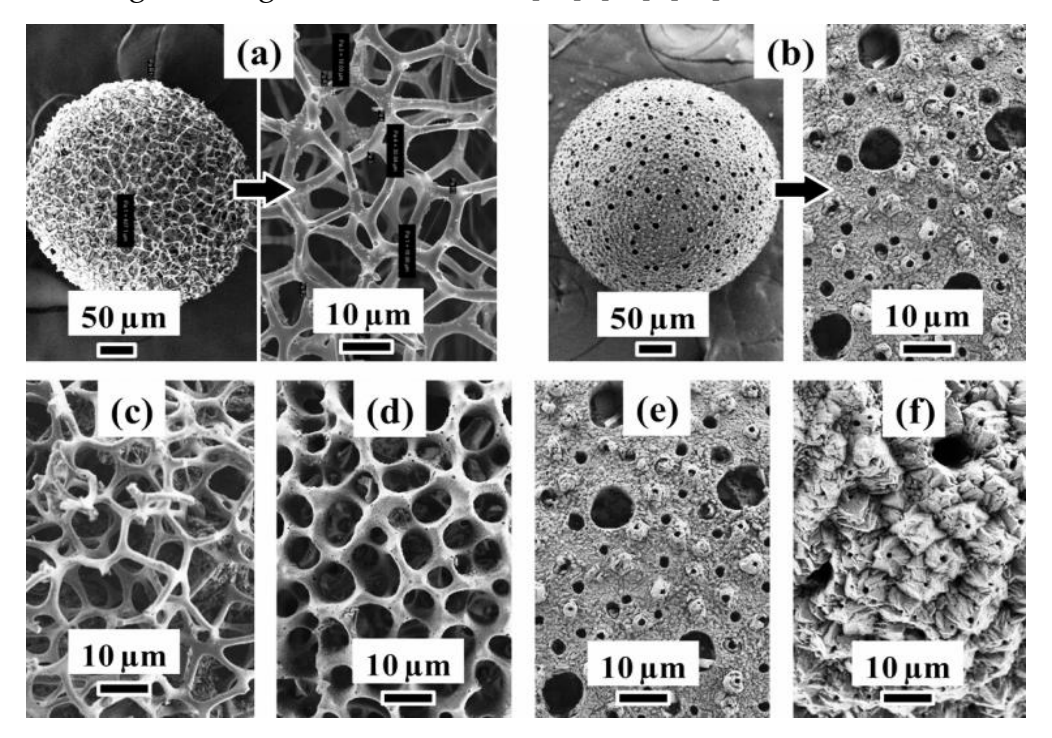


Fig.3 2 [Aquatic biominerals]: (a) radiolarian siliceous, (b) foraminifera calcareous skeleton, and (c)-(f) are microstructural evolution adopted to sustain neighbouring aquatic environment respectively (courtesy Prof. A. C Narayana unpublished data).

The building unit's attachment in systematic fashion by oriented attachment (OA), leads to an intermediate structure identified as mesocrystal [31]–[34]. The mesocrystals are single-crystalline in nature. After initial R Penn et al. TEM illustration [35] and continual exploration of OA during the ongoing attachment process is constantly under investigation to understand and develop new crystal growth avenues. Besides ongoing implementation of the OA in growing novel materials [36]–[40], most recent publication such as "OA Revisited: Does a Chemical Reaction Occur?" add valuable insights to the existing concepts [41]. Although development of mesocrystalline ceria structures had plenty of OA demonstrations [42], [43], this is not true in case of utilizing nanocrystalline spherical ceria (nc-ceria)

particulates as building units. An investigation relating to the existing Ce³⁺ surface charge steric difference, with that of the grain-interior Ce⁴⁺ observed in aqueous medium during hydrothermal processing is of significance to present study [44]. For illustration authors' data representing the aqueous hydrothermally processed mesocrystalline 1D-ceria morphological features, obtained from the nc-ceria spherical particulates by OA process is shown in figs. 3 3 (a) - (d). In it, individual nc-ceria spherical entities retain its microstructural distinctness but as a whole is single crystalline.

In realization of NCG for demonstration of the ongoing nanoscale physical ordering an essential part is played by the Transmission Electron Microscopy (TEM). The importance of such can be easily adjudged from the TEM micrographs presented in figs. 3 3 (a) - (d). In which a reaction quenched product not completely evolved into the 1D-nanorod localized structure is tracked for illustration. These microstructurally depict OA of nc-ceria spherical particles. It is the usual ex-situ TEM probe employed to validate NCG. However, frequent investigation employ dynamically tracking of NCG event by employing in-situ liquid cell TEM/STEM instrumentation[45]–[50]. Thus commonly, TEM electron beam (e-beam) is employed to probe. In contrast, its use for material modification in a controlled fashion is more limited [51]–[53]. Most recently Asghar et al. investigated nc-ceria employing TEM to justify its use as a standalone technique for probe and also tunable modification [52]. In his study, TEM e-beam activates water radiolysis and therefore acts as a direct participant in facilitating NCG growth derived 1D-ceria morphology.

Based on the literature reports on NCG, this chapter aims to design, develop and demonstrate NCG process in entirety, as a recipe. Nc-ceria is the prototypical material chosen for evaluation because of its unique attributes, such as (1) proven versatility in the field of biological applications, (2) cyclic oxidation-reduction, and (3) radiation damage injection and damage self-healing by introducing a change to its adjoining neighbour environment. These surface attributes are re-evaluated in the

present context specific to the role of aqueous oxidized and reduced immediate neighbour. The process of biomineralization is mimicked by designing nc-ceria water soluble colloidal dispersion. Lastly, it is demonstrated that the TEM e-beam can be explicitly employed as an in-situ probe as well as enabler of NCG. This particular case study of technologically important ceria can be extended to similar other radiation sensitive materials having also the radiation healing capacity for localized in-situ nanomaterials processing.

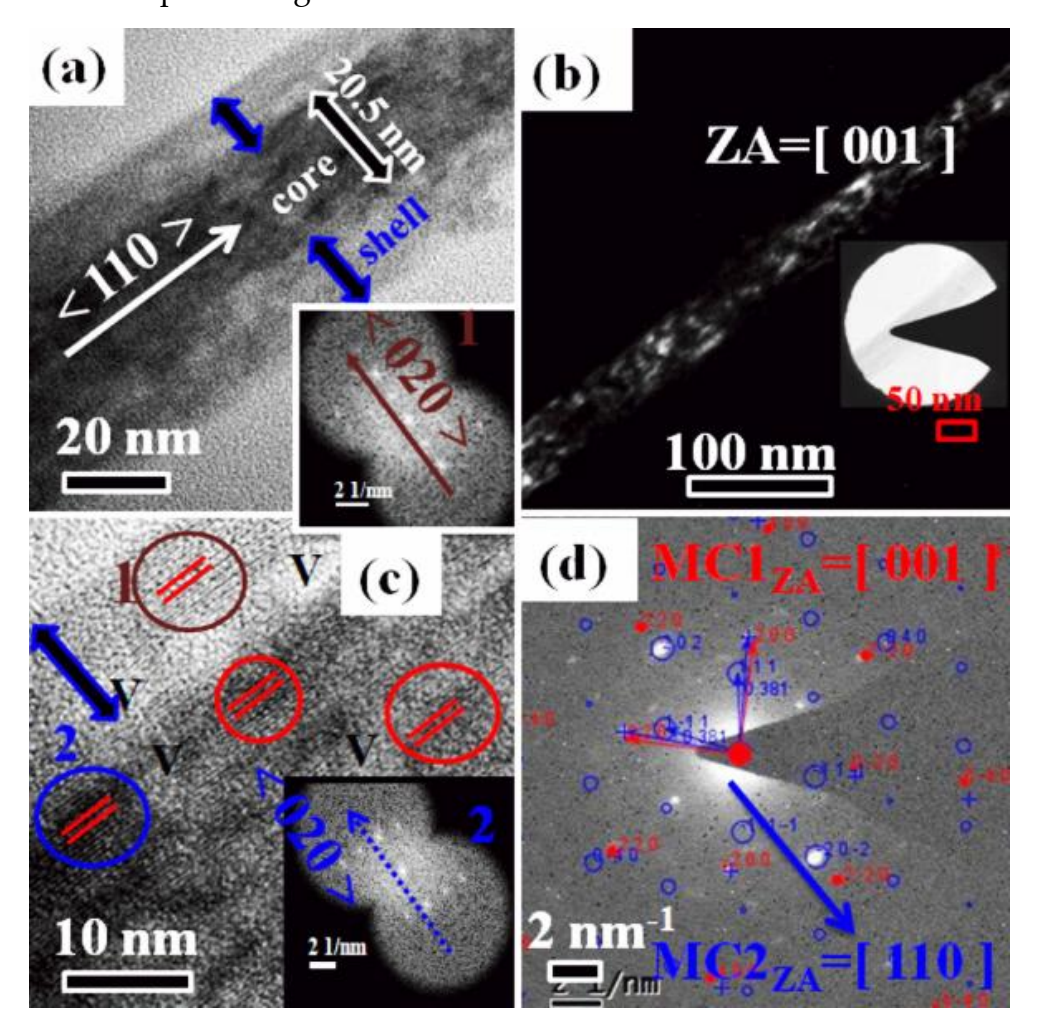


Fig.3 3 [1D-ceria Mesocrystal]: TEM (a) BF distinct core-shell region, (b) DF individual crystals as brighter dots, (c) FFT of nc-ceria crystal one from the core and other from shell region identical spot pattern with no rotation (shell crystal-1 inset in fig.1.2 (a), core crystal-2 as inset in fig.1.2 (c)), and (d) TEM-SAED spot pattern from the entire region showing lattice mismatch of core and shell an justification to OA character.

3.2 Materials and Methods

All experiments are carried out using ultrapure water Type-1 (Milli-Q water of resistivity =18.2 M Ω -cm at 25 °C, total organic carbon \leq 5 ppb). The 'ultrapure water Type-1' is referred to as DI-water. Measurements of pH are made on Digisun Electronics' digital pH meter model-707. Standard quartz cuvettes (3.5 mL, $45\times12\times12.5$ mm³, 190-2600 nm) of pathlength 10 mm is for UV-Vis spectroscopy, however for particle size distribution (PSD) of inner dimension $10\times10\times45$ mm³. Ammonium nitrate of Ranbaxy laboratory India and μ -ceria powder obtained from ESPI Metals USA are used.

THORLABS PM1000 laser power meter, carbon-coated Copper grids 200-mesh type-B are used in experiments. Energy-dispersive X-ray spectra (EDS) for compositional mapping is recorded with the Oxford Instruments X-MaxN SDD (50 mm²) system. The acquisition is made for 35 minutes at 15 kV, employing a SE2 signal.

3.3Synthesis and Charge Transfer transition

3.3.1 Synthesis Protocol

A RT precipitation-redispersion strategy is employed to deliver ultrafine and DI-water dispersible nc-ceria. One of the formulated protocol based on literature reports is adapted and is presented below [159]–[163]. 100 mM ammonium cerium (IV) nitrate (Sigma-Aldrich, 99.99 % trace metal basis) precursor dispersed in 25 % ethylene glycol (Finar reagent, 99 % assay)/ 75 % di-water mixed media as the solvent is prepared in a round bottom flask. To these a 10 mL of 25 % ammonia solution (Finar, 0.91 of density) stirred at 400 rpm is introduced rapidly. A pH~10 is achieved, resulting in the precipitation. The stirring is continued for 2 hrs and the obtained precipitate is allowed to settle overnight. The solid product is then separated by centrifugation and is allowed to dry at ambient laboratory conditions over a month.

This product, in the rest of the chapter, will be referred to as Ce@RT. Re-dispersion in DI-water is carried out with the use of 13 mm solid-ultrasonic horn (Sonics VCX 750W, 20 kHz) operated at its 50 % amplitude label. In the second case, the centrifuged 5 g precipitate is placed in the bottom of a 250 mL standard sonochemical reaction vessel having 150 mL DI-water as a solvent for the redispersion. The sonication time is fixed for 30 minutes. The sonication prepared water-soluble supernatant liquid, the sol settled at the vessel bottom obtained after overnight storage, and also the ambient dried solid recovered out of the settled sol are taken for detailed spectroscopic investigations. During the sonication, ice-water bath is maintained around the sonochemical reaction vessel to assimilate the sonication generated thermal effect. The sonication derived supernatant liquid (Sl), semi-solid sol (SS), and the semi-solid sol converted into solid power (SP) product will be subsequently coded as Ce_Sl@RT, Ce_SS@RT, and Ce_SP@RT respectively, in the rest of the chapter. The experimental elucidation of these three distinct (Ce_Sl@RT, Ce_SS@RT, and Ce_SP@RT) sonication products is discussed first. Based on the physical state of these products, a set of representative experimental data is collected and is presented below. These set of experimental data establishes the efficacy of ultrasonic cavitation induced product size reduction and dispersion devised synthetic protocol.

3.3.2. Charge Transfer transition

In this context, the Ce_Sl@RT product and its response to the introduction of another solvent H_2O_2 is followed by UV-Vis spectroscopy. The obtained spectral data sets are plotted and shown in the figs. 3 4 (a)-(c). The recorded spectral transmission curves (STC) of the Ce_Sl@RT product; is a sigmoidal shaped curve. The data shape of the STC is a manifestation of the transition from 100 % UV-A range (10-400 nm) absorption to almost 100 % visible wavelength transmission, interconnected by a finite width charge-transfer (CT, $O^2 \rightarrow Ce^{4+}$) edge associated with the $O_{2p}^6 \rightarrow Ce_{4p}^{-}$

electronic transition. The electrons gained by cerium atoms, chemically is a reduction process. Thus, an increased content of reduced cerium atoms will bring anisotropy to the sigmoidal shape of the STC, leading to a red shift in the transmission edge, tailing deeper into the visible wavelength range. As a consequence, this type of nc-ceria material is a probable candidate for visible-light photocatalytic applications. This CT aspect is inherent to ceria, in its variety of nanostructured morphological formulations.

The STC of a micron grain-sized ceria (coded as Ce_micron, blue-colored curve) considered to comprise the lowest fraction of reduced cerium atoms is included in the plot in fig. 3 4 (a) as the reference standard. A surface charge state transition is brought by introducing equivalent volume fraction of H₂O₂ into the Ce_Sl@RT product. The transmission edge of this modified Ce_Sl@RT product STC (coded as SPW H₂O₂, red-colored curve) almost becomes coincident to that of the Ce_micron. This implies near-complete oxidation of the Ce_Sl@RT product. It should be noted that, for all these UV-Vis spectral data acquisitions, the DI-water is the used solvent chosen to disperse and is considered as the baseline run.

The DI-water baseline trace (coded as DIW_b, maroon-colored) for the wavelength range analyzed has 100 % T and is also included in the plot. A set of transmittance kinks in the wavelength range=190-210 nm is observed and is assigned to the valency to the conduction band (VB to CB) electronic transition of ceria. The inset of fig. 3 4 (a) depicts cuvettes containing solution dispersions in their chemical states before, during, and also after oxidation in sequence, respectively. A fractional mass of neceria that settles at the bottom of the cuvette is isolated, with aging in the H_2O_2 modified dispersion. After oxidation, the STC of obtained supernatant (coded as SPW H_2O_2) with days of aging is also recorded and is plotted in the figs. 3 4 (b)-(c), respectively. Inset of fig. 3 4 (b) is included to demonstrate that the Ce_Sl@RT has oxidized inside the polyvinyl alcohol (PVA) matrix. The oxidation occurs inside the

PVA matrix, due to which settling derived mass is observed. The oxidation induced bright yellowish transparent coloration seen is retained for more than a year [164]–[169].

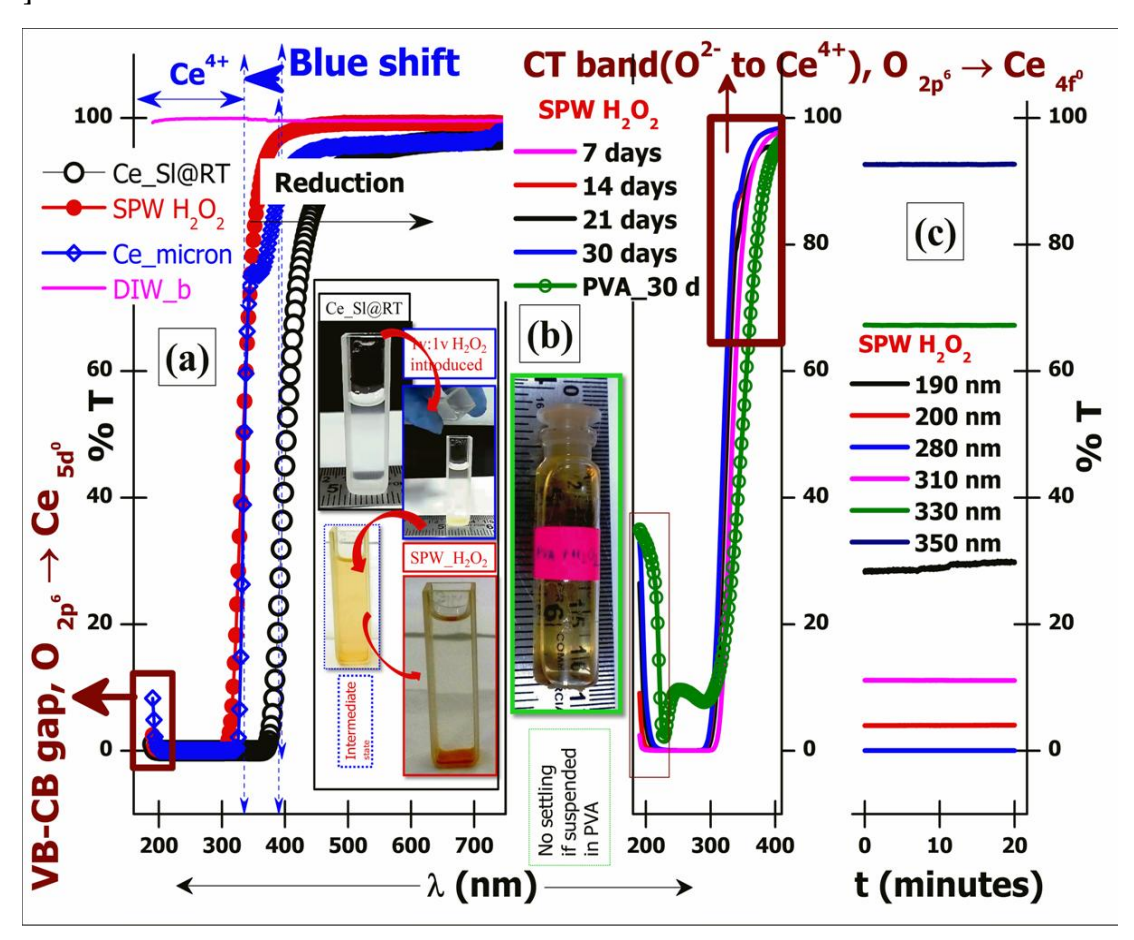


Fig.3 4 [UV-Vis optical spectra of the Ce_Sl@RT]: (a) The spectral transmission curves for original (Ce_Sl@RT) and interface modified (SPW H2O2) sample (b) SPW H2O2 aging stability, and (c) time dependent wavelength specific SPW H2O2 product measurements respectively.

The optical band gap values and correlation with the changes in absorption edge brought forward by diluting the Ce_Sl@RT with equivolume fraction of H_2O_2 is discussed now. This is significant because both the Ce_Sl@RT and SPW H_2O_2 products are of the same particle size dispersions (PSD), but one is in reduced state while the other has surface cerium atoms in the oxidized state. This fact can be conclusively inferred by carrying out the oxidation process inside the polyvinyl alcohol (PVA) matrix. With precisely the same PSD, the surface oxidation achieved

inside the PVA matrix (Fig. 3 4 (b), the PVA_30 d sample has almost the STC as that of the SPW H_2O_2). No particle settling and maintaining almost the same PSD is of significance. That is to say, H_2O_2 modification plays an important role in the surface oxidation of the cerium atoms, as is evident from the distinct STC of SPW H_2O_2 than Ce_Sl@RT. That is in ceria, the charged state of the surface cerium atoms will decide the absorption edge tailing tunably. The STC of Ce_micron is chosen as the standard representing the fully Ce⁴⁺-oxidized state at ambient laboratory environments. In the present context, Ce_micron data will be viewed as calibration for oxidation and reduction as well as the standard reference pattern.

The STC data processing for the optical band gap is carried out based on literature [170]–[175]. In brief, the absorption coefficient (α cm⁻¹) is extracted from the STC and its derivative with respect to the energy exhibits a point of inflection in the absorption edge distinguishing the high Tauc and low Urbach- energy regions, respectively. The highest achievable adj. R-square close to 1 iterative fit to these above mentioned regions is carried out. The adopted mathematical expression; (1) Non-linear Belehradek for bandgap, and (2) linear fit for Urbach energy is used. The computed parameters (like bandgap, type of transition, point of inflection, band-tail width, and electron-phonon interaction strength) are listed in the table-3.1. Also, the representative Tauc plots for optical band gap and PSD for Ce_micron, Ce_Sl@RT, and SPW H₂O₂ are presented in figs. 3 5 (a)-(b) respectively.

The main conclusions drawn from this analysis are presented now. The important outcomes are: (1) the blue shift in the STC in UV-A range is probably due to the CT optical transition associated with the valency fluctuations in surface oxidation states from $Ce^{3+}\leftrightarrow Ce^{4+}$. (2) It is evident from the coincident STC that the CT feature is not purely a surface effect as it is observed in both Ce_micron and SPW H_2O_2 . The particle size distribution (PSD) data of the both (Ce_micron D50=1092 nm, SPW H_2O_2 D50=7.5 nm) is presented in fig. 3 5 (b). (3) Other set of STC presented

suggest the CT feature is related to the surface charge states than size. The PSD data of Ce_Sl@RT (D50= 13.6 nm) is close to that of the PVA_30 d (D50= 18.5 nm).

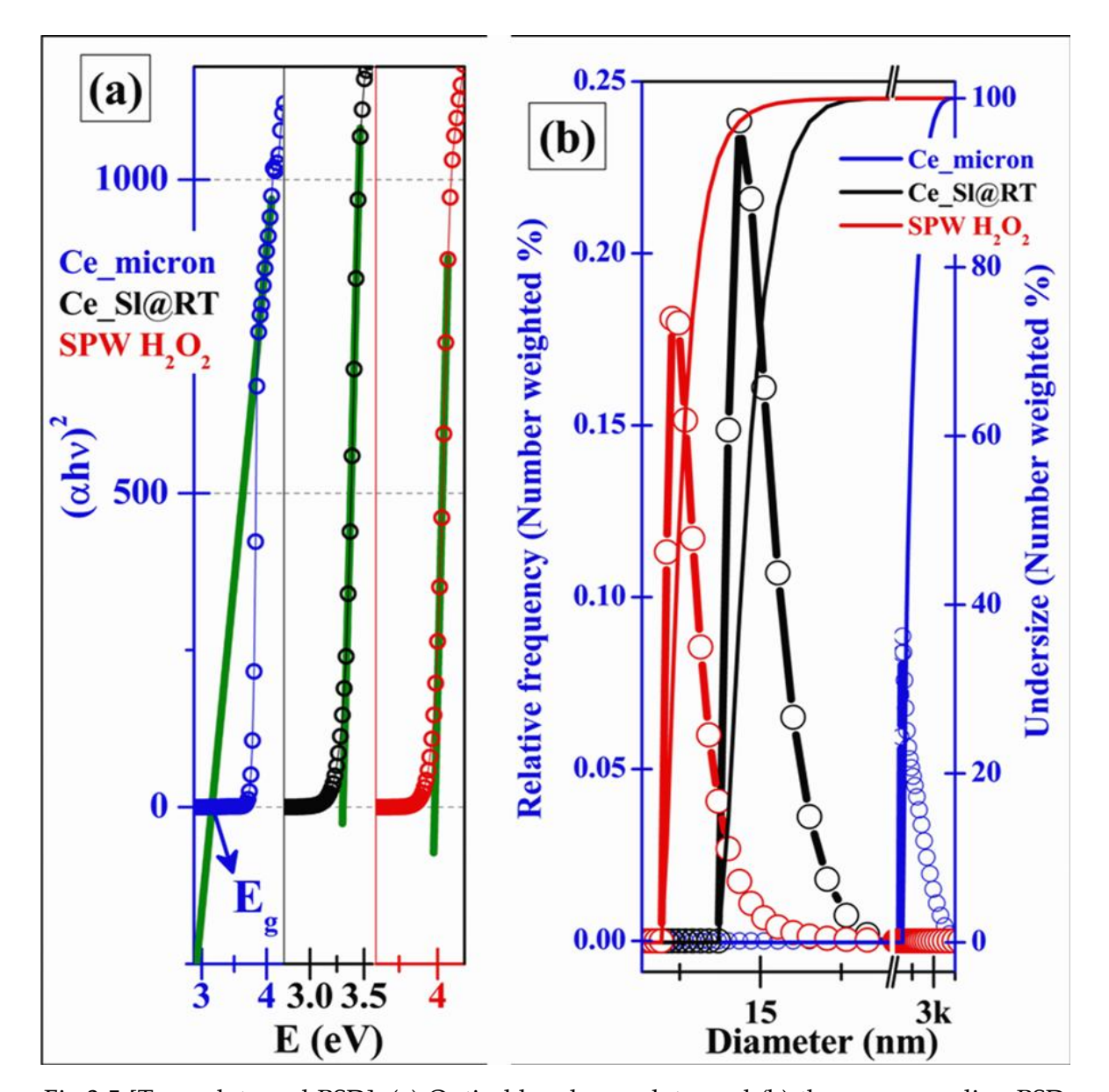


Fig.3 5 [Tauc plots and PSD]: (a) Optical band gap plots, and (b) the corresponding PSD data respectively.

However, it needs to be further supported by other spectroscopic probes. (4) Lastly, the data analysis suggests that the CT optical absorption is due to a direct electronic transfer rather than an indirect one. The Levenberg–Marquardt algorithm iteration deduced Belehradek fit to identify the type of optical transition $(Y=a(X-b))^c$; whether

c=0.5 (direct) or 2 (indirect)) is plotted for PVA_30 d to illustrate the direct optical transition as the most appropriate, and is shown below in the figs. 3 6 (a)-(b). These current observations are also in concurrence with those reports [176]–[182].

Table 3 1 Optical parameters extracted from the measured STC for different samples

Sample	Point of	Type of	Band gap	PSD	Band-tail width &	
code	inflection	transition,	(eV)	Poly dispersive	Electron-phonon	
	[d\alpha/d(h\nu)	Belehradek		Index (PDI)	interaction	
	=0] line	$Y=a(X-b)^c$			strength	
	width (lw)	c=0.5, direct			(E _{e-ph})	
		c=2, indirect				
Ce_micron	3.85 eV lw=0.2 eV	c=0.5	3.16(1)	D10=718 nm		
		R2=0.99769	3.10(1)	D50=1092 nm	66 meV &	
		c=2	0.70(4)	PDI=53 %	∝ Ee-ph=1.71	
		R ² =0.99867		D90=2224 nm		
Ce_Sl@RT	3.35 eV lw=0.1 eV	c=0.5	3.30	D10=8.16 nm	130 meV &	
		R ² =0.9967		D50=13.6 nm		
		c=2	3.01(2)	PDI=23.6 %	Ee-ph=3.33	
		R2=0.9813	5.01(2)	D90=17.24 nm		
SPW H ₂ O ₂	4.05 eV lw=0.1 eV	c=0.5	3.96	D10=5.58 nm		
		R ² =0.9994	3.90	D50=7.50 nm	170 meV &	
		c=2	3.58(3)	PDI=30.8 %	Ee-ph=4.44	
		R ² =0.9907	3.36(3)	D90=10.5 nm	-	
PVA_30 d		c=0.5	2.64	D10=8.14 nm	322.7(3.9) meV	
Same as	3.76 eV	R ² =0.9991	3.64	D50=18.5 nm	&	
SPW H ₂ O ₂	lw=0.3 eV	c=2	2.73(4)	PDI=28 %	Eo. mk=9.25	
Oxidation	111 0.0 0 1	R ² =0.9845	2.75(4)		Ee-ph=8.37	
inside PVA		10.7040		D90=23.5 nm		

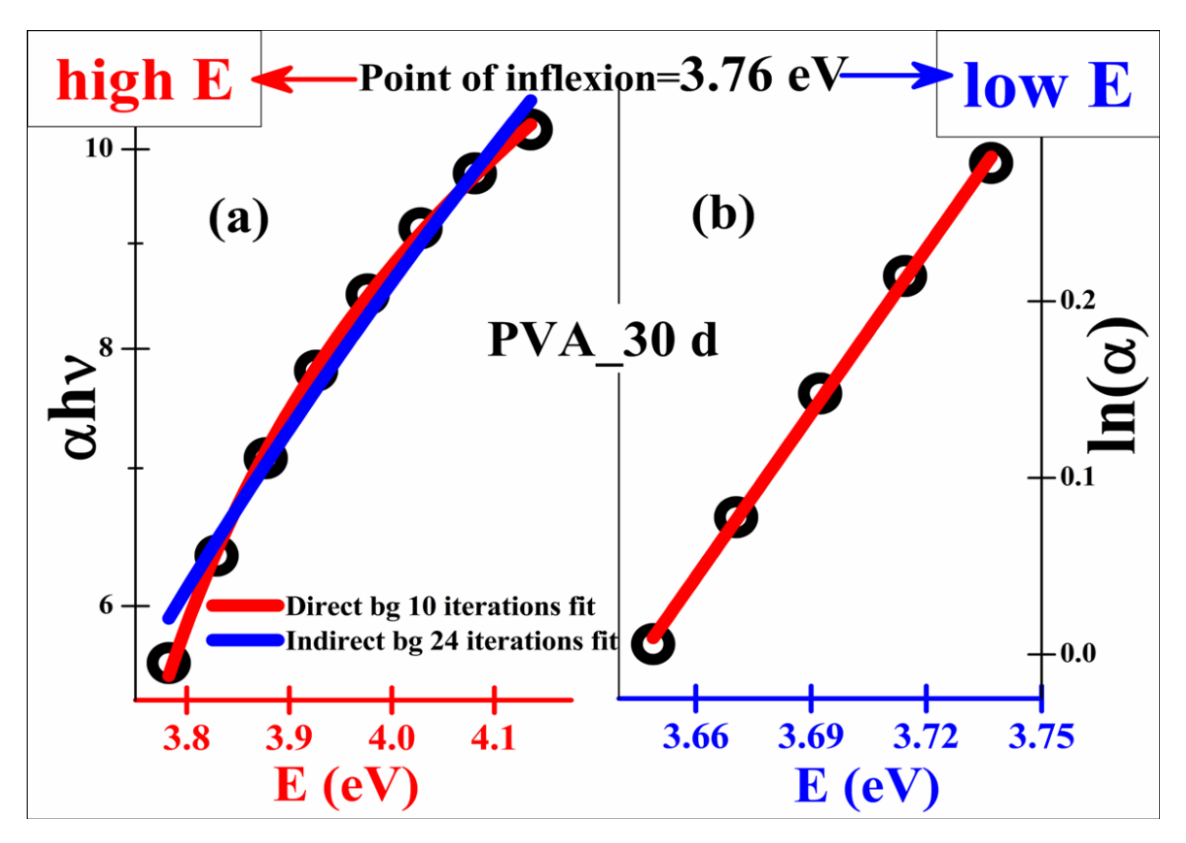


Fig.3 6 [Tauc and Urbach regions]: (a) identification of the optical transition type, and (b) linear fit for band tail width and Ee-ph strength computation respectively.

As stated in the previous paragraph that the origin of the observed blue shift, whether it is due to (1) surface CT feature, (2) quantum-size effect, or (3) a combination of both require further support by other subsidiary experimentation techniques which will be presented later. The gel-like Ce_SS@RT separated after supernatant liquid extraction during the process of the synthesis is used to address the above mentioned queries employing Raman spectroscopy. In the case of the Ce_SS@RT developed in the aqueous medium, the neighboring environment of a localized region can be easily changed by the addition of a few drops of H₂O₂ to bring about a CT transition of surface cerium atoms at RT with no effect all together on the PSD. The localized, oxidized and unoxidized regions with the Ce_SS@RT spread over an Al-foil wrapped BSG glass substrate can be probed employing the confocal-Raman spectroscopy instrumentation. The detailed analysis of such Raman

spectral acquisitions in a single spectral and time-series mode are discussed in the following sections.

3.3.3. Origin of the blue-shift

There has been much interest in the reversible switching feature in nc-ceria (crystallite size of about 7-8 nm or less, is the estimated Bohr exciton radius), in presence of different neighboring environments causing the autocatalytic regenerative CT transition of the surface cerium atoms (whether it is Ce⁴⁺/or at Ce³⁺) [183]–[188]. Most of the physicochemical and technological applications of nc-ceria are derived out of its tunable cyclic-CT feature. Based on this, the potential industrial utilities evolved are in the field of chemical mechanical planarization and polishing, catalysis, solid-oxide fuel cells of intermediate-temperature, and also activities in the field of sensors respectively [189]–[193]. However, there are contradictory reports that the reduction of the crystallite size will lead to increase in Ce³⁺ concentration (27% enhancement observed from size= 30 to 3 nm change) as other literature suggest that the same 3 nm nc-ceria crystallites don't have any Ce³⁺ [194], [195]. It underlines the importance of processing protocol in delivering either the fully oxidized or reduced cerium surface atoms in Bohr-excitonic sized nc-ceria formulations.

To achieve greater insight into the CT process, Ce_SS@RT is painted on a piece of gray emery paper to illustrate the adaptability to the changes in neighbouring environment. The painted Ce_SS@RT is colorless as seen in fig. 3 7 (a). The color change of this gel is adjudged with respect to white-colored Ce_micron powder, which is in the Ce⁴⁺ state based on the STC observations of the fig. 3 4 (a). The addition of few DI-water drops to the painted Ce_SS@RT region changes the gel color to white, indicating that DI-water acts as oxidant. It is particularly noteworthy to mention that in the earlier discussion, the separated supernatant DI-water nc-ceria dispersion (Ce_Sl@RT) ceria crystallites are in a reduced state. This, thus, confirms

large number of investigations that state "nc-ceria oxidation state is transient and regenerative in nature predominantly decided by the adjoining and neighboring environment changes." Due to this transient nature of the cerium oxidation state in nc-ceria composite formulations, an important requirement is to specify by experimental means the cerium oxidation state before any technological use. Below presented experiment demonstrates this characteristic oxidation-reduction transition.

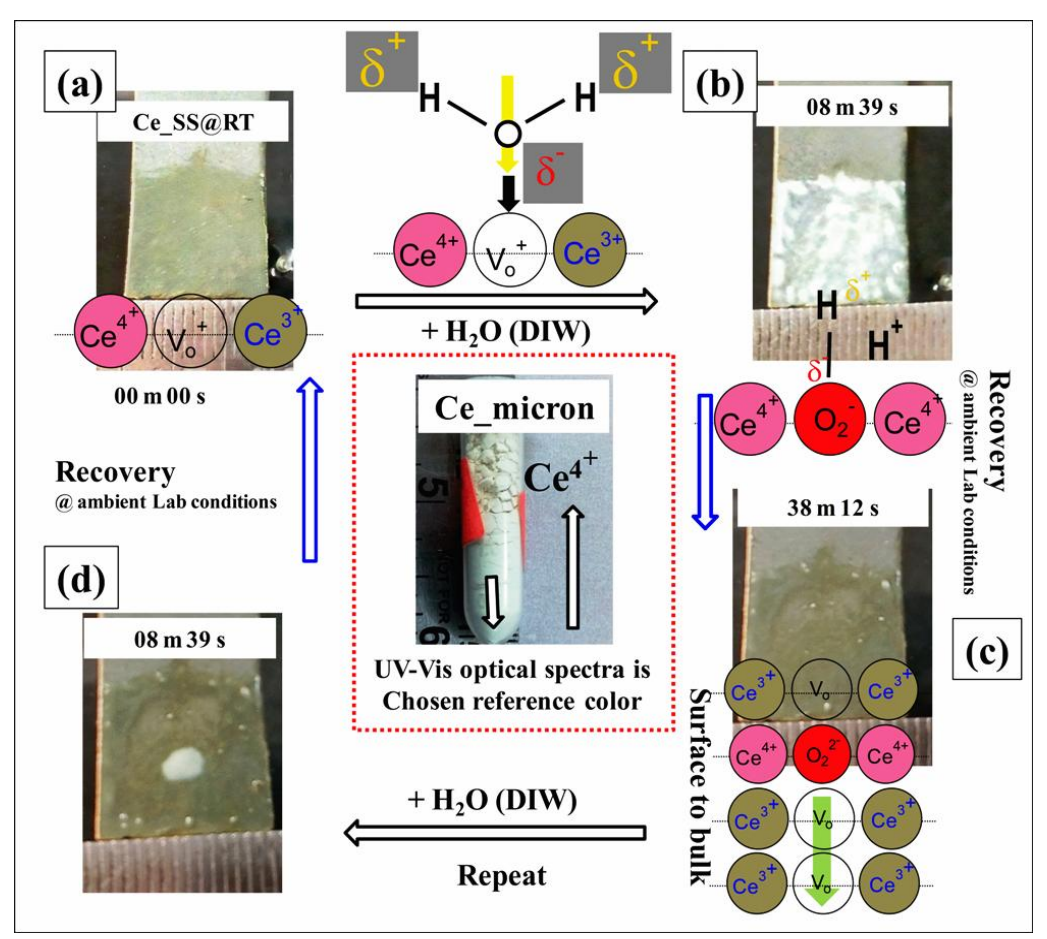


Fig.3 7 [Autocatalytic regenerative feature]: The time-evolved oxidative and reductive feature of Ce_SS@RT, snapshots in DI-water at ambient laboratory conditions (inset Ce_micron powder in an eppendorf tube, surface schematics are adapted from reference [196]–[199]).

A cycle of oxidation and its recovery, also termed as the auto regenerative feature of the nc-ceria at ambient laboratory condition with time evolved snapshots, are shown in the figs. 3 7 (a)-(d). Out of many possibilities, the probable surface cerium atomic

charge states most suitable for the present scenario is also schematically depicted for easy understanding, as adapted from literature [196]–[199].

In this section the interpretation of Raman spectral signatures of the Ce_SS@RT and that of the dried solid powder (namely Ce_SP@RT) obtained in the CT transition context is discussed. The Ce_SP@RT Raman data as a function of the excitation wavelength (λ_{excitation}=532, 633, and 785 nm are used) is presented in fig. 3 8 (a), which clearly reveals the 464 cm⁻¹ (wagging vibration of the oxygen atom between two Ce⁴⁺ ions) a characteristic Raman signature of the ceria [200]–[205]. For the case of the Ce_SP@RT, the observed broad significant photoluminescence (PL) band at 636 nm is of interest. The fig. 3 8 (c) demonstrates the dominant nature of 636 nm PL band on the 545 nm Raman spectral signature as obtained with the 532 nm excitation. The PL suppression is achieved with 785 nm excitation, i.e., moving away from the band gap or sub-band gap absorption observed by the 532 nm laser excitation. The physical illustration of PL suppression achieved using 3 different excitation sources is presented in fig. 3 8 (a).

Even for the 532 nm excitation, when the irradiance delivered to the Ce_SP@RT sample surface is 40 kW/cm² or above PL quenching is observed. In terms of power value when the localized region is exposed at 2.5 mW for continuously 12 minutes, the 545 nm Raman signature overtakes the PL signal. These dynamic changes highlighting PL quenching at the laser exposed region is continuously acquired in time series mode and is plotted in fig. 3 8 (c). The Ce_SP@RT surface in pristine, with laser ON spot size, and after 12 minutes laser modified regions by 532 nm exposure are presented in fig. 3 8 (b). Appearance of bright yellowish coloration compared to pristine sample with exposure hints at the possible surface modification. If the surface modification happens to be recoverable, the PL must recover which will be presented in later discussions. Thus the Raman spectroscopy conclusions for the Ce_SP@RT are; (A) A broad intense 636 nm emission overtakes small 545 nm Raman

signature, (B) the 636 nm PL is quenched by two ways-(1) by moving away from the band gap or the sub-band gap absorption observed for 532 nm, (2) by exploiting the surface modification using laser output power value on the sample.

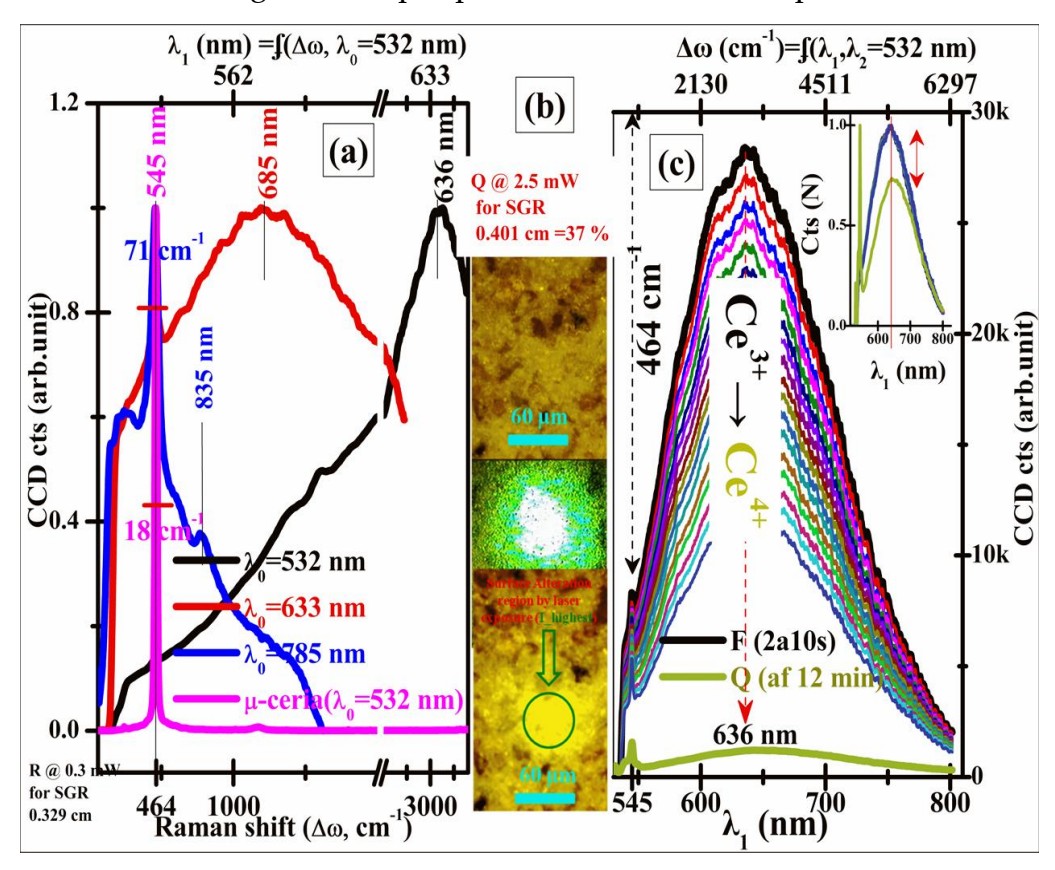


Fig.3 8 [Ce_SP@RT product CT luminescence]: (a) Separating the elastic scattered Raman phonon signature from inelastic PL photons by different laser excitation wavelength, (b) Optical micrographs of Ce_SP@RT; λ_{\circ} =532 nm laser surface modified region of Ce_SP@RT product (A 20x 0.4 NA objective is used to focus the laser to about 3-5 μ m spot), and (c) Quenching of the CT luminescence band employing λ_{\circ} =532 nm laser operated at 2.5 mW output maintained for 12 minutes demonstrating nc-ceria surface oxidation respectively.

The experimental probing on intervalence CT absorption in cerium (III, IV) oxide system having a broad, intense absorption band centered around 16300 cm⁻¹ (~ 613 nm) as reported by Allen et.al. [206]. In this work it is illustrated that the cerium (III) oxide absorption band at 613 nm undergoes quenching by air oxidation at RT. Also,

the various other possible CT transition bands associated with cerium are listed in the specific references in table-3.2.

These initial inferences about the cerium (III, IV) oxide system absorption bands will assist in analyzing the present case of Ce@RT and Ce_SP@RT products. The recorded optical absorption spectra of these products are plotted in fig. 3 9 (a). The data is fitted to multiple nonlinear Gaussian peaks combinations to generate the best fit (adj. R-square close to 1). While fitting, the peak centers are chosen closest to the reported absorption peaks. However, peak width is allowed to vary without much overlap. After suitable fitting to the original data, the number of extracted absorption peaks specific to the samples is identified.

Table 3 2 CT absorption band position in nm for the case of nc-ceria (reported and this work).

	References				
Ce^{3+} & $f \rightarrow d$	S: $Ce^{3+} - O^{2-}$ & $O^{2-} \rightarrow Ce^{3+}$	S: $Ce^{4+} - O^{2-}$ & $O^{2-} \rightarrow Ce^{4+}$	Interband transition	S: Ce^{3+}/Ce^{4+} & $Ce^{3+} \rightarrow Ce^{4+}$	S for surface
200-250	263	280	320-350	588	[207]
208-218	250	297	320-340		[208]
233		299		407, 485	Ce@RT
	E _{gd} =1.56 eV			E _{gd} =3.77 eV	This Work
			358	426,588	Ce_SP@RT
	E _{gd} =1.32 eV			E _{gd} =2.34 eV	This Work

An obvious noticeable feature in the Ce_SP@RT product is the hike in absorbance efficiency, i.e., the low energy absorption tail ramps up to approximately ten times higher value (see fig. 3 9 (a)) than the parent Ce@RT product. In contrast Ce@RT maintains its UV-A optical absorbance as evidenced by the blue dotted data curve of fig. 3 9 (a).

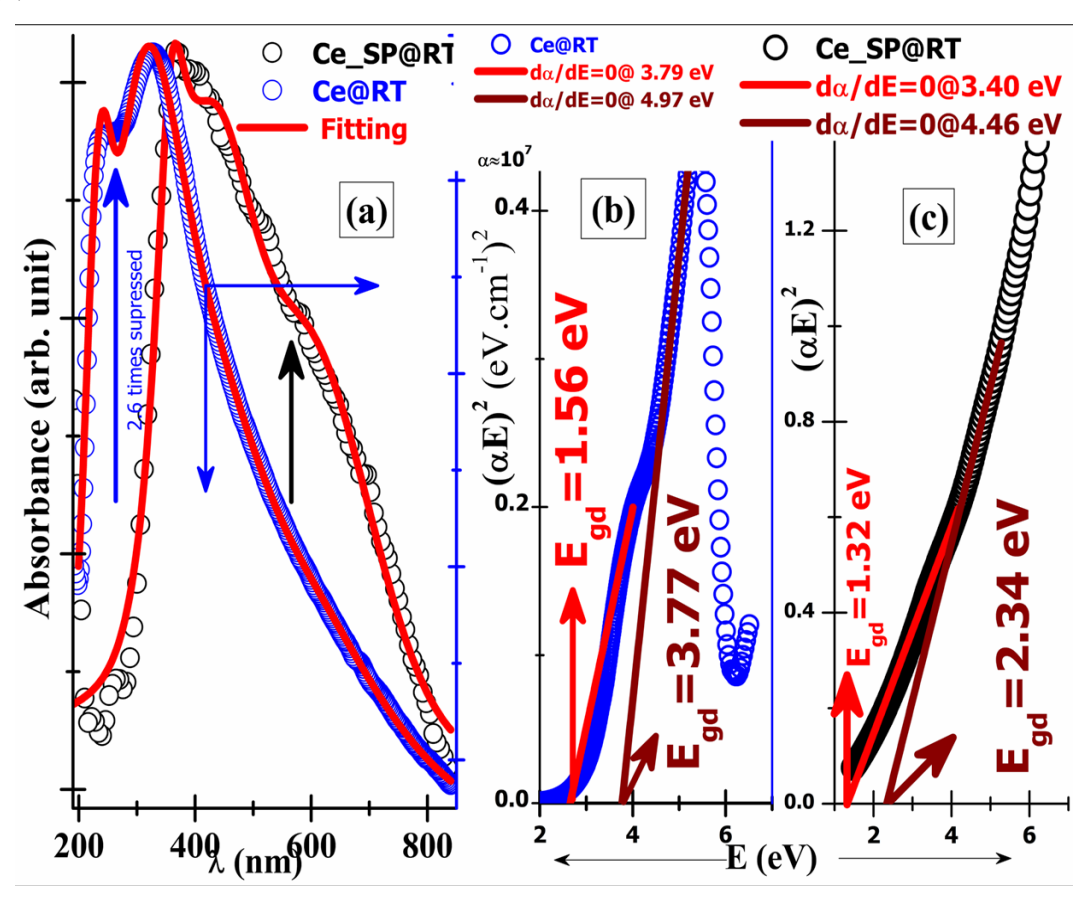


Fig.3 9 [Optical band gap Narrowed defective nc-ceria]: (a) Optical absorption spectra of ceria products i.e., Ce_SP@RT and Ce@RT, (b) and (c) are the respective Tauc plots demonstrating computed bandgap values.

Literature suggest the absorption edge of reduced ceria must have a strongest band around 400 nm attributed to absorption by Ce^{3+} at C_2 site. This is assisted by sidebands near 575 nm (absorption by Ce^{3+} at C_{3i} site) and 510 nm (absorption by Ce^{3+} at C_{3i} site) respectively [209]. The C_{3i} sites oxidize more slowly than the C_2 sites. Likewise, for oxidized ceria products having Ce^{4+} as a dominant fraction must exhibit

an intense absorption onset below 370 nm [210]. The representative computed sub-optical band gap values (plotted in fig. 3 9 (c)) reaffirms that the Ce_SP@RT product has defects. These defects fill the band gap with a variety of sub-levels that physically contribute to the optical band gap narrowing. One of the reasons for the observed redshift in the band gap is assigned to the increase of Ce³⁺ fraction in the sample [211]–[214].

The Ce_SP@RT product PL spectra in figs. 3 10 (a)-(c) justify the presence of subbandgap defect levels and assignments are consistent with literature [214]–[216]. The UV-VIS absorption spectroscopy in the earlier section the UV-Vis absorption spectroscopy confirms the sub-band gap absorption for Ce_SP@RT at or around 2.34 eV. The Raman spectral data presented in fig. 3 8 (a), acquired by 532 nm (2.33 eV) excitation with a broad intense emission at 636 nm is a direct affirmation. Further near band gap excitations implies a highly pronounced PL emission (fig. 3 10 (b)) of Ce_SP@RT than that of quenched like PL emission data observed for the Ce@RT. The PL emission spectra recorded for both the Ce_SP@RT and Ce@RT products are for $\lambda_{\text{excitations}}$ =325 and 300 nm, respectively) which is close to computed optical gap of 3.77 eV (329 nm) for Ce@RT. The intense major-violet and the blue emissions are $F^{++} \rightarrow Ce^{3+}4f^{1}$ and $F^{++} \rightarrow F^{+}$ transitions, whereas the weak minor-red and IR emission is ascribed to the $F^{0^*} \rightarrow F^0$ and $Ce^{3^+} 4f^1 \rightarrow O_{2n'}$ VB electronic relaxations respectively. The Ce³⁺4f¹ acts as a hole trap and creates an energy gap of ~3.1 to 3.3 eV with an empty Ce⁴⁺4f⁰ sub-band. The symbolic representation of oxygen vacancy with two trapped electrons is F⁰ while subsequent F⁺ and F⁺⁺ states represent the loss of one and two electrons respectively. The excited states are F^{+*} and F^{0*} , respectively. It is important to point out that the electron localization within the Ce³⁺4f¹ band is not fixed to a single energy. In fact, a spread of multiple defect states are realized all along the band gap based on lattice distortion and availability of oxygen vacancies near to the Ce^{3+} site [214]. In fig. 3 10 (a) is the photoluminescence excitation (PLE) spectra of the PL emission $\lambda_{emission}$ =666 nm excited by 300 nm excitation. The PLE curve has three absorption bands at (1) 275 nm ($O_{2p} \rightarrow Ce^{4+}4f^0$), (2) 375 nm ($Ce^{3+}4f^1 \rightarrow Ce^{4+}4f^0$), and (3) 561 nm respectively. These PLE absorption band positions agree with that of the previous UV-Vis optical absorption data presented in table-3.2.

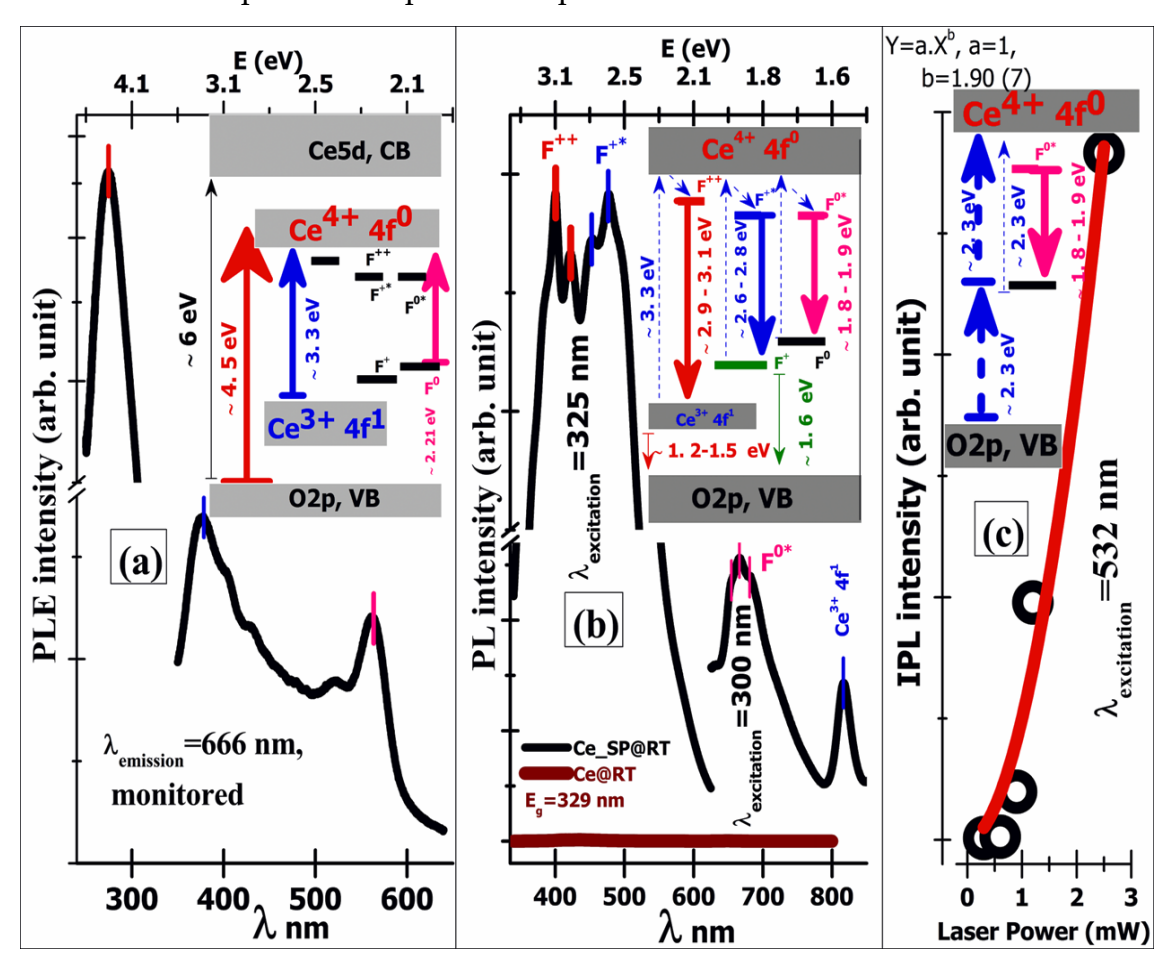


Fig.3 10 [Photoluminescence spectroscopy of Ce_SP@RT]: (a) PLE spectral data acquired for 666 nm PL (inset gives schematic of sub-optical gap absorption), (b) PL emission with probable defects, and (c) occurrence of the 2 photon absorption for 532 nm sub-band gap excitation respectively for Ce_SP@RT product.

Thereby it becomes another supportive data to the defects induced bandgap narrowing feature. Even though the Ce_SP@RT bandgap is in direct coincidence with the 532 nm photon for excitation, the variation of the laser power and its effect on the integrated PL intensity (IPL, fig. 3 10 (c)) indicates the possibility of two-photon

absorption. Here, laser power ramps the IPL value approximately in square term (LP=a×IPL²). Thus, ultrasonic activation of the Ce@RT carried out at RT to develop Ce_SP@RT product induces sets of sub-bandgap defects levels responsible for the observed bandgap narrowing and the broad 666 nm PL emission.

The question that needs to be addressed, whether the ultrasonic processing even at RT facilitate the Ce@RT size reduction? Powder X-ray diffraction (XRD) is employed to answer this question. The XRD data of Ce@RT and Ce_SP@RT are presented in fig. 3 11 (a), and analyzed employing the fundamental parameter approach (FPA) line profile fitting for the laboratory X-ray diffractometers [217]. The crystal structure refined calculated profile (Y_{cal}) , difference pattern $(Y_{obs} - Y_{cal})$, and the standard ICCD PDF: 81-0792 file Bragg positions as vertical lines are shown in fig. 3 11 (a). The refined FCC unit cell lattice parameter for the Ce_SP@RT (with GOF (χ^2) =1.33) and Ce@RT (with GOF (χ^2) =1.27) are: a=5.443(2), and 5.425(2) Å respectively. The lattice expansion observed with respect to the standard a=5.412 Å imply both these products are under tensile strain. The strain value of Ce_SP@RT is 2.25 times higher than that of the Ce@RT. While plotting (see fig. 3 11 (a)); the respective average strain values are scaled to zero, so that both XRD patterns are aligned with the standard ICCD PDF: 81-0792 file. XRD pattern of Ce_micron (bottom column fig. 3 11 (a)) is also plotted, to demonstrate peaks significant FWHM broadening characteristic to these nano size products. The crystallites size reduction from 2.95 (2) to 1.96 (2) nm is observed. It supports the role of 20 kHz ultrasonic probe in size reduction [218]. Furthermore, no structural phase of oxygen nonstoichiometric is observed. The list of all non-stoichiometric ceria phases, and their stability at ambient/non-ambient conditions is tabulated by T. Alessandro et.al., [219]. Thus, the highly-strained fluorite unit-cell of the 2 nm crystallites representing Ce_SP@RT is in support with the optical band gap narrowing and PL sub-band gap excitation results.

The following conclusions can be drawn about the 532 nm Nd-YAG laser irradiance use to demonstrate the observed CT luminescence. The utilized laser power levels snapshots on the polished side of the silicon substrate are shown in fig. 3 11 (b). The central laser spot area (neglecting the scattering generated spot spreading) is used for irradiance calculation. These are (1) 40 kW/cm² or higher irradiance is better for PL quenching, (2) between 5 to 20 kW/cm² is used for steady-state PL recordings (negligible change to IPL value in 535-800 nm range), and (3) 5-10 kW/cm² for IPL recovery.

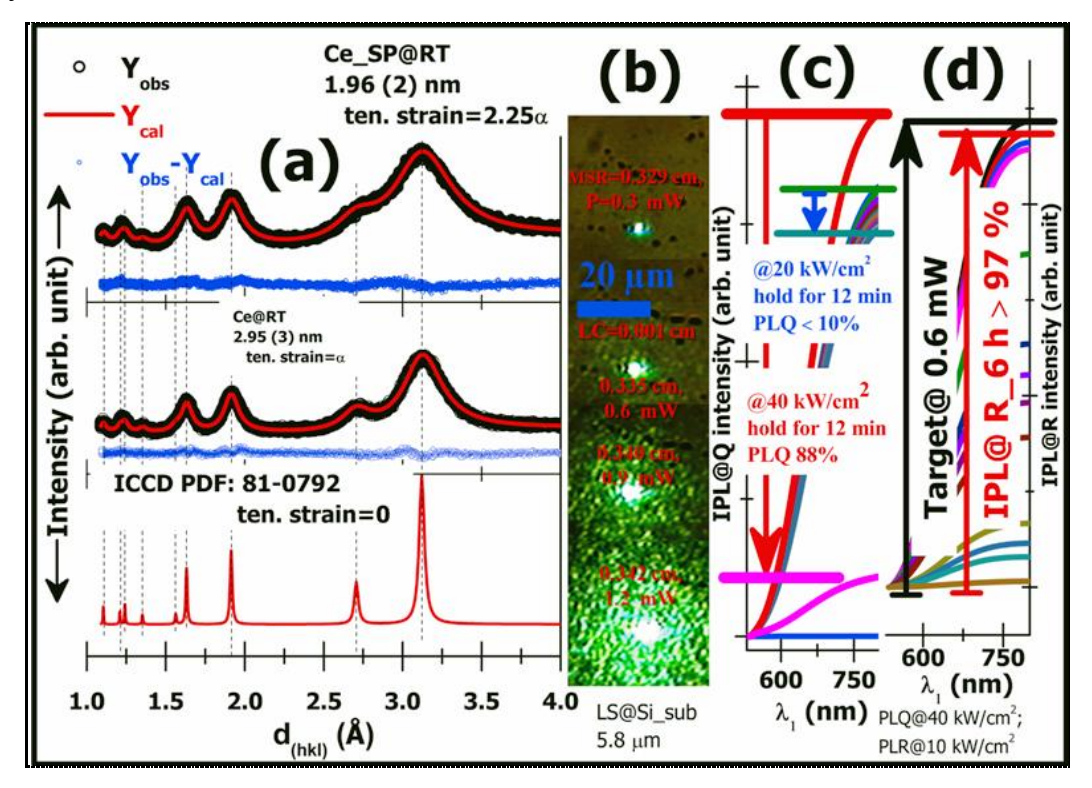


Fig.3 11 [Effect of the ultrasonication and 532 nm Nd-YAG laser irradiance on Ce_SP@RT product]: (a) XRD data of ultrasonic induced product size reduction; (b), (c), and (d) are the IPL observed by laser irradiance of 5, 10, 15, 20, and 40 kW/cm² respectively. In increasing order these set of values represent PL-recovery, steady-state, and quenching data recordings.

The plotted data in fig. 3 11 (c) points to: Ce_SP@RT (a) IPL quenching and (b) for steady-state PL recording. Whereas (c) fig.3.8 (d) presents 12 minutes 40 kW/cm² irradiance modified region, subsequent IPL recovery data. IPL recovery of almost 97

% is observed after 6 hrs of hold in ambient conditions. These experimental illustrations confirm that for 2 nm Ce_SP@RT band-gap narrowed crystallites, the CT luminescence is a surface attribute. This IPL quenching and its recovery is ascribed to the neighbouring environment gaseous components either desorption/adsorption in a vice-versa way recurrently [220]–[228].

3.4 Characterization of Ce_SS@RT product surface attributes using Raman spectroscopy

The data presented in figs. 3 7 (a)-(b), that demonstrated the autocatalytic regenerative feature of the Ce_SS@RT induced by the neighboring environment change (air to DI-water) is further explored by Raman spectroscopy. This study is expected to confirm, the introduction and depletion of DI-water as neighbour bringing the surface attribute changes of the Ce_SS@RT product. These data acquired at ambient condition is also useful to justify the earlier discussed CT transition. More specifically, the relative strength, presence, or absence of the Raman phonon modes over a micron-sized surface during the direct interaction with the oxidizing and reducing environment are in-situ mapped. This enables acquiring conclusive spectral and mapping information from the pristine and modified product surface region to illustrate the regenerative CT nature. The three specific Raman phonon modes of significance to the present nc-ceria surface analysis are first identified. These, with the increasing wavenumber are: (1) 460 cm⁻¹ (wagging vibration of oxygen atom between two Ce⁴⁺ ions), (2) 560 cm⁻¹ (oxygen-stretching vibration between the Ce³⁺ and Ce⁴⁺ ions near to oxygen defects), and (3) 600 cm⁻¹ (stretching vibration of M⁴⁺-O-Ce⁴⁺ without oxygen defects), respectively [200]–[205]. The Raman mapping is carried out for 8 hrs at ambient condition, by which time the only changes to the nc-ceria surface occur while maintaining the PSD. The conclusion is that the observed phenomenon is solely a surface effect with no obvious dependence on particle size.

Further, the physical significance of the above mentioned Raman modes in case of the metal-doped ceria ($M_xCe_{1-x}O_{2-d}$) composites, is extensively reported in literature and used to determine concentration of the (1) oxygen vacancies and (2) doped metal ions [200].

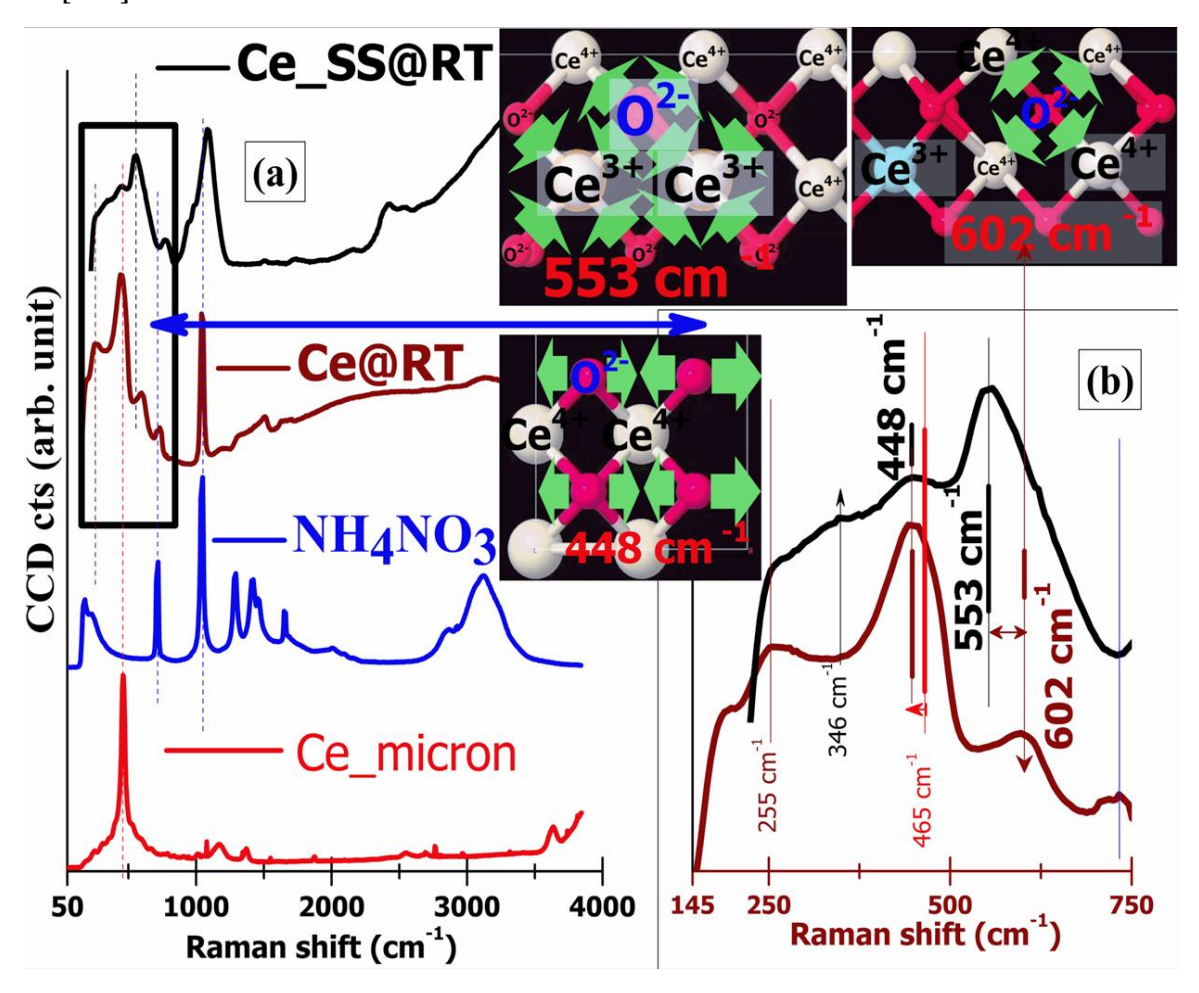


Fig.3 12 [Raman spectral phonon modes of the Ce_SS@RT product]: (a) Ce_SS@RT Raman spectral features and its associated products, and (b) 448 cm-1 (O-wagging), 553 cm-1 (O-stretching near oxygen vacancy), and 602 cm-1(O-stretching away from oxygen vacancy) phonon modes (schematic vibrations are adapted from reference [200]) respectively.

In the spectral data of fig. 3 12 (a), observed most intense Ce_micron mode at 465 cm⁻¹ shift to 448 cm⁻¹ for Ce_SS@RT. It gets broader with low-energy asymmetric shoulder and is attributed to the combined effect of lattice phonon confinement and strain in nc-ceria [229]–[231]. The 488 cm⁻¹ mode in Ce_SS@RT and Ce@RT exhibits an inverse relationship with the corresponding oxygen vacancy related mode at 553 cm⁻¹

as adjudged from fig. 3 12 (b) [i.e., as if appearance of one links to disappearance of other]. The reasoning reported is an introduced oxygen vacancy, in turn, leads to two-Ce³⁺ ions (ionic radius of 1.143 Å) in place of two-Ce⁴⁺ existing lattice ions (ionic radius of 0.97 Å). It in turn satisfies the charge neutrality, but brings an inbuilt tensile strain causing lattice expansion. The 2 nm Ce_SS@RT higher strained crystallites 488 cm⁻¹ mode is of much reduced intensity, and also have substantial peak broadening. A red shift of 17 cm⁻¹ and broadening aspect of 488 cm⁻¹ is presented in fig. 3 12 (b). Likewise, the 602 cm⁻¹ mode with increasing concentration of oxygen vacancies red shift to 553 cm⁻¹ mode gradually and subsequently merges [229]. Besides these, a pronounced mode at 346 cm⁻¹ representing the sub-surface oxygen vacancies is seen, linked to the diminished surface O-Ce stretching vibration mode observed at 255 cm ¹. Other observed phonon modes at 782, and 1083 cm⁻¹ are also literature identified based on the neighboring environment and the synthesis conditions used [229]. The investigation of the nc-ceria structural phase transition by in-situ Raman spectroscopy is fascinating. It is to be pointed out that in literature the 276 cm⁻¹ phonon mode (representing along the c-axis both the Ce and O-atoms opposite movement) is monitored to address the tetragonality development. Thereby, a reversible tetragonal (P42/nmc) to cubic (Fm-3m) nc-ceria structural phase transition between -25 to -75 °C by monitoring its tunability is recently demonstrated [232]. The absence of the 276 cm⁻¹ mode in the present study confirms the XRD analysis that both materials are in cubic phase and no tetragonal phase is present. Thus, the current Raman spectroscopic investigation illustrates the inter-dependence of specific nc-ceria phonon modes, in which the appearance of the one directs the disappearance of the other and vice-versa. These dynamic in-situ phonon modes changes are mapped for the case of the Ce_SS@RT with respect to the pristine Ce@RT as standard.

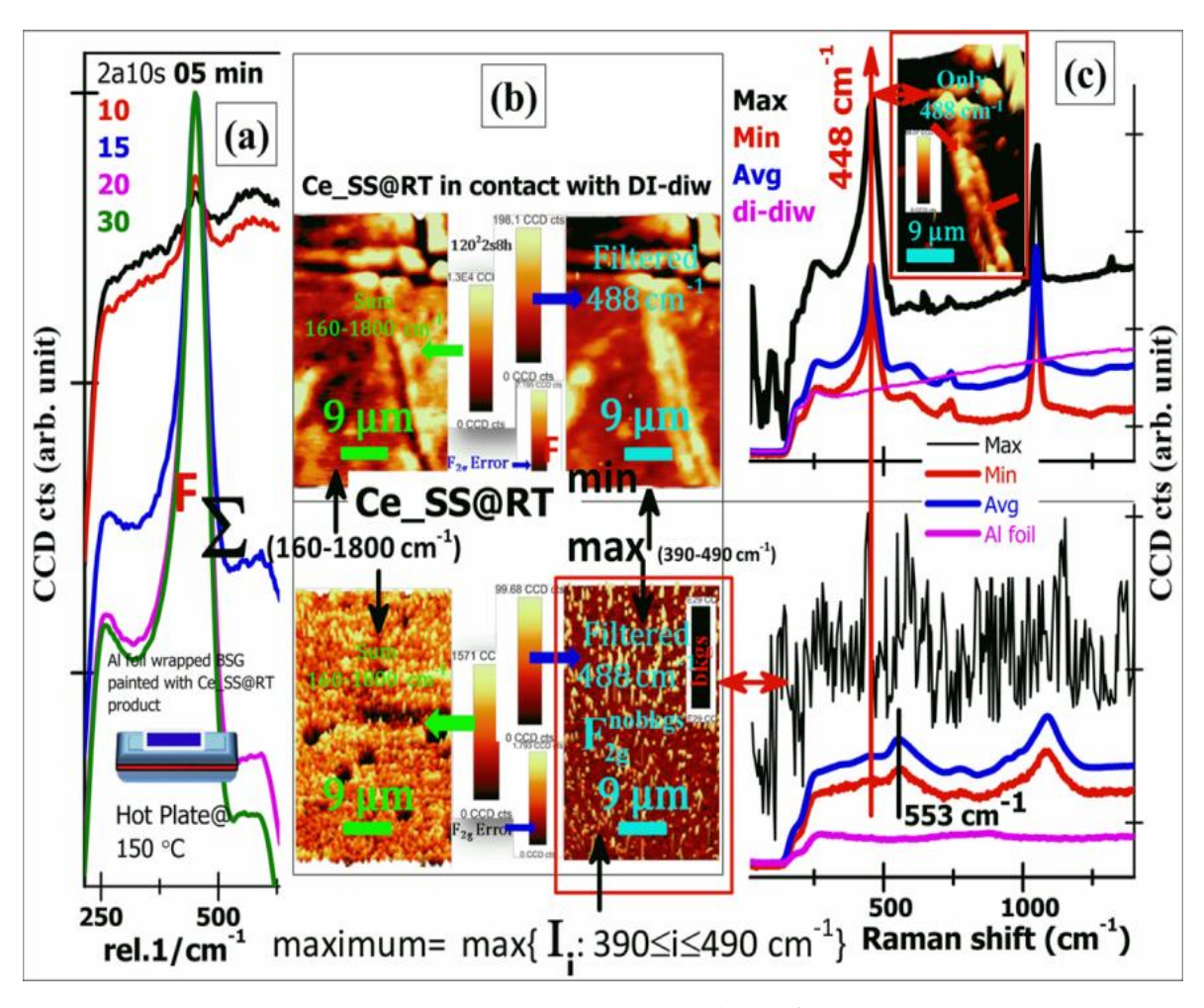


Fig.3 13 [Dynamic changes to the phonon-modes of Ce_SS@RT brought in by neighbouring environment changes]: (a) thermal oxidation on hot plate @ 150 °C spectral traces, and (b) Raman mapping data in which the product is maintained in continuous contact with DI-water. (c) Spectral data extracted out of the mapping data to demonstrate the appearance of 488 cm-1 mode respectively.

It confirms the possibility of localized laser-induced IPL thermal quenching, when investigated at 40 kW/cm² laser irradiance. The spectral data presented in fig. 3 8 (c) at this irradiance level from the same product location demonstrates the CT luminescence quenching. Also, the in-situ Raman mapping data acquired from the 50 µm² Ce_SS@RT product surface during 8 hrs DI-water in contact will further reaffirm, whether the CT quenching is surface oxidation or not. The adopted nc-ceria surface schematic presented earlier (see the inset of figs. 3 7 (b)-(c)), highlights the

recoverable surface oxidation scheme in contact with DI-water is published elsewhere [186], [197]–[199].

One of the standalone observations of the Ce_SS@RT product linked to Raman spectroscopy is highlighted here. The specific case of importance is the time-evolved oxygen vacancies elimination achieved in ambient by 150 °C hot plate annealing. In which the pristine broad diminished 488 cm⁻¹ mode recovers and strengthen with annealing time and saturates within 30 minutes. The probable reasoning for this observation might be linked to surface desorption of ambient environment species (like; hydroxyl, peroxides, superoxide's etc.) as literature reported leading to oxidation [220]–[228].

An aluminum foil wrapped optically flat micro-glass (76×25×1.35 mm³ borosilicate glass) slides painted with the Ce_SS@RT gel is chosen for the case of thermal healing in air by annealing. A set of 5 such Ce_SS@RT gel paintings are placed on a hot plate at 150 °C in the ambient condition and are withdrawn in intervals of 5 minutes individually. These samples are immediately taken for Raman acquisitions till a noticeable change of the 488 cm⁻¹ phonon mode is observed. The obtained individual Raman spectral data (2 accumulations each of 5 s) is normalized and are plotted in the fig. 3 13 (a) for interpretation. A strong, intense 488 cm⁻¹ mode assigned to the nc-ceria oxidation started to appear with annealing time. Based on this observation, the observed IPL quenching by laser irradiance generated localized heating cannot be ruled out. Also, the irradiance localized region appearance changes in respect to the pristine region of the Ce_SS@RT product add favorably to surface desorption. The optical micrograph of pristine and 40 kW/cm² irradiated surface region is presented in fig. 3 8 (b).

In the surface modified region this irradiance is maintained for 12 minutes to deliver noticeable 88 % IPL quenching (see fig. 3 11 (c)). Thus, this confirm surface desorption and localized oxidation induced by Nd-YAG laser-generated heating. The

97 % recovery data to the original reduced auto-catalytically by retaining the sample position in ambient for 6 hrs is shown in fig. 3 11 (d). In the oxidized product the intensity of the 488 cm⁻¹ mode overtakes the 553 cm⁻¹ mode. In contrast, although the interchangeability between these two modes is not established in the present study, oxidation occurrence by bringing in contact with DI-water and co-dependence between the modes can be seen in the fig. 3 13 (c).

The in-situ dynamic observations of the Raman spectral signatures in contact with the neighboring ambient environment changes are discussed here. The conclusions are; (A) in case of Ce_SS@RT product: (1) The maximum spectrum filtered in range 390-490 cm⁻¹ out of the sum filter (160-1800 cm⁻¹) happens to be noise, thereby no signature of the strongest 488 cm⁻¹ mode is observed over the mapped region of $50~\mu\text{m}^2$. (2) Its Raman map is featureless with uniform contrast. (3) The average and the minimum spectra retraced out of the total wavenumber mapped, exhibits the $553~\text{cm}^{-1}$ oxygen vacancy mode, in conformity with the nc-ceria defects (i.e., at reduced state).

Similarly, (B) for the case of Ce_SS@RT in continuous contact with the DI-water: (1) the Raman spectrum of the trench region of this product surface, sum filtered (160-1800 cm⁻¹), having DI-water in it is mapped. (2) The 488 cm⁻¹ is considered and is extracted out of this sum filter data. It can be seen as having differential contrast, implying the presence of significant oxidized cerium fraction on the mapped surface. (3) Away from the trench boundaries there is less surface oxidation. (4) An appropriate background subtraction from all over the mapped surface region is done to highlight the trench boundaries explicitly. It is shown as an inset in the fig. 3 13 (c). (5) The presence of the 448 cm⁻¹ mode even in the minimum spectra derived out of the entire 50 µm² region, illustrates the oxidative feature of the DI-water. These Raman spectroscopic mapping illustrations, along with the shown extracted spectra,

are in support of the autocatalytic regenerative feature snapshots of the Ce_SS@RT product presented earlier in figs. 3 7 (a)-(d).

3.5 Agglomeration of Ceria nanocrystals a boon or bane: a detailed evaluation in tune with the non-classical crystal growth route

Primary entities like atoms/ions/molecules their agglomerates and subsequent agglomerate aggregation are the generic evolution stages of developing molecular entities into a coarser particle. In-situ high-resolution Transmission Electron Microscopy (TEM) imaging is dominantly employed to elucidate and track these morphological evolutions linked with the crystal growth.

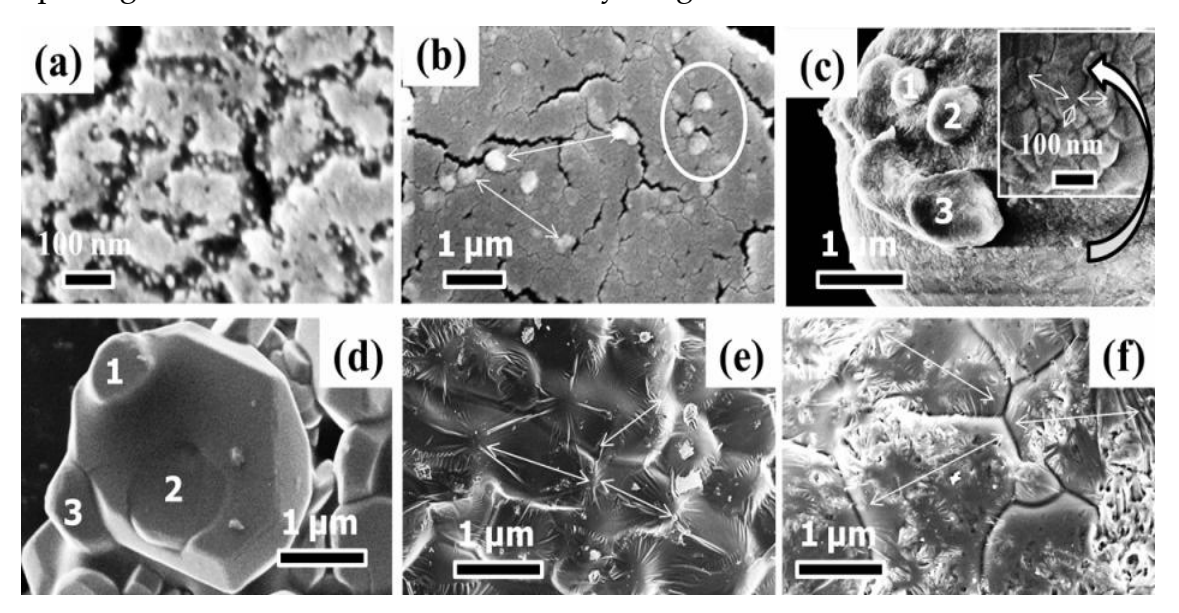


Fig.3 14 [Classical Crystal growth stages induced by thermal processing: FESEM illustration]: Nucleation: (a) monomers generation and adsorption, and (b) nucleating sites evolution; Ostwald ripening: (c) micron-Al surface, (d)-(e) ripening, (f) final evolved grain surface with larger crystallites.

Even the unexplored phenomenon of initial nucleation stage has also recently been observed to proceed via a two-step non-classical pathway [233]–[237]. The best-known fact about the classical crystal growth (stepwise layer-by-layer monomer adsorption derived growth) process is modeled as early as 1927 by Kossel et al.,

[238]. In this model, the solution-phase growth of a faceted crystal is presented. Without going much into the details of the classical growth, it can be stated that there are two main physical attributes: (1) overall free energy minimization drives nucleation, (2) in contrast overall surface energy minimization of the system directs crystal growth. This second physical parameter is the particle coarsening step and is also termed as Ostwald ripening [239].

The prevalent classical crystal growth major stages are followed from the thermally annealed micron-Al powder FESEM micrographs, which are presented in the figs.3 14 (c)-(f). The micrograph of fig. 3 14 (c) depicts a coarser μ -particle surface packed with nanoscale crystallites (inset in the micrograph) and also having smaller particles (identified in the same micrograph as 1, 2, and 3) as its surface attachments. The surface roughness of this μ -Al particle can be seen in the inset of the fig. 3 14 (c). The figs. 3 14 (d) and (e) represent micrographs of the LN₂ temperature quenched product made out of the sample shown in fig. 3 14 (c) particles held at 700 °C for 2 hrs. In fig. 3 14 (c) these previously surface attached smaller 1, 2, and 3 particles can be seen undergoing Ostwald ripening while in contact with the larger one.

Likewise, the process of evolution of μ -Al particle surface with smaller crystallites to a much larger crystallite is depicted in fig. 3 14 (e). Micrograph in fig. 3 14 (f) is for the corresponding furnace cooled RT product of sample presented micrograph fig. 3 14 (e). It highlights the actual surface evolution with a higher clarity. The micrographs in figs. 3 14 (a)-(b) are acquired to present a schematic view of the nucleation stage with the following steps: (1) individual monomers adsorption with each other giving rise to an amorphous matrix, (2) a mass density fluctuation inside the amorphous matrix driven by the maintained external parameters will initiate some random nucleating centers as highlighted in the fig. 3 14 (b). Nucleation is a single continual step (extremely small length 10^{-10} m and time 10^{-13} s scale).

However, it is divided into two micrographs for representative purposes to demonstrate it.

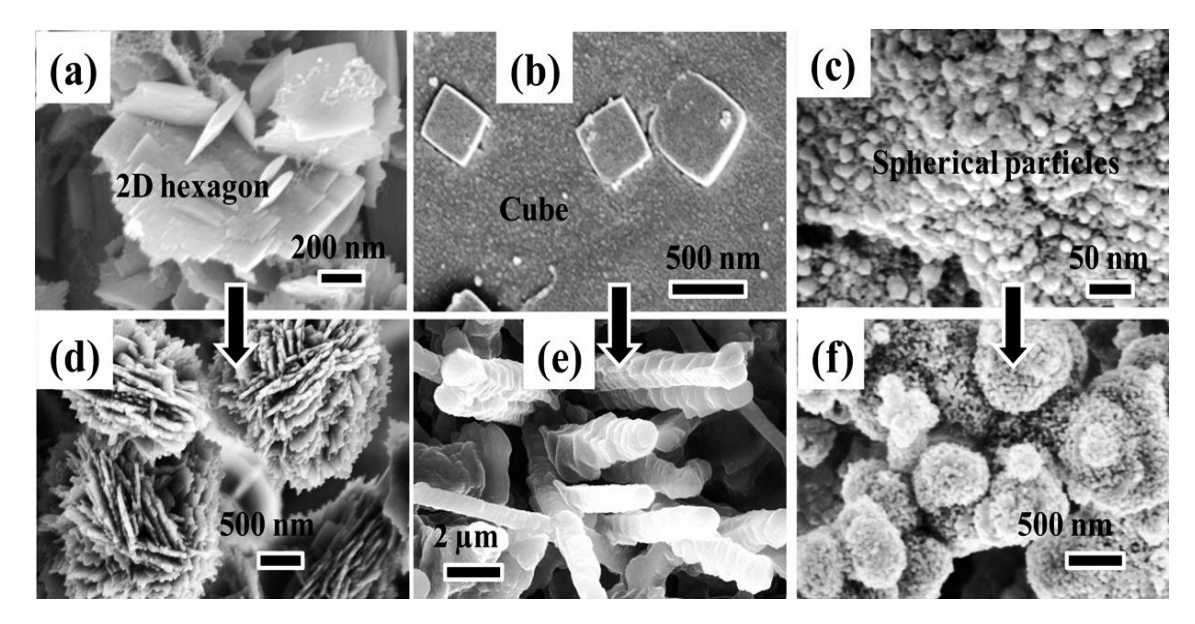


Fig.3 15 [Particle mediated two step non-classical crystal growth: FESEM illustration]: Building blocks of: (a) 2D hexagon, (b) cubes, and (c) spherical particles; Evolved morphologies: (d) flower like, (e) rods, and (f) nano porous microspheres respectively.

The micrographs from figs. 3 15 (a)-(c) represent the individual building units: (a) 2D hexagon, (b) a cube, and (c) spherical particles. The morphologies observed in figs. 3 15 (d)-(f) can be seen to be developed out of these smallest building units by systematic aggregation. In the available natural material today, about 90 % (specifically biominerals) belong to this depicted scheme of crystal growth. It is also termed as "the particle-mediated non-classical growth pathway". The subsequent discussions will be specific to non-classical crystal growth scheme of things leading to the primary question answer of whether nanocrystals agglomeration is a boon or bane. The most obvious response is that agglomeration is a boon, if it happens in a controlled fashion leading to fine-tuned targeted morphology evolution.

In particle-mediated non-classical growth, observation of the current study and literature illustrates particles oriented attachment (OA). The OA between two building units or more usually advance by the fusion of the identical (hkl) highest surface energetic crystal facets. The energetic crystals facets are brought into contact

with each other by undergoing appropriate rotation to develop into a single larger mesocrystalline feature. The detailing of such a mesocrystalline structures is mostly carried out by TEM-SAED mode investigation. However, in the present FESEM micrographs, the 2D hexagons will be mesocrystalline (see fig. 3 15 (a)).

3.6 1D-Ceria fibers growth by OA mechanism in DIwater facilitated biomineralization

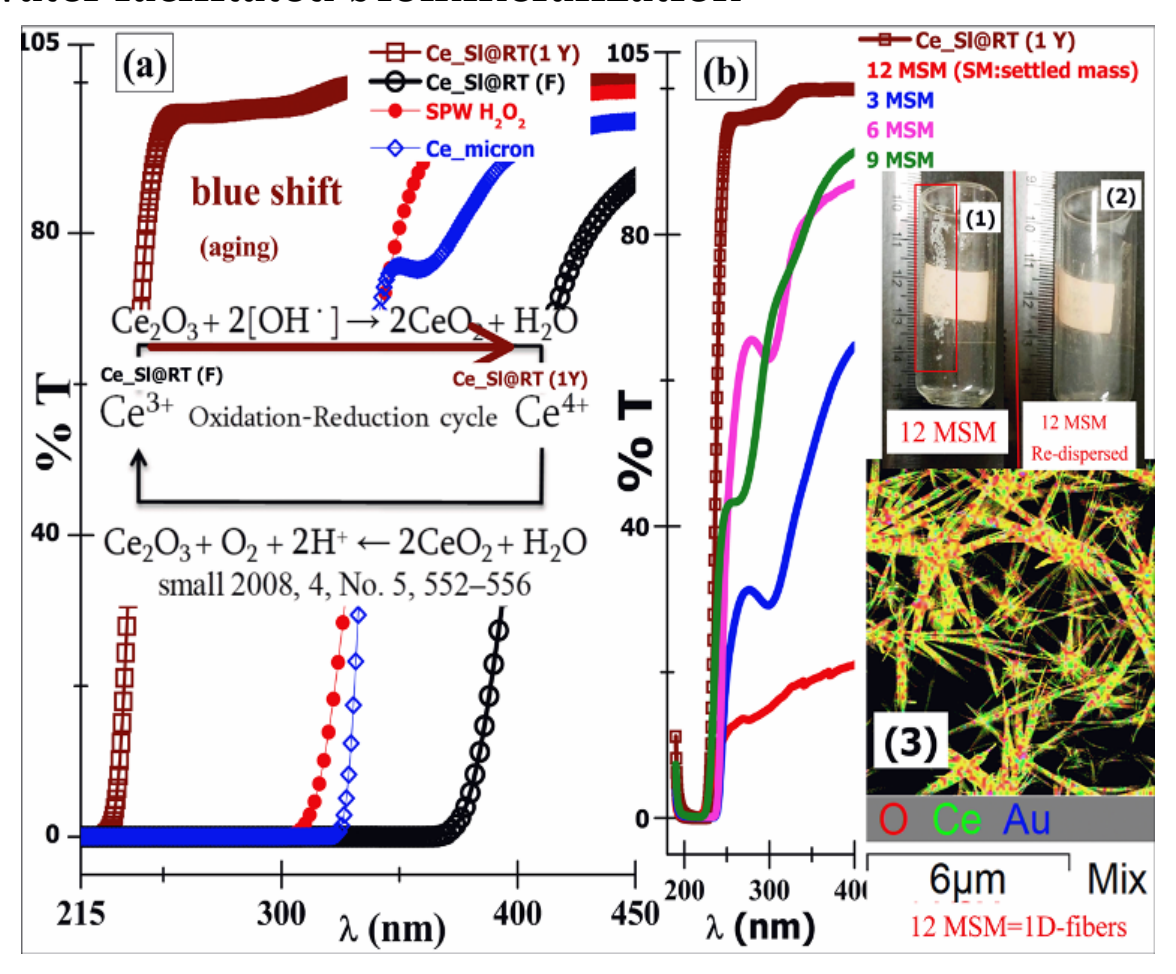


Fig.3 16 [Autocatalytic regenerative feature and biomineralization]: (a) Oxidation by aging; (b) optical spectra of progressive bio-mineralized products (with inset of 12 MSM products in glass vial (1), redispersion (2), and (3) morphology with composition).

As stated earlier, the freshly prepared Ce_Sl@RT product surface atomic cerium is in the +3 charge state. With aging for a year, the same supernatant Ce_Sl@RT auto recovers to its bulk +4 states gradually. The fresh supernatant and the aged supernatant will be denoted by Ce_Sl@RT (F) and Ce_Sl@RT (1Y), respectively, in the forthcoming discussions. The oxidation recovery of the surface cerium atoms with aging is confirmed by the blue-shift STC and can be seen in the fig. 3 16 (a).

This oxidation-reduction cycle is inherent to nc-ceria. Interestingly, settled entities at the bottom of the stored vial are isolated. These entities are DI-water facilitated OA driven bio-mineralized progressed 1D-ceria fibers. It is another experimental demonstration in support of the DI-water as the direct participant in mineralization, similar to many previous studies [26]–[28], [30], [225], [240]. The fig. 3 16 (b) inset shows the snapshots of the (1) 12 month settled mass (12 MSM), (2) its redispersion in the DI-water, and (3) EDS compositional map of these fibers drop cast on the carbon tape respectively.

The sequential settled mass extracted after every 3 months' duration is investigated with the UV-Vis optical spectroscopy. The obtained UV-Vis spectral data of each of these products (i.e., 3 MSM, 6 MSM, 9 MSM, and 12 MSM) are plotted in the fig. 3 16 (b). The absorption edge extension to the visible wavelength range with aging suggests the highly reduced state of the 12 MSM products. This is similar to the previously presented absorption data of the Ce_SP@RT.

3.7 Tyndall Effect

The simplest way to illustrate the nc-ceria settling with aging is to visually track the laser light path intensity, which is allowed to travel through a set of nc-ceria dispersions. As can be seen, the 532 nm laser path is quite diminished when compared with the fresh, and the PVA stabilized nc-ceria dispersions. The PVA stabilized product had no scattering intensity loss, even after being stored for more than a year. It reasserts that even though the devised transparent supernatant has 2 nm ceria water-soluble crystallites, the DI-water facilitates these individual crystallites to interact in an orderly fashion and aggregate. The growth of these

aggregates causes settling. The photograph of the Ce_Sl@RT product is presented in the figs. 3 17 (a)-(b). It is evident from figs. 3 17 (c)-(d) that the isolated 3 months settled mass (3 MSM) developed network type microstructure and its corresponding TEM micrograph concurrently favours DI-water as the growth directing agent. The direct participation of water in the biomineralization confirms reported earlier observations [13], [26]–[28], [30], [240].

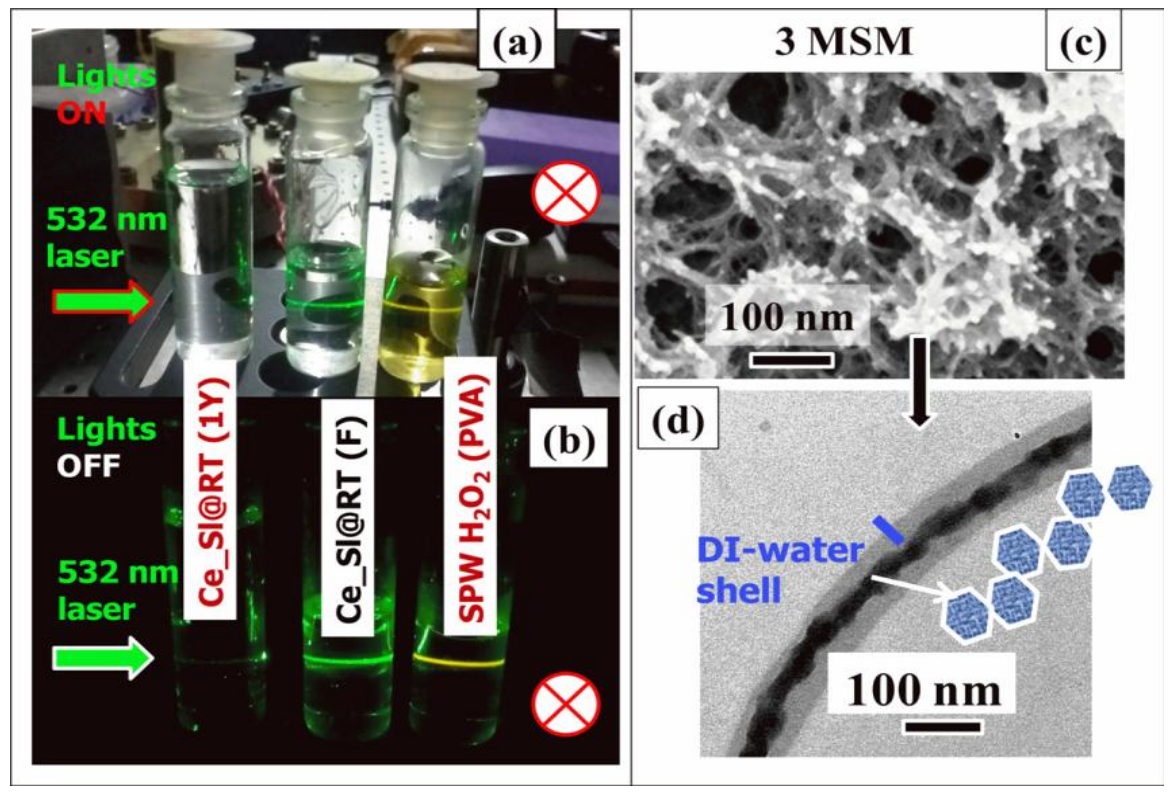


Fig.3 17 [Light Scattering efficacy of Ce_Sl@RT product]: Laboratory lights (a) ON, and (b) OFF state camera snaps illustrating scattering efficiency with 1year aged product. Microstructure of 3 months aged settled mass: (c) FESEM, and (d) TEM BF image respectively.

3.8 Validation of OA mechanism in 1D-Ceria grown fibers

The grazing incidence X-ray diffraction (GI-XRD) of the 12 MSM product drop cast on a fused silica surface is chosen to probe for 1D-Ceria fibers texture, and the structural phase analysis. The GI-XRD as a bulk characterization technique is more preferable than localized TEM investigation support for OA growth. Many TEM microstructural demonstrations already exist in literature, hence only a few localized TEM data from the 12 MSM individual fibers are acquired to supplement the GI-XRD data.

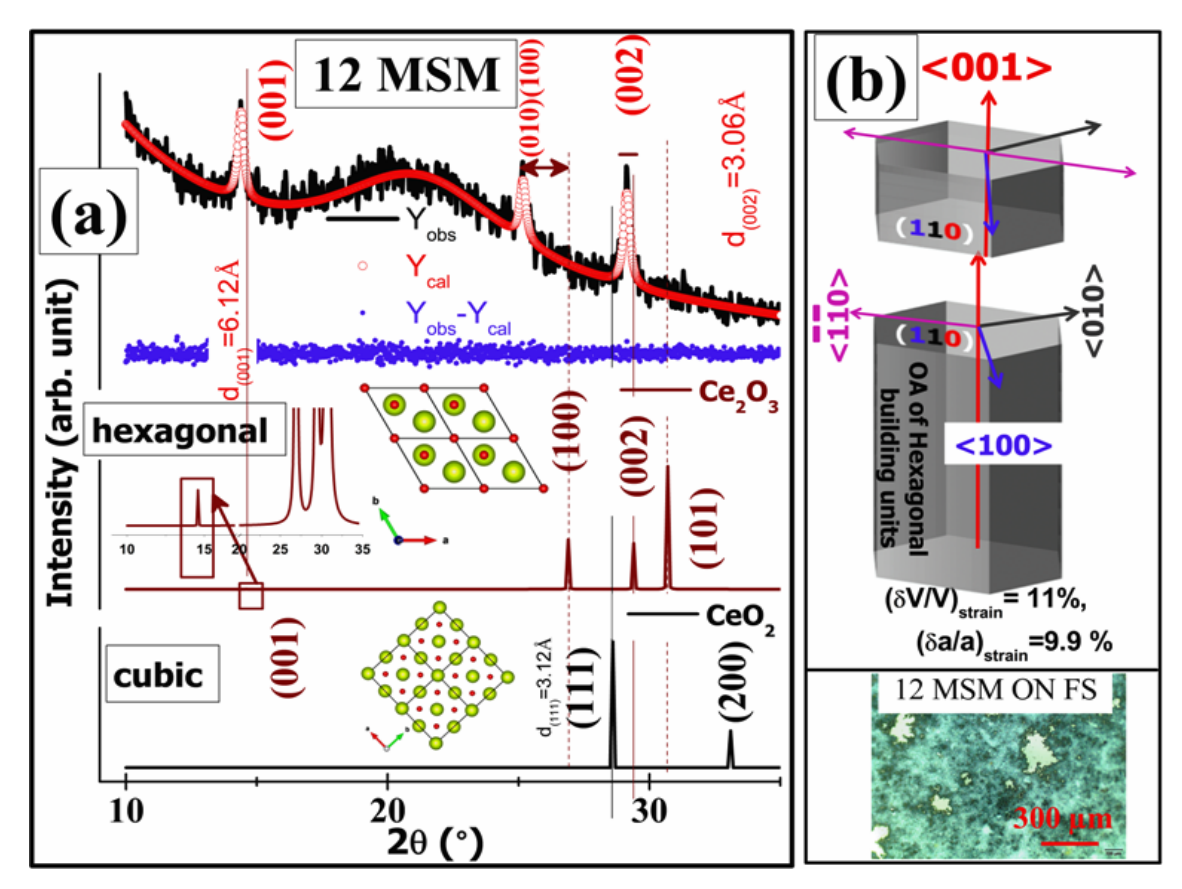


Fig.3 18 [GI_XRD data of 1D-Ceria fibers coated on fused silica substrates]: (a) 1D anisotropy induced cubic (CeO2) to hexagonal (Ce2O3) structural phase transition, and (b) schematic of the two hexagonal building units along (110) crystal plane OA, in accordance with the 1D-fiber obtained texture respectively.

The differentiation of near equal values of cubic CeO_2 most intense peak at $d_{(111)}$ =3.12 Å from hexagonal Ce_2O_3 $d_{(002)}$ =3.06 Å as the growth orientation is possible by XRD. However, in TEM for such ambiguity, the use of the SAED and HRTEM mode in a sequence is employed. The GI-XRD data of the 12 MSM product and the appropriate possible structural phases: (1) FCC CeO_2 (SG: 225, Fm-3m), and (2) hexagonal primitive Ce_2O_3 (SG: 164, p-3m1) are plotted row-wise in the fig. 3 18 (a). The FPA is

used to generate structural phase profile of 1D fibers Ce_2O_3 having <001> as the preferred orientation and also to extract crystallographic parameters [217]. The computed pattern (Y_{cal}) and also the difference pattern (Y_{obs} - Y_{cal}) are plotted in fig.3.15 (a) for inspection. These suggest a near convergence having the goodness of fit index (χ^2 =1.27) close to 1. The hexagonal structure refined unit cell parameters are: a=4.079(42) Å, c=6.121(88) Å, and V=88.2 (22) Å³, highlighting that 1D fiber product is under tensile volumetric strain.

Table 3 3: 12 MSM product bulk X-ray structural attributes extracted

Sample Code	Crystallite size (nm)	Orientation factor	<u>Tensile Strain</u>
12 MSM	32.6(5.8)	0.76	(δV/V)=11 %, (δa/a)=9.9 %
Ce ₂ O ₃	NA ~2-5 μm	polycrystalline 4.13×10^{-4}	.ideal case ~ zero.

The 12 MSM product crystal structure refined parameters of importance are listed in the table- 3.3. It can be seen that most of the volumetric strain is contained in the basal (110) plane, whereas the perpendicular c-axis direction is mostly relaxed and therefore contributes to the OA growth. A significant 5^{th} order, higher orientation factor, along the c-axis justifies the dominant 1D texture developed with respect to the μ -Ce₂O₃ ICCD PDF: 78-0484 file. Based on these GI-XRD assessments and subsequent indexing, a schematic of the OA growth consisting of two hexagonal building units is drawn for easy understanding in fig. 3 18 (b). To briefly summarize, the OA reported in literature is expected to lead to the growth of a 1D-ceria structure based on two scenarios: (1) OA along {110} planes with <001> growth, and (2) OA

along {211} planes having <111> as growth direction [241]–[248]. The present biomineralization case falls into the first growth scenario. Also, at the bottom of the fig. 3 18 (b), one recoded optical micrograph of the drop cast 12 MSM product on a fused silica substrate, which is chosen for the GI-XRD investigation, is included for observation.

3.9 TEM Validation of OA mechanism of Hexagonal building units to develop into a 1D-ceria grown fiber

The pictorial schematic of the progress of 1D-ceria fibers growth and development process is presented in figs. 3 19 (a)-(e). In literature, detailed TEM validations in concurrence with DFT theoretical models explain the evolutions of morphologies based on energy minimization. These specific morphologies become the basis of crystal growth and development. The specific cases of preferred exposed facets related to observed nc-ceria morphological features are in the following fashion: (1) {111} enclosed octahedrons, (2) {111} and {100} for truncated octahedrons, (3) {110} and {100} for rods, and (4) {100} for cubes [249]–[255]. The facets evolutions schematic in the figs. 3 19 (a)-(c), are adapted from the above mentioned publications. Whereas in figs. 3 19 (d)-(e) the gradual elimination of {111} planes along with <001> texture development is presented. The observation away from the <001> presents the 1Dceria fiber having {110} and {001} planes as facets, is shown in fig. 3 19 (e). However, in reality if the FCC unit cell is considered as the building unit, two important physical attributes need to be satisfied. Those are: (1) planes atomic packing surface density order should be $n_{(111)} > n_{(100)} > n_{(100)}$ and (2) their surface energy value is in the order $\gamma_{\{110\}} > \gamma_{\{100\}} > \gamma_{\{111\}}$ respectively. Based on these two physical attributes, FCC building unit derived 1D-ceria morphology should be enclosed by the {111} crystal facets. Contrary to this, the final 1D-ceria morphology reported in literature has no such faceting followed. In most of the reports the grown 1D-ceria morphology has facets with oxygen-deficiencies, leading to highly reactive facets in nature. These 1D-ceria having reactive facets have a lot of technological applications.

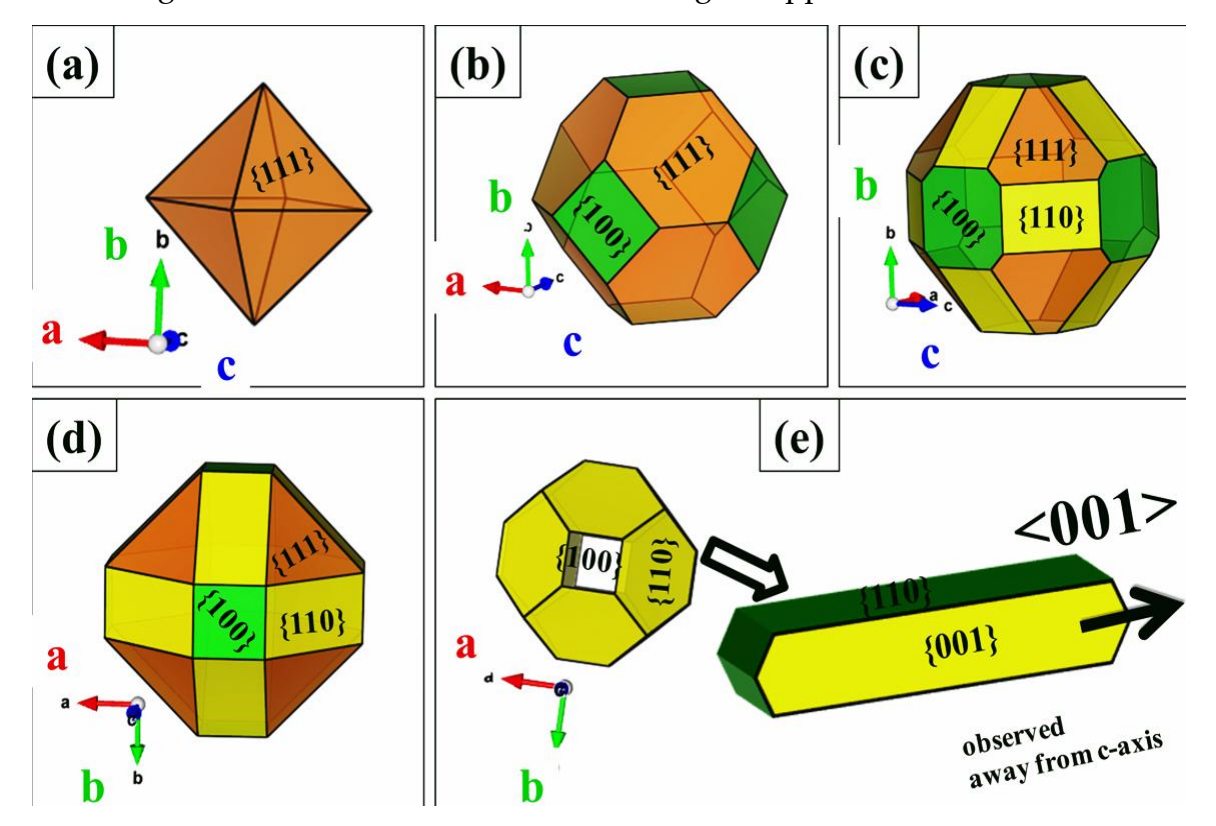


Fig.3 19 [Growth stages of 1D-ceria fibers: Schematic view]: Ceria unit cell; (a)-(c) depicts crystal facet development, (d) gradual elimination of {111} planes and <001> texture formation, (e) <001> textured 1D-ceria fiber observed along c-axis and away from the c-axis respectively.

This section is devoted to the localized TEM microstructural data acquired to support GI-XRD and presented inferences, leading to an insight into the OA mechanism guiding 1D nanostructures growth. It is important to identify the 1D-ceria fibers growth axis. To achieve this, a set of sequential HRTEM and SAED mode micrographs are acquired at the same localized region of the 1D-ceria fibers. Specifically, an edge portion of the fiber suitable to the TEM e-beam transparency is chosen and examined in detail. The TEM extracted microstructural and structural information with analysis from one such 1D-fiber is presented in the figs. 3 20 (a)-(e). These localized TEM microstructural observations are consistent with the bulk GI-XRD data presented in the fig. 3 18, highlighting 1D-ceria fibers to be made out of a

Ce₂O₃ hexagonal structural phase. The TEM-SAED acquired localized structural data iteratively processed for the possible zone-axis with less than 5 % tolerance, point to [110] as the preferred zone-axis. Indexing of the TEM-SAED data in this zone is then carried out. The three shortest d-spacing lattice planes of the hexagonal Ce₂O₃ unit cell nearest to the primary spot are evaluated and are found to be in concurrence with the XRD data. These are: (1) $d_{(002)}$ = 3.03 Å, $d_{(1-12) \text{ or}(012)}$ = 2.253 Å, $d_{(1-10) \text{ or }(100)}$ = 3.37 Å, and (2) m \angle (1-10) & m \angle (1-12)=48.04 °, m \angle (1-12) & m \angle (002)=41.96 °, m \angle (1-10) & m \angle (002)=90 ° respectively.

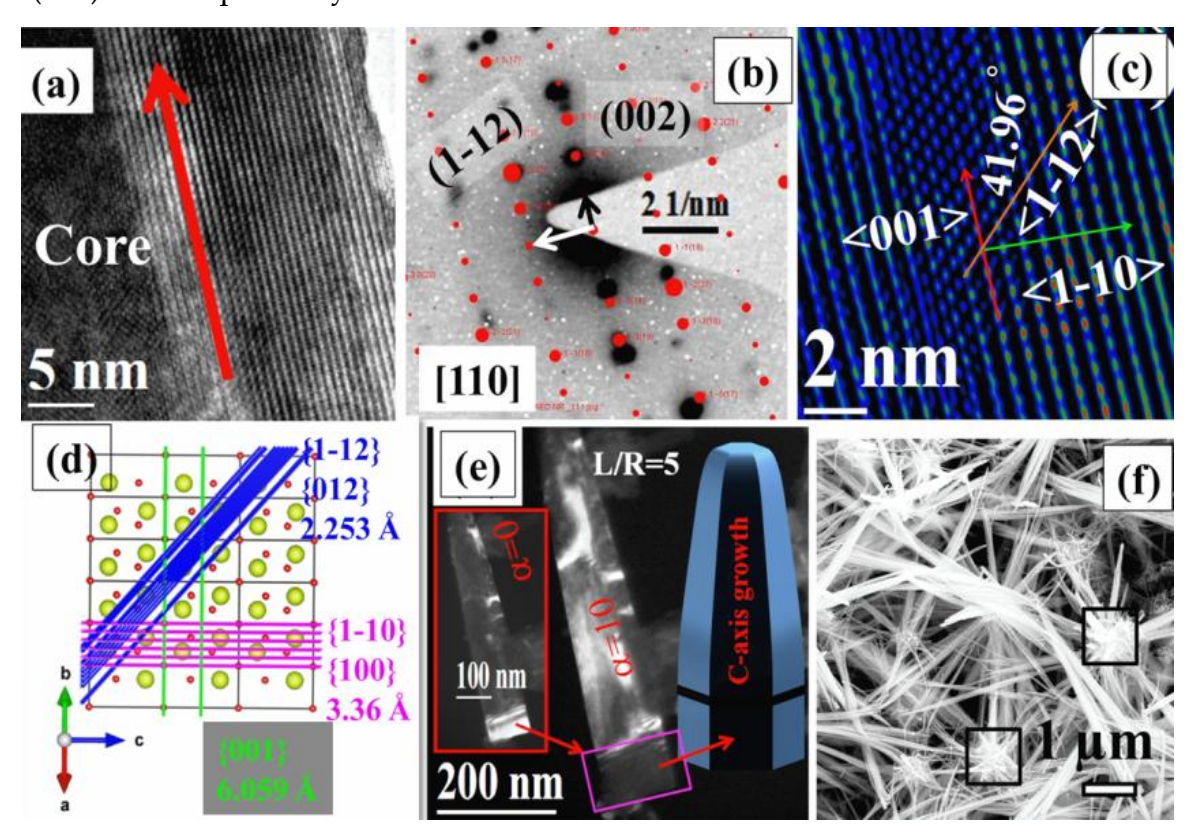


Fig.3 20 [Growth direction of 1D-ceria fibers by TEM]: TEM acquired; (a) BF, (b) SAED, (c) HRTEM, and simulated HRTEM of (c) justified in (d). (e) TEM DF for α =0, 10 micrographs, and (f) FESEM micrograph of 1 D-Ceria fibers respectively.

The one to one correspondence of the HRTEM data with Ce₂O₃ unit cell is realized by depicting this unit cell generated simulated HRTEM. The simulated HRTEM schematic is shown in fig. 3 20 (d). The single crystallinity of these fibers in the TEM DF mode is also accessed. It is evident that the fibers are of high crystallinity but

contain around 100 nm rectangular basal planes with a distinctly different orientation than the entire grown fiber portion above it. It resembles the seeded growth development scheme, in which a specific lattice-matched plane with a specific texture is facilitated to grow preferentially by the seed. It is hypothesized that an initial lumpy mass by nanoparticle aggregation gets initiated, which develops into a basal seed for the subsequent preferential growth of 1D-ceria fibers above it. The FESEM image provides direct evidence for the radial outflow of these 1D-ceria fibers from many-seed like entities. These entities are dominantly observed and are identified in fig. 3 20 (f) (rectangular magenta-colored regions).

3.10 In-situ TEM e-beam facilitated studies of OA mechanism

3.10.1 Prescribed Protocol for TEM e-beam Probe or Modification to be followed

Both in-situ electron modification and probe activities are sequentially done in FEI Tecnai G^2 20 S-TWIN TEM microscope equipped thermionic LaB₆ electron gun emission operating at 200 keV. A chosen specimen region is brought to focus under TEM e-beam at Mh 610 kX high-resolution mode (largest condenser aperture, 150 μ m, and 200 nm condensed spot), and is irradiated with step-4 LaB₆ electron emission current displaced in the TEM filament supervisor console (E4I=7.93 μ A, see fig. 3 21 (a)), for initiating the specimen dynamic in-situ modification. A nominal step-2 LaB₆ reduced emission (E2P=0.88 μ A, used to probe any further dynamic changes introduced) stage is employed for reloading and imaging of the radiation quenched localized modified regions of the specimen. These irradiated regions are initially fed to the stage control flap-out memory address so that retracing the exact location can be done as and when the subsequent sequential (probe or modification)

operative step needs to be reactivated without any specimen location ambiguity. One such E4I specimen exposure region with beam condensed to approximately 200 nm is depicted in fig. 3 21 (b), as an imprint highlighting the shape of the electron beam.

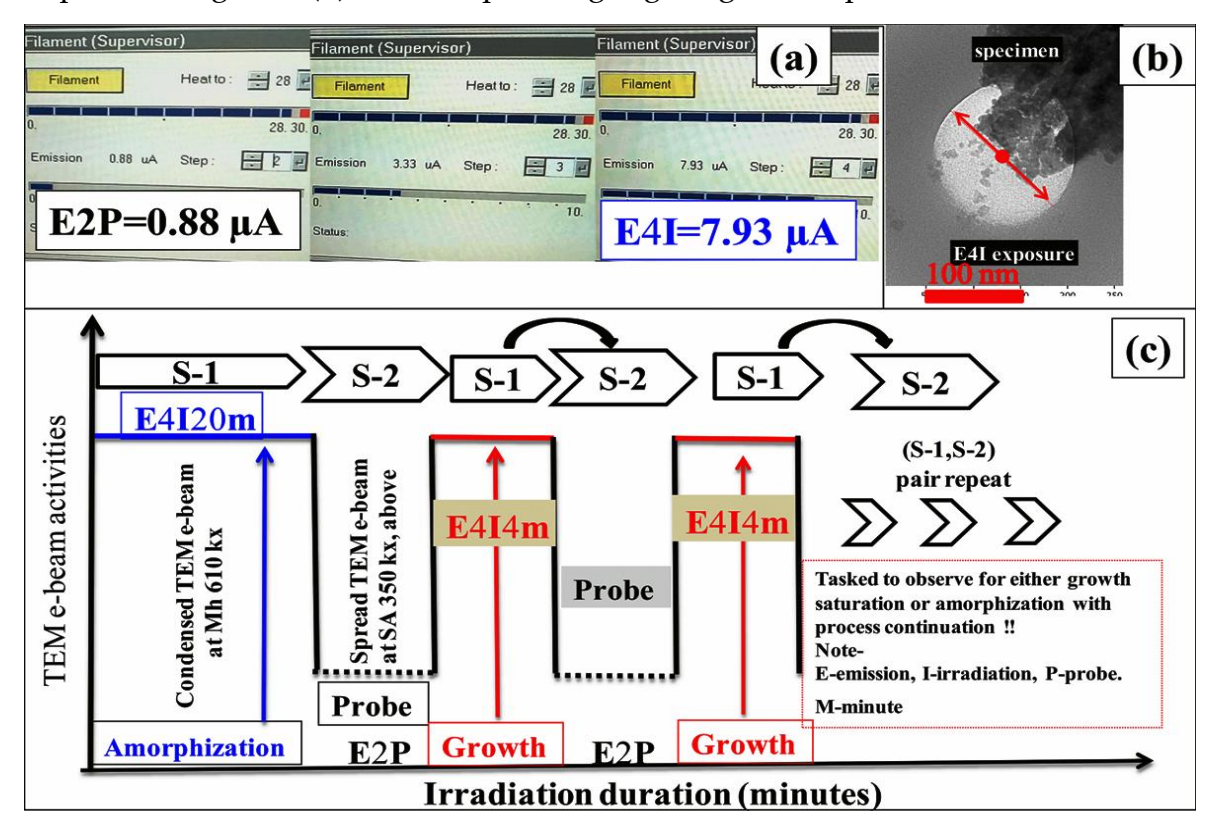


Fig.3 21 [Schematic of TEM e-beam activity]: (a) LaB6 filament emission to probe (E2P) and emission for irradiation (E4I), (b) E4I modified region, and (c) schematic for subsequent studies respectively.

It is to be noted here that the carbon support films are the standard support films in TEM because of its irradiation, thermal stability, and chemical inertness. However, various beam induced transformations such as C-atom sputtering in the beam focused region leading to thinning resulting in brighter contrast can be found in literature [256]. Beam spreading by the intensity knob and a simultaneous ~<30 s recovery to step-2 filament emission criteria recursively utilized for altering the beam attribute from material modification to probe tool. In TEMs having field emission gun (J=10⁵ Acm⁻² current density) as electron emitter, these dynamically tracked

changes will just get expedited in time scale because of three orders higher magnitude of the current density used.

In contrast the current dynamical occurrences will be at slower time scale, because of having LaB₆ thermionic emitter investigation [50], [257]–[260]. Significantly, even if the irradiation mode is stationary, live monitoring to retain the TEM e-beam center precisely at the specimen focused spot location is carried out concurrently as and when required. It is done to negate both the instrument specified probable specimen drift (<1 nm/min), and spot (<2 nm/min) drift respectively because of such high Mh range (approximate 25 nm × 25 nm region) data acquisitions.

Based on several repeated observations in the HRTEM mode an optimized combination E₂P Probe) E4I of (Emission to and (Emission Irradiation/modification) duration is quantified. The HRTEM modified region is probed employing TEM techniques like TEM BF, DF, and SAED mode etc. The optimized prescription schematic is drawn and is shown in the fig. 3 21 (c). The E2P time can extend to 10-15 minutes based on retracing and acquiring micrographs, whereas E4I sharply limited to 4 minutes. The E4I4m (Emission for Irradiation maintained for 4 minutes) is mostly devised to facilitate nc-ceria growth, out of the central region of the amorphized ceria layered flake utilizing an initial 20 minutes TEM e-beam hammering [261]. The purpose of activating TEM e-beam hammering is to develop a radiation-hardened region, i.e., to have almost negligible atomic lateral movements as a result of dense packing and void removal. It will also provide an electron transparent region for the TEM HRTEM mode imaging. Based on a few experiments, it is expected that a 20-minute electron hardening of the localized region will be able to sustain the same emission dose for at least a further subsequent period of 20 minutes without any degradation. As a result of this, the total 20 minutes irradiation/modification duration is further sub-divided into 5 divisions for the quantitative growth kinetics extraction. Incidentally, the optimized E4I4m

exposure produces HRTEM readable crystal lattice growth for all the subsequent TEM mode investigations.

3.10.2 TEM e-beam devised Hammering and Amorphization (E4I20m)

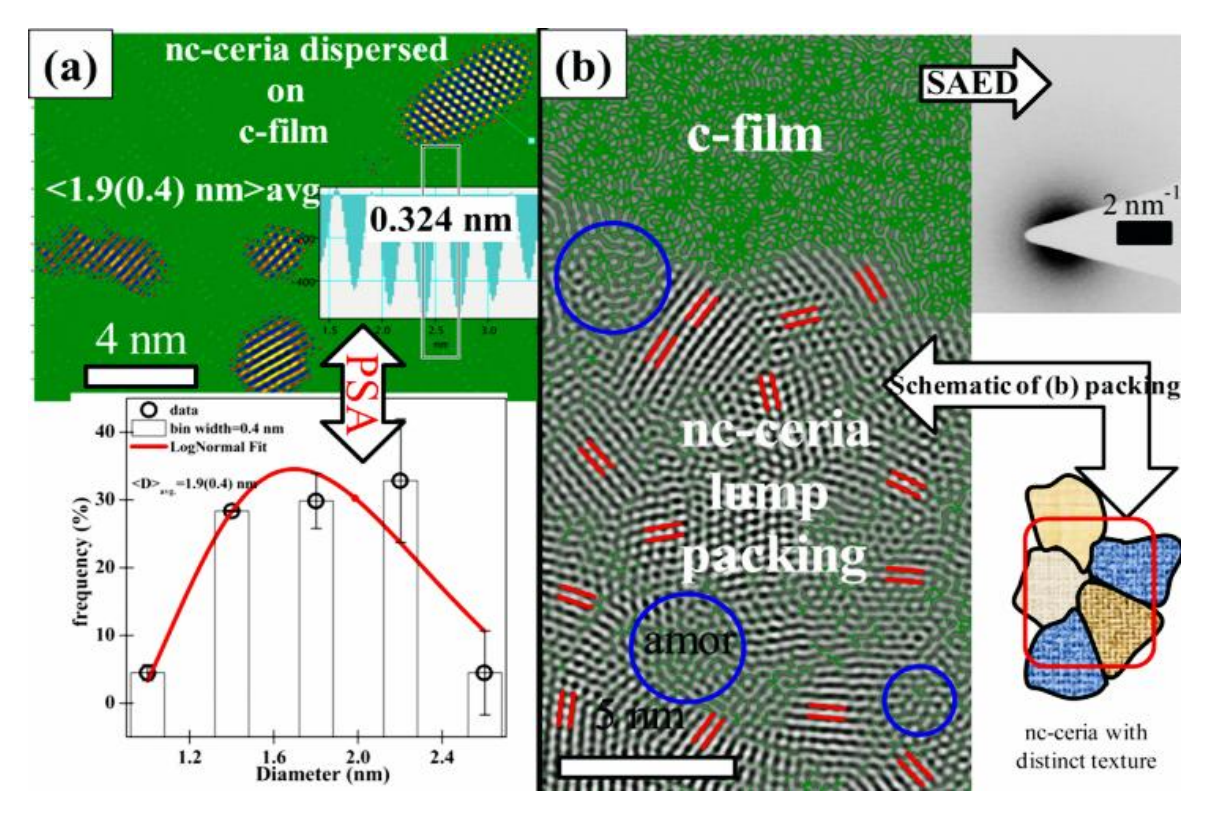


Fig.3 22 [Micrographs of two distinct nc-ceria formulations]: Ultrasonic (a) horn, (b) cleaning bath dispersed nc-ceria HRTEM micrographs respectively.

The TEM BF, HRTEM, and SAED mode are employed cooperatively to investigate many TEM e-beam hammered nc-ceria lump irradiated locations for "radiation hardening." The "radiation hardening" alludes to a localized TEM e-beam transparent; atomically dense (devoid of any pores, voids, or gaps) packed amorphized ceria thinned flat regions. As a result this region will have negligible lateral movement (radial expansion perpendicular to the e-beam direction) during the irradiation facilitated subsequent crystal growth investigations. The microstructurally distinct two regions of nc-ceria formulations that are observed in TEM BF micrographs are shown in fig. 3 22 (a)-(b). VCX 750 W 20 kHz ultrasonic processor with a 13 mm solid ultrasonic horn and operated at 50 % of its maximum

amplitude for 5 minutes, is employed to obtain nc-ceria dispersions in 25 mL of DI-water. A pinch of this nc-ceria powder dispersion is capillary drop cast over a TEM grid and the obtained nanoparticulate well-dispersed form in TEM BF mode is shown in fig. 3 22 (a). A statistical analysis of 5-6 such TEM BF micrographs over 100 particles suggests to the lognormal distribution, with average nanocrystal size, is of 1.9(0.4) nm. Similarly, the TEM BF images of nc-ceria lumps dispersed in a water-based ultrasonic cleaner (Ralsonics model R-80 W, 30 kHz) for 5 minutes are recorded. These micrographs indicate that the sample has crystallites with random orientation and nearly densely arranged as seen in the fig. 3 22 (b), and its representative drawn schematic respectively.

The presence of voids, pores, gaps, and amorphous ceria matrix regions connecting nanocrystallites is also observed. These nc-ceria lump formulations having nc-ceria crystallites in contact with the adjacent ones through crystal boundaries and ceria amorphous matrix is the specimen of choice for subsequent investigations. As presented in the previous section, E4I TEM e-beam focused onto the lump-edge gradually moved towards thick lump center at Mh 610 kX. It enables the lumps to flatten and develop into atomically thin fused electron transparent region of almost 25×25 nm dimension which is the minimum requirement for probing (see HRTEM micrograph fig. 3 23 (a)). The E4I hammering for thinning of the nc-ceria lump region is continued for 20 minutes (E4I20m), and the micrograph shown in the fig. 3 23 (a) suggests that the optimized time span is sufficient for fabricating ~ 25(+5) sq. nm radiation-hardened amorphized lamellar ceria matrix locally.

This operation (E4I hammering for 20 minutes) is tracked over many such aggregated lumps, and one such TEM BF colored micrograph is presented in the fig. 3 23 (b). To have a clear, distinct view (fig. 3 23 (b)), the TEM BF micrograph is color indexed. It is carried out by the digital micrograph "histogram palette" script to adjust colors. The rule being that the micrograph pixels with a specific range of

intensities in the image are colored as one entity. Thereby, the amorphous carbon support film (C-film), TEM e-beam hammered, and the pristine nc-ceria locations of the fig. 3 23 (b) are colored to green, dark-gray, and white individually for illustration purpose, respectively.

To ascertain the, TEM e-beam hammered morphological change leading to the amorphization process, TEM SAED aperture is introduced. The region-specific diffraction patterns are recorded. In fig. 3 23 (c) a comparison of two such regions recorded diffraction patterns of the nc-ceria before and after TEM e-beam hammering is shown. Both the diffraction patterns are overlaid with respect to each other, for which Al $d_{(111)}$ = 0.4277 Å⁻¹ is considered as the calibrating Debye ring. The nc-ceria region TEM SAED digital pattern is matched directly with the PROJECT/PCED2s crystal structure generated simulated pattern. By using the simulated pattern the recorded pattern spacing are extracted and are labeled as shown in the fig. 3 23 (c) [262]. The ring radii and the corresponding intensity level ratios are transformed into a simulated linear electron diffraction pattern (LDP). It has a clear match to that of stoichiometric cubic ceria structural phase. In the TEM e-beam amorphized region, the intensity of these Debye bottom half rings is almost nullified (zero contrast variation) after the first disc, validating TEM e-beam hammering induced amorphization. The distinction being that TEM e-beam hammering generated microstructure is dominated by a densely fused amorphous ceria matrix, having sparsely populated ceria nanocrystallites. All these ceria nanocrystals are seen to be of the same orientation (incidentally mesocrystal like appearance), suggesting that with an appropriate TEM e-beam excitation the surrounding disordered ceria matrix can be consumed, facilitating the subsequent growth of ceria nanocrystals.

The list of possible phenomena under the TEM e-beam are (1) mass loss, (2) valency state reduction, (3) phase decomposition, (4) precipitation, (5) gas bubble formation, (6) phase transformation, (7) amorphization, and (7) crystallization. These attributes, in the case of the oxides in TEM, are already reviewed and presented elsewhere

[263]. Here this literature is scrutinized to present a viable interpretation of the amorphization process. Assuming the TEM e-beam operation is confined to 200-1000 keV probe energy range, based on elastic collision, the maximum transferable energy must be 4-31 eV for Ce, and 33-269 eV for O ions respectively [264]. Similarly, the computed assumed displacement threshold energy of Ce-atom in ceria sub-lattice is 40 eV; likewise, for O-atom, it is 20 eV constituting the oxygen sub-lattice of the fluorite structured ceria [265].

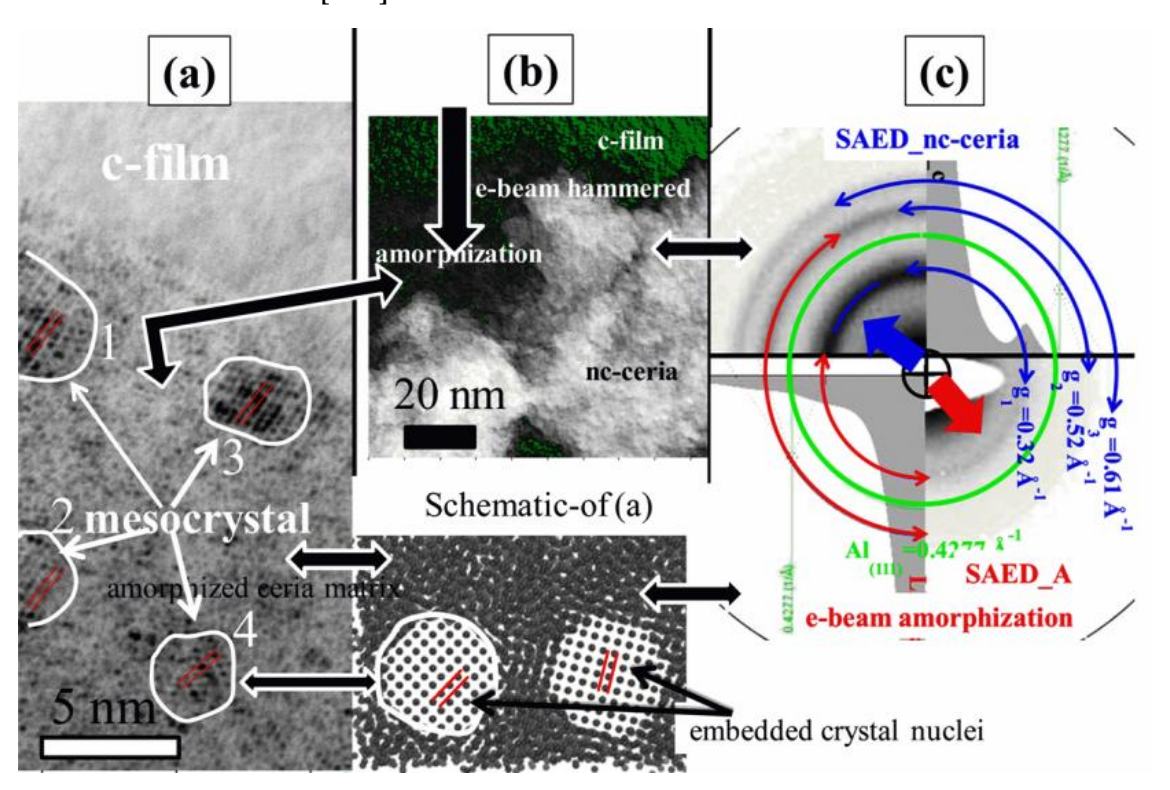


Fig.3 23 [Micrographs of TEM e-beam hammered amorphized region]: (a) nc-ceria lump with distinct e-beam hammered region, (b) HRTEM, and (c) comparative SAED patterns of nc-ceria and amorphized region respectively.

A comparison of these two energy values (i.e., maximum probable transferable energy, and displacement threshold energy) with TEM 200 keV e-beam operation suggest that generation of O-atoms knock—on displacements (non-thermal amorphization process) is the most probable process in nc-ceria fluorite structured oxygen sub-lattice. Another exciting facet of this fluorite structured ceria lattice is that these O-atoms associated defects are observed to be actively annihilated even

through the TEM microscope in ultra-high vacuum environment [266]. It will lead to O-defect creation and annihilation concurrently. Thus, the rule will be that if defects creation overtakes the recovery rate then, defects accumulation (point defects or chemical disorder) will substantially lead to the initiation of the localized topological disorder. This is consistent with an earlier study of Bhatta et al., who reported amorphization of 15 nm diameter nc-ceria under 200 keV TEM e-beam [267].

Also, nc-ceria as a facilitator of amorphization is reported in literature [268]. It is suggested that presence of nc-ceria in conjugation at the oxide heterointerfaces locally enhances the radiation-induced amorphization process of the adjoining oxide. Moreover, two primary models proposed for justifying the amorphization process under the TEM e-beam irradiation are (a) the mechanical thrust of the bombarding electrons delivered to the target atomic nuclei, i.e., knock-on mechanism; (b) electronic excitation by the electric field, i.e., radiolytic process [269]. The physical understanding of the amorphization and its corresponding reasoning, with a list of few specific materials investigated earlier includes: (a) electronic excitation intitanate pyrochlores (anion disorder in A₂Ti₂O₇, A=Y, Gd, and Sm), colloidal CsPbBr₃ nanocrystals, complex rare earth (Y(III), Eu(III), and La(III)) nanostructures etc., whereas (b) the frequently encountered knock-on displacements mechanism are observed in-SiC respectively [270]-[273]. More recently, fast and reversible phase transitions (amorphous to crystalline) have been observed in the case of the chalcogenide phase-change material (i.e., on GeSb₂Te₄ thin films) examined under TEM e-beam irradiation [274].

Taking a hint from reported data, the probable dominant mechanism responsible for the amorphization observed in the nc-ceria is attributed to the knock-on displacement of the O-atoms. Under continuous TEM e-beam exposure, the accumulation of these knock-on displaced O-atoms is practically feasible. Thus, the 20 minute continuous exposure accumulates enough O-atom point defects, which locally suppress the nc-ceria crystalline structure resulting in localized

amorphization. The amorphization region seems to cover the entire TEM e-beam exposed regions. Based on these inferences, the amorphized ceria matrix region can be identified as oxygen-deficient non-stoichiometric ceria fraction (see fig. 3 23 (a)).

Significantly a sharp time limit separating the; (1) first complete amorphization process, and (2) second initiation of the crystallization step is not easy to distinguish. It can be seen in the micrographs, both these processes overlap. The nucleation of a few embedded stoichiometric nc-ceria nuclei developing into a mesocrystalline structure starts evolving. These nucleated nc-ceria crystallites gradually consume the surrounding atomically disordered ceria matrix fraction to grow further. The periodic TEM e-beam excitement directly facilitates the growth. In order to present a comparative view of the amorphized process carried out under the TEM e-beam, two regions are shown in fig. 3 23 (a)-(b). The region identified in fig. 3 23 (a) is an amorphized region, whereas fig. 3 23 (b) is that of the corresponding pristine nc-ceria region respectively. Randomization in the context of TEM-SAED refers to the availability of the minimum crystalline fraction available to contribute in generating localized diffraction from the probed nanometric region.

3.10.3 Probing the TEM e-beam Grown Crystalline Region (E4I16m)

Localized growth under TEM e-beam from a nc-ceria lump is another possibility contrary to amorphization, which needs selected area structural investigation. The "region 1" marked in the fig. 3.24 (a) represents TEM e-beam localized irradiation grown 18-21 nm crystallite (based on the prescription presented in the previous section, see fig. 3 21 (c)) surrounded by irradiation unaffected nc-ceria lump "region 2". Typically, a TEM-SAED aperture inserted to the objective lens image plane with the specimen region of the importance of at least 15 nm in size can be inspected employing the TEM-SAED mode to extract localized structural information [275], [276]. As expected, this localized TEM e-beam grown region is single-crystalline, with a typical spot diffraction pattern, as shown in fig. 3 24 (b).

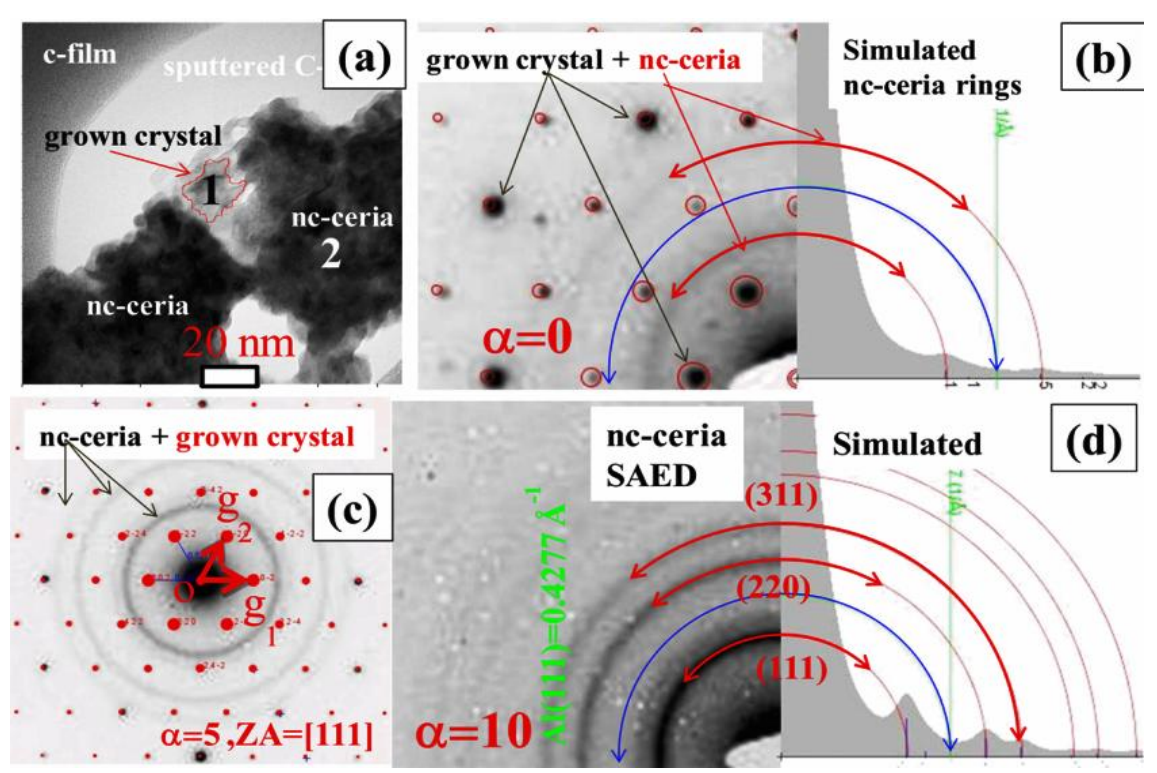


Fig.3 24 [Probing e-beam grown nano-crystallite]: (a) TEM BF micrograph of the e-beam grown nanocrystalline (marked as 1), and the original nc-ceria region (marked as 2) respectively. (b) α =0, (c) α =5, and (d) α =10 e-beam tilt series acquired SAED patterns acquired from (a) with the aperture centered on grown crystallite.

The surrounding region as diffuse rings present along with the highly diffracting spots pattern of grown nanocrystalline "region 1". The nanocrystalline region obtained intense spot pattern is shown in the fig. 3 24 (b). Subsequent beam tilting TEM-SAED recorded from the same region can be seen in figs. 3 24 (c) and (d). It improves the polycrystalline ring patterns of the surrounding nc-ceria region, which becomes dominantly observed for α =10 tilt. Possible zone-axis search by one to one reciprocal lattice matching is carried out with the simulated spot-patterns generated employing PROJECT/SAED2s [277]. The ceria structural data (ICCD PDF: 81-0792) is utilized to generate the simulated patterns, and the most appropriate pattern with a matching tolerance of less than 5 % is chosen. The simulated pattern of [111] zone-axis matches well the experimental TEM-SAED, with the reciprocal lattice mismatch

of about $g_{(2-20)}=1\%$, $g_{(20-2)}=1\%$, and in-between angle are of $m\angle g_{(2-20)}$ O $g_{(20-2)}=0.5\%$ respectively.

Similarly, the nc-ceria fingerprint electron diffraction digital ring pattern is matched directly with the PROJECT/PCED2s crystal structure generated simulated pattern, which is shown in the fig. 3 24 (d) [262]. The ring radii and the corresponding intensity level in the simulated linear electron diffraction pattern matched well, thus validating the structural phase to be that of the chemically ordered cubic ceria phase. Hence, the ability of the TEM e-beam in delivering localized nanocrystalline orderly region out of a fully radiation-hardened amorphous localized portion is demonstrated.

3.10.4 TEM e-beam Facilitated Aggregative Growth and Growth Kinetics:

After fabricating the localized amorphization (continuous E4I20m), and the subsequent in-situ mode tracking of the amorphized region for NCs growth (regular E4I4m pulses having an intermittent gap) is pivotal to understand growth kinetics. Many amorphized regions are considered, the best one having utmost digital clarity is presented for observation in the fig. 3 25. To compare the current experimentation using the pulsed TEM e-beam stimulus, the case study of metal NPs growth employing pulsed potential conditions is considered [278]. The point being that, in the presence of this pulsed electron stimulus (E4I4m), the fabricated amorphized ceria matrix region atoms get activated for atomic transport. This induces localized atomic order (atom cluster formation) with the possibility of simultaneous oxygen vacancy healing leading to many randomly nucleated crystalline nuclei. In the classical term, this amorphous ceria matrix embedded crystalline nuclei would consume the available surrounding randomized atoms for growth. In contrast, the non-classical case will be the co-operative interaction between the neighboring crystalline nuclei leading to the growth. A densely packed TEM e-beam randomized nc-ceria nuclei region is shown in the fig. 3 25 (a). The aim of amorphization is to

eliminate previously present intra-particulate voids. However, in the amorphized micrograph of the fig. 3 25 (a), these observed dark contrast regions are mostly the oxygen defects or oxygen cluster defects. These will be healed as and when TEM e-beam changes from the material modification to probe attribute, and thereby facilitating recovery.

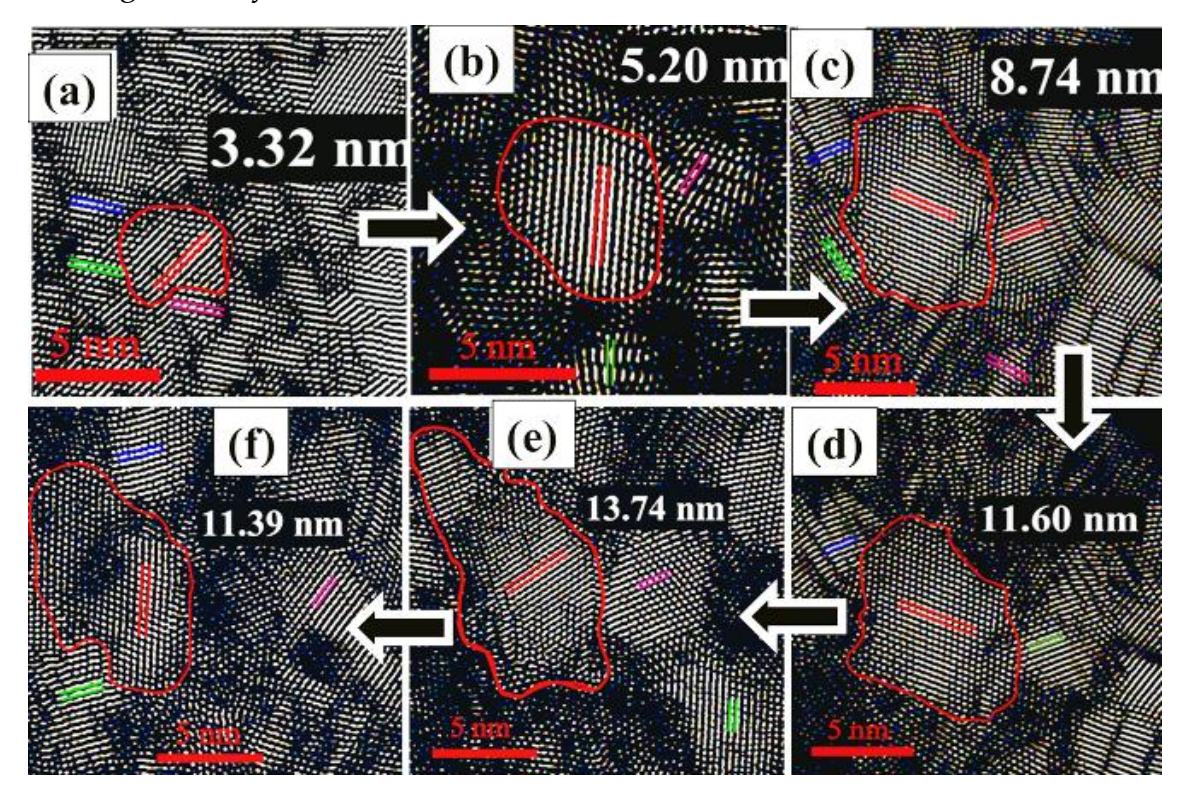


Fig.3 25 [Probe region TEM e-beam irradiation hardened]: Sequential time evolved BF images depicting a single nano-crystal growth form; (a) amorphized (t=0), (b) t=4, (c) t=8, (d) t=12, and (e) t=16 minutes of step-4 e-beam irradiation. Images for subsequent longer exposure snapped micrographs are in (f) t=20, and (g) t=24 minutes (not shown here) respectively.

The possibility of cationic surface reconstruction triggering during the TEM e-beam exposure also cannot be ruled out [279]. The explanation of why an amorphous, disordered structure (having relatively higher internal energy) will undergo energy lowering to develop into a crystalline (highly ordered) even in the presence of a constant TEM e-beam energy input impulse can be found elsewhere [261], [280], [281]. In addition, there are reports of in-situ liquid cell TEM tracking of two adjacent

distinct NPs coalescence through OA driven non-classical crystallization growth is plenty [282]–[285].

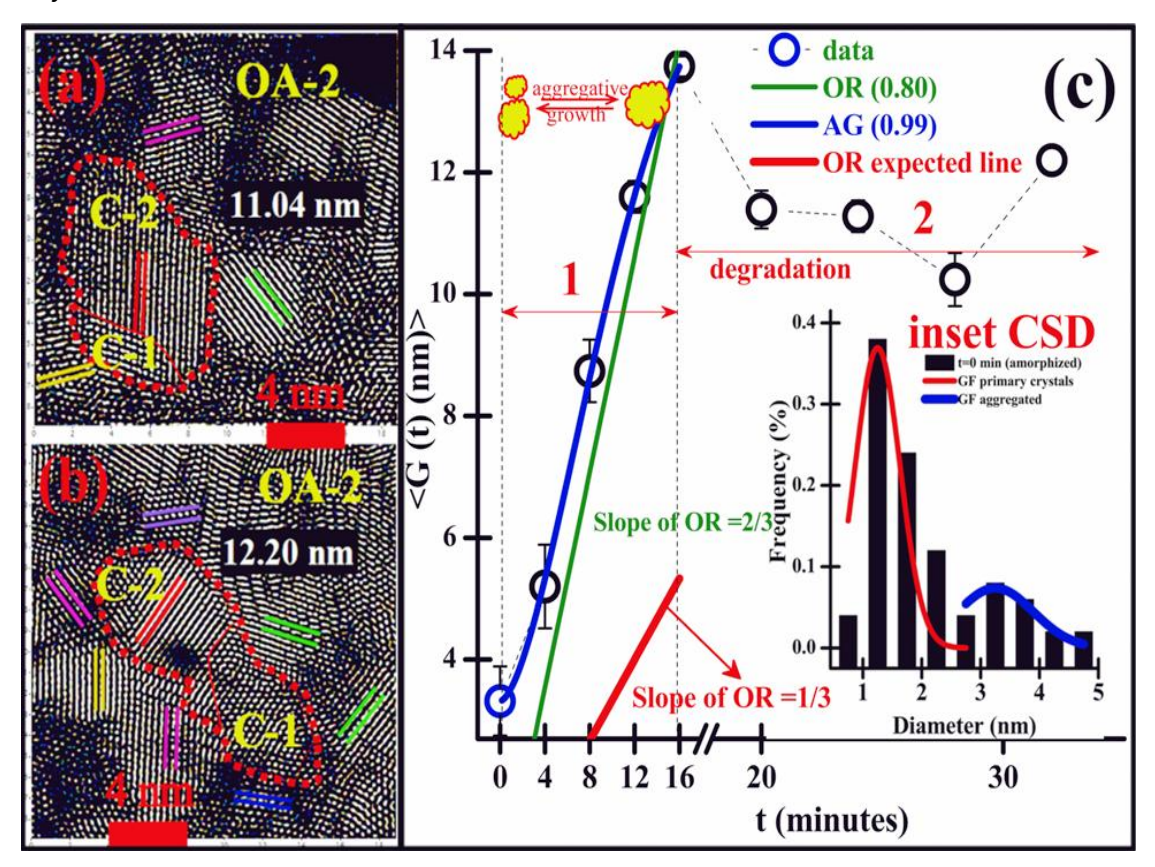


Fig.3 26 [Probe Region TEM e-beam irradiation Hardened]: Sequential time evolved micrographs for duration; (a) t=28, and (b) t=32 minutes respectively; (c) is the representative growth kinetics derived with the inset corresponding to CSD of t=0 min TEM e-beam amorphized region.

In the present context, one of the larger grown morphology demarcated crystallite is shown in the figs. 3 25 (a)-(f). Its time evolved quantitative growth after consuming adjacent primary crystallites like nutrients following the prescribed TEM e-beam protocol (see section 1) is recorded. The (nano) crystal size distribution (CSD) of t=0 minutes micrograph is plotted in the fig. 3 25 (c) (as inset is bimodal). The smaller distribution corresponds to primary nanocrystals, and the broader just initiated distribution represents aggregates of the primary.

Similar sets of experimentation are extended to almost 5 other regions for the timeevolved crystal growth data collections to present a quantitatively accurate assessment of the facilitated growth kinetics. This quantitative data is expected to lead to provide insight into conditions where OA is the sole dominant mechanism directing the observed crystal growth. By starting with an initially preformed densely packed crystal distribution (see the inset of fig. 3 26 (c)), the usual classical growth process is eliminated. The remnant aspect only is to distinguish between the aggregative growth (AG) and the Ostwald ripening (OR) mechanism. This approach, as presented previously, is also used in the present investigation [278].

The averaged time evolved growth data (<G (t)>) is plotted, with TEM e-beam irradiation time (t, in minutes) as shown in the fig. 3 26 (c). The maximum time evolved single-crystal dimension in the presence of the TEM e-beam is noted and is ascribed as the growth term (G (t)). These time-evolved micrograph snapshots (figs. 3 25-3 26) are insufficient to justify with clarity about the mechanistic occurrences under TEM e-beam. Given this for growth identification, the collected quantitative data is best suited to distinguish between the AG from the OR mechanism. An iterative fit to the avg. growth data by AG and OR models signify that AG (best fit with sigmoidal kinetics) is the mechanistic happening driving growth under TEM e-beam excitation. The attempted linear fit (of slope 2/3) representing the OR mechanism is unsatisfactory, since the expected slope is about 1/3 as reported for the case of nano-Ag growth [283], [286], [287]. This TEM e-beam facilitated AG through oriented attachment (OA) mechanism of primary crystallites by rotation is the predominant mechanism of crystal growth observed in nature.

3.10.5 OA Crystal Growth Facilitated by TEM e-beam Irradiation

The dynamical evolution of in-situ TEM e-beam facilitated OA crystal growth is investigated utilizing the HRTEM BF imaging mode. In order to have conclusive evidence previously optimized and fabricated ceria flake of (approximate 24.8 nm × 24.7 nm dimension recorded at and above 610 kX magnification) is modified and probed alternatively. In this context, TEM e-beam dual attribute for material

modification (when operated with step-4 LaB₆ filament emission, ~10.08 μ A) and also as a probing (sequential operation at step-2, ~0.88 μ A) tool is employed as per the requirement [53]. Immediately after modification duration is over, instant quenching is achieved by the compustage Goniometer α =15 tilt with a simultaneous recovery of ~30 s. This probe region (x, y) position, including tilt, is stored in the stage setting for accurate return to the same location with absolute certainty. A sequence of modification and quenching pairs are repeated over as many as 4-5 cycles to acquire data sets representing the actual dynamical occurrences by recording the HRTEM images. The acquired HRTEM images are further processed with the Gatan's Digital Micrograph to extract inferences. Also these digital micrographs demonstrate the unit or sub-unit cell length tracked ongoing crystalline changes that are associated with the OA driven crystal growth formalism.

For this illustration, three incoherently aligned nanocrystallites (of about ~4-6 nm) but intimately fused crystalline region is chosen to track the OA growth and is shown in the fig. 3 27 (a). The step-4 radiation-hardened ceria flake central region is selected for this task. Here, the identified nanocrystallites are in direct contact to restructure the conventional defective boundaries between them without being ruptured apart (i.e., free to rotate but confined for the lateral movement). The physical impetus for this type of crystal growth can be ascribed to the difference in excess energy of atoms at the crystal boundary (~1.08 J/m²) compared with that of interior atoms (0.77 J/m²). This process propels the boundary atoms to readjust with the immediate neighbouring crystal interior enabling growth [288]. The data presented provides clear dynamical insight into the mechanistic at nanoscale leading growth by particle-particle attachment scheme. This is unique, since previous reports focus mainly on liquid cell TEM observations in which the solution environment facilitates the OA but TEM e-beam is actively engaged for probing purpose only [47]–[49].

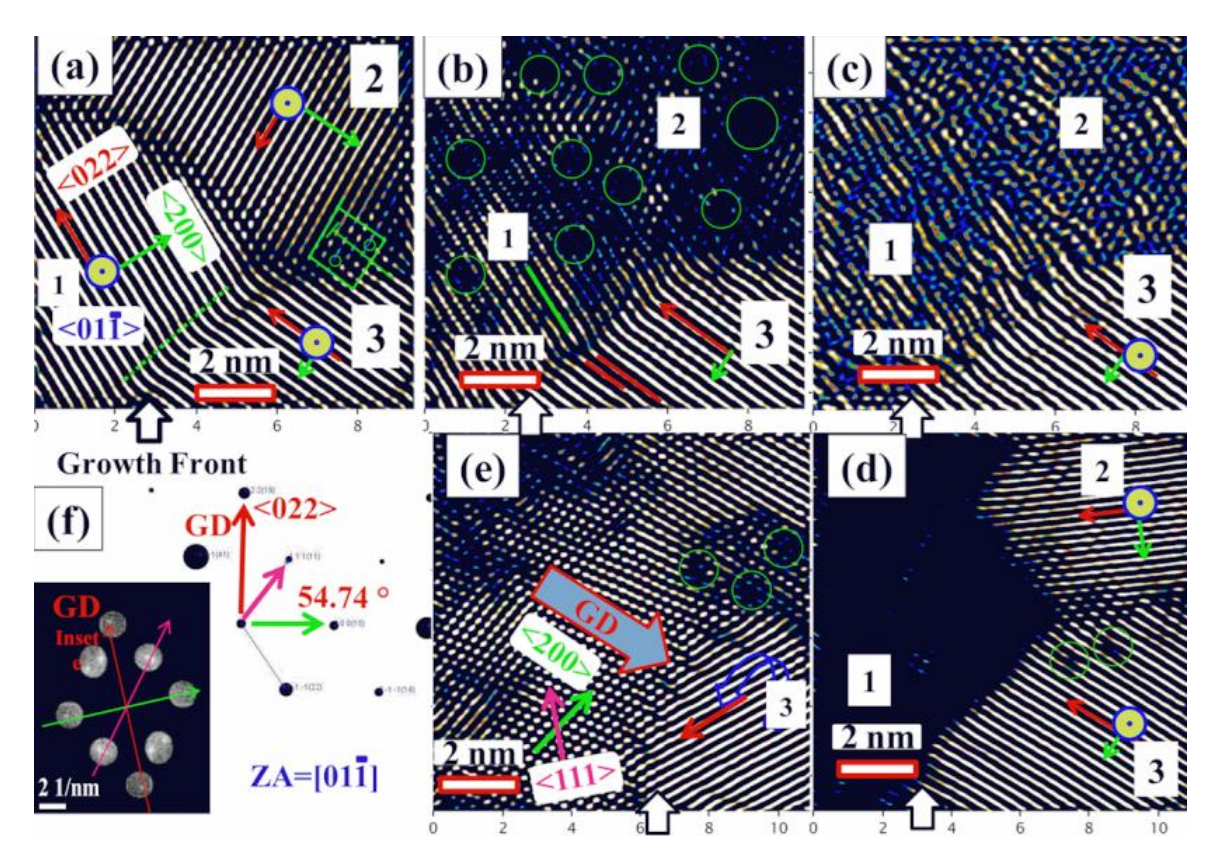


Fig.3 27 [Probing the TEM e-beam Radiation Hardened Region]: Sequential in-situ HR-TEM time evolved BF images after; (a) t=0, (b) t=4, (c) t=8, (d) t=12, and (e) t=16 minutes of step-4 e-beam fluence irradiation. Evolved nano-crystallite tracked in (e), growth direction is evident in (f).

The time evolved snapshots of the TEM e-beam facilitated non-classical pathway crystallite growth process imaged for demonstration, interpretation, and inferences respectively are presented in figs. 3 27 (b)-(e). As stated earlier, a fused grain formed out of the three crystallites (4-6 nm) without any core defects is shown in the fig. 3 27 (a). However, the crystalline boundaries enclosing these crystallites are embedded with defects as a result of inbuilt misorientations. This large angle misfit (initial misfit of 20 ° in both <022>, <200> directions) between crystal-1 and -3 induces twinning at the adjoining boundary (dislocation lines with two regions; regions of proper fit and regions of poor fit can be seen). In contrast, the vacancies and the edge dislocations constitute stress release centers at the other two crystal boundaries. All together these crystallites constitute a central tri-junction in this micrograph. The thickness of these crystal boundaries is of order of ~1 nm and is an extension of

crystal periodicity rather than an amorphous fraction. All three nanocrystals are viewed along the <011> direction.

The following 4 minutes of step-4 TEM e-beam irradiation-induced snapshot (see fig. 3 27(b)) elucidates the development of the crystal-1 and -2 into a single larger crystal filled with core vacancies (circular markings on the micrograph). Significantly, during this duration crystal-3 remains unperturbed. The reason for the crystal-3 being unperturbed up to 3 cycles irradiation exposure progress is the <011> directional attachment, which is previously investigated for imperfectly attached PbTe (FCC) nanocrystals [289]. A clear indication of the two diverging events that are (1) radiation-induced in-between boundary disappearance (crystal-1 and -2) and (2) bond breakage leading to vacancies generation. These are snapped in the micrograph of the fig. 3 27 (b). The present observation is in conformity with the case study of multitwinned Zn₂TiO₄ (FCC) nanowire examined under TEM e-beam over prolonged (28 minutes) period. In that study healing of the boundary dislocations to deliver larger single-crystalline subunits by fusing OA attached nanocrystallites is observed [290]. Similar to the current dislocations, healing investigation under irradiation (3 MeV Au⁺ ions) also validates that even an asymmetric nc-ceria crystal boundary can atomically rearrange itself to become symmetric, thereby lowering system energy by diffusing oxygen vacancies to the free surface [291]. It is also an investigated fact that nc-ceria possesses unique self-healing response to radiation damage at the crystal boundaries (volume fraction of interface region to the crystalline area for a 6 nm crystallite ~32 %) to control the crystallite size at the nanoscale [292]. Lastly, under irradiation, crystal growth is not asserted to be a thermal event, but irradiation-induced defect-stimulated mechanism at room temperature, with the primary defect being the oxygen vacancies [293], [294].

Furthermore, theoretical computation of parameters like activation energy and diffusion coefficients for cerium and oxygen atoms in ceria lattice demonstrates

extreme stability of cerium in both the interstitial and vacancy formulation. In contrast, oxygen in the interstitial position is metastable and also is highly mobile as a vacancy [295]. In which as that of the present 200 keV incident TEM e-beam energy interstitial-type non-stoichiometric dislocation loops of the oxygen platelets are also observed. In contrast, at least 1250 keV is the critical TEM e-beam energy that is necessary to induce cerium atom displacement (interstitial-type perfect dislocation loop) in ceria lattice [296]. Based on these literature reports, the missing atoms in the core region of the larger grown crystallite of the fig. 3 27 (b) can undoubtedly be ascribed to the oxygen vacancies. Ceria in its nanostructured form (nanocubes ~30 nm) under a 300 keV TEM e-beam exposure suggests reduction (oxygen vacancies creation) and also the simultaneous annihilation in vacuum [297]. It is stated that oxygen atoms of the order of 10⁶ are available within the ceria lattice. In contrast, within the TEM sample chamber there is oxygen molecules of the order of 10^{13} available to impinge into the ceria lattice. The magnitude of this differential strength in the number of oxygen molecules is sufficient to oxidize the reduced ceria sample at RT in short span of time about minutes [297], [298]. After t=8 minutes of elapsed irradiation the recovery and reordering by oxygen vacancies filling at the interior region with respect to the stationary crystal-3 is seen. This t=8 minutes recorded HRTEM image is shown in fig. 3 27 (c). The physics of this process is similar to the solid-state lattice-mending around nanopores in the case of laser annealing for which the impetus to generate crystalline order comes from the combined effect of pressure and the atomic thermal diffusion efficacy [299]–[301].

This process is similar to bond-breaking and bond-making phenomenon, which is driven by the defect-induced system energy minimization. Significantly, this is also observed in nanocrystalline CuO nucleation and growth progression by in-situ TEM studies by the present author [53]. In which studied 2D-Cu₂(OH)₃NO₃ single-crystalline nanoflakes are used as a representative material. The demonstration of

nanocrystalline CuO growth under TEM e-beam is supportive of the present argument. The uniqueness lies in reliving the (differential dislocation densities, crystalline boundary curvature, strain, etc.) energetically different crystalline entities either individually or as a combination which get stimulated healing under the influence of the TEM e-beam fluence in a controlled fashion [53], [302]–[305]. Thus, the oxygen vacancy generation, lattice-mending around these oxygen vacancies and the oxygen vacancies annihilation facilitates the reordering under TEM e-beam as is quite evident from fig. 3 27 (c). Subsequent snapshot in the fig. 3 27 (d) indicates development of a renewed orderly nanocrystalline region in the previously spotted crystal-2 (see fig. 3 27 (a) crystal-2 at t=0 min) having a rotation between <022> direction of approximately 12°, observed in [01-1] zone axis. Further, the orderly crystalline region extends to crystal-1 region (see fig. 3 27 (a) crystal-1 at t=0 min) after a time-lapse of t=16 min snapped in the fig. 3 27 (e) as a 14 nm larger subunit, which actually lacks atomic periodicity. Hence, it is missing after contrast enhancement with respect to the background shown in the fig. 3 27 (d). The growth front analysis of the 14 nm grown subunit in fig. 3 27 (e), is realized. The one to one correspondence of HRTEM lattice fringes and corresponding FFT of the grown crystal suggests that the OA happens in {011} with the probe TEM e-beam traveling in [01-1] as the zone-axis. As stated in the earlier subsection, this TEM e-beam facilitated OA growth will continue until the entire TEM e-beam hammered flattened flake region grows into a single larger subunit.

3.10.6 TEM e-beam Un-hammered region under e-beam exposure

A region having crystallites free to move laterally is continually observed under TEM e-beam. Even reordering of an amorphous core of a crystallite with time occurred. However, no attachment of the oriented crystallites leading to growth is observed. Snapshots of all these in-situ traced features are presented in the figs. 3 28 (a)-(d). The colored TEM BF images of figs. 3 28 (a) & (d), corresponding black and white (BW)

images shown in figs. 3 28 (A) & (D) respectively, for clarity in illustration. It justifies the importance of the TEM e-beam hammering and preparation of a radiation-hardened region having crystallites to demonstrate the OA mechanism and subsequent growth facilitated under TEM e-beam as the driving agent.

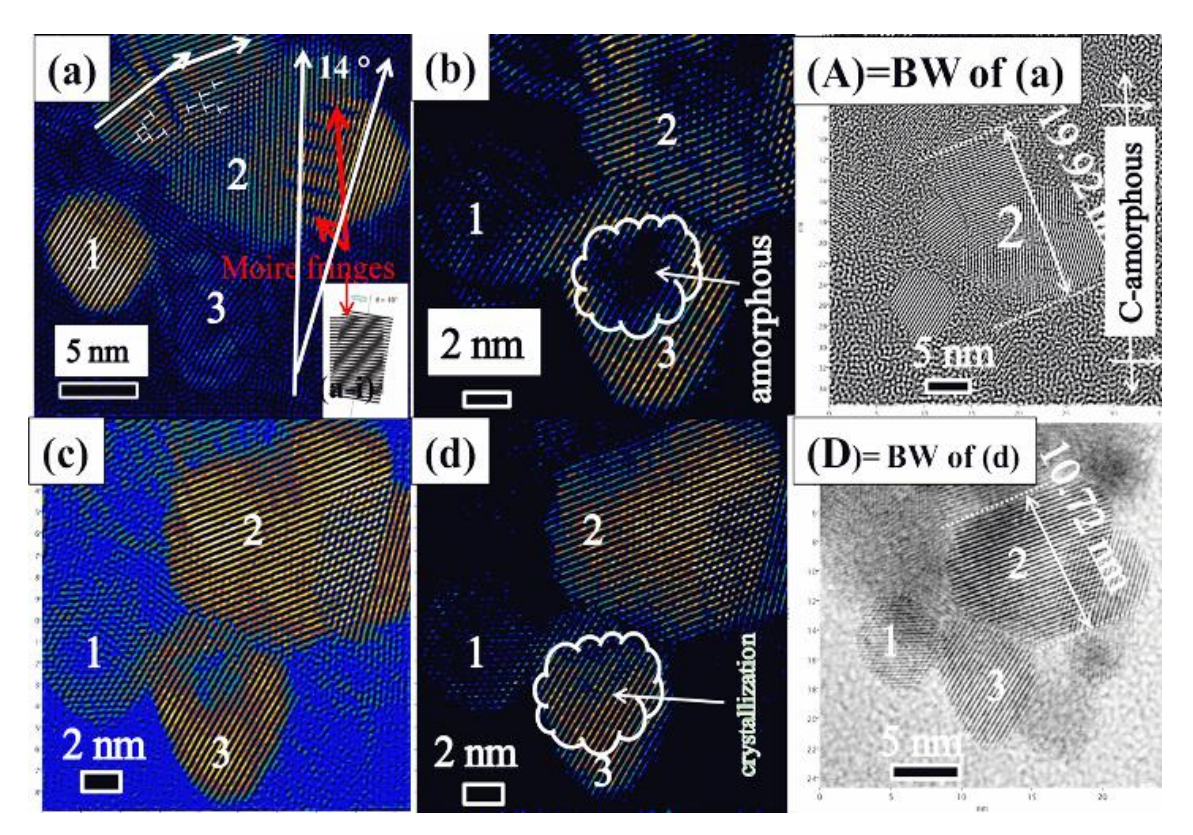


Fig.3 28 [Probe Region within which crystallites are free to move laterally]: Simultaneous reordering and damage of crystallites sequential in-situ HRTEM time evolved BF images after; (a) t=0, (b) t=4, (c) t=8, and (d) t=12 minutes of step-4 TEM ebeam fluence irradiation. Tracked specific nano-crystallite exposed to TEM e-beam that undergoes size reduction.

3.11 Conclusions

The chapter findings are summarized now. These are listed below.

(1) Morphological hierarchy, mesocrystals of intermediate formations and the biominerals' growth pathway progress are motivating in writing this chapter. Dominantly observed, aquatic-medium biominerals' growth process is mimicked.

The aquatic neighbor's participation in achieving biomineralization, whether an active or as an inert medium, is investigated.

- (2) Nanoscale ceria, having demonstrated versatility in biological applications, is the prototype material of choice to regenerate aquatic environment observed calcium and silicon compound developed macrostructures by organisms.
- (3) Nanocrystalline ceria ambient crystallization is favorable. However, at physiological pH=7.4 sparingly soluble in water. Thereby ultrasonic probe sonication is employed at RT to deliver water-soluble stable, transparent nc-ceria supernatant colloidal dispersion.
- (4) The supernatant is stable for a month, and subsequent gradual settling with aging is investigated. A set of settled mass recovered sequentially for 12 months is observed to follow the NCG pathway. Spectroscopic (Raman and UV-Vis optical) analysis done for this sequential settled products demonstrates surface autoregenerative CT attribute with aging.
- (5) However, the instant settling achieved by adding H_2O_2 as the oxidant to the ncceria supernatant colloidal dispersion had no characteristic NCG pathway signature, i.e., lumpy aggregates.
- (6) The presented NCG pathway by utilizing aging at ambient is one of the parameters shown to contribute to mineral growths, whereas in an aquatic medium, several other parameters also contribute (pressure, temperature, chemical species, and aquatic-medium participation itself). Also, the nc-ceria RT crystallization aspect enables bio-mimicking the presented particle-particle attachment scheme without the use of any additional thermal input.
- (7) Also, the DI-water direct participation in delivering 1D-ceria fibers is observed.
- (8) These ambient NCG protocol grown 1D-ceria fibers is in the hexagonal-Ce₂O₃ crystal phase, illustrating growth anisotropy generated cubic to a hexagonal phase transition. These fibers crystal facets are evolved out of the highly reactive ceria planes will be a candidate for catalysis applications.

(9) The dual role of the TEM e-beam as a material modification and probe tool is demonstrated. Crystal growth is a radiation-induced defect-stimulated defect healing process at RT. It is demonstrated that the near-neighbor environment around the ncceria In the TEM chamber can be used effectively to control growth kinetics and, therefore, properties.

Intentionally Page Kept Blank

Chapter-IV

Viability of Ultrasonic Sonochemical processing for nanostructures: Case study of Aluminum-crystal growth and Poly (vinylpyrrolidone)-graphitization

Cite this document as

https://arxiv.org/abs/2006.05947

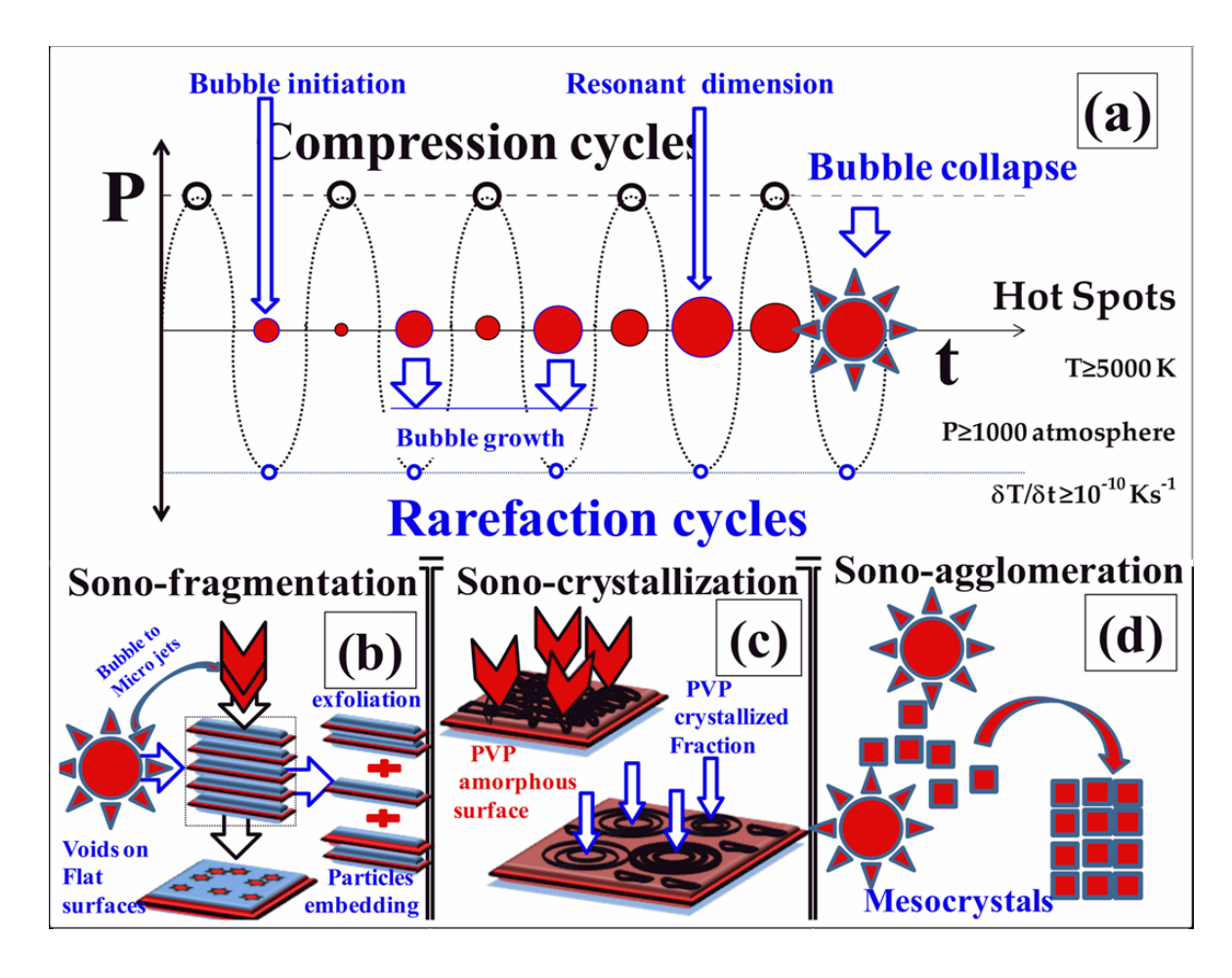
Keywords:

Sonocrystallization, Sono-agglomeration, Sono-fragmentation, Poly (Vinylpyrrolidone), Nanostructured-Aluminum, Expandable-Graphite, In-situ TEM, Electron Beam Irradiation, Aluminum Crystal Growth

Abstract

The viability of ultrasonic sonochemistry is investigated in the context of delivering air-stable metallic Al rich-PVP composite. The physiochemical processes intensification, investigated are; sono-(1) process (2) crystallization, (3) agglomeration, and (4) fragmentation, respectively. The conventional solvent of nhexadecane is employed as pressure transmitting medium to carry sound field generated by sonotrode to illustrate the above mentioned physiochemical sonoprocess viables. Two precursors, (1) Poly (vinylpyrrolidone) (PVP) a polymeric and (2) Aluminum chloride (AlCl₃) an inorganic material respectively, are chosen to investigate and demonstrate these viabilities of the ultrasonic induced processing. Temperature controlled investigations at ambient and higher temperature assist in achieving; (a) PVP-graphitization, and (b) Al-crystal growth phenomenon, respectively. The current experiments aid in helping to isolate and identify actual mechanistic happenings. The investigation, thus, has a fabrication protocol of shortened processing-duration, native amorphous oxide-free, metal-rich air-stable product that leads to 10 g of processed composite for fuel applications.

Graphical Abstract



[Ultrasonic Sonochemical Viable for Nanoscience] Schematic presentation of: (a) Ultrasonic pressure waves leading to initiation of cavitation to implosive collapse generating extreme conditions, (b) Sono-fragmentation (exfoliation, particle intercalation in 2D-materials), (c) Sono-crystallization in PVP, and (d) Sono-agglomeration of Al crystals building units generating large 2D mesocrystalline lumps, respectively.

4.1 Introduction

The widespread applicability of ultrasound under environmentally benign conditions delivering industrial scale product quality enrichment and material development is fascinating. The application areas include: food science and its associated technology (processing, preservation and extraction) development [54]-[60], water remediation [61]–[66], biomedical field [67]–[69], and also the process intensification of variety of synthetic processes [59], [70]–[73], etc respectively. It is a demonstrated fact that ultrasound-assisted protocol is more effective than its corresponding conventional (physical, chemical, and biological) approach [74], [75]. In this context, the use of ultrasound in process intensification to deliver organometallic complexes (e.g., organo-lithium, -magnesium, and -aluminum, etc.) can be traced back as early as the 1950s, demonstrating its utility [76]. A few well known specific cases of metals activation by ultrasound leading to substantially shortened reaction duration (sonic acceleration) demonstrations of synthetically significant protocols are; (1) Zinc-induced Reformatsky reaction [77], (2) Copperinduced Ullmann couplings [78], and (3) Lithium-induced Barbier reaction [79], respectively. In addition to these specific cases, the principles of ultrasound-induced activation of metals and its use in accelerating (process intensification) organic synthesis are reported in terms of many book chapters [80]-[84]. The point being ultrasound-induced shortened-in-time synthetic protocol development is an actively engaged ongoing process. It is worth noting here that the ultrasound-induced cavitation and its cavitation implosive collapse generated mechanical effects (like liquid microjets, turbulent mixing, shock waves, and acoustic streaming) are the dominant phenomena responsible for these synthetic process sono-acceleration [85].

Since its invention in 1927, sonocrystallization is another significant physiochemical process of ultrasonic sonochemistry [86]–[89]. Investigations on possible mechanistic reasoning of sonocrystallization are actively ongoing. The question whether sonocrystallization is ambient RT and mostly athermal shock wave-

dominated phenomena needs exploration. In fact, demonstration of the sonocrystallization phenomenon includes (1) aspirin as model for the molecular crystal [90], (2) organic molecules [91], (3) alkali halides as the ionic crystals [92]. The outputs of such studies suggest it as a direct particle-particle and shock wave interaction is responsible for facilitating such phenomena. Still, a general acceptance of sonocrystallization out of these few individual case studies on crystallization and acoustic cavitation is not sufficient. This has also been suggested in a recent detailed review of possible mechanisms of sonocrystallization in solution [93], [94].

Likewise, sono-agglomeration is linked to the high-velocity inter-particle collision and subsequent fusion by melting delivered grain growth is also another significant physio-chemical attribute. Literature on some unusual sonochemical-assisted assemblies developed are: (1) graphene oxide (GO) and carbon nanotube (CNT) [95], (2) 2D-materials (graphene, MoS₂, h-BN etc) on flexible polymer substrates [96], (3) mesocrystals of TiO₂ and BaTiO₃ [97]–[100], and (4) silica spheres [101] etc. The case of metals sono-agglomeration during sonoprocess is extensively investigated by Suslick and co-authors et al [102]–[104]. Two particular outcomes of the metal sono-agglomeration studies are; if (1) particles collide head-on, it leads to agglomeration; otherwise if (2) the collision is at glancing angle leads to the removal of the inbuilt respective metals surface oxide layer by cracking and finally making the surface highly reactive. Thus, sonocrystallization leads to the generation of the crystalline nuclei while the subsequent sono-agglomeration drives these generated nuclei to coalescence resulting in building unit and thereby crystal growth.

Given these promising physio-chemical viables of ultrasonic sonochemistry, this chapter is an attempt to realize, demonstrate, and falicitate plausible mechanistic of the phenomenon like; (a) process-intensification of chemical reaction, (b) sonocrystallization, (c) sono-aggregation. These phenomenon are investigated using precursors; (1) N-polyvinyl pyrrolidone (PVP), and (2) anhydrous AlCl₃ in conventional hexadecane solvent respectively, as case studies. The PVP polymer is

used to adjudge sono-crystallization phenomena without bulk solution heating at ambient laboratory conditions. This judgment is to isolate, whether or or it is an athermal shock-wave generated shear/pressure linked or temperature linked process. In contrast, metallic Al is used to understand the crystal growth aspect employing "ultrasonic-assisted process intensification activity" based on conventional solution-phase chemical Al precursor reduction process to deliver Al nanoparticles. As stated, sonoprocess generated Al nanoparticles of uniform dimension and surface oxide-free are incorporated into the sonocrystallized PVP matrix. The motivation of this chapter is to employ sono-process for achieving the graphitic carbon (GC), and Al (M) incorporated air-stable composite. Further is to examine the loss of metallic content after year-long laboratory storage, which is essential for fuel application.

In this context, generic protocols to fabricate oxide-free Al nanocrystals involve either; (1) direct solution-phase reduction of Al precursor reduction leading to Al crystal growth, or via an (2) alane-precursor based thermal decomposition schemes [306]–[308]. In these schemes for safe laboratory handling, surface passivation of the Al nanostructured product is achieved either by (a) controlled air exposure (help in developing thin amorphous Al₂O₃ outer shell) or (2) an appropriate polymer surface coating respectively. Most importantly, these protocols run over several long hours to complete. It is important to note that, besides sono-chemical, attempts to superimpose with electric and microwave field stimulation on many conventional approaches for reaction process-intensification is also reported [309], [310]. Significantly, the introduction of sonochemical stimulation to the organic alane-precursor based thermal decomposition (protocol-2) reaction scales down, remarkably, to just several minutes [311]. Although the use of inorganic Al precursor also attempted in sono-electrochemical, electrochemical template deposition and polymer stabilization, the process still runs over several hours resulting in nonuniform larger particle size, scale-up limitations, and energy content inefficiencies [312]–[315]. The inorganic case (will be termed as protocol-1 in theis thesis) is the

most utilized conventional case, is considered to be investigated employing heterogeneous sonochemistry as standalone stimulation for synthetic process-intensification studies.

4.2 Materials and Methods

Chemicals and precursors used in this chapter are of Analytical Reagent (AR) grade. Chemicals received from the different vendors are used without any further purification. Aluminum chloride (AlCl₃, Reagent plus (R), 99%), Lithium Aluminum Hydride (LiAlH₄, pellets, Reagent grade, 95%), Poly (vinylpyrrolidone) (PVP, molecular weight 10,000), n-Hexadecane (CH₃ (CH₂)₁₄CH₃, anhydrous, 99%), and UHP Argon are used. Glassware related accessories cleaned by standard laboratory procedures, and the nitrogen glove box is used to handle moisture-sensitive chemicals.

Sonochemical processing is carried out with Sonics VCX-750 watt ultrasonic processor. Sonochemical reaction vessel (40-250 mL processing capacity, three 14/20 side necks, glass chamber height 62 mm), with the adapter (Part number: 830-0014) is screwed into the special long full-wave solid probe (Titanium alloy Ti-6Al-4V, 13 mm tip, 245 mm long) at the nodal point. The glass sonochemical reaction vessel slides on the adapter and is fixed in a place as required by the bushing which is screwed into the reaction vessel, with an O-ring compress. The reaction vessel movement on the adapter facilitates the probe portion extension out of the adapter required to be immersed into the sample. A continuous mode of operation for 2 hrs (process control from 1s to a maximum of 10 hrs) processing can be carried out with ice water (20 °C) circulation based on the requirement. The UHP argon bubbling at 30 bubbles /minute is also maintained during sonoprocessing. The snapshots of the sonochemical reaction vessel with the sonotrode arrangement are shown in figs. 4 1.

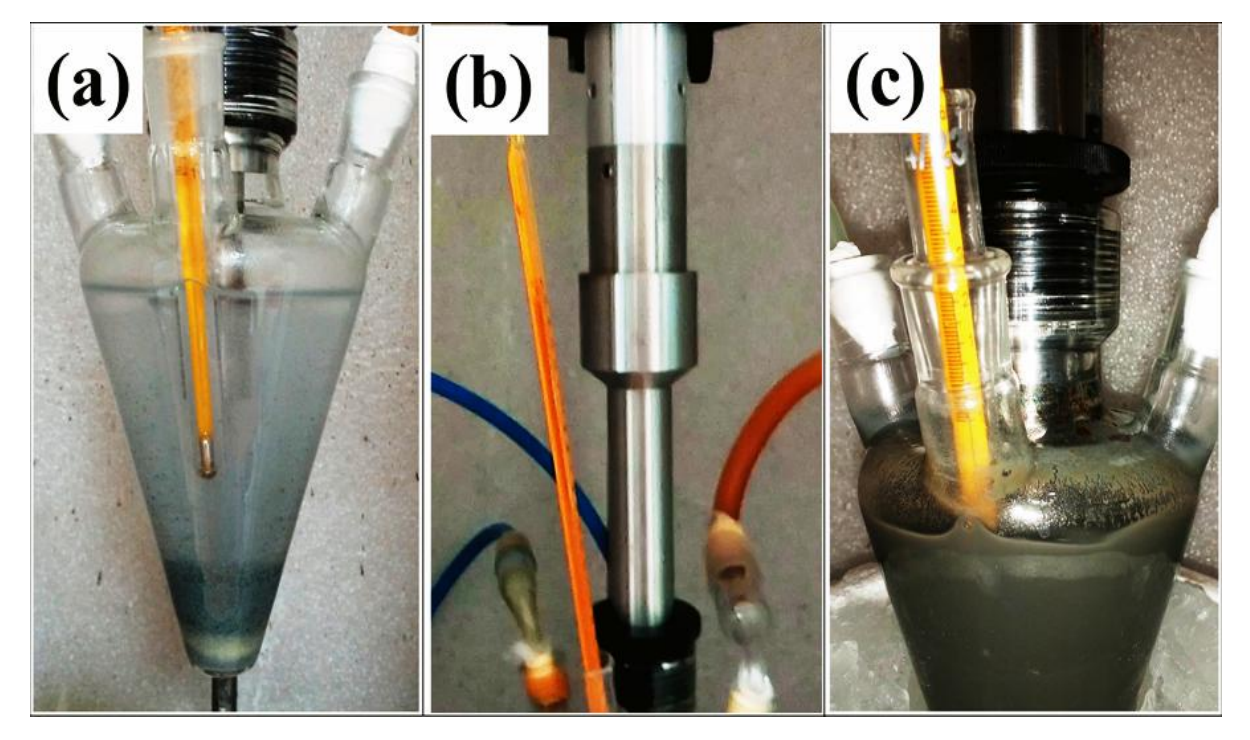


Fig.4 1 [Sonochemical Reaction Vessel]: Photographic snapshots (a) precursor before ultrasonication, (b) long full-wave solid probe fixed onto the adapter (c) after sonication respectively.

4.3 Results and Discussion

4.3.1 PVP TEM Investigations

4.3.1.1PVP Pristine

PVP powder spread onto a TEM grid inside a nitrogen glove box is transferred to the TEM sample holder immediately and is imaged. Irregular shape μ -size bulky aggregates of PVP macromolecules bulky aggregates confined to one of the TEM grid square-mesh is shown in fig. 4 2 (a). Subsequent sequential increased magnification TEM BF images are recorded and are shown in figs. 4 2 (b)-(d). Individual lumps (see fig. 4 2 (a)) edge portions are imaged and depict layered morphology having smooth (no crystallized or foreign entities as an embedded fraction) surface microstructure. The increasing dark contrast (i.e., increased thickness) is a result of PVP

macromolecules' layered aggregation in sequential fashion when observed from any of the bulky lump edges to the center.

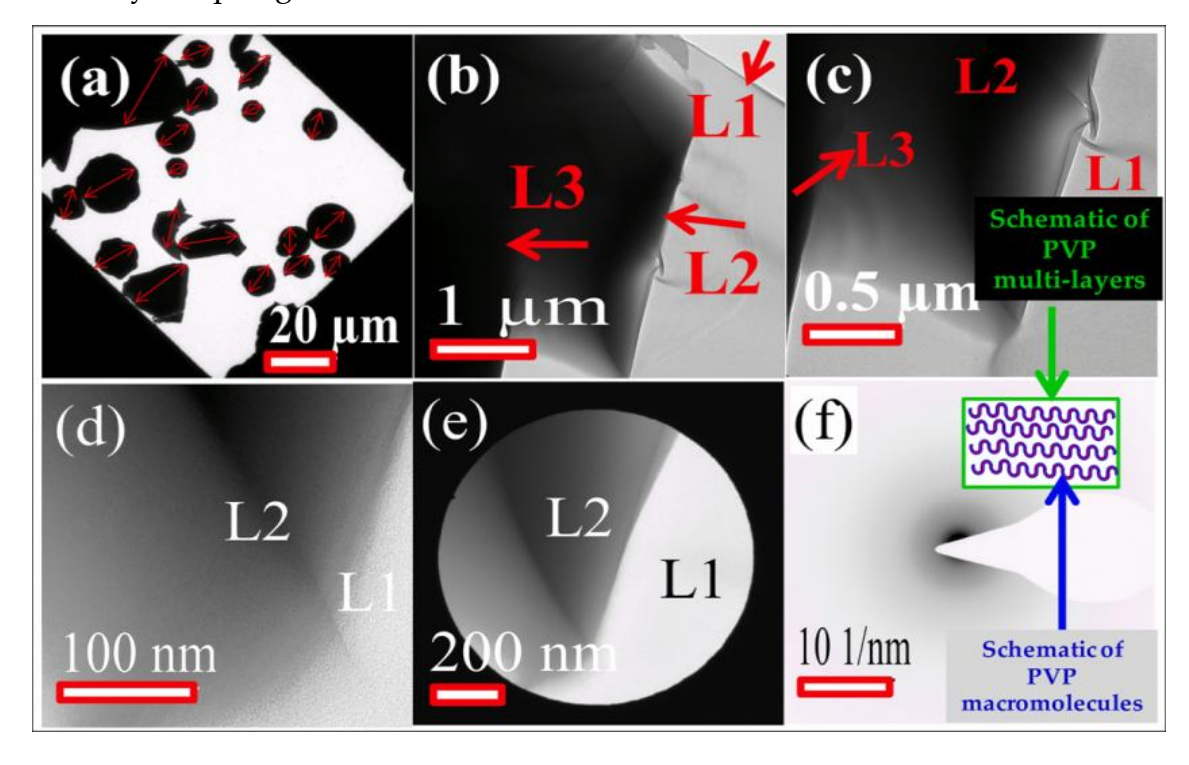


Fig.4 2 [Pristine PVP TEM observations]: TEM BF (a) lumps, (b)-(e) PVP layers, and TEM SAED aperture, (f) characteristic halo disc pattern overlaid with PVP as multilayered shell schematic as inset respectively.

The TEM-SAED recorded from these layers has the characteristic halo-disc shape of amorphous materials. One such localized region with SAED aperture and obtained SAED pattern are shown in figs. 4 2 (e), and (f), respectively. The PVP material is stable under step-2 TEM e-beam investigation used for probing, as evident from lack of changes to these layers surface microstructures in the present illustrations. Based on the current TEM-BF study (figs. 4 2 (b)-(e)) and literature, a representative schematic of PVP lumps concurrent with the observations is overlaid on fig. 4 2 (f) as inset [316]. Ethanol solvent dispersed PVP spin-coated on to a silicon substrate is imaged by employing the non-contact dynamic force microscopy (DFM) mode in an AFM. PVP lumps 3D view is acquired to support TEM 2D observations depicting no contrast. A larger PVP globule is chosen, and its acquired 3D topography is shown in fig. 4 3 (a). Acquired globule represents one TEM lump and is about micron thick,

thereby non-transparent to TEM e-beam, hence is of darker contrast. Many micron-sized smaller spherical aggregates constituting this lump can be seen in topography, but are recorded with better contrast for differentiation in the phase image shown in fig. 4 3 (b) [317]–[319]. The existing individual aggregate walls are of 100-400 nm thick and are marked on the corresponding phase-contrast microscopy image with single-headed arrows (see fig. 4 3 (b)).

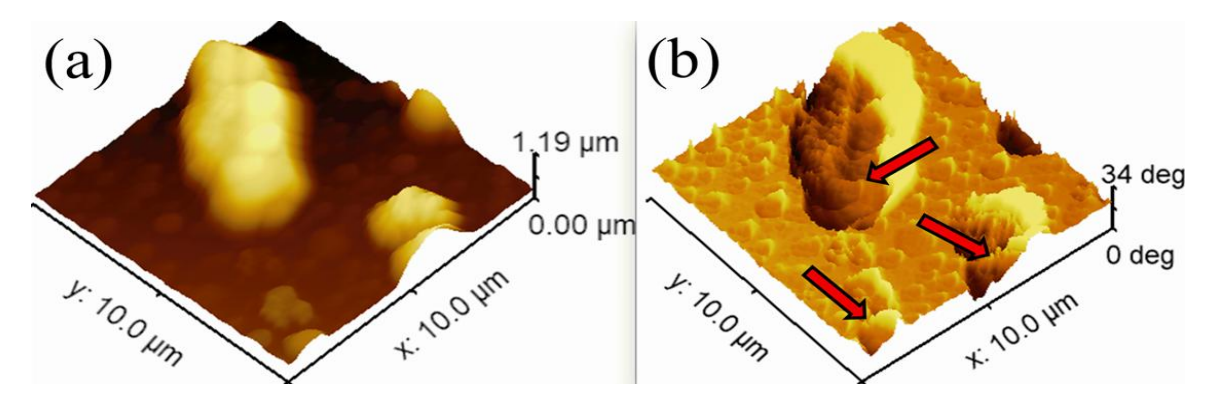


Fig.4 3 [Pristine PVP AFM observations]: DFM operation for obtaining; (a) 3D-topography, and (b) corresponding phase contrast image (arrows indicate lump wall) respectively.

4.3.1.2 PVP Sonicated

Reports of cavitational reactors delivered process intensification had many demonstrations [320]–[328]. In this context, 20 kHz ultrasound pressure wave's irradiation generated mechanochemical alterations to PVP polymer are investigated first. For this purpose, a 2 hrs long (previously optimized) ultrasound irradiation processed PVP polymer product transferred onto TEM grids are imaged. Sonochemical vessel of 250 mL capacity with 1.08 g of PVP at its bottom is ultrasonic irradiated (Sonics VCX 750W, 13 mm solid ultrasonic horn is operated at 50 % amplitude) through hexadecane solvent as pressure wave transmitting medium.

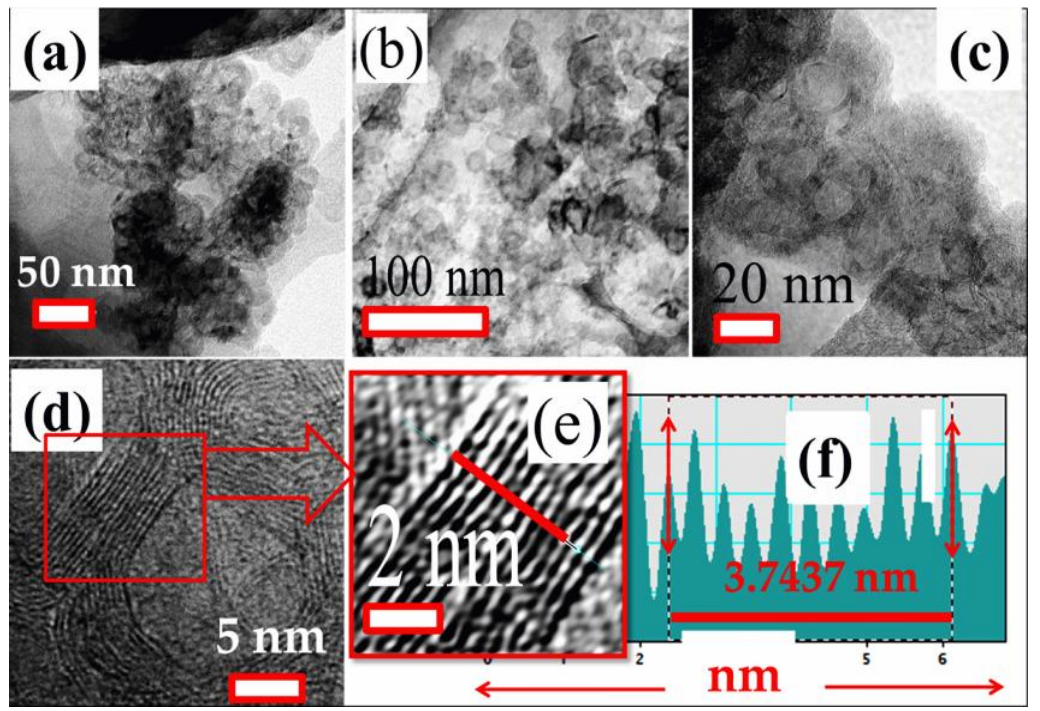


Fig.4 4 [PVP sonicated TEM observations]: TEM BF (a)-(c) concentric onion shell graphitic carbon nano rings, (d) HRTEM, (e) zoomed portion of (d), (f) stacking spacing respectively.

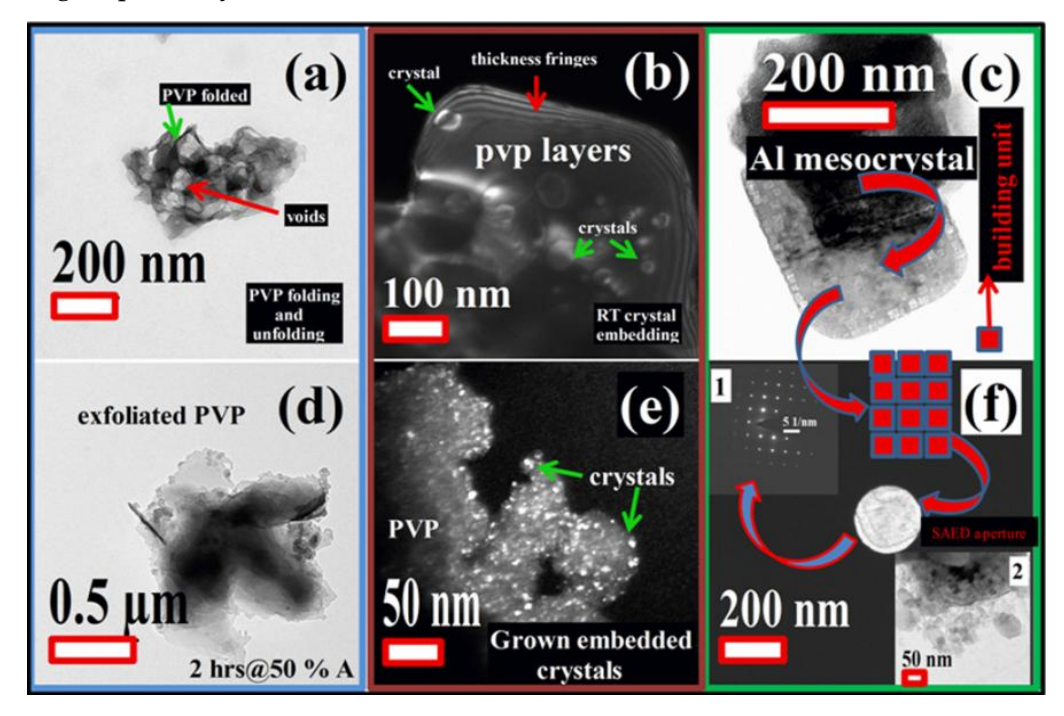


Fig.4 5 [Sonochemical Mechanochemical deliverables]: (a)-(d) exfoliation, (b)-(e) growth and embedding, and (c)-(f) aggregation respectively.

Out of many, the specific effects of ultrasonic irradiation generated features of importance specific to the current study are shown in figs. 4 4 (a)-(c) as TEM BF images. The two notable PVP polymer surface observed attributes are; (1) surface rupture, and (2) evolved randomly distributed crystalline features presence respectively. The first aspect is mechanical, a physical activity termed as sonofragmentation [329]-[336]. While the second feature highlights ultrasound application in solution mediated materials crystallization (otherwise known as sonocrystallization) processes, respectively [337]–[340]. The major sonochemical attributes encountered are schematically presented as shown in figs. 4 5 (b)-(d). To achieve these, the implosive bubble collapse impetus driven ultrasonic mechanochemistry is depicted in fig. 4 6 (a). TEM BF images, of ultrasonic irradiation hexadecane solvent medium processed products, acquired justify these occurrences are displayed in figs. 45 (a)-(f) respectively.

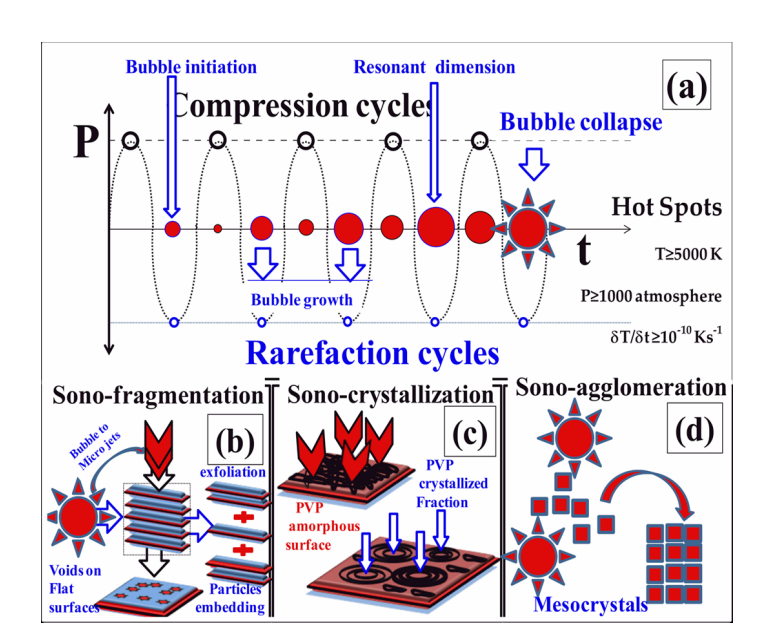


Fig.4 6 Schematic presentation of: (a) Ultrasonic pressure waves leading to initiation of cavitation to implosive collapse generating extreme conditions, (b) Sono-fragmentation (exfoliation, particle intercalation in 2D-materials), (c) Sono-crystallization in PVP, and (d) Sono-agglomeration of Al crystals building units generating large 2D mesocrystalline lumps, respectively.

4.3.1.3 DFM probing PVP Sono-fragmentation

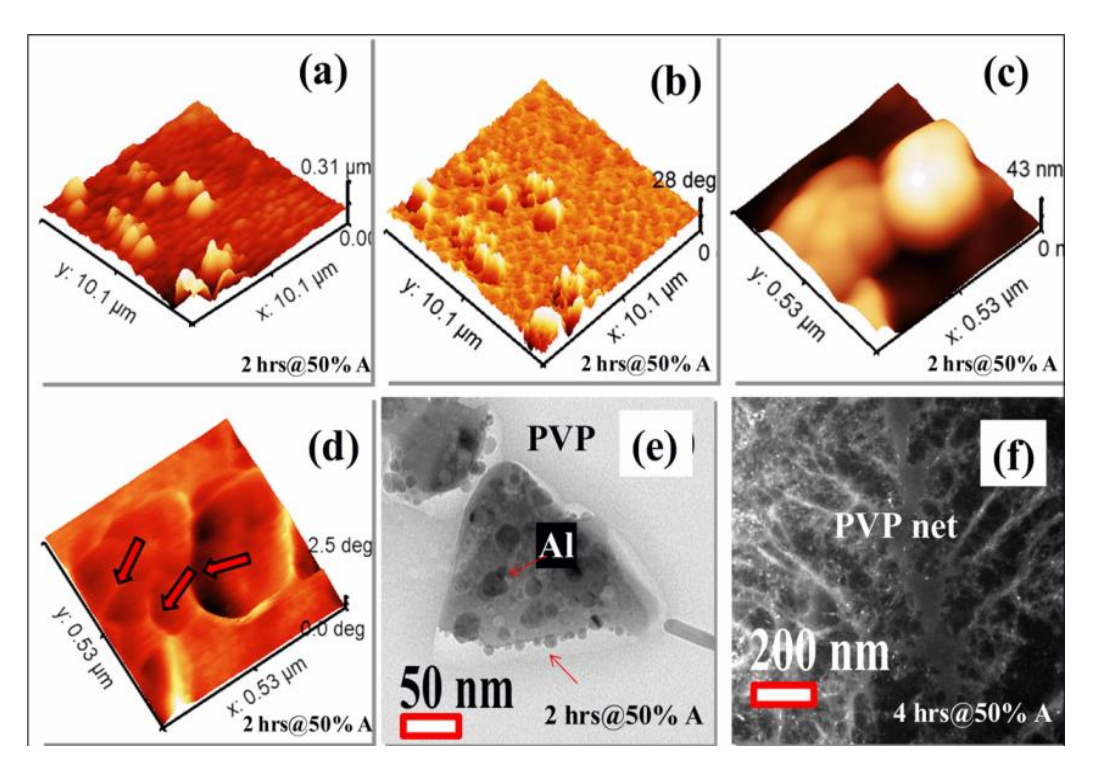


Fig.4 7 [Sono-fragmentation]: (a)-(d) DFM mode observation of PVP in topography and phase, (e) growth and embedding of nano-Al, and (f) PVP network after extended sonication respectively.

A detailed guideline for liquid-phase exfoliation (LPE) employing ultrasonication and its slightly modified, adapted techniques for 2D-layered materials published elsewhere is followed [341]–[348]. Three notable reasons delivering LPE identified are; (1) cavitational bubble collapse leading to stemming generated mechanical energy in the form of compressive/tensile stress wave in an unbalanced manner to overturn the inbuilt layers attraction, resulting exfoliation, (2) shock waves breaking bulk into thin flakes, (3) cutting of flakes due to frictional force resulting from high strain rates up to 10⁹ s⁻¹, and (4) combination of all these processes acting simultaneously respectively. In the present case, the fragmentation of PVP layers is achieved in hexadecane (Sonics VCX 750W, 13 mm solid ultrasonic horn is operated at 50 % amplitude) ultrasonic irradiated for 2 and 4 hrs, respectively. The non-contact DFM mode observation in both topography and phase shown in figs. 4 7 (a)-(d),

imply thickness almost approachable to 50 nm indicating flat 2D nanostructured layers. One such layer having nano-Al embedded in it is shown in fig. 4 7 (e). Likewise, PVP sonicated for extended 4 hrs makes it network like and is, hence, not appropriate for nano-Al embedding and growth. This extracted product examined in TEM is observed to have around 80-90 nm Al particles wrapped in GC network. Also, the development of the amorphous-Al₂O₃ layer is seen to be present after laboratory storing for a week.

4.3.1.4 TEM probing PVP Sono-crystallization

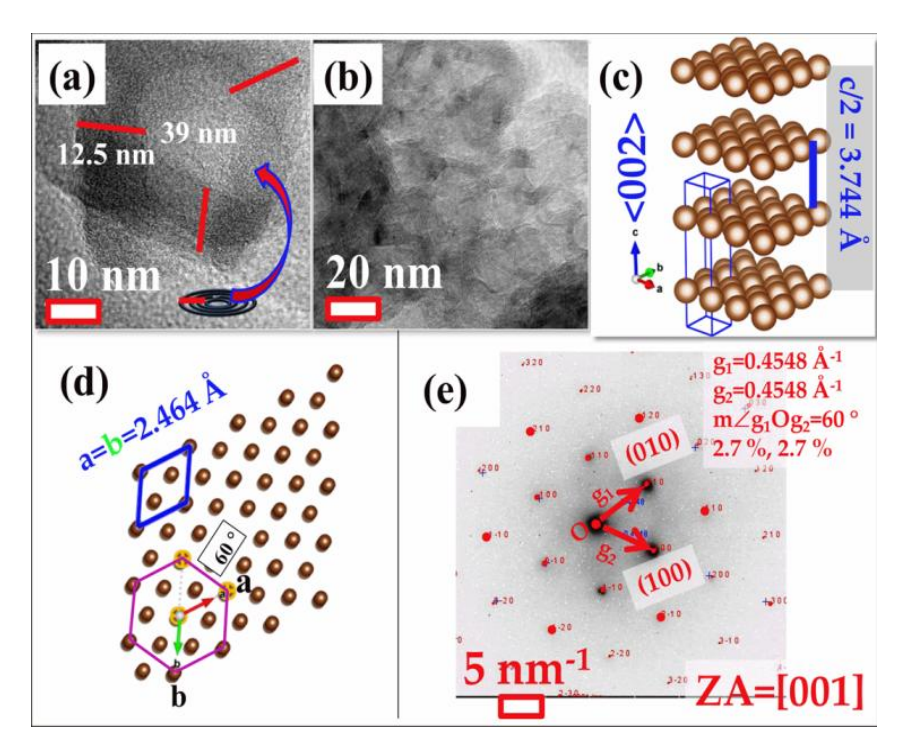


Fig.4 8 [Sono-crystallization]: (a) PVP surface initiation of onion like features, (b) densely populated such features, (c)-(e) microstructural evaluation respectively.

The use of ultrasound in delivering crystallization in pharmaceutical had widespread demonstrations, but the physical mechanism underlying this process physical happenings is still under exploration [333], [339], [349]. Sonocrystallization of poly-3-hexylthiophene (P3HT) chains to nanofibers by the application of the ultrasonic field is proposed based on nucleation and growth aspects. This is a consequence of ultrasound assist in delivering sufficient mechanical energy to overcome the local

energy barrier to trigger a small crystalline nuclei nucleation [337]. The evolved crystalline nuclei act as the seed for the subsequent growth of large nanofibers. In this context, consistent with many previous reports, experimental validation highlighting PVP crystallization to graphitic carbon (GC) is shown in figs. 4 8 (a)-(b). Initiation of onion-like stripes after 1 h (see fig. 4 8 (a)) and filling of such stripes all over the PVP surface (see fig. 4 8 (b)) after 2 hrs of ultrasonication in hexadecane is observed. The TEM microstructural data from these generated structures locally in HR-TEM (see figs. 4 2 (d)-(f)) and SAED (fig. 4 8 (e)) mode confirms PVP crystallization. The microstructural data extraction and schematic presentation of the same shown in figs. 4 8 (c)-(e), indicates hexagonal GC along with c-axis tensile strained in comparison with that of the standard ICDD PDF-2: 89-7213 file.

4.3.1.4 TEM probing Aluminum Sono-agglomeration

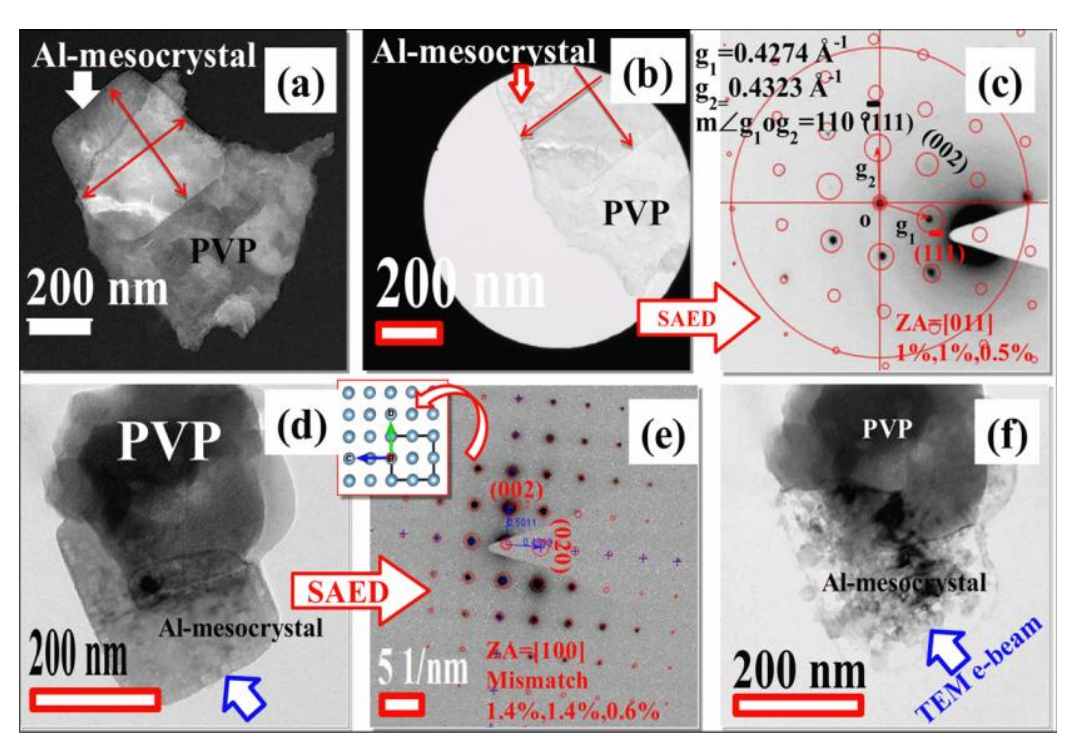


Fig.4 9 [Sono-agglomeration]: (a)-(d) Al mesocrystal, (b), (c), (e) TEM-SAED characterization, and (f) TEM e-beam de-agglomeration respectively.

Ultrasonic de-agglomeration is a frequently observed event, but literature on materials agglomeration during sonochemical processing is also not rare.

Ultrasonic's during sonoprocessing in generating agglomeration of metallic particles investigated by Suslick and group et al. had two interesting outcomes [350]-[355]. They are; if (1) particles collide head-on, the result is agglomeration, otherwise; (2) glancing angle collisions lead to surface oxide layer cracking and thereby its loss, respectively. In case of Al nanoparticles the surface oxide layer is a hindrance for its use as fuel; hence its growth is favorably inhibited (stated outcome 2) during sonoprocessing bringing about a positive development. The mesocrystalline Al formulations are shown in TEM BF/DF images in figs. 4 9 (a) and (d) are the implication of presented outcome 1. Likewise, TEM-SAED acquired, as shown in figs. 4 9 (c) and (e) is that of the Al structural phase. The identified zone axis from the experimental SAED implies a lattice mismatch of less than 2 % between that of the standard ICDD PDF: 04-0787 and experimental obtained TEM-SAED pattern. Besides TEM-SAED, the investigation of Al particle surface (i.e., HRTEM mode) for the presence of surface oxide is attempted. However, HRTEM surface oxide isolation remained unsuccessful in isolating surface oxide validates the outcome 2 presented. The Al mesocrystal has shown in fig. 4 9 (d) just exposed to HRTEM mode e-beam exposure (E4I5M) initiates the disintegration of the mesocrystalline formulation of cubical building unit (see drawn schematic in fig. 4 3 (f)). The disintegrated Al mesocrystal after 5 minutes of step-4 HRTEM mode exposure is shown in fig. 4 9 (f). This implies Al cubical building units are loosely agglomerated (facile disintegration under TEM e-beam) but in a periodic coherent order to behave as a whole single crystalline unit. Similar to present observation of Al mesocrystal formation under ultrasonic irradiation, case studies of materials orderly arrangement achieved in materials during sonoprocessing are; (1) BaTiO₃ mesocrystals, (2) layered arrangement of CaCO₃, and (3) TiO₂, etc [356]–[360].

Although the ultrasonic irradiation-induced inter-particle collision is the leading attribute contributing to sono-agglomeration, another essential contributor that needs mention linked to the solvent physical attribute (i.e., surface tension,

viscosity, and vapor pressure, etc) used in sonolysis process. In brief preferred solvents having low viscosity, low surface tension, and less vapor pressure are the most preferred [361]. The list of conventional solvents mostly employed for sonochemical processing is; hexane, hexadecane, pentane, dichloromethane, etc [362], [363]. Also, in the case of polar (methanol, ethyl alcohol) vs non-polar solvent (diethyl ether, hexadecane) solvent effect during sonoprocessing for fabricating μ-CuO agglomerates; highlights non-polar solvents acts effectively [364]. The current Al mesocrystals extraction is done out of the hexadecane solvent fabricate Al-rich compositions with Al (M)/ PVP (P) ratio higher than 1:1 ratio. This product develops surface oxide after storage for a week in laboratory conditions, hence not useful for fuel applications.

4.4 Al Characterization

4.4.1 Nanostructured Al Stabilization

Synthesizing oxide-free Al nanoparticles stabilized in the PVP matrix, in gram quantities, for fuel application is the key objective. In doing so, the sonication induced "process-intensification" activity is to be evaluated. Therefore one of the previously optimized Al chemical synthetic protocols is considered for experimentation. But an additional ultrasonic stimulus is introduced to achieve "process-intensification". There is published literature illustrating the specific chemical synthetic protocol to be replicated [365]–[367]. In order to have assertive quantification of the "process-intensification" in a quantitative term a physical variable namely "degree of crystallinity (DOC)" linked to the crystalline Al diffracting volume fraction is chosen [368]–[370]. It is the integrated intensity of the crystalline Al diffracting component to that of the total integrated intensity of both the crystalline Al and amorphous PVP fractions. The process followed is to estimate DOC of the products is to employ Rietveld whole-pattern fitting method. Bruker

AXS TOPAS (Total Pattern Analysis Solution) Version 5 program is used [371]–[373]. For analysis, the XRD broad signal from the amorphous phase is fitted with a split pseudo-Voigt (SPV) function. The peak position, the area, the left, and right FWHM, and the Lorentz fraction for the left and right SPV profiles are refined. The area under the curve of the SPV function is used as an effective scale factor for the amorphous phase.

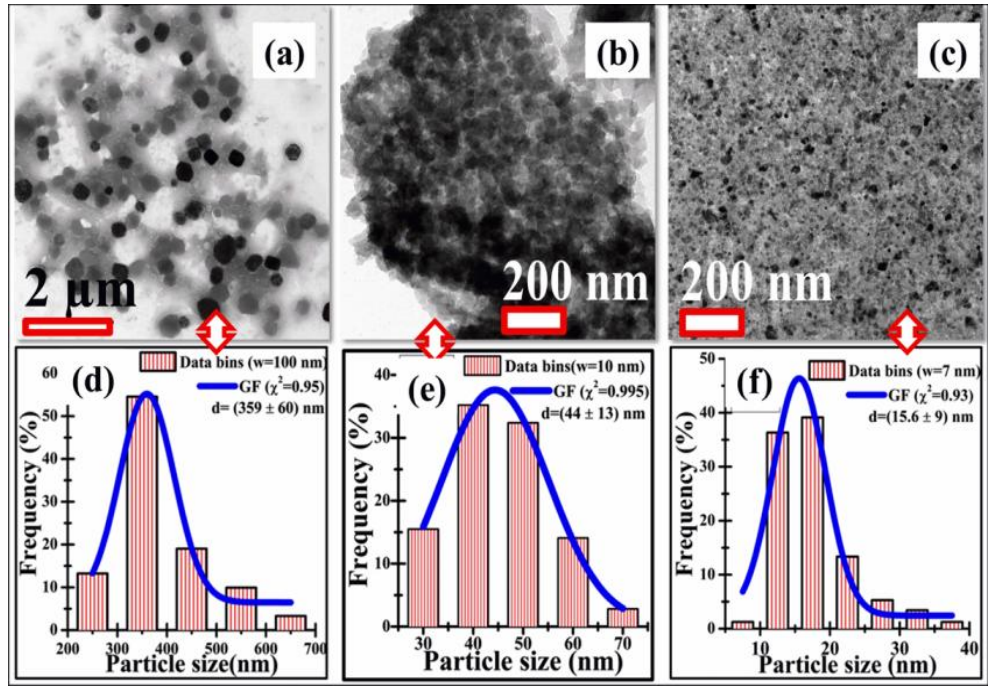


Fig.4 10 [Nano-Al PVP surface stabilization]: (a) 4:1 (b) 2:1, (c) 1:1 Al (M)/PVP (P) compositions. (d), (e), (f) are the corresponding nano-Al particle size, respectively.

The reflection profiles of crystalline phases are fitted with profile generated by fundamental parameter approach (FPA), most suited for diffractometer using Bragg-Brentano geometry [374]. The background intensity is modeled by Chebychev polynomial of 5th order with 1/X background checked implemented in TOPAS. The implementation of this is subsequently done, but the synthetic chemical protocol to deliver Al rich fractions is attempted first. Those three Al (M)/ PVP (P) compositions to having Al theoretical DOC (T) of 80, 66, and 50 % are synthesized. Out of these, the 1:1 Al-PVP composite having DOC (T) =50 % has the smallest average Al particle size

of (15.6±9) nm. Thereby this composite is the material of choice for subsequent further studies. The details of particle size distributions of these three Al-rich composites counted out of their corresponding TEM-BF images are shown in figs. 4 10 (a)-(f). It is important to note that using intensified ultrasound-assisted stimulus approach to deliver nanostructured Al; (1) [bottom up chemical processing employing Al precursor] require 30 minutes of processing time [375], whereas in (2) [top down processing employing Al foil] takes almost 36 hrs [376]. Thus, in the ongoing experimentation, the ultrasonic "process-intensification" shortens the existing chemical processing protocol-1 from 24 hrs to just about 2 hrs, based on DOC=50 % quantification for 1:1 Al/PVP composite.

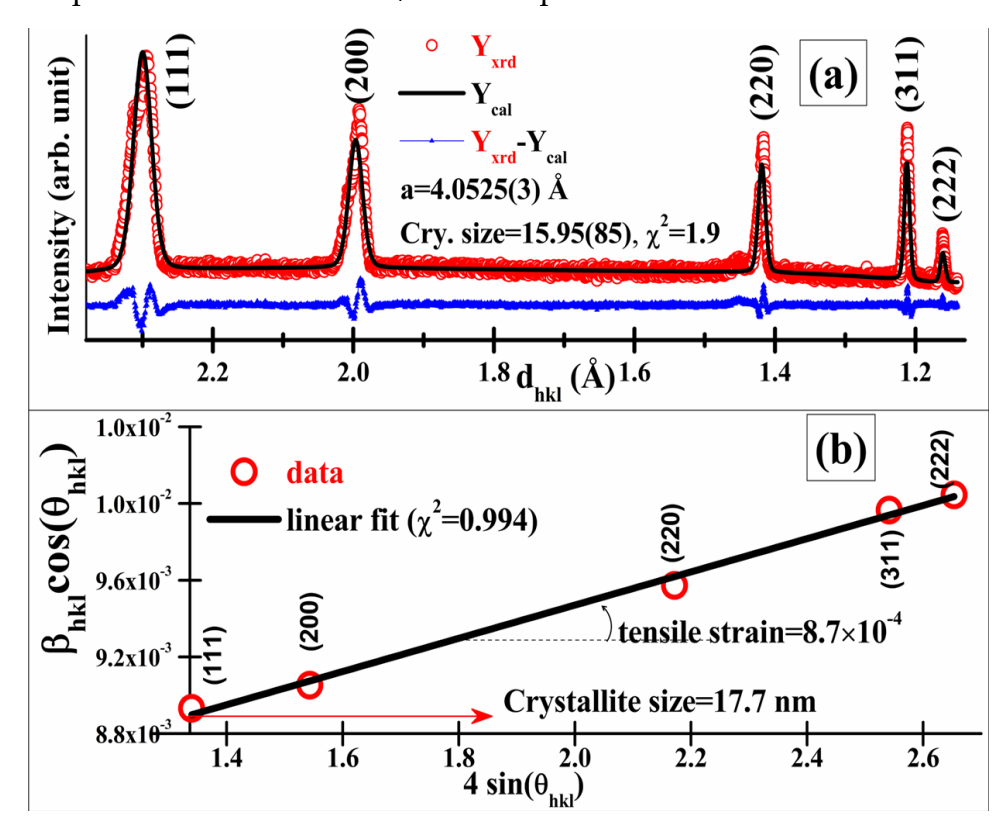


Fig.4 11 [XRD structural analysis of nano-Al]: (a) whole pattern profile fit, (b) WH plot respectively.

The lattice constant and phase purity of the embedded crystalline Al particles in the PVP matrix is estimated from the XRD data. The Al XRD data with profile fitting for lattice parameter extraction is plotted in fig. 4 11. The profile fitting refinement is

terminated after reaching acceptable values of standard agreement triplets (weighted profile R factor (R_{wp} %), expected R factor (R_{exp} %), R-pattern (R_p %), and goodness of fit index (χ^2), with χ^2 =1 representing an exact refinement. The agreement triplets reached are 6.22, 11.13, and 8.60, with χ^2 =1.9, respectively. The obtained final profile fit and difference pattern are shown as Y_{cal} and Y_{diff} = Y_{xrd} – Y_{cal} in fig. 4 11 (a). The refined face-centered cubic (FCC) unit cell is tensile strained with a=4.052 Å and is higher than 4.049 Å representing standard ICDD PDF: 04-0787 file. The Williamson-Hall (WH) plot (β Cos(θ) Vs. 4Sin(θ)) taken from the (111), (200), (220), (311), and (222) miller indexed lattice planes is shown in fig. 4 11 (b). The slope of the fitted line is positive, providing a direct indication of the tensile strain state of the Al phase as evaluated by the profile fitting computation. No crystalline or amorphous characteristic of the oxide phase is observed, indicating phase purity of synthesized nano-Al.

4.4.2 Sonocrystallization of PVP at RT

The sono-mechanochemical driven PVP graphitization (i.e., sonocrystallization) process is investigated by using the bulk powder-XRD method. The analysis of such bulk XRD data is a reaffirmation and validation of the presented TEM localized microstructural graphitization previously. The specific outcomes being; (1) graphitized PVP fraction quantification, (2) graphitized carbon structural parameters evaluation, and (3) developed structural phase identification, respectively. A set of the sonochemical designed composites of x wt% PVP/y wt% Al (denoted as xPVP-yAl; where x/y=1/1, 2/1, and 4/1) products are processed. The XRD pattern of RT sonicated 3PVP-2Al composite (denoted as RTSC/PVP-Al) concurrent to the present discussion is plotted along with the parent-PVP in fig. 4 12.

The amorphous parent-PVP has characteristic broad humps at 2θ =11.6 and 20.2°, respectively [377]–[380]. The broad hump at 2θ =20.2 ° develops to a sharpened peak implying PVP crystallization, along with its simultaneous structural phase

evolution to graphitic carbon (GC) form. This process of crystallization and subsequent GC phase formation is achieved by probe sonication at RT in solution-phase chemical processing of the RTSC/PVP-Al composite product. The mechanistics of the ultrasonic pressure waves devised crystallization is similar to that observed under laser or electron beam [381]–[388]. The XRD pattern of RTSC/PVP-Al composite also highlights the process of; (1) intercalation, (2) growth, and (3) stabilization of metallic Al nanoparticulate phase achieved in the designed crystallized matrix of PVP and GC respectively.

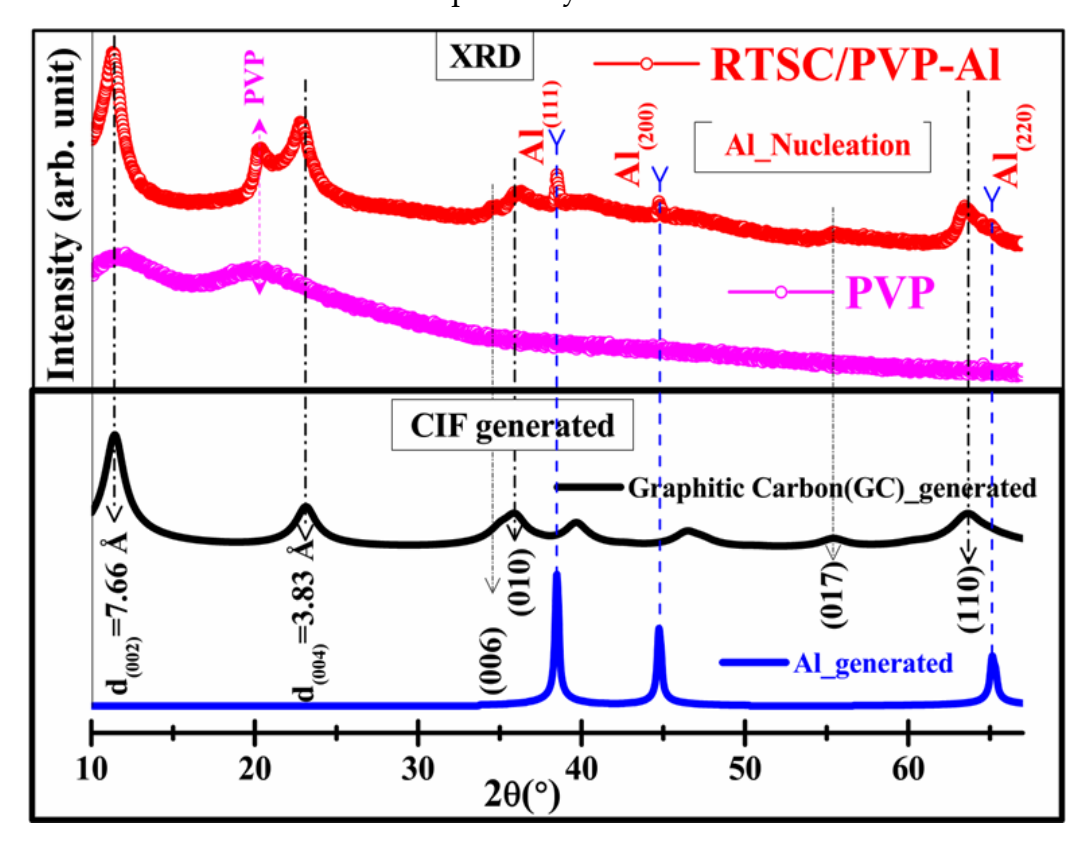


Fig.4 12 [Sonocrystallization of PVP at RT]: Obtained RTSC/3PVP-2Al composite XRD pattern plotted with crystal structure generated patterns below for developed peak phase identification.

In the designed RTSC/3PVP-2Al composite product, the PVP crystallized GC fraction structural phase identification is made employing Match! - program [389]. The fabricated GC structural phase has a match (i.e., the identified file is of the highest figure of merit) with that of the reference ICDD PDF-2: 89-7213 file with expanded C-

axis. To reaffirm this further, the crystallographic information file (CIF) generated XRD patterns are included in the plot as Graphitic Carbon (GC) _generated in fig. 4 12. A perfect match between GC_ generated with that of the GC phase of the fabricated RTSC/3PVP-2Al composite product is elucidated for observation. Also, in continuation of the earlier discussions, the reference ICDD PDF-2 file: 04-0787 identified in the previous sections, remains the perfect match for the metallic Al phase representing the other composite fraction. This metallic Al structural phase fraction can be seen as in the initial stage of nucleation, having very well intercalated into its surface stabilizing GC and crystallized PVP matrix component, respectively. Similarly, the Al reference ICDD PDF-2: 04-0787 CIF file generated XRD pattern plotted as Al_generated, matches well with that of the RTSC/3PVP-2Al composite product Al phase completing crystallographic phase identification step. No other impurity phase corresponding to the initial untreated precursor and other reaction generated unwanted phases are observed, even though the sonocrystallization process progress is achieved at RT. Ice cooled chilled water maintained at 20 °C is circulated all around the sonochemical reaction vessel to dissipate bulk solution heat accumulation during 2 h long continuous mode sonochemical processing.

Among the allotropes of carbon, hexagonal GC crystal form in ABABAB... carbon layers stacking sequence is a fascinating microstructural feature enriching extensive research and development activities [390]–[396]. Significantly, this carbon forms layers one above other in parallel stacking (see fig. 4 13 (a)) which makes GC soft and slippery nature due to contributions of these carbon layers facile expansion along the c-axis. These c/2 stacked carbon layers are the x-ray diffracting entities that produce a pronounced (002) diffraction peak, representing layers spacing. Any changes to this c/2 spacing brought in can easily be tracked by XRD measurement. The inset shown in fig. 4 13 (a) is the XRD patterns of graphite, and one of its c-axis expanded structures, indicates this one to one correspondence of c-axis stretching leading to XRD peak shift to lower angles. It is important to note here that for

material under stress-strain investigation, in the elastic region below, yield point stress is proportional to strain [397]. A graphical schematic of the generic physical shape for materials stress-strain curve in both the elastic and plastic regions is plotted in fig. 4 13 (c).

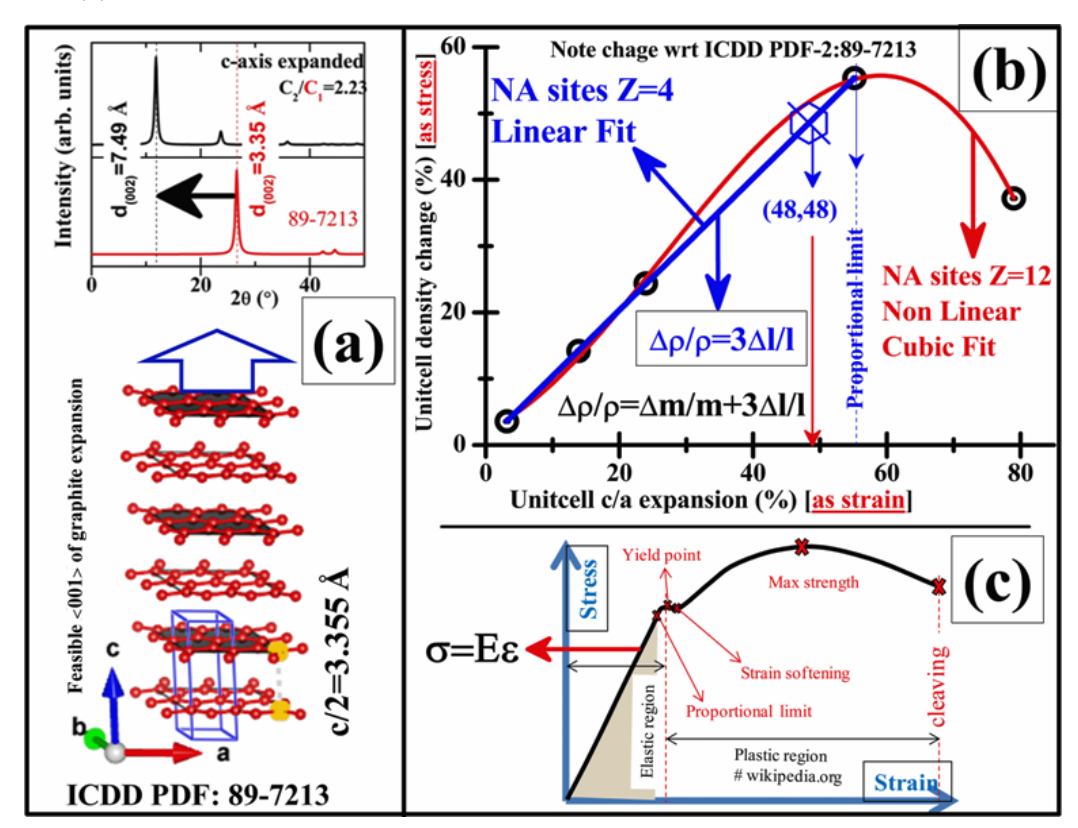


Fig.4 13 [Expandable GC]: (a) schematic of Graphite unit cell and its generated XRD pattern (b) change in unit cell density versus lattice expansion as stress-strain curve, and (c) physical shape of stress-stain curve adopted from Wikipedia respectively.

Thereby in the elastic region, observation the stress versus strain proportionality behavior observation is analogously extended to the material density changes brought in by c-axis elongation. This presumption is correct until no external mass flows into or out of this hexagonal carbon unit cell (GC, crystal system- hexagonal, space group number-194, space group symbol-P63/mmc) is strictly prohibited. That is, elongation proportionally reduces unit-cell density. Based on this fact, both the c-axis elongation and corresponding possible density changes of a variety of GC unit-cells are plotted in fig. 4 13 (b). The expansions of these GC unit-cells are with respect

to the ICDD PDF-2: 89-7213 standard file. The set of expandable GC unit cells utilized are tabulated in table-1 taken from "The material project: A material genome approach to accelerating material innovation" [398]. Two implications of this correlation are; (1) a nonlinear cubic power law is the best fit (red curve, χ^2 =0.999) to the entire dataset considered, when there is mass flow into the unit cell. That is, once the number of carbon atomic sites in the unit cell is increased from z=4 to z=12. The physical appearance of both the plots of fig. 4 13 (b) and (c) becomes analogous. (2) A linear fit is the best fit (blue line, χ^2 =0.999) until the GC lattice expansion reaches 55% (proportional limit); and the number of GC atomic site is maintained at z=4. An unit cell expansion of less than 55% is recoverable, and the expandable graphite is in the elastic region.

Table 4 1 GC unit cell taken from the material project (mp) [398] and ICSD database

<u>ID mp-48</u>	<u>ID mp-</u> 606949	<u>ID mp-</u> <u>997182</u>	<u>ICSD-</u> <u>426931</u>	<u>ICSD-</u> <u>617290</u>	<u>ICDD-</u> <u>897213</u>
a=b=2.467 Å c=7.803 Å	a=b=2.467 Å c=31.983 Å	a=b=2.468 Å c=14.998 Å	a=b=2.469 Å c=8.841 Å	a=b=2.470 Å c=6.930 Å	a=b=2.464 Å c=6.711 Å
α=β=90° γ=120°	α=β=90° γ=120°	α=β=90° γ=120°	α=β=90° γ=120°	α=β=90° γ=120°	α=β=90° γ=120°
Z=4	Z=12	Z=4	Z=4	Z=4	Z=4
ρ=1.94 g/cm ³	ρ=1.42 g/cm ³	ρ=1.01 g/cm³	ρ=1.71 g/cm ³	ρ=2.18 g/cm ³	ρ=2.26 g/cm ³

In the fabricated RTSC/PVP-Al composite d (002) =7.66 Å (see Fig.4.10 GC_ generated) represents 48 % elongation, thereby is in the elastic region. One-to-one

correspondence employing fig. 4 13 (b) plots, it is estimated that the expanded GC density must be 1.17 g/cm³. Thereby the material project mp-99182 file represents the ideal current sonocrystallized expanded GC unit cell parameters. This illustration of the soft and expandability feature of the GC, by bringing a correlation with well-established materials stress-strain plot is most illustrative. This analysis also stands in justification and support of its broad applicability to the field of batteries as an electrode material, where repeated charging and discharging are linked to reversible expansion/ contraction of graphite composite electrodes [399]–[401].

4.4.3 Intercalation of metallic Al in sonocrystallized GC and PVP Matrix composite

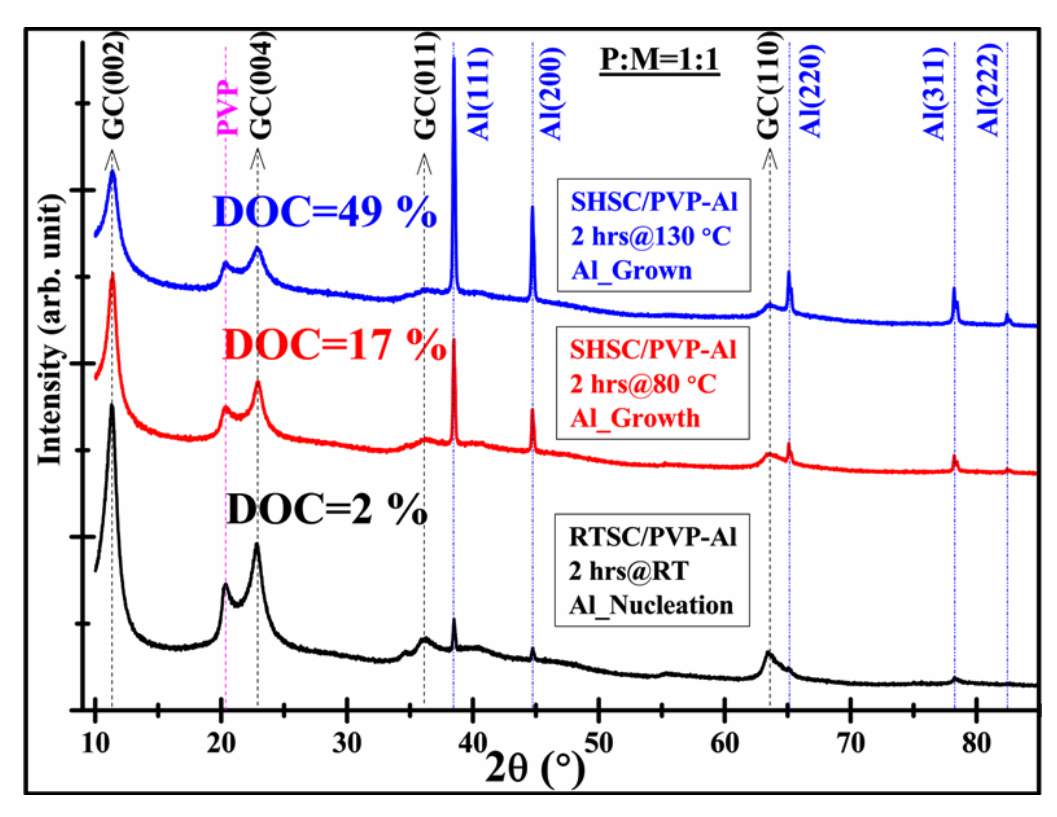


Fig.4 14 [Intercalation of metallic Al]: Metallic Al nucleation and growth by 2hrs sonication generated self heating (SH). Composite processed at RT (RTSC/PVP-Al), 80 °C (SHSC/PVP-Al), 130 °C (SHSC/PVP-Al) respectively.

The sonication generated self-heating (SH) is utilized as one of the effective means to facilitate nanocrystalline Al growth, suitably embedded, and stabilized in the

sonocrystallized GC and PVP Matrix fraction delivering required 1:1= polymer(P) to metal(M) composite. A quantifying parameter, i.e., "degree of crystallinity" (DOC) representing only the Al crystalline phase fraction, is evaluated to justify the synthesis of the desired composite. For example, the P: M=1:1, 4:1 composites based on the definition must have DOC of about 50 and 20 % of Al, respectively. The XRD data are shown in fig. 4 14 highlights two distinguishable processing aspects; (1) PVP fraction sonocrystallization at RT, (2) metallic Al crystal growth utilizing the bulk heating generated by the continuous mode 2 hrs sonochemical processing.

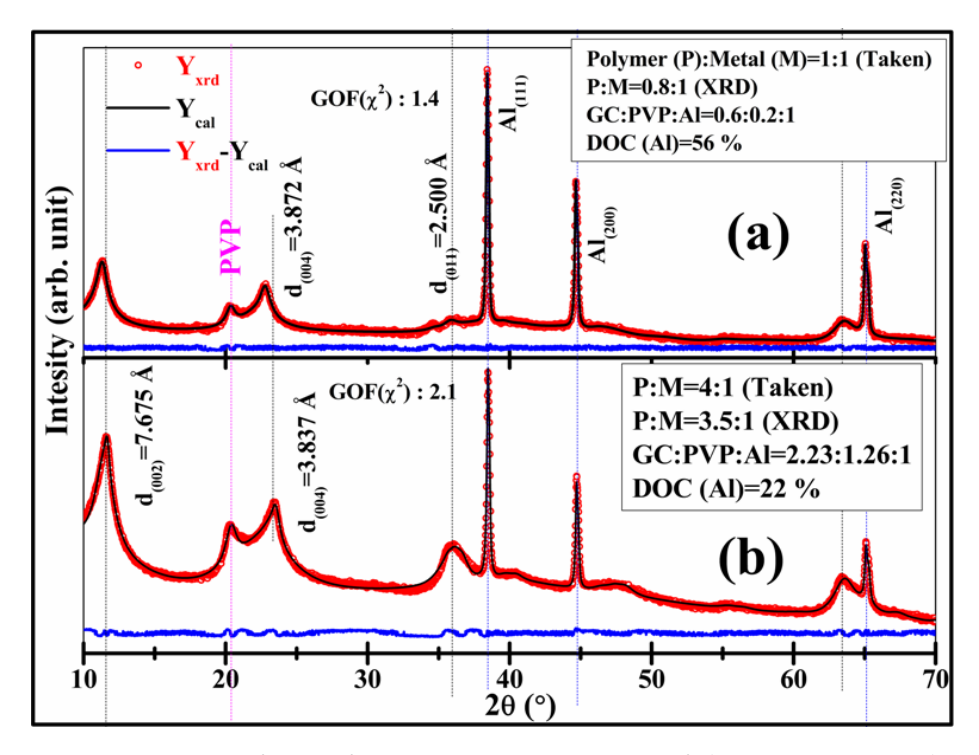


Fig.4 15 [A set of P: M fraction]: XRD patterns of the (a) P: M=1:1, (b) P: M=4:1 composites respectively.

The Al grown phase fraction reaches DOC= 49 % is as per the desired P: M=1:1 composite. It is pertinent to mention here that two sonochemical SH temperatures 80 °C and 130 °C respectively, reached after 1 h and 2 hrs of continuous processing, are utilized for Al crystal growth. Also, to illustrate DOC values computation, two processed P: M fraction XRD data (Y_{xrd}) is shown in fig. 4 15. The CIF of the identified crystallized structural phases of GC, PVP, and Al are used to generate the whole XRD pattern. Each structural phase is refined, and the individual peak phase is

generated using fundamental parameters profile fitting (FPPF) approach [374]. The extracted DOC of 56 and 22 % are as per the fraction of 1:1 and 4:1 chosen for P: M, respectively. The obtained final profile fit (Y_{cal}), the difference pattern (Y_{xrd} - Y_{cal}), and along with goodness of fit index (χ^2) is shown in fig. 4 15 (a), (b).

4.5 Metallic Al Crystal Growth

The synthesized RTSC/PVP-Al composite having the least DOC=2 % of Al, is the precursor chosen to illustrate the Al crystal growth. In fact the RTSC/PVP-Al composite is having the Al phase is at its nucleating state (Al_Nucleation). To facilitate Al crystal growth the sonochemical processing generated solution self heating is considered. The 80 °C reached with 1 h of processing is maintained another 1 h. A total 2 hrs of processing at 80 °C increases the DOC to 17 % representing Al growth (Al_Growth). In contrast 130 °C reached during 2 hrs of processing further increases DOC to 49 %, almost approaching the 50 % theoretical DOC limit chosen. Therefore, the DOC=49 % achieved product is identified as Al_Grown. Clearly these XRD quantitative DOC data extracted from the product XRD patterns shown in fig. 4 14, can be identified with Al nucleation, growth and grown features respectively, in the absence of any crystal growth mechanistics.

In the present context, the feasible way to provide a mechanistic understanding of crystal growth is to employ an appropriate tool that facilitates crystallization. One is the utilization of the TEM electron beam (e-beam) irradiation. There are many reports of localized crystallization under TEM e-beam [402]–[406]. The progress of amorphous to crystalline phase transition under TEM e-beam is divided into two categories. These are; (1) (beam energy is large to overtake displacement energy) the crystallization is achieved by the creation/annihilation of point defects and inducing increased atomic mobility [404], [407]–[409], or (2) (for lower beam energy not sufficient for creating atomic displacements) crystallization gets initiated at the amorphous to crystalline interface with the breaking of

incorrectly formed interfacial bonds and subsequently rearranges itself to regular crystalline order [403], [410]–[415]. The reason for athermal nature of this TEM ebeam induced crystallization and also why an amorphous (of high relative internal energy) material ends up into an ordered crystalline structure under continuous ebeam impetus can be found elsewhere [402], [416], [417].

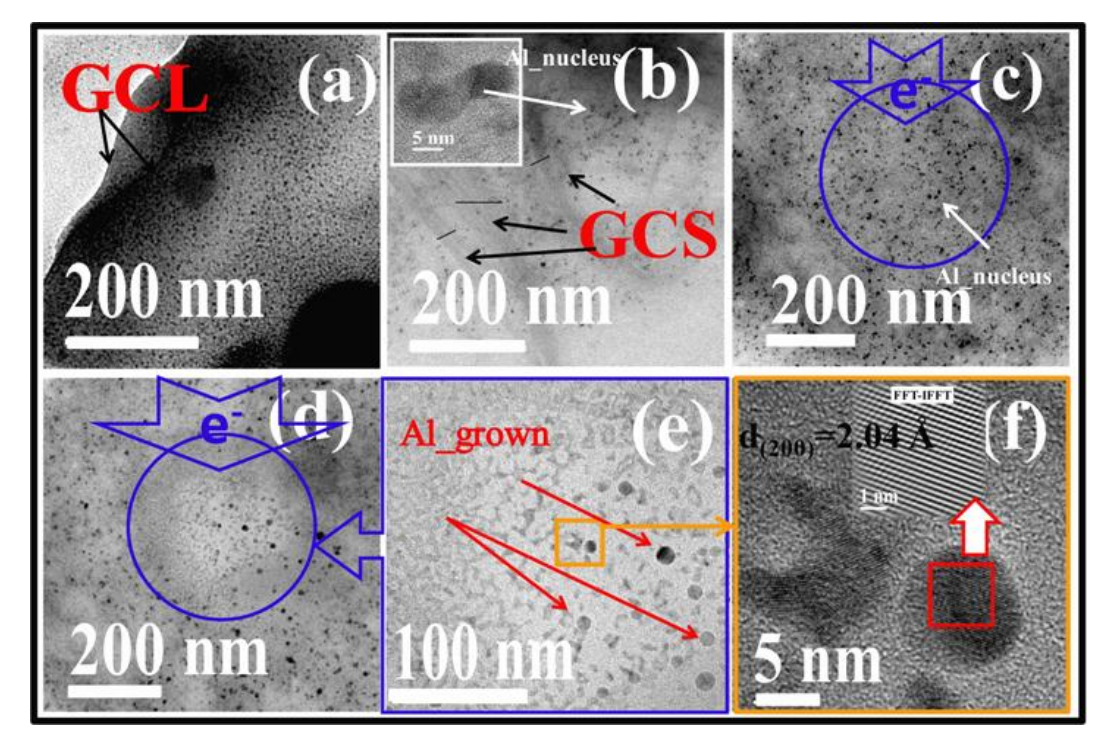


Fig.4 16 [Nano-Al crystal nuclei]: synthesized RTSC/PVP-Al composite TEM analysis.

Computed experimental data suggest to create point defects in crystalline Al displacement energy of 19 eV is required corresponding to 210 keV primary TEM e-beam [418]. But in the present case of amorphous material having differing local environment than its crystalline form, the displacement energy can be as low as 10 eV [419]. Therefore having 200 keV TEM e-beam operating at step-4 emission mode with well above the predicted displacement threshold energy is expected to create the required effect. It suggests achieved amorphous to crystalline transition is dominantly controlled by point defects creation and annihilation, thereby falls in category 1, as stated. With this brief TEM e-beam irradiation, an athermal

crystallization enhancement (DOC increase) tool appropriate to mimic the actual Al crystal growth observed by sonication generated SH can be simulated.

The RTSC/PVP-Al composite having DOC=2 % representing Al is imaged in TEM-BF mode, and the micrographs are shown in figs. 4 16 (a)-(c) respectively. GC in layer (fig. 4 16 (a)) and stacking (fig. 4 16 (b)) having 5-8 nm dark spots well embedded densely packed and uniformly spread can be seen. One of the HR-TEM imaging of these dark spots suggests dense liquid-like material embedding and its flow behavior, having no signature of Al lattice fringes. The inset in fig. 4 16 (b) contains one such Al nucleus (Al_nucleus) in HR-TEM observation. In order to facilitate crystal growth employing TEM e-beam, the protocol schematized by the present author in the previous chapter-III (section3.1.4) is followed [420]. In the TEM BF micrograph shown in fig. 4 14 (c), the blue encircled region is TEM e-beam irradiated (E4I5M) for 5 minutes in HR-TEM mode with step-4 LaB₆ electron emission current. The micrograph shown in fig. 4 16 (e) is the e-beam irradiated region from which there is disappearance of black spots (liquid-like containment), undergoes crystallization leading to the growth of spherical Al nanoparticles. The grown spherical Al nanoparticles are of 15-18 nm in diameter. The central section of the E4I5M irradiated region shown in fig. 4 16 (e) is further probed for crystallinity development using HR-TEM mode. The obtained HR-TEM micrograph shown in fig. 4 16 (e), indicates the e-beam irradiation grown Al nanoparticles are crystalline and have lattice fringes of Al d-spacing 2.04 Å. This observation is in concurrence with earlier reports on crystallinity development employing TEM e-beam irradiation as a localized tool.

To gain further insight, whether Al crystal growth is by classical Ostwald's ripening (OR) or by particle mediated non-classical (OA) scheme TEM microstructural characterization is employed [420]–[424]. A GC flake having embedded Al nuclei of RTSC/PVP-Al composite shown in fig. 4 17 (a) is half portion (TEM BF) and the portion that is subsequently completely E4I5M e-beam irradiated

is shown in fig. 4 17 (b). The observed clear brighter spots in TEM DF imaging mode all over the GC flake validates the crystallinity of embedded nanoparticulate. The entire GC flake portion acquired in TEM SAED mode validates nanoparticulate entities to Al structural phase ring indexing (see fig. 4 17 (c)).

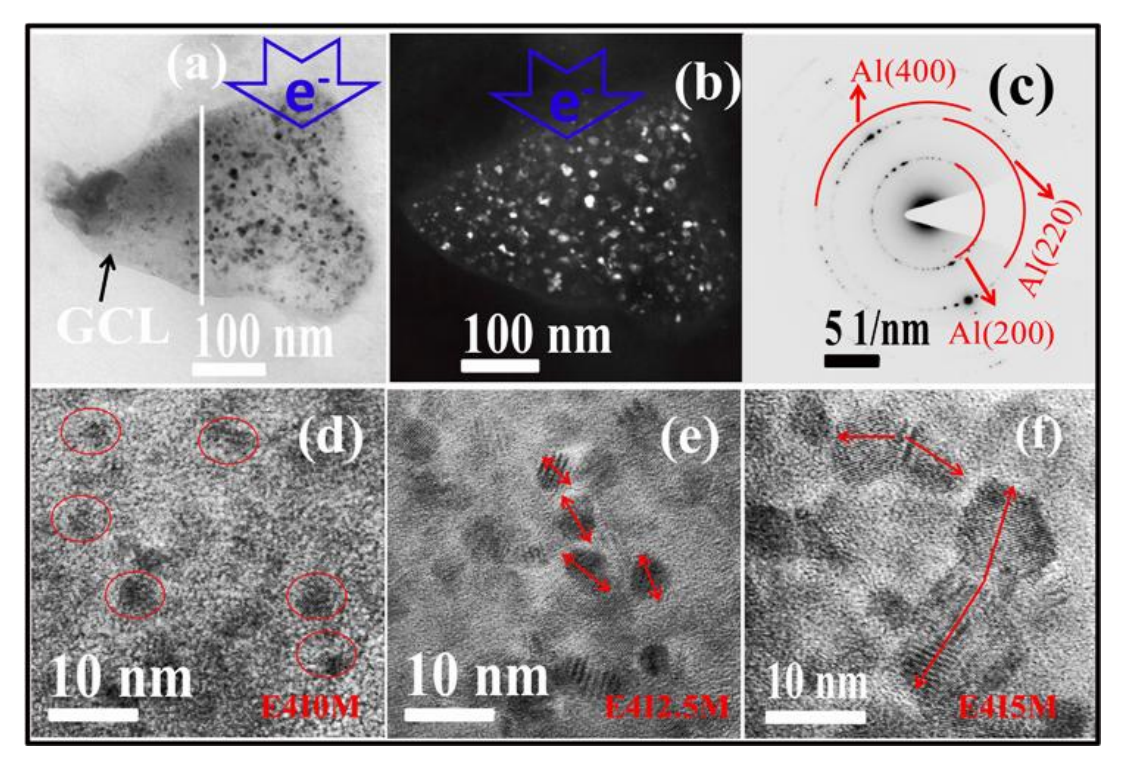


Fig.4 17 [Al Crystal growth under TEM e-beam]: synthesized RTSC/PVP-Al composite TEM analysis after exposure to TEM e-beam; (d)-(f) snapshot of the same region illustrating Al crystal growth, (a), (b) demonstrate TEM e-beam gradual movement from right to left facilitating growth in a GCL respectively.

Sequential e-beam irradiated RTSC/PVP-Al composite portion after 0, 2.5, and 5 minutes exposure is shown in figs. 4 17 (d)-(f) validates crystal growth and supports particle attachment. TEM e-beam electron transparency in the HR-TEM micrographs of figs. 4 17 (d)-(f) to classify whether the particle attachment is OR or OA scheme. Another GC flake already once E4I5M irradiated having a comparatively larger 10-15 nm size is chosen for crystal growth observation. One of the edge portions of the flake having 9 Al nanocrystallites is shown in fig. 4 18 (b). Subsequent E4I2.5M exposure few smaller ones disappear, highlighting coarsening of smaller ones coarsening by OR scheme. This is further illustrated in a still larger particulate

marked as-1 is shown in fig. 4 18 (d). The OR of particles 2, 3, and simultaneous growth and evolution of particle-1 shape is in support of OR, leading to Al crystal growth. This physical evidence demonstrated under TEM e-beam is consistent with literature on metallic particles crystal growth by ultrasonic induced head-on collision facilitated agglomeration, particle fusion by melting, and coalescence [350]–[355]. The similarity being both (TEM e-beam and Ultrasonic) Al crystal growth is by classical OR mechanism. The difference being that the first is athermal, while in the second, localized temperature rise above melting resulting coalescence is the proven reasoning.

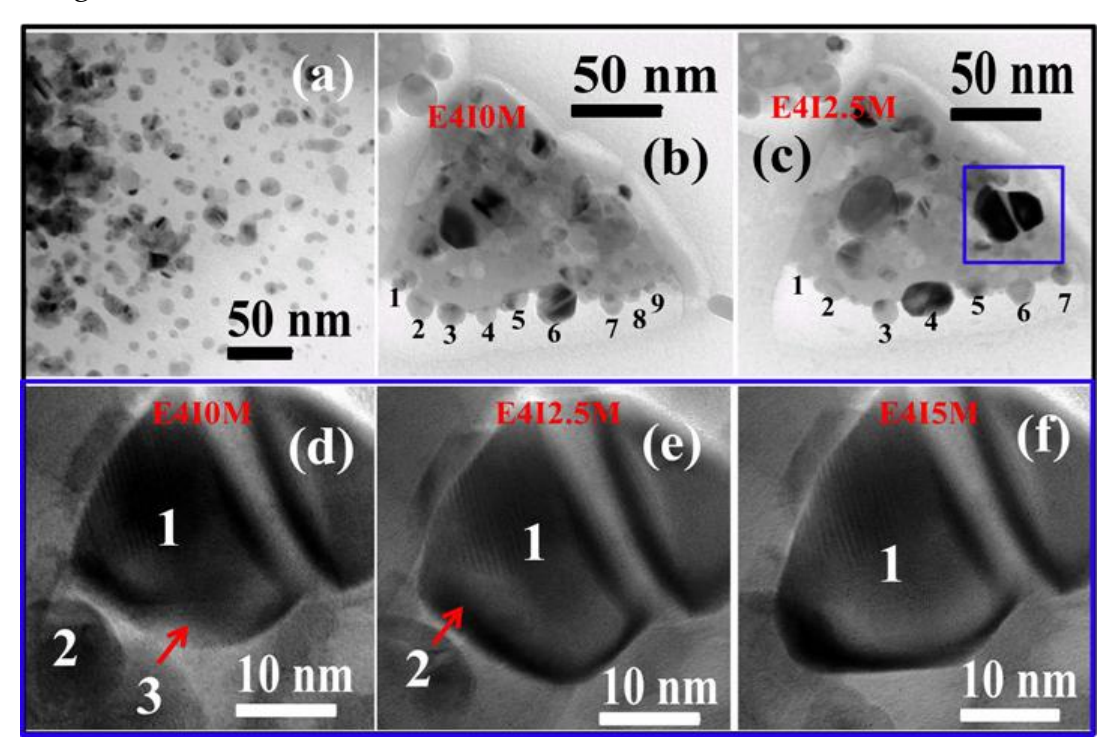


Fig.4 18 [Nano-Al Crystal growth under TEM e-beam]: (d)-(f) already exposed larger Al-crystallite is seen to undergoes OR by consuming smaller adjacent ones; (a)-(c) particle attachment illustrations respectively.

4.6 Conclusions

The specific conclusions drawn from this chapter in the process of synthesizing airstable metallic-Al particles embedded in the PVP matrix are listed below.

- 1) The sonocrystallization of PVP to graphitic carbon (GC) at RT indicates the process as athermal, thereby favors the dominant role of ultrasonic shock waves in causing it.
- 2) Similarly, the RT processed composite (RTSC/PVP-Al) only has metallic Al in its nucleating state, thereby also in agreement with cited literature that sonocrystallization leads to generation of Al nuclei or a nucleating phase of any sonoprocessed mater.
- 3) The nano-Al crystal growth is only achieved when the solution is allowed to self-heat during sonoprocessing. The bulk solution heating probably causes an increase in the rate of the head-on collision of these RT generated Al nuclei to fuse. The nuclei fusion generates a crystalline building unit, which subsequently grows by further coalescence based on the duration of sonoprocessing.
- 4) To validate Al crystals growth by building unit coalescence, Al-rich compositions with Al (M)/ PVP (P) ratio higher than 1:1 ratio investigated indicates building units sono-agglomeration. In this case, the reduced fraction of PVP surfactant offers less hindrance to agglomerate almost 10 nm Al cubes in sidewise fashion to deliver around 359 nm Al 2D-large lumps devoid of an oxide phase. When exposed to TEM e-beam, the de-agglomeration of individual building units is observed.
- 5) In the case of Al (M)/ PVP (P) fraction= 1:1, the sono-agglomeration of nano-Al building units is actively suppressed by the PVP fraction to deliver approximately 15 nm Al crystallites densely packed inside the PVP matrix. The degree of crystallinity of the Al phase as expected is 56 % (XRD extraction), slightly above the theoretical expected 50 % in line with the composite fraction considered.
- 6) The arrangement/attachment of nano-Al crystals at the edges of the GC indicates almost all the major features linked to the Al phase like; nucleation, coalescence, and growth mostly happen in the n-hexadecane medium. Simultaneous gradual embedding of grown nano-Al crystals into the GC layers results in intercalation, and leading thereby its c-axis expansion.

- 7) The crystal structural data of the expandable GC extracted indicates that its expansion is 48 % higher with respect to the standard ICDD structure, to accommodate 56 % nano-Al fraction.
- 8) The generated composite is air-stable, Al-rich with no amorphous surface oxide and is expected to have many years storability making it suitable for fuel applications.
- 9) Finally, the conventional protocol-1, which requires around 24 hrs processing time, is shortened to just about 2 hrs highlights another physical demonstration of sonic-assisted process-intensification activity.

Intentionally Page Kept Blank

Chapter-V

Investigation of energetics of 1:1 stoichiometric Al/PVP-fuel and nc-CeO₂-oxidizer nanocomposite material

S. Gottapu, **S.K. Padhi**, M.G. Krishna, and K. Muralidharan, Poly (vinylpyrrolidone) stabilized aluminum nanoparticles obtained by the reaction of SiCl₄ with LiAlH₄. New Journal of Chemistry, 39(7), **2015**, pp.5203-5207.

Cite this document as

https://arxiv.org/abs/2006.05972

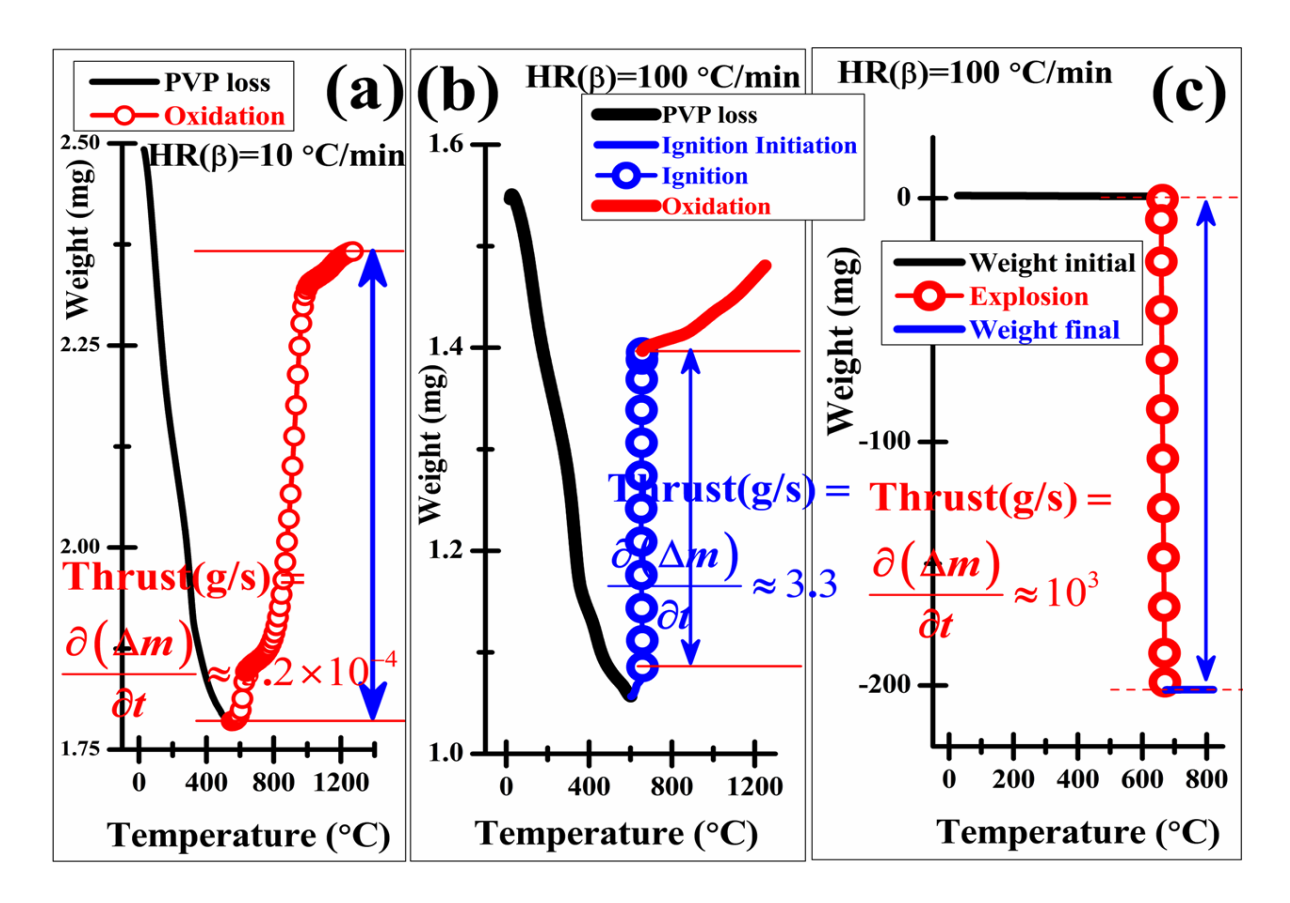
Keywords

Nanostructured-Al powder, thermo-oxidative reaction, nanostructured ceria, solid-oxidizer, ignition, exotherm, activation energy

Abstract

The investigations of the nanostructured-Al (nano-Al) based thermo-oxidative reaction attributes are detailed in this chapter-5. Two products are selected for the thermo-oxidative reaction studies. They are (1) Nano-Al embedded in PVP matrix (will be termed as fuel) and (2) its physically mixed 1:1 stoichiometric nanocomposite processed with the ultrafine nc-ceria oxidizer (also will be termed as nanoenergetic material (NEM)), respectively. The graphical abstract presented below illustrates an overview of the thermo-oxidative reactions recorded for fuel employing thermogravimetric analysis (TGA) method. Similar TGA experimentation of the designed NEMs is carried out to assemble scientific data validating, whether or not a desired acceptable reaction attribute is achieved. Also, in concurrence with the TGA oxidation event, a synchronous exothermic energy release event in differential scanning calorimetry (DSC) trace is observed. The above mentioned two products and their thermo-oxidative reaction behaviour employing TGA/DTA and TGA/DSC thermal traces is compared and interpreted based on the literature.

Graphical Abstract



Al/PVP-fuel: (a) Oxidation, (b) Ignition, and (c) Explosion attributes respectively tracked by thermogravimetric analysis (TGA) method.

5.1 Introduction

Conventional thermites made of micron-sized metals and the oxide of a less reactive metal as components have low-rate of energy release and long-ignition delay are used in rail road-track welding applications [105]-[107]. The conventional thermite reaction is a diffusion controlled energy release limited by aluminum oxide shell covering the Aluminum (Al) particle [108]-[110]. Pre-stressing of the micron-sized Al core-shell particles to improve reactivity is also attempted. This has shown that flame rate of 68 % is achievable, which is similar to that of for the best case of Al nanoparticles [111]. However, the nanostructured formulation of intimately mixed Al and metal oxide composites dominates the energetic applications [112]–[120]. These composites otherwise termed as metastable intermolecular composites (MICs; also termed as nanoenergetic materials (NEMs)), have enhanced thermo-physical performance as a result of increased interfacial contact area for heterogeneous reaction and reduced diffusion distance. Composite metastability is inertness prior to thermal, laser, or electrical actuation, and also ignition by impact, spark, and frictional force [121]-[127]. For example, when ignited these MICs undergo a selfsustained exothermic reaction to produce almost twice higher volumetric enthalpy (i.e., TNT (conventional explosive) = 7.22 kJcm^3 , and $Al/I_2O_5 \text{ (MIC)} = 25.7 \text{ kJ cm}^3$) compared to that of the conventional monomolecular high energy explosives [128].

Metallic Al is an ideal, widely utilized, candidate as fuel for example in propellant NEMs, because its high heat of combustion (Enthalpy = 31 kJ/g) increases propellant energy density, lowers combustion instability, and facilitates the formation of low molecular weight exhaust gases [129]. It leads to increase in specific impulse of the system at economically lower cost. Also another detailed investigation of a set of NEMs by Zachariah et al., on whether gas phase oxygen generation from oxidizer is a prerequisite for initiation of NEMs reaction had interesting implications [120]. It is found that for Al/Bi₂O₃ and Al/SnO₂ NEMs ignition results below the oxygen release temperature from its corresponding oxidizers, whereas for the second

set of NEMs like: Al/Co₃O₄ results ignition above its oxidizers oxygen release temperature. Further, Al/MoO₃, Al/Sb₂O₃, and Al-WO₃ respectively, have oxidizers that did not release any oxygen/ gas. In spite of this, they are seen to ignite showing that oxygen/gas release is a necessary but not sufficient condition which determines the initiation of these NEMs reactions. Therefore, NEMs reaction is the result of direct interfacial contact between Al-fuel and an oxidizer, facilitated by the condensed phase mobility of the reactive species termed as reactive sintering [120], [130]. Many synthetic approaches for NEMs fabrication to develop nano-architecture having Al fuel and oxidizer intimately packed for safer handling include; (1) NEMs composite developed into core-shell structure [131], (2) filling the oxidizer in protein cages (bio-thermite) [132], [133], (3) nanowire-based thermite membrane [134], (4) on carbon nano-fibers [127], and (5) in the form of both bi-layer/multilayer nanofoil formulations [135]–[139]. These are demonstrated to achieve tunable and efficient NEMs thermo-chemical and energetic performance.

Cerium (IV) oxide (CeO₂) is an active candidate widely used in solid oxide fuel-cells and in catalytic converter of toxic species of the automobile exhausts, because of its exceptional reversible reduction-oxidation attribute (2CeO₂ ↔ Ce₂O₃ +1/2 O₂) [140]–[146]. Significantly, the performance of low-emission power generation sources such as solid-oxide fuel-cells depend on the ability of nanocrystalline-ceria (nc-ceria) to accept, store, release, and transport oxygen ionic species. Reducing environments lead nc-ceria to form a series of non-stoichiometric oxide phases with Ce₂O₃ as end reduced product. This end product, in turn, easily can take-up oxygen in oxidizing environment to return to it's fully oxidation state. Temperature programmed reduction (TPR) experiments on nc-ceria highlights a four-fold increase in oxygen storage capacity (OSC), and the presence of more reactive surface superoxide (O²) ions [147]–[149]. Theoretical density functional investigations on structure stabilization conducted also reaffirms this experimental evaluated increase in OSC, to fully surface adsorbed supercharged superoxide ions

rather than bulk-lattice oxygen species [148]. This supercharging effect is particle size dependent leading to largest OSC for the ultrafine nc-ceria particulate. Thereby a increase in OSC becomes the active source of oxygen species at much lower temperatures (TPR peaks at ≈ 325 °C and 425 °C), in addition to higher bulk and surface lattice oxygen TPR peaks [149]. These unique fascinating properties of ncceria like larger OSC and its facile release are the relishing attributes, which is the motivating basis of the current work to investigate nc-ceria as an oxidizer for nano-Al. The synthesized poly (vinylpyrrolidone) (PVP) stabilized nm-Al composite is used as fuel [425]. To the best of the current author's knowledge this is one of the first attempts to employ nc-ceria in NEMs for promising thermo-physical and energetic properties evaluation.

5.2 Materials and Methods

Non-isothermal oxidation at different heating rate runs are acquired by employing TA Instruments STD Q600 dual DSC/TGA (differential scanning calorimetry/thermal gravimetric analysis) instrument. For TGA/DSC, 2.5(\pm 0.2) mg powder samples are taken in alumina cups (90 μ L) at a constant flow (100 cm³/min) of nitrogen. The TGA/DSC runs is carried out from ambient temperature to 1573.15 K. TGA and DTA (differential thermal analysis) sensitivity are 0.1 μ g and 0.001 °C, respectively. DSC calorimetric accuracy is of \pm 2 % based on the metal standard utilized. Field emission scanning electron microscope (FESEM) [Zeiss-make Ultra 55 model, Everhart-Thornley detector for SE2 and BS electron imaging (20 eV – 30 KeV)] and with attached Oxford Instruments INCA 350 Energy Dispersive X-ray Spectrometer (EDX/EDS) probe are employed for microstructural and chemical investigation (minimum detectable limit for EDX spectroscopy is of about ~0.2 Wt %). Transmission electron microscopy (TEM, FEI TECNAI G² S-Twin) in both bright field (BF) and dark field (DF) mode is employed for microstructural detailing at an accelerating voltage of 200 kV.

5.3 Results and Discussion

5.3.1 NEMs Physically Mixed Reaction Investigation

Physical-mixing is the most straightforward route to develop NEMs in powder formulation [426]–[429]. The reactive components dispersion in hexane (boiling point 68 °C) are probe-sonicated (VCX-750 W ultrasonic processor, 50 % amplitude, 13 mm solid-probe) for different (i.e., 1, 1 h. 30 m, 2 hrs, and 2 hrs 30 m respectively) durations. The NEM powder form is extracted by evaporating the hexane at 80 °C. The physically mixed composite reaction assessment is carried out by TG/DTA, which is to access information on the oxidation initiation temperature, structural phase-change, and energy release attributes, respectively. The NEMs and a conventional energetic material (CEM; nc-ceria oxidizer plus 40 nm-Al from US Nano) TG/DTA data for comparison are shown in fig. 5 1.

Typically, a batch of approximately 1 g of 1:1 stoichiometric NEMs powder preparation involves physical-mixing of the Al/PVP-fuel with that of the nc-ceria-oxidizer, in hexane as dispersant. The self-heating during sonication is dissipated by maintaining ice-cool water circulation at 20 °C around the sonication vessel. The reaction inferences of this NEM composition based on the TG/DTA plot of figs. 5 1 (a)-(b) are; (1) the oxidation of NEMs initiates at 511.13 °C, and also has a corresponding explicit DTA exotherm at 596.70 °C. (2) The oxidation of NEMs proceeds by two stage-wise weight gain events, i.e., oxidation-1 (Ox-1), and oxidation-2 (Ox-2), is resulting in a total of 35 % of weight gain. Based on the expected Al-fuel fraction, the designed NEMs composition (i.e., nm-Al (Fuel): PVP (stabilizer): nc-ceria (oxidizer) = 1:1:1) should deliver 33 % weight gain, which in this case is close to the 35 % obtained. (3) For NEM ignition at 511.13 °C, the required slope of the Ox-1 or Ox-2 stage must be that of the vertical dotted line drawn (see fig. 5 1 (a)).

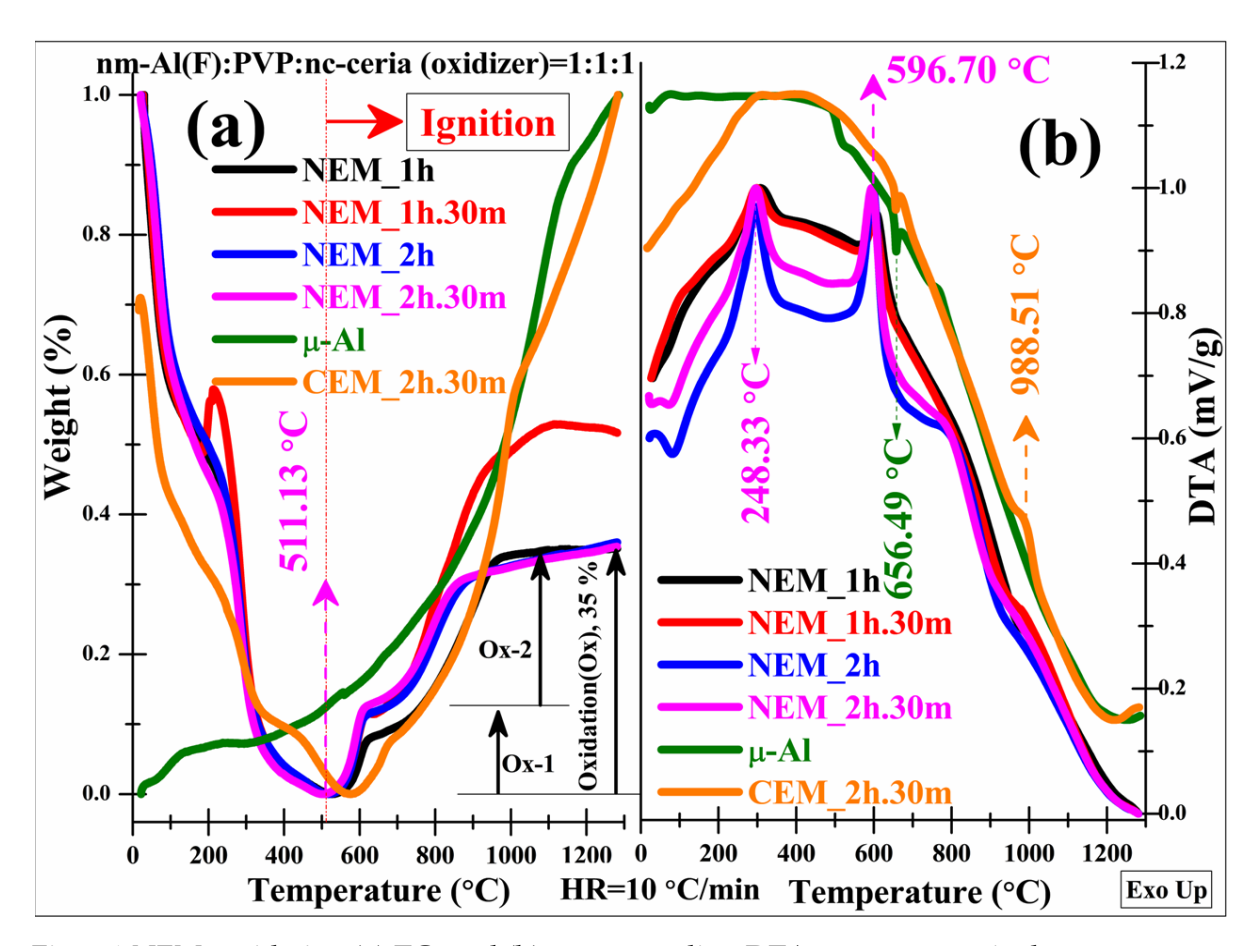


Fig.5 1 NEMs oxidation (a) TG, and (b) corresponding DTA traces respectively

In other words, initiated oxidation becomes the ignition with an oxidation rate enhancement. (4) Out of the two steps, stepper oxidation like Ox-1 is essential for energy release applications (i.e., have an associated DTA exotherm at 596.70 °C); whereas the gradual slow oxidation event like Ox-2 is not favorable. (5) Once the Ox-1 results in NEM ignition, the exothermic energy release helps in keeping the reaction self-sustained until the total NEM is exhausted. (6) The micron-Al (μ -Al) gradual weight gain is similar to that of the CEM. Both the CEM and μ -Al products indicate Al melting structural phase-transition represented by an endotherm at around 656.49 °C. But (7) in case of our PVP surface stabilized nm-Al product, the melting transition is suppressed and exhibits an oxidation exotherm below it. That is, oxidation is probably by condensed state oxygen delivered from nc-ceria oxidizer. (8) The CEM also has an exotherm after Al melting around 988.51 °C. (9) A low-temperature exotherm observed at 248.33 °C is linked to the weight loss (might be of

PVP polymer or nc-ceria grain growth by crystallization or both). The experimental reasoning of having the first exotherm is to be discussed later. (10) Finally, these sets of NEM processed TG/DTA data have a favorable affirmation to use nc-ceria as oxidizer. A minimum 2 hrs physical mixing is adjudged to be good enough physical mixing; to develop 1:1 stoichiometric NEM. The intimately mixed uniformly distributed reactive components inside the PVP are one of the nanocomposites for further evaluation.

5.3.2 Nano-Al inherent Surface oxide phase (i.e., in µ-Al, CEM) as inhibitor

The ineffective exothermal energy release of the CEM made out of a similar stoichiometric 1:1 proportion of nc-ceria oxidizer and 40 nm-Al purchased from US nanomaterials (US1050 product ID made by electrical explosion method have density 0.2 gcm⁻³) as observed is further investigated. The electron microscopy imaging techniques of FESEM and TEM are employed. The obtained microstructural data is presented in fig. 5 2. Also, the micron-Al (μ -Al, (9±0.4) μ m) powder 1200 °C oxidation product quenched to LN₂ temperature employing a vertical furnace microstructural information is included for comparison.

To justify why μ -Al is ineffective in delivering the much needed exotherm for energetic application is linked to the existing surface alumina oxide crust. For elucidation, the μ -Al quenched product powder regions of importance are tracked using FESEM. They are; (1) Al-melt expulsion through particles grain boundaries and isolation of many broken alumina bowls (see fig. 5 2 (a), ruptured alumina shell) with solidified Al-melt is observed. (2) The oxide crust surface shown in fig. 5 2 (b) has clearly defined grain boundaries with well separated highlights of individual grains interior comprising filled nanoscale whiskers, needles, and triangle edged feathers. These local structures grow mostly by outward diffusion of Al³⁺ cations through the Al particle surface structural defect sites and transforms finally into α -Al₂O₃ phase with increasing oxidation duration and holding time. Tolpygo et al. have examined

these solidified Al-melt expulsions and have reported that even after the transformation to α -Al₂O₃, these observed structural features are retained for longer duration, depending on the oxidation temperature and surface diffusion processes collectively [430].

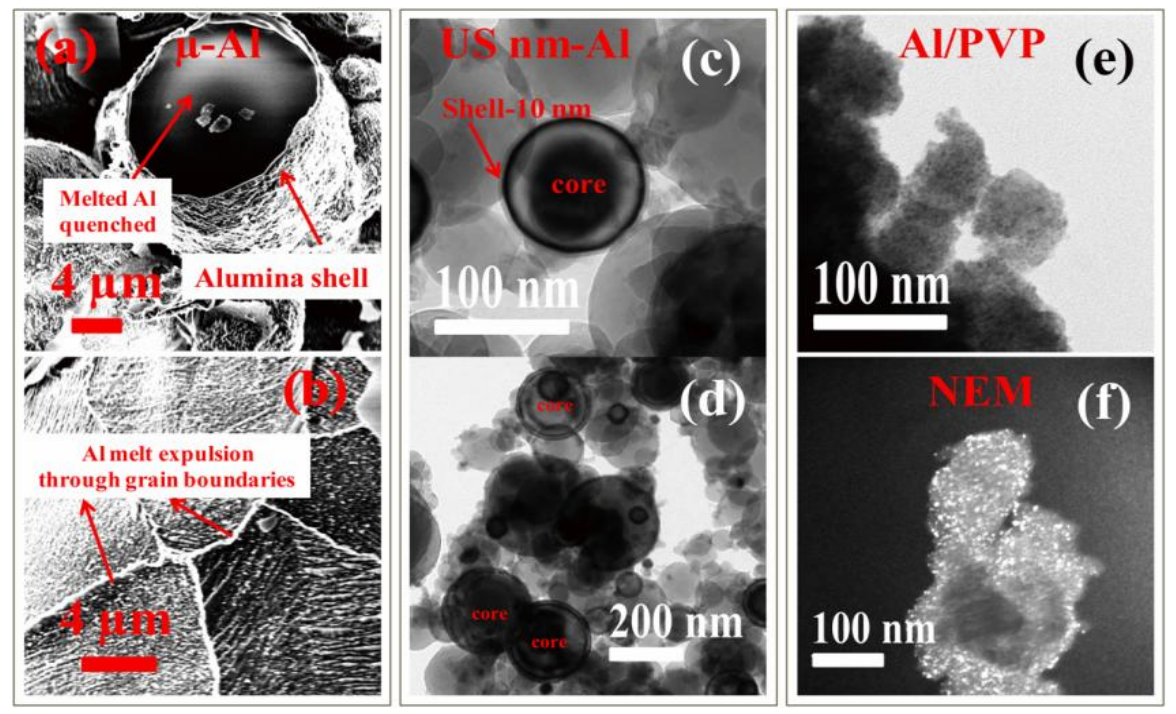


Fig.5 2 Microstructural observations of Al fuel; (a)-(b) μ -Al quenched at 1200 °C, (c)-(d) 40 nm-Al procured from US Nano, and (e)-(f) Al/PVP along with its obtained NEM respectively.

Thereby inefficacy to deliver exothermic process out of the μ -Al oxidation progress is mostly linked to the oxide crust diffusion-controlled gradual core oxidation (chemical reaction), and the accompanying structural phase transformation [108], [110]. After Al-core melting, volume expansion outward thrust ruptures the oxide shell (alumina melting=2072 °C) then bringing the already melted Al-core for ignition. Likewise, in the designed CEM, almost similar is the case. That is because of (1) the existence of 10 nm thick alumina oxide shell, and (2) the obtained Al-fuel is of least 0.2 gcm⁻³ densities, thereby no exothermicity in CEM DTA trace is evident. The TEM-BF micrographs of 40 nm-Al US Nano product particles are illustration of coreshell type structures and are shown in fig. 5 2 (c) and (d), respectively. The

chemically processed Al/PVP fuel utilized is shown in fig. 5 2 (e), and the corresponding physically mixed NEM developed is shown in fig. 5 2 (f) as TEM-DF mode. The densely packed bright spots representing both of fuel and oxidizer crystals inside the PVP matrix (TEM-DF fig. 5 2 (f)) observed, supports intimate contact between these reacting components and, therefore, lead to energetic efficacy. Lastly, the identification in case of μ-Al powder particles (shown in figs. 5 2 (a)-(b), data not shown) Al-core and alumina oxide shell is carried out employing composition by EDX facility. The average EDX elemental composition from over 10 different random regions on the ruptured crust provides, Al= (54.97±1.2) wt. % and O= (45.03±1.2) wt. % quantitatively similar to that of 52.93 and 47.03% expected in Al₂O₃. Likewise, the solidified melt region is Al rich, and having (91.71±1.62) wt. % of Al by EDX, in support of remnant un-oxidized Al mass fraction.

5.3.2 Al/PVP Fuel and nc-ceria Oxidizer TG/DTA investigation

To have conclusive inference of the observed exotherm at 248.33 °C in the weight loss region of NEMs (see fig. 5 1 (a)), both Al/PVP fuel and nc-ceria oxidizer TG/DTA analysis is carried out. The TG/DTA plots of both are plotted in figs. 5 3 (a)-(b) respectively. The nc-ceria oxidizer has one broad exotherm peaked at 564.28 °C representing gradual weight loss region L-2, whereas the subsequent weight loss region denoted as L-3 is associated with endotherm at 815.13 °C respectively. The weight loss for L-2 is gradual, but L-3 progresses at a faster rate. Based on the previous available literature it is inferred that; (1) first exotherm is probably linked to the gradual release of chemisorbed reactive superoxide ions release at TG L-2 range [431]–[433], whereas (2) endotherm is the lattice oxygen release thereby initiating ncceria reduction [434]–[436].

In case of the fuel, the low-temperature range below Al melting has two exotherms at 394.89 and 626.29 °C, respectively. The first exotherm, in this case, is the PVP fraction degradation, whereas the higher exotherm at 626.29 °C is associated

with oxidation of embedded Al fraction. A comparison of both HEM and Al/PVP fuel exotherms suggest the nc-ceria oxidizer catalyzes these two processes occurrences to lower temperatures. The PVP degradation lowers to 248.33 °C (oxidizer as catalyst), whereas Al oxidation exotherm is facilitated to 596.70 °C, probably by the release of surface adsorbed superoxide ion release respectively.

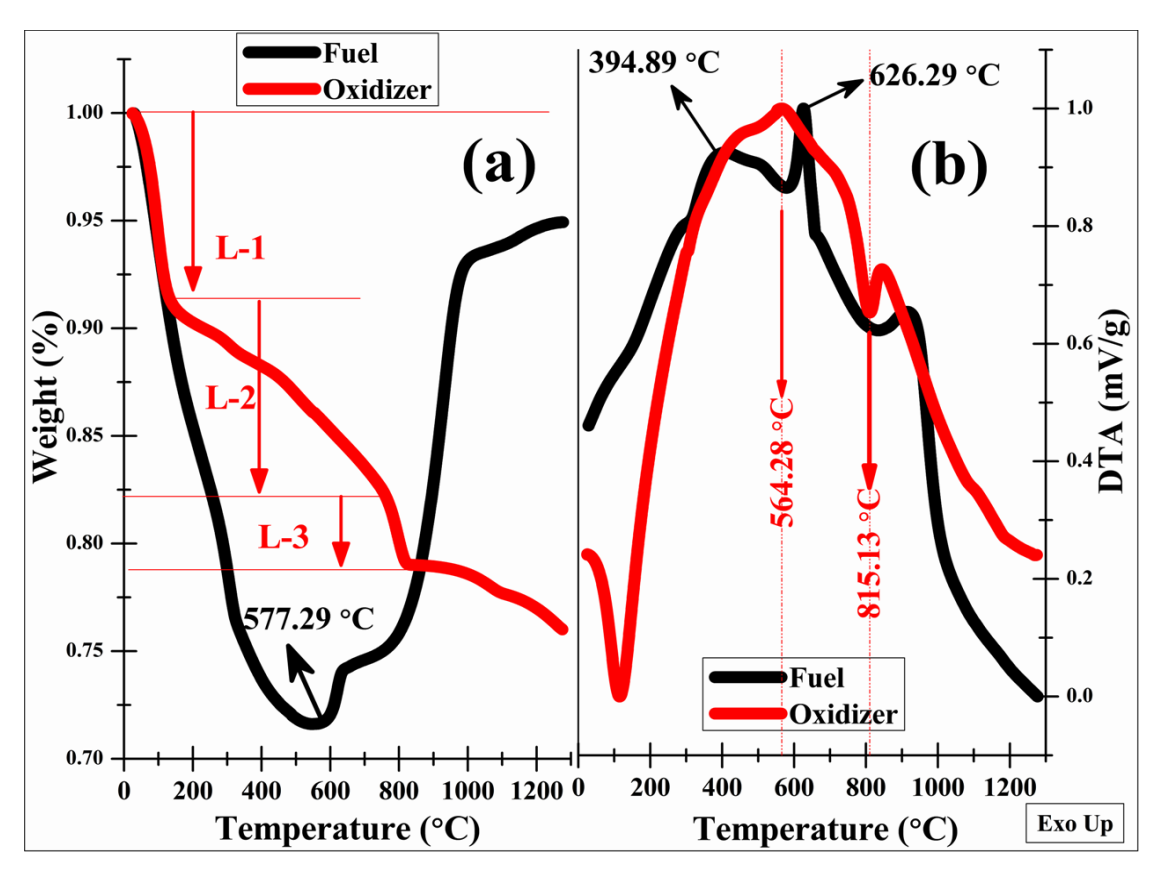


Fig.5 3 TG/DTA analysis of Fuel and Oxidizer at 10 °C/min; (a) TG, and (b) DTA plots respectively.

5.3.3 NEM and Al-PVP Ignition and Energy release investigation

The thermo-chemical reaction properties investigation of both the Al-PVP fuel and NEM are carried out based on TG/DTA and TG/DSC experiments [437]–[444]. In order to present a comparative view both products TG/DSC data recorded at heating rate (HR) at 100 °C/min is plotted in figs. 5 4 (a)-(b). At this one order higher heating rate (i.e. oxidation at 10 °C/min initiates weight gain of 0.52 mg per second for the fuel data shown in fig. 5 3 (a)) than conventional oxidation reaction, the weight gain

almost approaches 3.3 g per second. It is about 4 orders higher weight gain than the conventional oxidation, and thereby is termed as ignition.

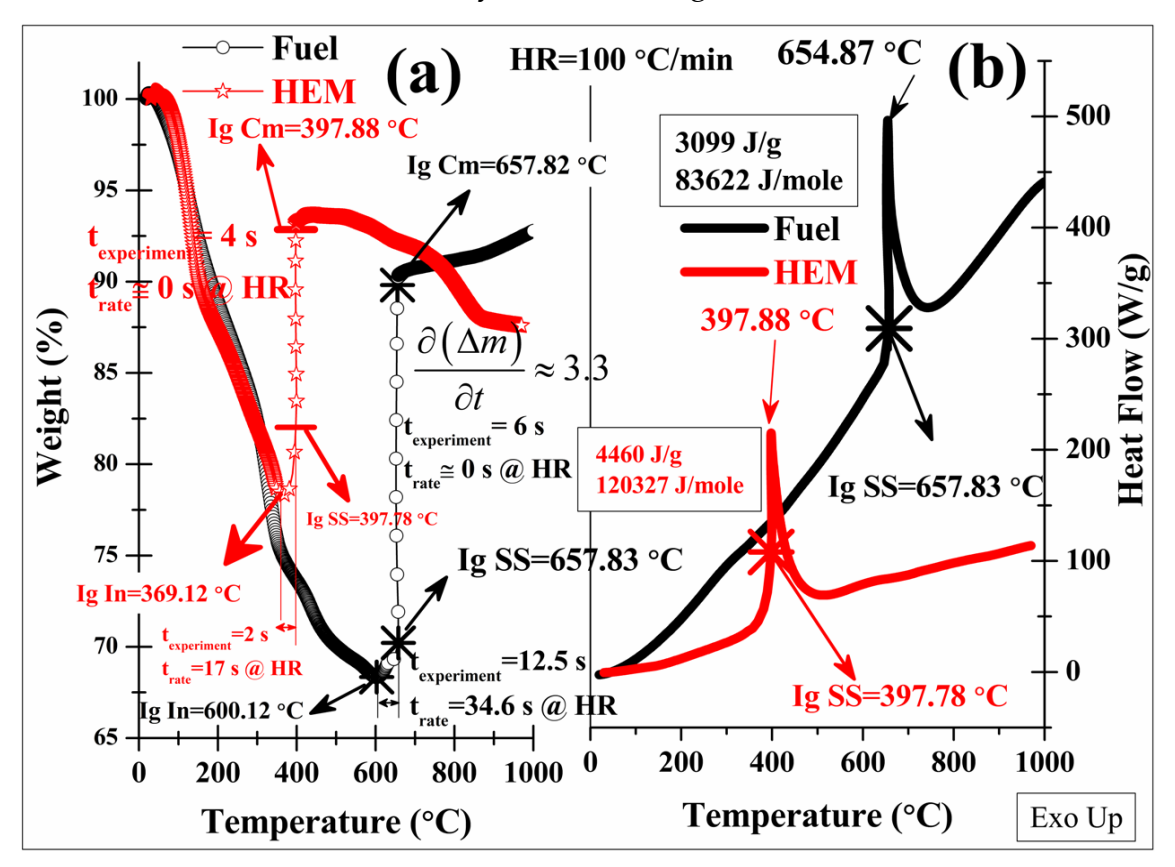


Fig.5 4 At heating rate of 100 °C/min; (a) TG, and (b) DSC of fuel and HEM respectively.

The distinction in these two HR in inducing a sharp exotherm below Al-melting transition (i.e. at 658.46 °C observed for HR=10 °C/min, bulk Al-melting at 660.32 °C) for higher HR is shown in fig. 5 7. Likewise, for HR=100 °C/min designed HEM undergoes initiation of ignition (Ig In) at 369.12 °C and completion at around 397.88 °C. Both exotherms occurs below Al melting; but in the first case, (1) the heterogeneous oxidation (solid and gas as reactants) is achieved in the TGA furnace gaseous environment, whereas in the second (2) intimately mixed condensed nc-ceria donated oxide ions facilities the same. Therefore, the oxidation in presence of nc-ceria becomes homogeneous solid-solid phase reaction. This is induced by condensed solid phase reactive oxygen ions transportation from nc-ceria oxidizer to nc-Al fuel.

The nc-ceria induced exotherm in HEM is at 397.88 °C much lower than 654.87 °C, observed for that of fuel.

Also in presence of the nc-ceria solid oxidizer HEM energy release at lower temperature is enhanced by almost about 44 %. A set HR DSC curve of HEM is shown in fig. 5 6 (b), in which the HR generated DSC peak thermal drag (i.e. increase in HR drags the DSC peaks to higher temperature) is used for HEM activation energy computation. The HEM activation energy for inducing ignition is of 170 kJ/mole. It is closer to the activation energy required for the growth of γ -Al₂O₃ phase[445], [446] . The obtained enhancement in energy outflow is believed to be the result of intimacy in contact achieved between ultrafine 2 nm nc-ceria with that of 3-15 nm Al in PVP matrix. That is a comparatively larger Al particles surfaces are observed to be decorated with many smaller nc-ceria oxidizer all around, as illustrated from the HR-TEM microstructural detailing (see fig. 5 2 (f) intimacies and density of packing of brighter spots can be seen), supporting the predicted reasoning. In this regard, a table containing ignition characteristics, energy release data obtained and that taken from literature for comparison is tabulated in Table-1.

Table 5 1 Ignition and Energy release data obtained and literature

NEMs	Ignition	Ignition	Energy	References
	Initiation (°C)	Temperature	Released	
		(°C)	(E/T)(in kJ/g)	
Al/CuO	520	540	1.8/4.1	Kim et al [447]
Al/NiFe2O4	300	Laser Ignition	2.9/6.21	Shi et al [448]
(Al/CuO)/TNT	242	225	1.2/6.21	Zaky et al [449]
Al/CeO2	369	397	4.5/6.21	Current study

Besides the tabulated (table 5 1) energy release, few literatures having more or less closest exothermic energy release in concurrence with current one are; (a) (1)

perfluorodecalin coated Al fuel release 4.65 kJ/g , (2) 4.40 kJ/g for toluene coated Al, and (3) 4.20 kJ/g for Al coated with isopropyl alcohol respectively [450], and (b) 4.95 kJ/g for dioctyl sebacate coated Al [451]. Also, the use of carbon nanomaterials (carbon nanotube, expanded graphite, graphene, graphene oxide, and fullerenes) to develop highly energetic compositions is under investigation[452]. The use of carbon nanomaterials case studies involve; (1) 'reactivity modulation' of Al/WO₃ EM [453] , (2) 5 wt % graphene oxide in Al/B₂O₃ nanocomposite enhances fuel to oxidizer contact resulting 'enhanced reactivity' [454] , (3) 5 wt % carbon black is suitable 'desensitizer' for Al/MnO₂ EM [455], (4) tuning 'gas pressure discharge' by adding carbon nanotube in EMs[456], and also (5) tailoring 'oxidation' of Al [446] respectively.

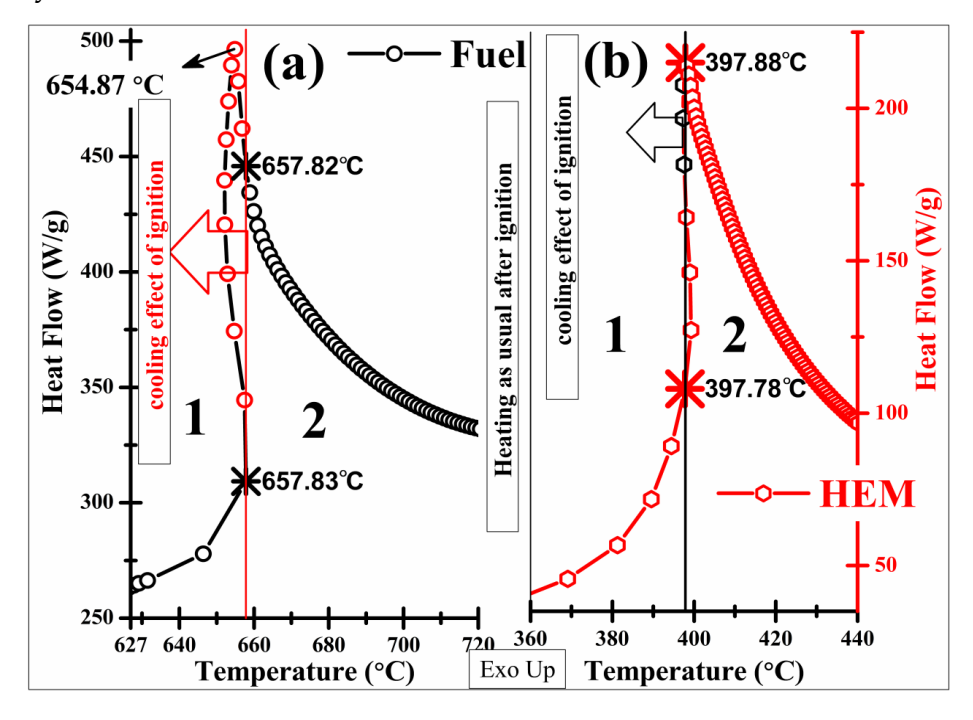


Fig.5 5 DSC data illustrating cooling after ignition initiation in both (a) fuel, and (b) HEM respectively.

Lastly, it is observed that Al exothermic enthalpy had a strong dependence on CNT content, about 188 kJ/g heat release reported at 20 wt % CNT [446]. The approximately 6-fold higher energy release than 31 kJ/g expected from Al oxidation, is of much current interest. It, thus, indicates that the designed NEM from Al-PVP

fuel and nc-ceria oxide is quite effective combination in terms of energy release and also having lower temperature of ignition. But further enhancement in energy released is quite possible based on the above literature by designing these two reactive fractions contained in graphitic carbon matrix.

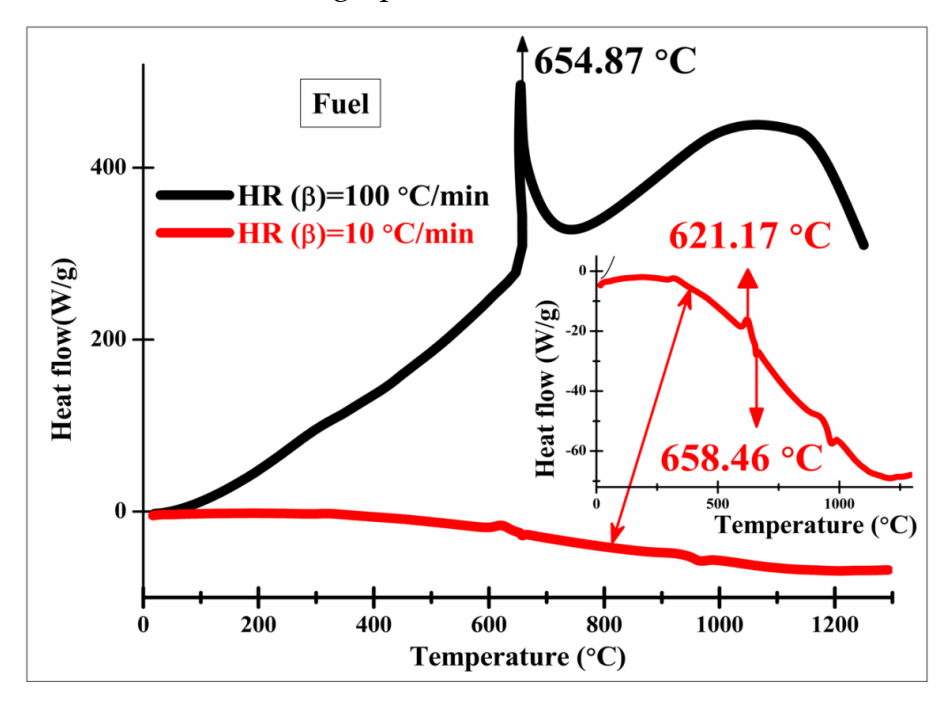


Fig.5 6 DSC data illustrating effect of the HR in igniting the fuel, inset indicates slow HR Al melting transition.

Another significance observation in ignition exotherm is the cooling after ignition, like the coined phrase "evaporation causes surface cooling". It is well known that once the ignition is got initiated the subsequent Al oxidation becomes a self-sustained process. The self-ignition linked rate of heat generation within the material must over take the rate of heat loss through the material surface[437]. That is, the volumetric heating rate achieved within the material exceeds the experimental heating rate provided to probe ignition. It causes an imbalance to provide few data points of ignition exotherm at lower temperature, than ignition initiation. These identified data points are in the region-1 of the vertical lines drawn in figs. 5 5 (a)-(b). Likewise, an attempt with higher initial fuel mass of \geq 10 mg is investigated at HR (β) =100 °C/min indicates the blowing away of the 90 μ L alumina sample pan containing it. The blowing away happens just after the fuel ignition temperature observed at

657.83 °C, which is evidenced by a sharp weight change of the TGA furnace weight balance (sensitivity=0.1 μg), implying occurrence of explosion. 10 mg is the least sample mass required (hit and trial method, and repeated for 3 times) to initiates explosion bringing almost 7 orders higher thrust representing rate of mass change. Thereby, the fuel thrust rate extracted from TG analysis is in the order of; oxidation: ignition: explosion=1:10³:10⁷ for the employed Al/PVP composite. The Al/PVP explosion recorded TG data is shown in fig. 5 7 (a). The TG of explosion is Z- step like appearance with no sign of recovery, whereas after oxidation and ignition data recording goes on until the last operating temperature reached.

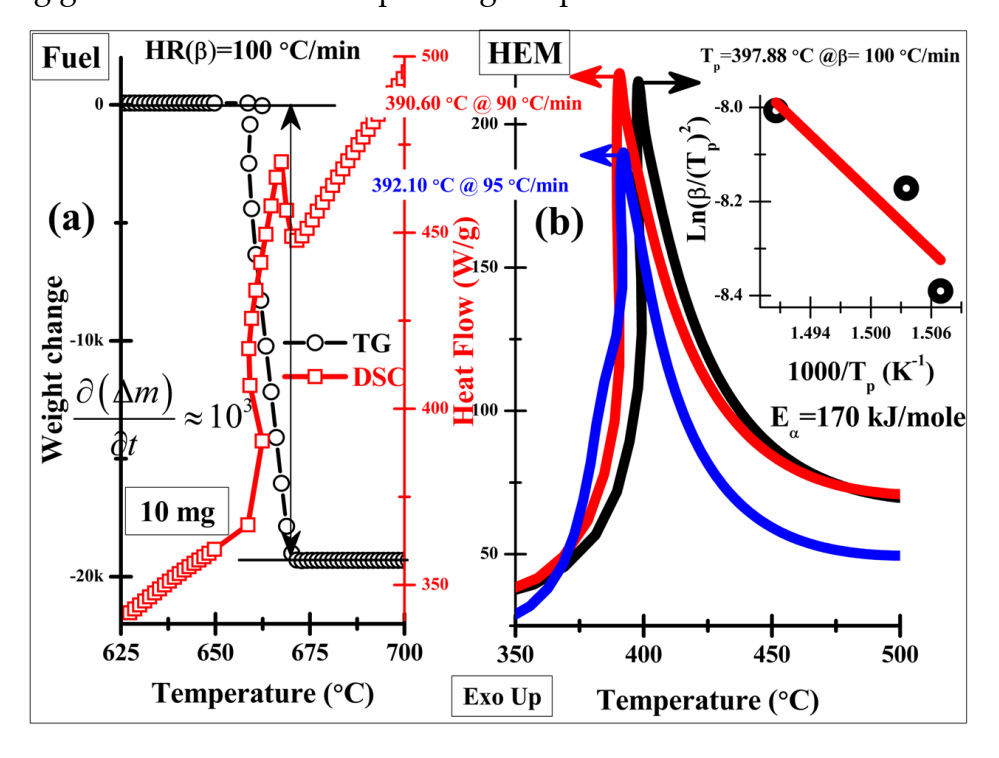


Fig.5 7 (a) TG of Al/PVP fuel representing explosion, (b) HEM DSC recorded at varying heating rates for activation energy calculation respectively.

5.4. Conclusions

The evaluation of "nc-ceria as an oxidizer" in the stoichiometric nanoenergetic composite formulation has promising implications. The fundamental regenerative adaptability of nc-ceria lattice, whether to act as a source or sink for oxygen release or

intake in regards to the neighbor, is utilized. Specifically, the nc-ceria lattice condensed phase oxygen transfer to nano-Al lattice is established. It leads to much lower ignition in the designed HEM at 397 °C than 657 °C, that of the parent Al/PVP fuel. Also, a jump of 44% in the exothermic energy of HEM is achieved. Based on the HR-TEM microstructural detailing of observed

- oxidizer fuel intimacy,
- dense packing of ultrafine 2 nm ceria (oxidizer) all along the surface of slightly larger
 3-15 nm of Al (fuel), and
- Contained in the PVP matrix appears to be the reasons for the observed behavior.

The HEM computed activation energy of ignition is 170 kJ/mole, is close to the predicted activation energy required for γ -Al₂O₃ phase growth concurrence to Al oxidation.

Chapter-VI

Thesis summary, Conclusions and Scope for the future work

6.1 Thesis Pictorial Summary

The research work carried out in this thesis started some years ago, aiming at design, development, and energetic evaluation of nano-Al fuel based nanocomposite HEM for propellant applications. A thesis pictorial summary of the research organization done with physical properties investigated and data flow for easy illustration is given below.

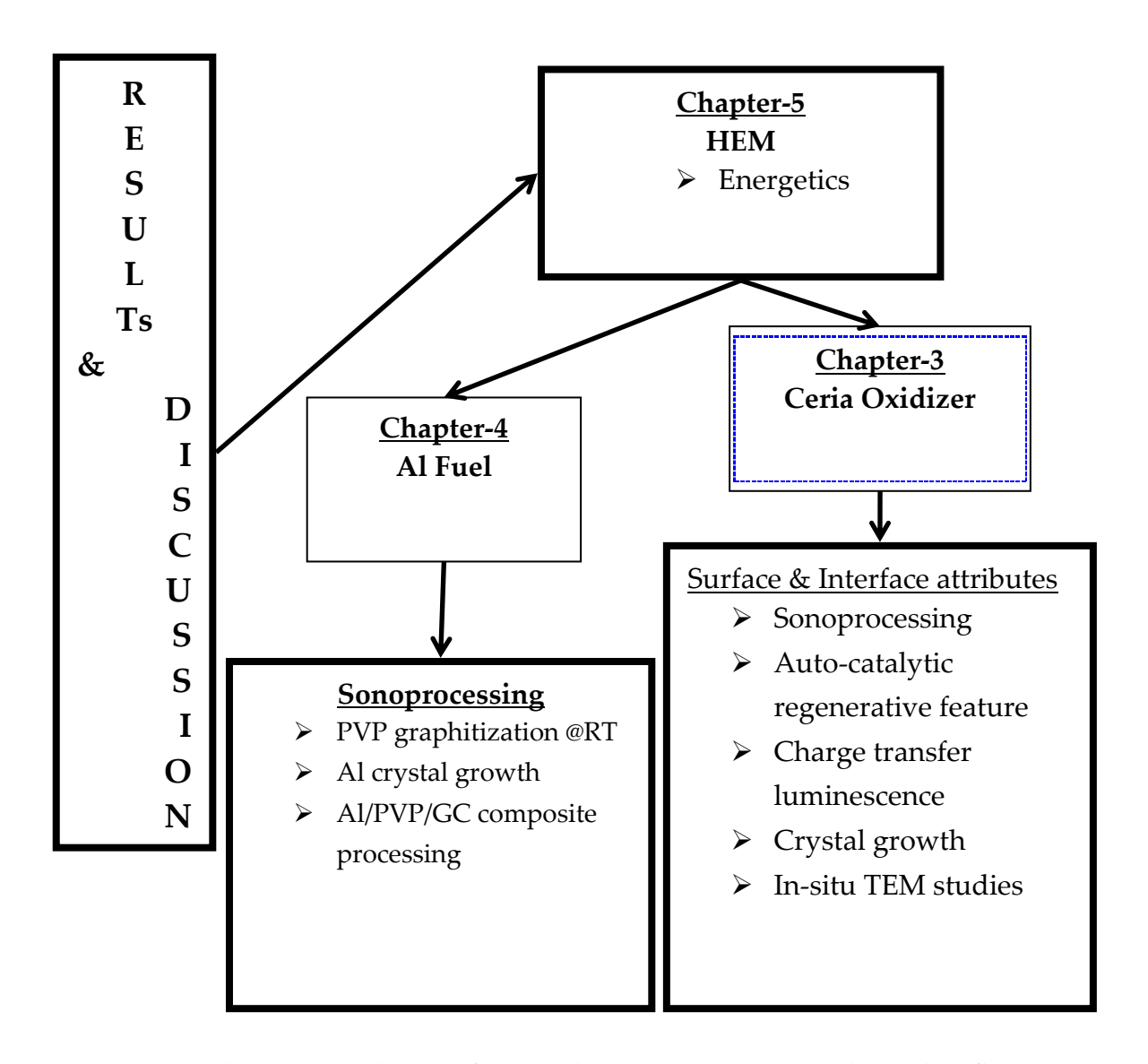


Fig.6 1 Thesis Pictorial view of physical properties investigated and data flow

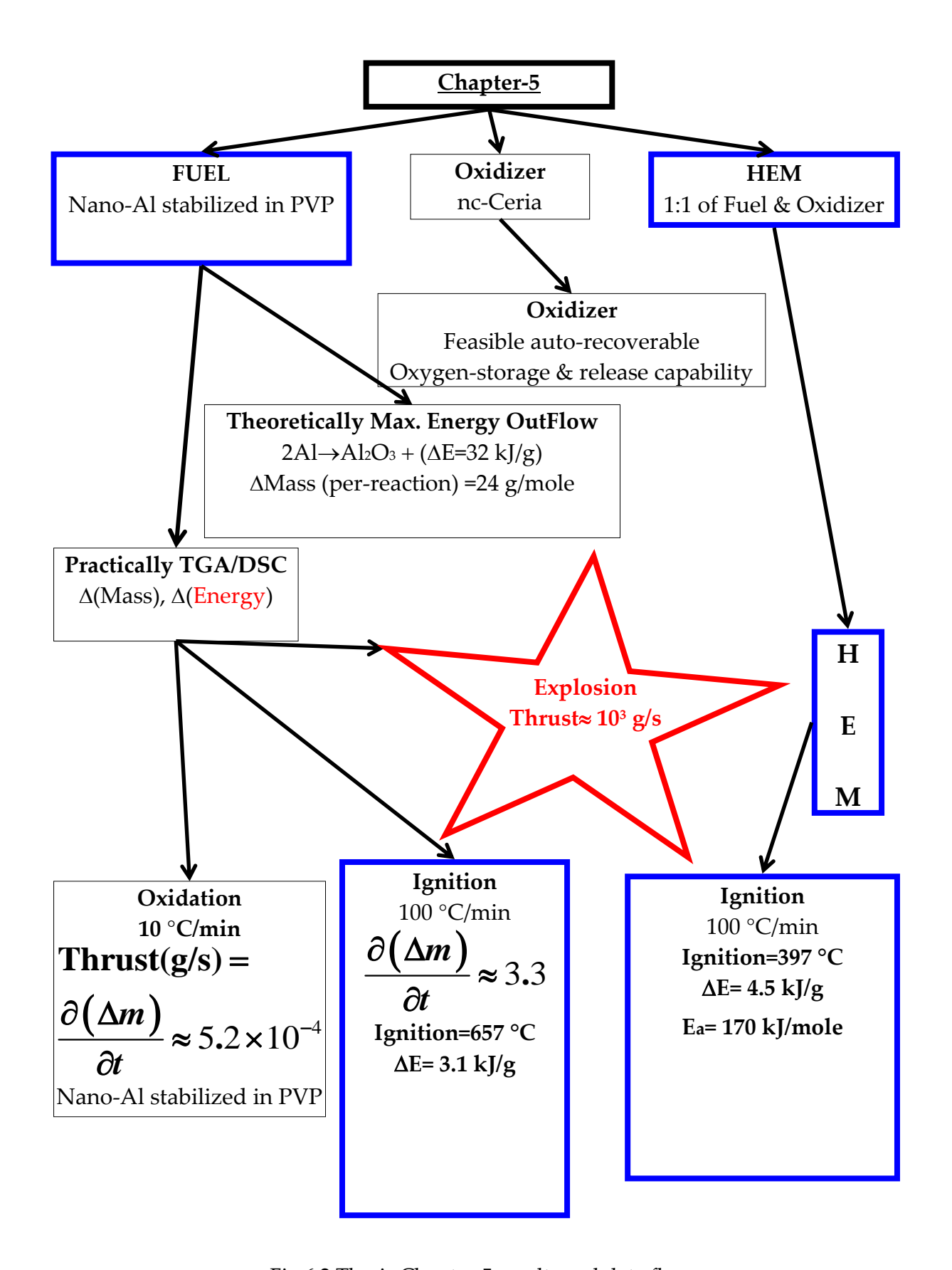


Fig. 6 2 Thesis Chapter-5 results and data flow

The conclusions of the thesis can be summarized in the following points

Presented result and discussion of individual chapters' conclusion sections is assembled below as thesis summary-

- ➤ An exothermic energy release of 44 (±2) % increment is achieved, by employing nc-ceria as solid oxidizer in the designed stoichiometric HEM.
- ➤ Designed stoichiometric HEM ignites at 397 °C at much lower than 657 °C ignition of that of the parent Al/PVP fuel. This establishes nc-ceria lattice oxygen mobility in enriching the nano-Al oxidation. Thereby a suitable candidate as oxidizer in HEM.
- Fig. The three-heating rate ignition experiment imply the nano-Al oxidation activation energy is of 170 kJ/mole. This is concurrent to that for γ-Al₂O₃ phase growth, suggesting incomplete oxidation at employed at higher heating rates.
- ➤ The observed sonocrystallization of PVP to graphitic carbon (GC) at RT indicates the process is athermal, thereby supports the dominant role of ultrasonic shock waves in causing it.
- ➤ Similarly, the RT processed composite (RTSC/PVP-Al product) only has metallic Al in its nucleating state. Thereby also in agreement with cited literatures of this chapter is that, sonocrystallization facilitates in generating Al nuclei or that of a nucleating phase of any sonoprocessed mater.
- ➤ The nano-Al crystal growth is only achieved, when the solution is allowed to self-heat during sonoprocessing. It is understood, this bulk solution heating probably causes an increase in the rate of the head-on collision of these RT generated Al nuclei to fuse. The nuclei fusion generates a crystalline building unit, which subsequently grows by further coalescence based on the duration of sonoprocessing.
- To validate Al crystals growth resulting from building units coalescence, Alrich compositions with Al (M)/ PVP (P) ratio higher than 1:1, are investigated

supports nano-Al building units sono-agglomeration. In this case, the reduced fraction of PVP surfactant offers less hindrance to agglomerate almost 10 nm Al cubes (face centered cubic unit cells) in sidewise fashion to grow upto 359 nm Al 2D-lumps devoid of an oxide phase. When exposed to TEM e-beam, the de-agglomeration of individual building units is observed.

- ➤ In the case of Al (M)/ PVP (P) fraction= 1:1, the sono-agglomeration of nano-Al building units is actively suppressed by the PVP fraction to deliver approximately 15 nm Al crystallites densely embedded into the PVP matrix. The degree of crystallinity of the Al phase as evaluated is 56 % (XRD extraction), and is slightly above the theoretical expected 50 % in line with the composite fraction considered.
- ➤ The arrangement/attachment of nano-Al crystals at the edges of the GC indicates almost all the major activates linked to the Al phase like; nucleation, coalescence, and growth mostly happen in the n-hexadecane medium. Simultaneous gradual embedding of grown nano-Al crystals into the GC layers results in intercalation, and thereby its c-axis expandability is justified.
- ➤ The crystal structural data of the expandable GC extracted indicates it is 48 % higher expanded with respect to its standard ICDD structure to accommodate 56 % nano-Al fraction as intercalated fraction.
- ➤ The generated composite is air-stable, Al-rich, no amorphous surface oxide with years of storage probably suitable entity for fuel applications.
- ➤ Finally, the conventional solution phase nano-Al synthesis (termed as protocol-1), which runs around 24 hrs processing time, is shortened to just 2 hrs of processing demonstrates sonic-assisted process intensification activity.
- ➤ Morphological hierarchy, mesocrystals as intermediate crystalline formations and the biominerals' growth pathway progression convey crucial information on crystal growth. Dominantly observed, aquatic-medium biominerals' growth process mimicking is attempted. The aquatic neighbor's participation

- in achieving biomineralization, whether an active or as an inert medium, is investigated.
- Nanoscale ceria, having demonstrated versatility in biological applications, is the prototype material of choice to regenerate aquatic environment observed calcium and silicon compound developed macrostructures by organisms.
- ➤ Nanocrystalline ceria ambient crystallization is favorable. However, at physiological pH=7.4 sparingly soluble in water. Thereby ultrasonic probe sonication is employed at RT to deliver water-soluble stable, transparent ncceria supernatant colloidal dispersion.
- ➤ The supernatant is stable for a month, and subsequent gradual settling with aging is investigated. A set of settled mass recovered sequentially for 12 months is observed to follow the NCG pathway. Spectroscopic (Raman and UV-Vis optical) analysis is carried out sequentially on settled products, demonstrates surface auto-regenerative CT attribute with aging.
- ➤ However, the instant settling achieved by adding H₂O₂ as the oxidant to the nc-ceria supernatant colloidal dispersion had no characteristic NCG pathway progression, i.e., lumpy aggregates are observed.
- The presented NCG pathway by utilizing aging at ambient is one of the parameters shown to contribute to mineral growths, whereas in an aquatic medium, several other parameters also contribute (pressure, temperature, chemical species, and aquatic-medium participation itself). Also, the nc-ceria RT crystallization aspect enabled us to bio-mimick, the presented particle-particle attachment scheme without the use of any additional thermal input. Therby a purely water directed nanocrystals surface energy minimization process.
- ➤ Also, the DI-water direct participation in delivering 1D-ceria fibers is observed.

- ➤ These ambient NCG protocol grown 1D-ceria fibers is in the hexagonal-Ce₂O₃ crystal phase, illustrating growth anisotropy associated oxygen deficiency propelled cubic to hexagonal structural phase transition. These fibers crystal facets are observed to be enclosed by highly reactive ceria planes, will be of intrest for catalysis applications.
- ➤ The dual role of the TEM e-beam as a material modification and probe tool is demonstrated. Crystal growth is a radiation-induced defect-stimulated defect healing process at RT for nc-ceria. It is brought to the realization that the near-neighbor environment around the nc-ceria, in the TEM chamber can be used effectively to control crystal growth kinetics and, therefore, its properties.

6.2 Future Research activities need to be undertaken

The current research protocol on design and development of HEM, graphitization at RT, crystal growth and energetics evaluation can be extended to many other materials. Lists of few future case studies for realization are listed below:

- Sonocrystallization investigation of other amorphous polymeric materials at RT.
- Ceria-stabilized zirconia is also a famous oxygen superionic conductor. Its nanostructured form containing Al, oxygen ion conductivity, energetics will be of future investigation.
- Away from the stoichiometric HEM, other fuels to oxidizer ratio for energy outflow and ignition temperature optimization require investigation.

Development of AI (Fuel) and nc-Ceria (Oxidizer) Nanocomposites – Sonoprocess, Crystal growth, and Energetics

by Santanu Kumar Padhi

Submission date: 10-Jun-2020 10:44AM (UTC+0530)

Submission ID: 1341131895

File name: SKPadhi_Thesis__v4.pdf (9.96M)

Word count: 34640 Character count: 191479

Development of Al (Fuel) and nc-Ceria (Oxidizer) Nanocomposites – Sonoprocess, Crystal growth, and Energetics

ORIGINALITY REPORT		•		
46% SIMILARITY INDEX	45% INTERNET SOURCES	3% PUBLICATIONS	2% STUDENT	PAPERS
PRIMARY SOURCES		M-Manas	lmam =	
export.a Internet Source	Students	Prof. M. GHANASH Centre for Advance	YAM KRISHNA ed Studies in a & Technology ersity of Hyderabad	43
diva-por				1
Next? Ti Electron	vid C., and Natas ne Future Directi Microscopy", Lo opy Principles an	ons in Low Volt w Voltage Elec	tage tron	<19
Sullivan, "Nanoth generati	oqiang, Snehaur, and Michael R. ermite reactions: on from the oxygsite to ignition?", 2013.	Zachariah. Is gas phase c en carrier an e	oxygen ssential	<19
Diffracto	ission Electron Meteria	ls", Springer Sc		<1



Dr. M. GHANASHYAM KRISHNA Professor, CASEST, School of Physics University of Hyderabad Hyderabad-500 046 INDIA

> Ph: (+)91-40-23134382 FAX: (+)91-40-23010227 Email: mgksp@uohyd.ac.in mgksp@uohyd.ernet.in

> > 10th June, 2020

To The Librarian IGML, University of Hyderabad

Dear Sir,

This is to certify that I carried out the plagiarism check on thesis of my student Mr. Santanu Kumar Padhi (10ACPP10) titled "Development of Al (Fuel) and nc-Ceria (Oxidizer) Nanocomposites – Sonoprocess, Crystal growth, and Energetics" using Turnitin. It is further certified that the first source indicated in the record as "export.arxiv.org" showing 43% similarity is a publication (https://arxiv.org/abs/1911.07454) of the student uploaded on 18/11/2019 on the website https://arxiv.org/maintained by Cornell University to upload preprints in different areas of Physics.

Hence, the effective similarity index excluding this source is 46-43% = 3% which is lower than the 10% stipulated by University guidelines.

In view of this, it is requested that the student may kindly be permitted to submit his thesis.

Yours Sincerely

Prof. M. GHANASHYAM KRISHNA
Centre for Advanced Studies in
Electronics Science & Technology
School of Physics, University of Hyderabad
HYDERABAD-500 046, Telangana, India.

M. Translyam

References

- [1] D. P. Woodruff, "How does your crystal grow? A commentary on Burton, Cabrera and Frank (1951) 'The growth of crystals and the equilibrium structure of their surfaces," *Philos Trans A Math Phys Eng Sci*, vol. 373, no. 2039, Apr. 2015, doi: 10.1098/rsta.2014.0230.
- [2] H. F. Greer, "Non-classical crystal growth of inorganic and organic materials," *Materials Science and Technology*, vol. 30, no. 6, pp. 611–626, May 2014, doi: 10.1179/1743284713Y.0000000433.
- [3] J. Wang, G. Lian, H. Si, Q. Wang, D. Cui, and C.-P. Wong, "Pressure-Induced Oriented Attachment Growth of Large-Size Crystals for Constructing 3D Ordered Superstructures," *ACS Nano*, vol. 10, no. 1, pp. 405–412, Jan. 2016, doi: 10.1021/acsnano.5b05108.
- [4] Z. Zhuang, X. Xue, and Z. Lin, "Self-assembly of SnO2 quantum dots into hierarchically ordered structures assisted by oriented attachment," *Phys. Chem. Chem. Phys.*, vol. 17, no. 7, pp. 4845–4848, Feb. 2015, doi: 10.1039/C4CP05057F.
- [5] I. V. Kolesnik, D. A. Kozlov, A. S. Poluboyarinov, A. V. Garshev, and V. K. Ivanov, "Non-classical growth of brookite nanorods," *CrystEngComm*, vol. 21, no. 37, pp. 5673–5681, Sep. 2019, doi: 10.1039/C9CE00682F.
- [6] H. F. Greer, "Non-classical crystal growth of inorganic and organic materials," *Mater. Sci. Technol.*, vol. 30, no. 6, pp. 611–626, Jun. 2014, doi: 10.1179/1743284713Y.0000000433.
- [7] V. K. Ivanov, P. P. Fedorov, A. Y. Baranchikov, and V. V. Osiko, "Oriented attachment of particles: 100 years of investigations of non-classical crystal growth," *Russ. Chem. Rev.*, vol. 83, no. 12, pp. 1204–1222, Dec. 2014, doi: 10.1070/RCR4453.
- [8] C. Lu and Z. Tang, "Advanced Inorganic Nanoarchitectures from Oriented Self-Assembly," *Advanced Materials*, vol. 28, no. 6, pp. 1096–1108, 2016, doi: 10.1002/adma.201502869.

- [9] K. Wen and W. He, "Can oriented-attachment be an efficient growth mechanism for the synthesis of 1D nanocrystals via atomic layer deposition?," *Nanotechnology*, vol. 26, no. 38, p. 382001, Sep. 2015, doi: 10.1088/0957-4484/26/38/382001.
- [10] K.-S. Cho, D. V. Talapin, W. Gaschler, and C. B. Murray, "Designing PbSe Nanowires and Nanorings through Oriented Attachment of Nanoparticles," *J. Am. Chem. Soc.*, vol. 127, no. 19, pp. 7140–7147, May 2005, doi: 10.1021/ja050107s.
- [11] Y. Cheng *et al.*, "Near surface nucleation and particle mediated growth of colloidal Au nanocrystals," *Nanoscale*, vol. 10, no. 25, pp. 11907–11912, Jul. 2018, doi: 10.1039/C8NR03408G.
- [12] J. J. D. Yoreo *et al.*, "Crystallization by particle attachment in synthetic, biogenic, and geologic environments," *Science*, vol. 349, no. 6247, p. aaa6760, Jul. 2015, doi: 10.1126/science.aaa6760.
- [13] X. Zhang *et al.*, "Direction-specific interaction forces underlying zinc oxide crystal growth by oriented attachment," *Nat Commun*, vol. 8, no. 1, pp. 1–8, Oct. 2017, doi: 10.1038/s41467-017-00844-6.
- [14] Y. Yuan *et al.*, "Atomistic Insights into the Oriented Attachment of Tunnel-Based Oxide Nanostructures," *ACS Nano*, vol. 10, no. 1, pp. 539–548, Jan. 2016, doi: 10.1021/acsnano.5b05535.
- [15] R. Zhao, M. Li, Z. Ren, Y. Zhu, and G. Han, "Three-dimensional oriented attachment growth of single-crystal pre-perovskite PbTiO3 hollowed fibers," *CrystEngComm*, vol. 20, no. 4, pp. 448–453, Jan. 2018, doi: 10.1039/C7CE01780D.
- [16] B. Tangeysh, K. Moore Tibbetts, J. H. Odhner, B. B. Wayland, and R. J. Levis, "Triangular Gold Nanoplate Growth by Oriented Attachment of Au Seeds Generated by Strong Field Laser Reduction," *Nano Lett.*, vol. 15, no. 5, pp. 3377–3382, May 2015, doi: 10.1021/acs.nanolett.5b00709.
- [17] V. Jordan, U. Javornik, J. Plavec, A. Podgornik, and A. Recnik, "Self-assembly of multilevel branched rutile-type TiO2 structures via oriented lateral and twin attachment," *Sci Rep*, vol. 6, p. 24216, Apr. 2016, doi: 10.1038/srep24216.
- [18] X. Liang *et al.*, "Self-assembly of birnessite nanoflowers by staged three-dimensional oriented attachment," *Environ. Sci.: Nano*, vol. 4, no. 8, pp. 1656–1669, Aug. 2017, doi: 10.1039/C6EN00619A.

- [19] S. Weiner and P. M. Dove, "1 An Overview of Biomineralization Processes and the Problem of the Vital Effect," *REV MINERAL GEOCHEM*, vol. 54, no. 1, pp. 1–29, Jan. 2003, doi: 10.2113/0540001.
- [20] E.-I. Ochiai, "Biomineralization: Principles and applications in bioinorganic chemistry-V," *J. Chem. Educ.*, vol. 68, no. 8, p. 627, Aug. 1991, doi: 10.1021/ed068p627.
- [21] C. F. Böhm, J. Harris, P. I. Schodder, and S. E. Wolf, "Bioinspired Materials: From Living Systems to New Concepts in Materials Chemistry," *Materials*, vol. 12, no. 13, p. 2117, Jan. 2019, doi: 10.3390/ma12132117.
- [22] E. García-Romero and M. Suárez, "A structure-based argument for non-classical crystal growth in natural clay minerals," *Mineralogical Magazine*, vol. 82, no. 1, pp. 171–180, Feb. 2018, doi: 10.1180/minmag.2017.081.031.
- [23] E. Zolotoyabko and B. Pokroy, "Biomineralization of calcium carbonate: structural aspects," *CrystEngComm*, vol. 9, no. 12, pp. 1156–1161, Nov. 2007, doi: 10.1039/B708704G.
- [24] A. Schulz, H. Wang, P. van Rijn, and A. Böker, "Synthetic inorganic materials by mimicking biomineralization processes using native and non-native protein functions," J. Mater. Chem., vol. 21, no. 47, pp. 18903–18918, Nov. 2011, doi: 10.1039/C1JM12490K.
- [25] M. Sumper, "Biomimetic Patterning of Silica by Long-Chain Polyamines," *Angewandte Chemie International Edition*, vol. 43, no. 17, pp. 2251–2254, 2004, doi: 10.1002/anie.200453804.
- [26] J. R. Dorvee and A. Veis, "Water in the formation of biogenic minerals: Peeling away the hydration layers," *Journal of Structural Biology*, vol. 183, no. 2, pp. 278–303, Aug. 2013, doi: 10.1016/j.jsb.2013.06.007.
- [27] U. Anand, J. Lu, D. Loh, Z. Aabdin, and U. Mirsaidov, "Hydration Layer-Mediated Pairwise Interaction of Nanoparticles," *Nano Lett.*, vol. 16, no. 1, pp. 786–790, Jan. 2016, doi: 10.1021/acs.nanolett.5b04808.
- [28] Y. Wang *et al.*, "Water-mediated structuring of bone apatite," *Nature Mater*, vol. 12, no. 12, pp. 1144–1153, Dec. 2013, doi: 10.1038/nmat3787.
- [29] M. Duer and A. Veis, "Bone mineralization: Water brings order," Nat Mater, vol. 12, no. 12, pp. 1081–1082, Dec. 2013, doi: 10.1038/nmat3822.

- [30] H. Imada, K. Kimura, and H. Onishi, "Water and 2-Propanol Structured on Calcite (104) Probed by Frequency-Modulation Atomic Force Microscopy," *Langmuir*, vol. 29, no. 34, pp. 10744–10751, Aug. 2013, doi: 10.1021/la402090w.
- [31] H. Cölfen and M. Antonietti, "Mesocrystals: Inorganic Superstructures Made by Highly Parallel Crystallization and Controlled Alignment," *Angewandte Chemie International Edition*, vol. 44, no. 35, pp. 5576–5591, 2005, doi: 10.1002/anie.200500496.
- [32] X. Fei, W. Li, Z. Shao, S. Seeger, D. Zhao, and X. Chen, "Protein Biomineralized Nanoporous Inorganic Mesocrystals with Tunable Hierarchical Nanostructures," *J. Am. Chem. Soc.*, vol. 136, no. 44, pp. 15781–15786, Nov. 2014, doi: 10.1021/ja509334x.
- [33] Y.-Y. Kim *et al.*, "A critical analysis of calcium carbonate mesocrystals," *Nat Commun*, vol. 5, no. 1, pp. 1–14, Jul. 2014, doi: 10.1038/ncomms5341.
- [34] E. V. S. (née Rosseeva) and H. Cölfen, "Mesocrystals: structural and morphogenetic aspects," *Chemical Society Reviews*, vol. 45, no. 21, pp. 5821–5833, 2016, doi: 10.1039/C6CS00208K.
- [35] R. L. Penn and J. F. Banfield, "Imperfect Oriented Attachment: Dislocation Generation in Defect-Free Nanocrystals," *Science*, vol. 281, no. 5379, pp. 969–971, Aug. 1998, doi: 10.1126/science.281.5379.969.
- [36] Z. Huang *et al.*, "A welding phenomenon of dissimilar nanoparticles in dispersion," *Nat Commun*, vol. 10, no. 1, pp. 1–8, Jan. 2019, doi: 10.1038/s41467-018-08206-6.
- [37] M. J. Crane, E. P. Pandres, E. J. Davis, V. C. Holmberg, and P. J. Pauzauskie, "Optically oriented attachment of nanoscale metal-semiconductor heterostructures in organic solvents via photonic nanosoldering," *Nat Commun*, vol. 10, no. 1, pp. 1–7, Oct. 2019, doi: 10.1038/s41467-019-12827-w.
- [38] Z. Zhang *et al.*, "Rapid synthesis of quantum-confined CsPbBr3 perovskite nanowires using a microfluidic reactor," *Nanoscale*, vol. 11, no. 40, pp. 18790–18796, Oct. 2019, doi: 10.1039/C9NR06726D.
- [39] A. R. C. McCray, B. H. Savitzky, K. Whitham, T. Hanrath, and L. F. Kourkoutis, "Orientational Disorder in Epitaxially Connected Quantum Dot Solids," *ACS Nano*, vol. 13, no. 10, pp. 11460–11468, Oct. 2019, doi: 10.1021/acsnano.9b04951.

- [40] S. H. Moon and S. H. Im, "Multi-amine-assisted crystal growth of large-sized α-MoO3 elongated nano-plates," *Nanoscale*, vol. 11, no. 39, pp. 18037–18045, Oct. 2019, doi: 10.1039/C9NR06944E.
- [41] Y. Liu *et al.*, "Oriented Attachment Revisited: Does a Chemical Reaction Occur?," *Matter*, vol. 1, no. 3, pp. 690–704, Sep. 2019, doi: 10.1016/j.matt.2019.05.001.
- [42] Y. Kubota, T. Kishi, T. Yano, and N. Matsushita, "Anisotropic growth of gas–liquid precipitated ceria mesocrystals to wires several micrometers in length," *RSC Adv.*, vol. 8, no. 43, pp. 24370–24375, Jul. 2018, doi: 10.1039/C8RA05362F.
- [43] X. Lu, X. Li, F. Chen, C. Ni, and Z. Chen, "Hydrothermal synthesis of prism-like mesocrystal CeO2," *Journal of Alloys and Compounds*, vol. 476, no. 1–2, pp. 958–962, May 2009, doi: 10.1016/j.jallcom.2008.09.198.
- [44] T. Taniguchi, K. Katsumata, S. Omata, K. Okada, and N. Matsushita, "Tuning Growth Modes of Ceria-Based Nanocubes by a Hydrothermal Method," *Crystal Growth & Design*, vol. 11, no. 9, pp. 3754–3760, Sep. 2011, doi: 10.1021/cg101585b.
- [45] D. A. Welch, T. J. Woehl, C. Park, R. Faller, J. E. Evans, and N. D. Browning, "Understanding the Role of Solvation Forces on the Preferential Attachment of Nanoparticles in Liquid," ACS Nano, vol. 10, no. 1, pp. 181–187, Jan. 2016, doi: 10.1021/acsnano.5b06632.
- [46] W. Wei *et al.*, "Observing the Growth of Pb3O4 Nanocrystals by in Situ Liquid Cell Transmission Electron Microscopy," *ACS Appl. Mater. Interfaces*, vol. 11, no. 27, pp. 24478–24484, Jul. 2019, doi: 10.1021/acsami.9b08524.
- [47] C. Zhu *et al.*, "In-situ liquid cell transmission electron microscopy investigation on oriented attachment of gold nanoparticles," *Nature Communications*, vol. 9, no. 1, p. 421, Jan. 2018, doi: 10.1038/s41467-018-02925-6.
- [48] T. Ngo and H. Yang, "Toward Ending the Guessing Game: Study of the Formation of Nanostructures Using In Situ Liquid Transmission Electron Microscopy," *J. Phys. Chem. Lett.*, vol. 6, no. 24, pp. 5051–5061, Dec. 2015, doi: 10.1021/acs.jpclett.5b02210.
- [49] W. Wei *et al.*, "Observing the Growth of Pb3O4 Nanocrystals by in Situ Liquid Cell Transmission Electron Microscopy," *ACS Appl. Mater. Interfaces*, vol. 11, no. 27, pp. 24478–24484, Jul. 2019, doi: 10.1021/acsami.9b08524.

- [50] E. Longo, W. Avansi, J. Bettini, J. Andrés, and L. Gracia, "In situ Transmission Electron Microscopy observation of Ag nanocrystal evolution by surfactant free electron-driven synthesis," *Sci Rep*, vol. 6, no. 1, p. 21498, Aug. 2016, doi: 10.1038/srep21498.
- [51] T. J. Woehl, J. E. Evans, I. Arslan, W. D. Ristenpart, and N. D. Browning, "Direct in Situ Determination of the Mechanisms Controlling Nanoparticle Nucleation and Growth," ACS Nano, vol. 6, no. 10, pp. 8599–8610, Oct. 2012, doi: 10.1021/nn303371y.
- [52] M. S. A. Asghar, B. J. Inkson, and G. Möbus, "In situ formation of 1D nanostructures from ceria nanoparticle dispersions by liquid cell TEM irradiation," *J Mater Sci*, pp. 1–11, Oct. 2019, doi: 10.1007/s10853-019-04140-0.
- [53] S. K. Padhi, S. N. Gottapu, and M. G. Krishna, "Electron-beam irradiation induced transformation of Cu2(OH)3NO3 nanoflakes into nanocrystalline CuO," *Nanoscale*, vol. 8, no. 21, pp. 11194–11201, May 2016, doi: 10.1039/C6NR02572B.
- [54] F. Chemat, null Zill-e-Huma, and M. K. Khan, "Applications of ultrasound in food technology: Processing, preservation and extraction," *Ultrason Sonochem*, vol. 18, no. 4, pp. 813–835, Jul. 2011, doi: 10.1016/j.ultsonch.2010.11.023.
- [55] M. Gallo, L. Ferrara, and D. Naviglio, "Application of Ultrasound in Food Science and Technology: A Perspective," Foods, vol. 7, no. 10, Oct. 2018, doi: 10.3390/foods7100164.
- [56] A. D. Alarcon-Rojo, L. M. Carrillo-Lopez, R. Reyes-Villagrana, M. Huerta-Jiménez, and I.
 A. Garcia-Galicia, "Ultrasound and meat quality: A review," *Ultrason Sonochem*, vol. 55, pp. 369–382, Jul. 2019, doi: 10.1016/j.ultsonch.2018.09.016.
- [57] K. S. Ojha, B. K. Tiwari, and C. P. O'Donnell, "Effect of Ultrasound Technology on Food and Nutritional Quality," *Adv. Food Nutr. Res.*, vol. 84, pp. 207–240, 2018, doi: 10.1016/bs.afnr.2018.01.001.
- [58] Ó. Rodríguez, V. Eim, C. Rosselló, A. Femenia, J. A. Cárcel, and S. Simal, "Application of power ultrasound on the convective drying of fruits and vegetables: effects on quality," J. Sci. Food Agric., vol. 98, no. 5, pp. 1660–1673, Mar. 2018, doi: 10.1002/jsfa.8673.
- [59] V. Sivakumar, J. L. Anna, J. Vijayeeswarri, and G. Swaminathan, "Ultrasound assisted enhancement in natural dye extraction from beetroot for industrial applications and

- natural dyeing of leather," *Ultrason Sonochem*, vol. 16, no. 6, pp. 782–789, Aug. 2009, doi: 10.1016/j.ultsonch.2009.03.009.
- [60] M. Virot, V. Tomao, C. Le Bourvellec, C. M. C. G. Renard, and F. Chemat, "Towards the industrial production of antioxidants from food processing by-products with ultrasound-assisted extraction," *Ultrasonics Sonochemistry*, vol. 17, no. 6, pp. 1066–1074, Aug. 2010, doi: 10.1016/j.ultsonch.2009.10.015.
- [61] R. A. Al-Juboori and L. Bowtell, "Ultrasound Technology Integration into Drinking Water Treatment Train," *Sonochemical Reactions*, Aug. 2019, doi: 10.5772/intechopen.88124.
- [62] A. Bakhtiari, T. Berberashvili, and P. Kervalishvili, "Water Treatment Improvement by Ultrasonic Approach," *American Journal of Condensed Matter Physics*, vol. 7, no. 4, pp. 81–86, 2017.
- [63] M. R. Doosti, R. Kargar, and M. H. Sayadi, "Water treatment using ultrasonic assistance: A review," p. 15, 2012.
- [64] V. V. Goncharuk, V. V. Malyarenko, and V. A. Yaremenko, "Use of ultrasound in water treatment," J. Water Chem. Technol., vol. 30, no. 3, pp. 137–150, Jun. 2008, doi: 10.3103/S1063455X08030028.
- [65] I. Holmes, "Sound cleans up water purification," *Nature*, May 2002, doi: 10.1038/news020413-4.
- [66] C. Pétrier, "31 The use of power ultrasound for water treatment," in *Power Ultrasonics*, J. A. Gallego-Juárez and K. F. Graff, Eds. Oxford: Woodhead Publishing, 2015, pp. 939–972.
- [67] A. Carovac, F. Smajlovic, and D. Junuzovic, "Application of Ultrasound in Medicine," Acta Inform Med, vol. 19, no. 3, pp. 168–171, Sep. 2011, doi: 10.5455/aim.2011.19.168-171.
- [68] X. Jiang and A. M. Al-Jumaily, "Ultrasound Transducers for Biomedical Imaging and Therapy," *ASME J of Medical Diagnostics*, vol. 1, no. 4, Nov. 2018, doi: 10.1115/1.4041422.
- [69] A. M. Buerger and K. R. Clark, "Point-of-Care Ultrasound: A Trend in Health Care," *Radiol Technol*, vol. 89, no. 2, pp. 127–138, Nov. 2017.

- [70] A. Dalmoro, A. A. Barba, G. Lamberti, and M. d'Amore, "Intensifying the microencapsulation process: Ultrasonic atomization as an innovative approach," *European Journal of Pharmaceutics and Biopharmaceutics*, vol. 80, no. 3, pp. 471–477, Apr. 2012, doi: 10.1016/j.ejpb.2012.01.006.
- [71] U. N. Hatkar and P. R. Gogate, "Process intensification of anti-solvent crystallization of salicylic acid using ultrasonic irradiations," *Chemical Engineering and Processing: Process Intensification*, vol. 57–58, pp. 16–24, Jul. 2012, doi: 10.1016/j.cep.2012.04.005.
- [72] B. Naveena, P. Armshaw, and J. Tony Pembroke, "Ultrasonic intensification as a tool for enhanced microbial biofuel yields," *Biotechnology for Biofuels*, vol. 8, no. 1, p. 140, Sep. 2015, doi: 10.1186/s13068-015-0321-0.
- [73] S. R. Shirsath, S. H. Sonawane, and P. R. Gogate, "Intensification of extraction of natural products using ultrasonic irradiations—A review of current status," *Chemical Engineering and Processing: Process Intensification*, vol. 53, pp. 10–23, Mar. 2012, doi: 10.1016/j.cep.2012.01.003.
- [74] A. I. Stankiewicz and J. A. Moulijn, "Process Intensification: Transforming Chemical Engineering," p. 13.
- [75] D. F. Rivas, E. Castro-Hernández, A. L. Villanueva Perales, and W. van der Meer, "Evaluation method for process intensification alternatives," *Chemical Engineering and Processing Process Intensification*, vol. 123, pp. 221–232, Jan. 2018, doi: 10.1016/j.cep.2017.08.013.
- [76] C. Einhorn, J. Einhorn, and J.-L. Luche, "Sonochemistry The Use of Ultrasonic Waves in Synthetic Organic Chemistry," *Synthesis*, vol. 1989, no. 11, pp. 787–813, 1989, doi: 10.1055/s-1989-27398.
- [77] B. H. Han and P. Boudjouk, "Organic sonochemistry. Sonic acceleration of the Reformatsky reaction," *J. Org. Chem.*, vol. 47, no. 25, pp. 5030–5032, Dec. 1982, doi: 10.1021/jo00146a044.
- [78] J. Lindley, T. J. Mason, and J. P. Lorimer, "Sonochemically enhanced Ullmann reactions," *Ultrasonics*, vol. 25, no. 1, pp. 45–48, Jan. 1987, doi: 10.1016/0041-624X(87)90011-4.

- [79] J. C. De Souza-Barboza, C. Petrier, and J. L. Luche, "Ultrasound in organic synthesis. 13. Some fundamental aspects of the sonochemical Barbier reaction," *J. Org. Chem.*, vol. 53, no. 6, pp. 1212–1218, Mar. 1988, doi: 10.1021/jo00241a017.
- [80] A. Fürstner, *Active Metals: Preparation, Characterization, Applications*. John Wiley & Sons, 2008.
- [81] J.-L. Luche and P. Cintas, "Ultrasound-Induced Activation of Metals: Principles and Applications in Organic Synthesis," in *Active Metals*, A. Frstner, Ed. Weinheim, Germany: Wiley-VCH Verlag GmbH, 1995, pp. 133–190.
- [82] A. Fürstner, "Chemistry of and with Highly Reactive Metals," *Angew. Chem. Int. Ed. Engl.*, vol. 32, no. 2, pp. 164–189, Feb. 1993, doi: 10.1002/anie.199301641.
- [83] K. S. Suslick and R. E. Johnson, "Sonochemical activation of transition metals," *J. Am. Chem. Soc.*, vol. 106, no. 22, pp. 6856–6858, Oct. 1984, doi: 10.1021/ja00334a073.
- [84] R. D. Rieke, "Preparation of highly reactive metal powders and their use in organic and organometallic synthesis," *Acc. Chem. Res.*, vol. 10, no. 8, pp. 301–306, Aug. 1977, doi: 10.1021/ar50116a005.
- [85] J. H. Bang and K. S. Suslick, "Applications of Ultrasound to the Synthesis of Nanostructured Materials," Advanced Materials, vol. 22, no. 10, pp. 1039–1059, 2010, doi: 10.1002/adma.200904093.
- [86] P. W. Cains, P. D. Martin, and C. J. Price, "The Use of Ultrasound in Industrial Chemical Synthesis and Crystallization. 1. Applications to Synthetic Chemistry," *Org. Process Res. Dev.*, vol. 2, no. 1, pp. 34–48, Jan. 1998, doi: 10.1021/op9700340.
- [87] G. Ruecroft, D. Hipkiss, T. Ly, N. Maxted, and P. W. Cains, "Sonocrystallization: The Use of Ultrasound for Improved Industrial Crystallization," *Org. Process Res. Dev.*, vol. 9, no. 6, pp. 923–932, Nov. 2005, doi: 10.1021/op050109x.
- [88] J. Jordens *et al.*, "Sonocrystallisation: Observations, theories and guidelines," *Chemical Engineering and Processing Process Intensification*, vol. 139, pp. 130–154, May 2019, doi: 10.1016/j.cep.2019.03.017.
- [89] W. T. Richards and A. L. Loomis, "THE CHEMICAL EFFECTS OF HIGH FREQUENCY SOUND WAVES I. A PRELIMINARY SURVEY," *J. Am. Chem. Soc.*, vol. 49, no. 12, pp. 3086–3100, Dec. 1927, doi: 10.1021/ja01411a015.

- [90] B. W. Zeiger and K. S. Suslick, "Sonofragmentation of Molecular Crystals," *J. Am. Chem. Soc.*, vol. 133, no. 37, pp. 14530–14533, Sep. 2011, doi: 10.1021/ja205867f.
- [91] J. R. G. Sander, B. W. Zeiger, and K. S. Suslick, "Sonocrystallization and sonofragmentation," *Ultrasonics Sonochemistry*, vol. 21, no. 6, pp. 1908–1915, Nov. 2014, doi: 10.1016/j.ultsonch.2014.02.005.
- [92] H. N. Kim and K. S. Suslick, "Sonofragmentation of Ionic Crystals," *Chem. Eur. J.*, vol. 23, no. 12, pp. 2778–2782, Feb. 2017, doi: 10.1002/chem.201605857.
- [93] S. Nalesso, M. J. Bussemaker, R. P. Sear, M. Hodnett, and J. Lee, "A review on possible mechanisms of sonocrystallisation in solution," *Ultrasonics Sonochemistry*, vol. 57, pp. 125–138, Oct. 2019, doi: 10.1016/j.ultsonch.2019.04.020.
- [94] V. S. Nalajala and V. S. Moholkar, "Investigations in the physical mechanism of sonocrystallization," *Ultrason Sonochem*, vol. 18, no. 1, pp. 345–355, Jan. 2011, doi: 10.1016/j.ultsonch.2010.06.016.
- [95] Z. Zheng et al., "Unusual Sonochemical Assembly between Carbon Allotropes for High Strain-Tolerant Conductive Nanocomposites," ACS Nano, vol. 13, no. 10, pp. 12062– 12069, Oct. 2019, doi: 10.1021/acsnano.9b06366.
- [96] D. Zhou et al., "Sono-Assisted Surface Energy Driven Assembly of 2D Materials on Flexible Polymer Substrates: A Green Assembly Method Using Water," ACS Appl. Mater. Interfaces, vol. 11, no. 36, pp. 33458–33464, Sep. 2019, doi: 10.1021/acsami.9b10469.
- [97] N. B. Sumina *et al.*, "Low Temperature Synthesis of High Energy Facets Exposed Sheet–like Anatase TiO2 Mesocrystals Show Reduced e–/h+ Pair Recombination Rates and Enhanced Photoactivity," *ChemistrySelect*, vol. 1, no. 19, pp. 6221–6229, 2016, doi: 10.1002/slct.201601412.
- [98] C. Tang, L. Liu, Y. Li, and Z. Bian, "Aerosol spray assisted assembly of TiO2 mesocrystals into hierarchical hollow microspheres with enhanced photocatalytic performance," *Applied Catalysis B: Environmental*, vol. 201, pp. 41–47, Feb. 2017, doi: 10.1016/j.apcatb.2016.08.006.
- [99] F. Dang, K. Kato, H. Imai, S. Wada, H. Haneda, and M. Kuwabara, "Growth of BaTiO3 nanoparticles in ethanol-water mixture solvent under an ultrasound-assisted

- synthesis," *CHEM ENG J (LAUSANNE)*, vol. 170, no. 1, pp. 333–337, May 2011, doi: 10.1016/j.cej.2011.03.076.
- [100] F. Dang, K. Kato, H. Imai, S. Wada, H. Haneda, and M. Kuwabara, "Oriented aggregation of BaTiO 3 nanocrystals and large particles in the ultrasonic-assistant synthesis," *CrystEngComm*, vol. 12, no. 11, pp. 3441–3444, 2010, doi: 10.1039/C003587D.
- [101] N. Enomoto, S. Maruyama, and Z. Nakagawa, "Agglomeration of silica spheres under ultrasonication," *Journal of Materials Research*, vol. 12, no. 5, pp. 1410–1415, May 1997, doi: 10.1557/JMR.1997.0192.
- [102] K. S. Suslick, "Sonochemistry," Science, vol. 247, no. 4949, pp. 1439–1445, Mar. 1990, doi: 10.1126/science.247.4949.1439.
- [103] T. Prozorov, R. Prozorov, and K. S. Suslick, "High Velocity Interparticle Collisions Driven by Ultrasound," J. Am. Chem. Soc., vol. 126, no. 43, pp. 13890–13891, Nov. 2004, doi: 10.1021/ja049493o.
- [104] K. S. Suslick and D. J. Casadonte, "Heterogeneous sonocatalysis with nickel powder," J. Am. Chem. Soc., vol. 109, no. 11, pp. 3459–3461, May 1987, doi: 10.1021/ja00245a047.
- [105] S. H. Fischer and M. C. Grubelich, "Theoretical energy release of thermites, intermetallics, and combustible metals," Sandia National Labs., Albuquerque, NM (US), SAND--98-1176C, CONF-980728--658208, Jun. 1998.
- [106] M. L. Pantoya and J. J. Granier, "Combustion Behavior of Highly Energetic Thermites: Nano versus Micron Composites," *Propellants, Explosives, Pyrotechnics*, vol. 30, no. 1, pp. 53–62, 2005, doi: 10.1002/prep.200400085.
- [107] D. G. Piercey and T. M. Klapötke, "Nanoscale Aluminum Metal Oxide (Thermite) Reactions for Application in Energetic Materials," Cent. Eur. J. Energ. Mater., vol. 7, no. 2, pp. 115–129, 2010.
- [108] M. A. Trunov, M. Schoenitz, and E. L. Dreizin, "Effect of polymorphic phase transformations in alumina layer on ignition of aluminium particles," *Combustion Theory and Modelling*, vol. 10, no. 4, pp. 603–623, Aug. 2006, doi: 10.1080/13647830600578506.

- [109] S. Chowdhury, K. Sullivan, N. Piekiel, L. Zhou, and M. R. Zachariah, "Diffusive vs Explosive Reaction at the Nanoscale," *J. Phys. Chem. C*, vol. 114, no. 20, pp. 9191–9195, May 2010, doi: 10.1021/jp906613p.
- [110] F. Saceleanu, S. Atashin, and J. Z. Wen, "Investigation of the effects of phase transformations in micro and nano aluminum powders on kinetics of oxidation using thermogravimetric analysis," *Phys Chem Chem Phys*, vol. 19, no. 29, pp. 18996–19009, Jul. 2017, doi: 10.1039/c7cp02692g.
- [111] V. I. Levitas, J. McCollum, and M. Pantoya, "Pre-Stressing Micron-Scale Aluminum Core-Shell Particles to Improve Reactivity," *Sci Rep*, vol. 5, p. 7879, Jan. 2015, doi: 10.1038/srep07879.
- [112] H. Wang, G. Jian, G. C. Egan, and M. R. Zachariah, "Assembly and reactive properties of Al/CuO based nanothermite microparticles," *Combustion and Flame*, vol. 161, no. 8, pp. 2203–2208, Aug. 2014, doi: 10.1016/j.combustflame.2014.02.003.
- [113] M. Comet, C. Martin, F. Schnell, and D. Spitzer, "Nanothermites: A short Review. Factsheet for Experimenters, Present and Future Challenges," *Propellants, Explosives, Pyrotechnics*, vol. 44, no. 1, pp. 18–36, 2019, doi: 10.1002/prep.201800095.
- [114] M. G. Zaky, A. M. Abdalla, R. P. Sahu, I. K. Puri, M. Radwan, and S. Elbasuney, "Nanothermite colloids: A new prospective for enhanced performance," *Defence Technology*, vol. 15, no. 3, pp. 319–325, Jun. 2019, doi: 10.1016/j.dt.2018.08.016.
- [115] R. R. Nellums, B. C. Terry, B. C. Tappan, S. F. Son, and L. J. Groven, "Effect of Solids Loading on Resonant Mixed Al-Bi2O3 Nanothermite Powders," *Propellants, Explosives, Pyrotechnics*, vol. 38, no. 5, pp. 605–610, 2013, doi: 10.1002/prep.201300038.
- [116] C. Rossi, "Two Decades of Research on Nano-Energetic Materials," *Propellants, Explosives, Pyrotechnics*, vol. 39, no. 3, pp. 323–327, 2014, doi: 10.1002/prep.201480151.
- [117] V. E. Sanders, B. W. Asay, T. J. Foley, B. C. Tappan, A. N. Pacheco, and S. F. Son, "Reaction Propagation of Four Nanoscale Energetic Composites (Al/MoO3, Al/WO3, Al/CuO, and B12O3)," *Journal of Propulsion and Power*, vol. 23, no. 4, pp. 707–714, 2007, doi: 10.2514/1.26089.
- [118] J. L. Cheng, H. H. Hng, H. Y. Ng, P. C. Soon, and Y. W. Lee, "Synthesis and characterization of self-assembled nanoenergetic Al–Fe2O3 thermite system," *Journal*

- of Physics and Chemistry of Solids, vol. 71, no. 2, pp. 90–94, Feb. 2010, doi: 10.1016/j.jpcs.2009.08.017.
- [119] C. Badiola, M. Schoenitz, X. Zhu, and E. L. Dreizin, "Nanocomposite thermite powders prepared by cryomilling," *Journal of Alloys and Compounds*, vol. 488, no. 1, pp. 386–391, Nov. 2009, doi: 10.1016/j.jallcom.2009.08.146.
- [120] G. Jian, S. Chowdhury, K. Sullivan, and M. R. Zachariah, "Nanothermite reactions: Is gas phase oxygen generation from the oxygen carrier an essential prerequisite to ignition?," *Combustion and Flame*, vol. 160, no. 2, pp. 432–437, Feb. 2013, doi: 10.1016/j.combustflame.2012.09.009.
- [121] P. Gibot, Q. Miesch, A. Bach, F. Schnell, R. Gadiou, and D. Spitzer, "Mechanical Desensitization of an Al/WO3 Nanothermite by Means of Carbonaceous Coatings Derived from Carbohydrates," *C Journal of Carbon Research*, vol. 5, no. 3, p. 37, Sep. 2019, doi: 10.3390/c5030037.
- [122] C. Weir, M. L. Pantoya, G. Ramachandran, T. Dallas, D. Prentice, and M. Daniels, "Electrostatic discharge sensitivity and electrical conductivity of composite energetic materials," *Journal of Electrostatics*, vol. 71, no. 1, pp. 77–83, Feb. 2013, doi: 10.1016/j.elstat.2012.10.002.
- [123] J. J. Granier and M. L. Pantoya, "Laser ignition of nanocomposite thermites," *Combustion and Flame*, vol. 138, no. 4, pp. 373–383, Sep. 2004, doi: 10.1016/j.combustflame.2004.05.006.
- [124] J. H. Kim *et al.*, "Flash-ignitable nanoenergetic materials with tunable underwater explosion reactivity: The role of sea urchin-like carbon nanotubes," *Combustion and Flame*, vol. 162, no. 4, pp. 1448–1454, Apr. 2015, doi: 10.1016/j.combustflame.2014.11.011.
- [125] T. BAZYN, N. GLUMAC*, H. KRIER, T. S. WARD, M. SCHOENITZ, and E. L. DREIZIN, "Reflected Shock Ignition and Combustion of Aluminum and Nanocomposite Thermite Powders," *Combustion Science and Technology*, vol. 179, no. 3, pp. 457–476, Mar. 2007, doi: 10.1080/00102200600637261.
- [126] J. L. Cheng, H. H. Hng, Y. W. Lee, S. W. Du, and N. N. Thadhani, "Kinetic study of thermal- and impact-initiated reactions in Al–Fe2O3 nanothermite," *Combustion and*

- *Flame*, vol. 157, no. 12, pp. 2241–2249, Dec. 2010, doi: 10.1016/j.combustflame.2010.07.012.
- [127] B. Siegert, M. Comet, O. Muller, G. Pourroy, and D. Spitzer, "Reduced-Sensitivity Nanothermites Containing Manganese Oxide Filled Carbon Nanofibers," J. Phys. Chem. C, vol. 114, no. 46, pp. 19562–19568, Nov. 2010, doi: 10.1021/jp1014737.
- [128] K. S. Martirosyan, "Nanoenergetic Gas-Generators: principles and applications," *J. Mater. Chem.*, vol. 21, no. 26, p. 9400, 2011, doi: 10.1039/c1jm11300c.
- [129] E. W. Price and R. K. Sigman, "Behavior of Aluminum in Solid Propellant Combustion.:," GEORGIA INST OF TECH ATLANTA SCHOOL OFAEROSPACE ENGINEERING, 1982, Fort Belvoir, VA, Nov. 1976.
- [130] N. W. Piekiel, K. T. Sullivan, S. Chowdhury, and M. R. Zachariah, "The Role of Metal Oxides in Nanothermite Reactions: Evidence of Condensed Phase Initiation:," Defense Technical Information Center, MARYLAND UNIV COLLEGE PARK; 2010 Jan., Jan. 2010.
- [131] A. Prakash, A. V. McCormick, and M. R. Zachariah, "Tuning the Reactivity of Energetic Nanoparticles by Creation of a Core–Shell Nanostructure," *Nano Lett.*, vol. 5, no. 7, pp. 1357–1360, Jul. 2005, doi: 10.1021/nl0506251.
- [132] J. M. Slocik, C. A. Crouse, J. E. Spowart, and R. R. Naik, "Biologically tunable reactivity of energetic nanomaterials using protein cages," *Nano Lett.*, vol. 13, no. 6, pp. 2535–2540, Jun. 2013, doi: 10.1021/nl400590k.
- [133] J. M. Slocik, R. McKenzie, P. B. Dennis, and R. R. Naik, "Creation of energetic biothermite inks using ferritin liquid protein," *Nat Commun*, vol. 8, p. 15156, 27 2017, doi: 10.1038/ncomms15156.
- [134] Y. Yang *et al.*, "Nanowire membrane-based nanothermite: towards processable and tunable interfacial diffusion for solid state reactions," *Sci Rep*, vol. 3, p. 1694, 2013, doi: 10.1038/srep01694.
- [135] J. Kwon *et al.*, "Interfacial Chemistry in Al/CuO Reactive Nanomaterial and Its Role in Exothermic Reaction," *ACS Appl. Mater. Interfaces*, vol. 5, no. 3, pp. 605–613, Feb. 2013, doi: 10.1021/am3019405.
- [136] H. Sui, S. Atashin, and J. Z. Wen, "Thermo-chemical and energetic properties of layered nano-thermite composites," *Thermochimica Acta*, vol. 642, pp. 17–24, Oct. 2016, doi: 10.1016/j.tca.2016.08.019.

- [137] Y. Yin *et al.*, "Fabrication of electrophoretically deposited, self-assembled three-dimensional porous Al/CuO nanothermite films for highly enhanced energy output," *Materials Chemistry and Physics*, vol. 194, pp. 182–187, Jun. 2017, doi: 10.1016/j.matchemphys.2017.03.018.
- [138] N. Yan, L. Qin, H. Hao, L. Hui, F. Zhao, and H. Feng, "Iron oxide/aluminum/graphene energetic nanocomposites synthesized by atomic layer deposition: Enhanced energy release and reduced electrostatic ignition hazard," *Applied Surface Science*, vol. 408, pp. 51–59, Jun. 2017, doi: 10.1016/j.apsusc.2017.02.169.
- [139] H. Sui, L. LeSergent, and J. Z. Wen, "Diversity in Addressing Reaction Mechanisms of Nano-Thermite Composites with a Layer by Layer Structure," *Advanced Engineering Materials*, vol. 20, no. 3, p. 1700822, 2018, doi: 10.1002/adem.201700822.
- [140] K. Reed *et al.*, "Exploring the properties and applications of nanoceria: is there still plenty of room at the bottom?," *Environ. Sci.: Nano*, vol. 1, no. 5, pp. 390–405, 2014, doi: 10.1039/C4EN00079J.
- [141] G. Kim, "Ceria-promoted three-way catalysts for auto exhaust emission control," *Ind. Eng. Chem. Prod. Res. Dev.*, vol. 21, no. 2, pp. 267–274, Jun. 1982, doi: 10.1021/i300006a014.
- [142] R. J. Gorte, "Ceria in catalysis: From automotive applications to the water-gas shift reaction," *AIChE J.*, vol. 56, no. 5, pp. 1126–1135, 2010, doi: 10.1002/aic.12234.
- [143] S. Dey and G. C. Dhal, "Cerium catalysts applications in carbon monoxide oxidations," *Materials Science for Energy Technologies*, vol. 3, pp. 6–24, 2020, doi: 10.1016/j.mset.2019.09.003.
- [144] M. Ajmal Khan *et al.*, "Synthesize and characterization of ceria based nano-composite materials for low temperature solid oxide fuel cell," *International Journal of Hydrogen Energy*, vol. 43, no. 12, pp. 6310–6317, Mar. 2018, doi: 10.1016/j.ijhydene.2018.01.166.
- [145] B. C. H. Steele and A. Heinzel, "Materials for fuel-cell technologies," vol. 414, p. 8, 2001.
- [146] A. Trovarelli, "Structural and Oxygen Storage/Release Properties of CeO ₂ -Based Solid Solutions," *Comments on Inorganic Chemistry*, vol. 20, no. 4–6, pp. 263–284, Jan. 1999, doi: 10.1080/02603599908021446.

- [147] D. Du, J. Kullgren, K. Hermansson, and P. Broqvist, "From Ceria Clusters to Nanoparticles: Superoxides and Supercharging," *J. Phys. Chem. C*, vol. 123, no. 3, pp. 1742–1750, Jan. 2019, doi: 10.1021/acs.jpcc.8b08977.
- [148] J. Kullgren, K. Hermansson, and P. Broqvist, "Supercharged Low-Temperature Oxygen Storage Capacity of Ceria at the Nanoscale," *J. Phys. Chem. Lett.*, vol. 4, no. 4, pp. 604–608, Feb. 2013, doi: 10.1021/jz3020524.
- [149] J. Xu et al., "Size dependent oxygen buffering capacity of ceria nanocrystals," Chem. Commun., vol. 46, no. 11, p. 1887, 2010, doi: 10.1039/b923780a.
- [150] B. D. Cullity and J. W. Weymouth, "Elements of X-Ray Diffraction," *Elements of X-ray Diffraction. Addison-Wesley Publishing*.
- [151] Goodhew, Peter J. and Humphreys, FJ, Electron Microscopy and Analysis, Third Edition
 Peter J. Goodhew, John Humphreys, Richard Beanland Google Books. Electron microscopy and analysis. CRC Press, 2000.
- [152] Energy Dispersive X-ray Analysis in the Electron Microscope. Garland Science, 2003.
- [153] D. B. Williams and C. B. Carter, *Transmission electron microscopy: a textbook for materials science*, 2. ed. New York: Springer, 2009.
- [154] N. D. Klein, K. R. Hurley, Z. V. Feng, and C. L. Haynes, "Dark Field Transmission Electron Microscopy as a Tool for Identifying Inorganic Nanoparticles in Biological Matrices," Anal. Chem., vol. 87, no. 8, pp. 4356–4362, Apr. 2015, doi: 10.1021/acs.analchem.5b00124.
- [155] C. Kumar, Ed., *UV-VIS and Photoluminescence Spectroscopy for Nanomaterials Characterization*. Berlin, Heidelberg: Springer Berlin Heidelberg, 2013.
- [156] C. S. S. R. Kumar, Ed., *Raman Spectroscopy for Nanomaterials Characterization*. Berlin, Heidelberg: Springer Berlin Heidelberg, 2012.
- [157] E. Smith and G. Dent, *Modern Raman spectroscopy: a practical approach*. Hoboken, NJ: J. Wiley, 2005.
- [158] P. Eaton and P. West, Atomic force microscopy. Oxford: Oxford University Press, 2018.
- [159] A. Sehgal, Y. Lalatonne, J.-F. Berret, and M. Morvan, "Precipitation–Redispersion of Cerium Oxide Nanoparticles with Poly(acrylic acid): Toward Stable Dispersions," *Langmuir*, vol. 21, no. 20, pp. 9359–9364, Sep. 2005, doi: 10.1021/la0513757.

- [160] H.-I. Chen and H.-Y. Chang, "Homogeneous precipitation of cerium dioxide nanoparticles in alcohol/water mixed solvents," *Colloids and Surfaces A: Physicochemical and Engineering Aspects*, vol. 242, no. 1–3, pp. 61–69, Aug. 2004, doi: 10.1016/j.colsurfa.2004.04.056.
- [161] A. S. Karakoti, S. V. N. T. Kuchibhatla, K. S. Babu, and S. Seal, "Direct Synthesis of Nanoceria in Aqueous Polyhydroxyl Solutions," *J. Phys. Chem. C*, vol. 111, no. 46, pp. 17232–17240, Nov. 2007, doi: 10.1021/jp076164k.
- [162] F. Caputo *et al.*, "A novel synthetic approach of cerium oxide nanoparticles with improved biomedical activity," *Sci Rep*, vol. 7, no. 1, p. 4636, Dec. 2017, doi: 10.1038/s41598-017-04098-6.
- [163] N. W. Pettinger, R. E. A. Williams, J. Chen, and B. Kohler, "Crystallization kinetics of cerium oxide nanoparticles formed by spontaneous, room-temperature hydrolysis of cerium(IV) ammonium nitrate in light and heavy water," *Phys. Chem. Chem. Phys.*, vol. 19, no. 5, pp. 3523–3531, 2017, doi: 10.1039/C6CP08227K.
- [164] F. Goubin, X. Rocquefelte, M.-H. Whangbo, Y. Montardi, R. Brec, and S. Jobic, "Experimental and Theoretical Characterization of the Optical Properties of CeO ₂ , SrCeO ₃ , and Sr ₂ CeO ₄ Containing Ce ⁴⁺ (f ⁰) lons," *Chem. Mater.*, vol. 16, no. 4, pp. 662–669, Feb. 2004, doi: 10.1021/cm034618u.
- [165] Z. Wang, Z. Quan, and J. Lin, "Remarkable Changes in the Optical Properties of CeO ₂

 Nanocrystals Induced by Lanthanide Ions Doping," *Inorg. Chem.*, vol. 46, no. 13, pp. 5237–5242, Jun. 2007, doi: 10.1021/ic0701256.
- [166] G. Ranga Rao and H. R. Sahu, "XRD and UV-Vis diffuse reflectance analysis of CeO2-ZrO2 solid solutions synthesized by combustion method," *J Chem Sci*, vol. 113, no. 5–6, pp. 651–658, Oct. 2001, doi: 10.1007/BF02708797.
- [167] P. O. Maksimchuk and K. Ukraine, "Spectroscopically Detected Formation of Oxygen Vacancies in Nano-Crystalline CeO2 x," *Journal of Nano-and Electronic Physics*, vol. 5, no. 1, pp. 1004–1005, 2013.
- [168] J. H. Maeng and S. C. Choi, "The effect of cerium reduction on light emission in cerium-containing 20Y2O3-25Al2O3-55SiO2 glass," *Journal of the Optical Society of Korea*, vol. 16, no. 4, pp. 414–417, Dec. 2012, doi: 10.3807/JOSK.2012.16.4.414.

- [169] M.-L. Brandily-Anne, J. Lumeau, L. Glebova, and L. B. Glebov, "Specific absorption spectra of cerium in multicomponent silicate glasses," *Journal of Non-Crystalline Solids*, vol. 356, no. 44–49, pp. 2337–2343, Oct. 2010, doi: 10.1016/j.jnoncrysol.2010.02.020.
- [170] R. D. Tarey and T. A. Raju, "A method for the deposition of transparent conducting thin films of tin oxide," *Thin Solid Films*, vol. 128, no. 3–4, pp. 181–189, Jun. 1985, doi: 10.1016/0040-6090(85)90070-7.
- [171] J. Tauc and A. Menth, "States in the gap," *Journal of Non-Crystalline Solids*, vol. 8–10, pp. 569–585, Jun. 1972, doi: 10.1016/0022-3093(72)90194-9.
- [172] K. Lakshun Naidu and M. Ghanashyam Krishna, "Effect of thermal annealing on disorder and optical properties of Cr/Si bilayer thin films," *Philosophical Magazine*, vol. 94, no. 30, pp. 3431–3444, Oct. 2014, doi: 10.1080/14786435.2014.959578.
- [173] I. Studenyak, M. Kranjec, and M. Kurik, "Urbach Rule in Solid State Physics," International Journal of Optics and Applications, vol. 4, no. 3, pp. 76–83, 2014.
- [174] A. Abu El-Fadl, A. S. Soltan, and N. M. Shaalan, "Temperature dependence of the indirect band gap, steepness parameter and related optical constants of [Kx(NH4)1-x]2ZnCl4 mixed crystals," Optics & Laser Technology, vol. 39, no. 7, pp. 1310–1318, Oct. 2007, doi: 10.1016/j.optlastec.2006.12.004.
- [175] A. S. Hassanien and A. A. Akl, "Optical characteristics of iron oxide thin films prepared by spray pyrolysis technique at different substrate temperatures," *Appl. Phys. A*, vol. 124, no. 11, p. 752, Oct. 2018, doi: 10.1007/s00339-018-2180-6.
- [176] S. Tsunekawa, T. Fukuda, and A. Kasuya, "Blue shift in ultraviolet absorption spectra of monodisperse CeO2–x nanoparticles," *Journal of Applied Physics*, vol. 87, no. 3, pp. 1318–1321, Jan. 2000, doi: 10.1063/1.372016.
- [177] S. Tsunekawa, J.-T. Wang, Y. Kawazoe, and A. Kasuya, "Blueshifts in the ultraviolet absorption spectra of cerium oxide nanocrystallites," *Journal of Applied Physics*, vol. 94, no. 5, pp. 3654–3656, Sep. 2003, doi: 10.1063/1.1600520.
- [178] N. N. Dao, M. D. Luu, Q. K. Nguyen, and B. S. Kim, "UV absorption by cerium oxide nanoparticles/epoxy composite thin films," Adv. Nat. Sci: Nanosci. Nanotechnol., vol. 2, no. 4, p. 045013, Dec. 2011, doi: 10.1088/2043-6262/2/4/045013.

- [179] M. G. Sujana, K. K. Chattopadyay, and S. Anand, "Characterization and optical properties of nano-ceria synthesized by surfactant-mediated precipitation technique in mixed solvent system," *Applied Surface Science*, vol. 254, no. 22, pp. 7405–7409, Sep. 2008, doi: 10.1016/j.apsusc.2008.05.341.
- [180] S. Tsunekawa, R. Sahara, Y. Kawazoe, and A. Kasuya, "Origin of the Blue Shift in Ultraviolet Absorption Spectra of Nanocrystalline CeO_{2−<I>x</I>} Particles," *Mater. Trans., JIM*, vol. 41, no. 8, pp. 1104–1107, 2000, doi: 10.2320/matertrans1989.41.1104.
- [181] R. A. Kumar, K. S. Babu, A. Dasgupta, and R. Ramaseshan, "Enhancing the dual magnetic and optical properties of co-doped cerium oxide nanostructures," *RSC Adv.*, vol. 5, no. 125, pp. 103465–103473, Dec. 2015, doi: 10.1039/C5RA15336K.
- [182] Z. Wang, Z. Quan, and J. Lin, "Remarkable Changes in the Optical Properties of CeO ₂

 Nanocrystals Induced by Lanthanide Ions Doping," *Inorg. Chem.*, vol. 46, no. 13, pp. 5237–5242, Jun. 2007, doi: 10.1021/ic0701256.
- [183] M. Das *et al.*, "Auto-catalytic Ceria Nanoparticles Offer Neuroprotection to Adult Rat Spinal Cord Neurons," *Biomaterials*, vol. 28, no. 10, pp. 1918–1925, Apr. 2007, doi: 10.1016/j.biomaterials.2006.11.036.
- [184] J. M. Perez, A. Asati, S. Nath, and C. Kaittanis, "Synthesis of Biocompatible Dextran-Coated Nanoceria with pH-Dependent Antioxidant Properties," *Small*, vol. 4, no. 5, pp. 552–556, May 2008, doi: 10.1002/smll.200700824.
- [185] C. Xu and X. Qu, "Cerium oxide nanoparticle: a remarkably versatile rare earth nanomaterial for biological applications," *NPG Asia Mater*, vol. 6, no. 3, pp. e90–e90, Mar. 2014, doi: 10.1038/am.2013.88.
- [186] Y. Malyukin, V. Klochkov, P. Maksimchuk, V. Seminko, and N. Spivak, "Oscillations of Cerium Oxidation State Driven by Oxygen Diffusion in Colloidal Nanoceria (CeO2 x),"

 Nanoscale Res Lett, vol. 12, no. 1, p. 566, Oct. 2017, doi: 10.1186/s11671-017-2339-7.
- [187] V. K. Klochkov *et al.*, "Oxidation-reduction processes in CeO2-x nanocrystals under UV irradiation," *Journal of Photochemistry and Photobiology A: Chemistry*, vol. 364, pp. 282–287, Sep. 2018, doi: 10.1016/j.jphotochem.2018.06.025.

- [188] V. Patel *et al.*, "Ligand-mediated reversal of the oxidation state dependent ROS scavenging and enzyme mimicking activity of ceria nanoparticles," *Chem. Commun.*, vol. 54, no. 99, pp. 13973–13976, 2018, doi: 10.1039/C8CC08355J.
- [189] K. Reed *et al.*, "Exploring the properties and applications of nanoceria: is there still plenty of room at the bottom?," *Environmental Science: Nano*, vol. 1, no. 5, pp. 390–405, 2014, doi: 10.1039/C4EN00079J.
- [190] P. Janoš *et al.*, "Chemical mechanical glass polishing with cerium oxide: Effect of selected physico-chemical characteristics on polishing efficiency," *Wear*, vol. 362–363, pp. 114–120, Sep. 2016, doi: 10.1016/j.wear.2016.05.020.
- [191] T. Montini, M. Melchionna, M. Monai, and P. Fornasiero, "Fundamentals and Catalytic Applications of CeO $_2$ -Based Materials," *Chem. Rev.*, vol. 116, no. 10, pp. 5987–6041, May 2016, doi: 10.1021/acs.chemrev.5b00603.
- [192] B. Zhu *et al.*, "Innovative low temperature SOFCs and advanced materials," *Journal of Power Sources*, vol. 118, no. 1–2, pp. 47–53, May 2003, doi: 10.1016/S0378-7753(03)00060-0.
- [193] M. Ornatska, E. Sharpe, D. Andreescu, and S. Andreescu, "Paper Bioassay Based on Ceria Nanoparticles as Colorimetric Probes," *Anal. Chem.*, vol. 83, no. 11, pp. 4273– 4280, Jun. 2011, doi: 10.1021/ac200697y.
- [194] S. Deshpande, S. Patil, S. V. Kuchibhatla, and S. Seal, "Size dependency variation in lattice parameter and valency states in nanocrystalline cerium oxide," *Appl. Phys. Lett.*, vol. 87, no. 13, p. 133113, Sep. 2005, doi: 10.1063/1.2061873.
- [195] J.-D. Cafun, K. O. Kvashnina, E. Casals, V. F. Puntes, and P. Glatzel, "Absence of Ce3+ Sites in Chemically Active Colloidal Ceria Nanoparticles," *ACS Nano*, vol. 7, no. 12, pp. 10726–10732, Dec. 2013, doi: 10.1021/nn403542p.
- [196] Y. Malyukin, V. Klochkov, P. Maksimchuk, V. Seminko, and N. Spivak, "Oscillations of Cerium Oxidation State Driven by Oxygen Diffusion in Colloidal Nanoceria (CeO2 x),"

 Nanoscale Res Lett, vol. 12, no. 1, p. 566, Oct. 2017, doi: 10.1186/s11671-017-2339-7.
- [197] F. Dvořák *et al.*, "Bulk Hydroxylation and Effective Water Splitting by Highly Reduced Cerium Oxide: The Role of O Vacancy Coordination," *ACS Catal.*, vol. 8, no. 5, pp. 4354–4363, May 2018, doi: 10.1021/acscatal.7b04409.

- [198] I. Celardo, J. Z. Pedersen, E. Traversa, and L. Ghibelli, "Pharmacological potential of cerium oxide nanoparticles," *Nanoscale*, vol. 3, no. 4, p. 1411, 2011, doi: 10.1039/c0nr00875c.
- [199] R. Mehmood, N. Ariotti, J. L. Yang, P. Koshy, and C. C. Sorrell, "pH-Responsive Morphology-Controlled Redox Behavior and Cellular Uptake of Nanoceria in Fibrosarcoma," *ACS Biomater. Sci. Eng.*, vol. 4, no. 3, pp. 1064–1072, Mar. 2018, doi: 10.1021/acsbiomaterials.7b00806.
- [200] Y. Xu *et al.*, "Resolving a Decade-Long Question of Oxygen Defects in Raman Spectra of Ceria-Based Catalysts at Atomic Level," *J. Phys. Chem. C*, vol. 123, no. 31, pp. 1889–18894, Aug. 2019, doi: 10.1021/acs.jpcc.9b00633.
- [201] C. Schilling, A. Hofmann, C. Hess, and M. V. Ganduglia-Pirovano, "Raman Spectra of Polycrystalline CeO2: A Density Functional Theory Study," J. Phys. Chem. C, vol. 121, no. 38, pp. 20834–20849, Sep. 2017, doi: 10.1021/acs.jpcc.7b06643.
- [202] S. V. N. T. Kuchibhatla *et al.*, "An unexpected phase transformation of ceria nanoparticles in aqueous media," *J. Mater. Res.*, vol. 34, no. 3, pp. 465–473, Feb. 2019, doi: 10.1557/jmr.2018.490.
- [203] A. Nikolenko *et al.*, "In situ Raman study of laser-induced stabilization of reduced nanoceria (CeO2–x) supported on graphene," *Journal of Raman Spectroscopy*, vol. 50, no. 4, pp. 490–498, 2019, doi: 10.1002/jrs.5542.
- [204] E. Sartoretti *et al.*, "In situ Raman analyses of the soot oxidation reaction over nanostructured ceria-based catalysts," *Sci Rep*, vol. 9, no. 1, pp. 1–14, Mar. 2019, doi: 10.1038/s41598-019-39105-5.
- [205] M. Guo, J. Lu, Y. Wu, Y. Wang, and M. Luo, "UV and Visible Raman Studies of Oxygen Vacancies in Rare-Earth-Doped Ceria," *Langmuir*, vol. 27, no. 7, pp. 3872–3877, Apr. 2011, doi: 10.1021/la200292f.
- [206] G. C. Allen, M. B. Wood, and J. M. Dyke, "Spectroscopic properties of some mixed-valence transitional metal chalcogenides," *Journal of Inorganic and Nuclear Chemistry*, vol. 35, no. 7, pp. 2311–2318, Jul. 1973, doi: 10.1016/0022-1902(73)80295-7.
- [207] C. Binet, A. Badri, and J.-C. Lavalley, "A Spectroscopic Characterization of the Reduction of Ceria from Electronic Transitions of Intrinsic Point Defects," J. Phys. Chem., vol. 98, no. 25, pp. 6392–6398, Jun. 1994, doi: 10.1021/j100076a025.

- [208] G. Ranga Rao and H. R. Sahu, "XRD and UV-Vis diffuse reflectance analysis of CeO2-ZrO2 solid solutions synthesized by combustion method," *J Chem Sci*, vol. 113, no. 5–6, pp. 651–658, Oct. 2001, doi: 10.1007/BF02708797.
- [209] G. A. Slack, S. L. Dole, V. Tsoukala, and G. S. Nolas, "Optical absorption spectrum of trivalent cerium in Y203, Ba2 GdTaO6, ThO2, and related compounds," JOSA B, vol. 11, no. 6, pp. 961–974, Jun. 1994.
- [210] W. M. Yen, U. Happek, M. Raukas, and S. Basun, "Luminescence and photoconductivity of cerium compounds," *Acta Physica Polonica. Series A*, vol. 90, no. 2, pp. 257–266, 1996.
- [211] S. A. Ansari, M. M. Khan, M. O. Ansari, S. Kalathil, J. Lee, and M. H. Cho, "Band gap engineering of CeO2 nanostructure using an electrochemically active biofilm for visible light applications," *RSC Adv.*, vol. 4, no. 32, pp. 16782–16791, Apr. 2014, doi: 10.1039/C4RA00861H.
- [212] M. M. Khan, S. A. Ansari, D. Pradhan, D. H. Han, J. Lee, and M. H. Cho, "Defect-Induced Band Gap Narrowed CeO ₂ Nanostructures for Visible Light Activities," *Ind. Eng. Chem. Res.*, vol. 53, no. 23, pp. 9754–9763, Jun. 2014, doi: 10.1021/ie500986n.
- [213] M. E. Khan, M. M. Khan, and M. H. Cho, "Ce3+-ion, Surface Oxygen Vacancy, and Visible Light-induced Photocatalytic Dye Degradation and Photocapacitive Performance of CeO2-Graphene Nanostructures," *Sci Rep*, vol. 7, no. 1, p. 5928, 19 2017, doi: 10.1038/s41598-017-06139-6.
- [214] B. Choudhury, P. Chetri, and A. Choudhury, "Annealing temperature and oxygen-vacancy-dependent variation of lattice strain, band gap and luminescence properties of CeO2 nanoparticles," *Journal of Experimental Nanoscience*, vol. 10, no. 2, pp. 103–114, Jan. 2015, doi: 10.1080/17458080.2013.801566.
- [215] S. Aškrabić, Z. D. Dohčević-Mitrović, V. D. Araújo, G. Ionita, M. M. de Lima, and A. Cantarero, "F-centre luminescence in nanocrystalline CeO2," *J. Phys. D: Appl. Phys.*, vol. 46, no. 49, p. 495306, Nov. 2013, doi: 10.1088/0022-3727/46/49/495306.
- [216] S. Tiwari *et al.*, "Oxygen and cerium defects mediated changes in structural, optical and photoluminescence properties of Ni substituted CeO2," *Journal of Alloys and Compounds*, vol. 782, pp. 689–698, Apr. 2019, doi: 10.1016/j.jallcom.2018.12.009.

- [217] R. W. Cheary, A. A. Coelho, and J. P. Cline, "Fundamental parameters line profile fitting in laboratory diffractometers," *J. Res. Natl. Inst. Stand. Technol.*, vol. 109, no. 1, p. 1, Jan. 2004, doi: 10.6028/jres.109.002.
- [218] J. H. Bang and K. S. Suslick, "Applications of Ultrasound to the Synthesis of Nanostructured Materials," Advanced Materials, vol. 22, no. 10, pp. 1039–1059, 2010, doi: 10.1002/adma.200904093.
- [219] T. Alessandro, Catalysis By Ceria And Related Materials. World Scientific, 2002.
- [220] D. R. Mullins, "The surface chemistry of cerium oxide," *Surface Science Reports*, vol. 70, no. 1, pp. 42–85, Mar. 2015, doi: 10.1016/j.surfrep.2014.12.001.
- [221] Lj. Kundakovic, D. R. Mullins, and S. H. Overbury, "Adsorption and reaction of H2O and CO on oxidized and reduced Rh/CeOx(111) surfaces," *Surface Science*, vol. 457, no. 1, pp. 51–62, Jun. 2000, doi: 10.1016/S0039-6028(00)00332-0.
- [222] T. Kropp, J. Paier, and J. Sauer, "Interactions of Water with the (111) and (100) Surfaces of Ceria," *J. Phys. Chem. C*, vol. 121, no. 39, pp. 21571–21578, Oct. 2017, doi: 10.1021/acs.jpcc.7b08150.
- [223] A. Vincent *et al.*, "Tuning Hydrated Nanoceria Surfaces: Experimental/Theoretical Investigations of Ion Exchange and Implications in Organic and Inorganic Interactions," *Langmuir*, vol. 26, no. 10, pp. 7188–7198, May 2010, doi: 10.1021/la904285g.
- [224] J. Gaillard *et al.*, "Effect of hydration and thermal treatment on ceria surface using non-intrusive techniques," *Journal of Nuclear Materials*, vol. 444, no. 1–3, pp. 359–367, Jan. 2014, doi: 10.1016/j.jnucmat.2013.10.018.
- [225] A. Symington, M. Molinari, S. Moxon, J. Flitcroft, D. Sayle, and S. C. Parker, "Strongly Bound Surface Water Affects the Shape Evolution of Cerium Oxide Nanoparticles," Aug. 2019, doi: 10.26434/chemrxiv.9247709.v2.
- [226] S. Hayun, T. Y. Shvareva, and A. Navrotsky, "Nanoceria Energetics of Surfaces, Interfaces and Water Adsorption," *Journal of the American Ceramic Society*, vol. 94, no. 11, pp. 3992–3999, 2011, doi: 10.1111/j.1551-2916.2011.04648.x.
- [227] O. Matz and M. Calatayud, "H2 Dissociation and Oxygen Vacancy Formation on Ce2O3 Surfaces," *Top Catal*, vol. 62, no. 12, pp. 956–967, Sep. 2019, doi: 10.1007/s11244-019-01183-0.

- [228] O. Matz and M. Calatayud, "Breaking H2 with CeO2: Effect of Surface Termination.," ACS Omega, vol. 3, no. 11, pp. 16063–16073, Nov. 2018, doi: 10.1021/acsomega.8b02410.
- [229] Y. Lee, G. He, A. J. Akey, R. Si, M. Flytzani-Stephanopoulos, and I. P. Herman, "Raman Analysis of Mode Softening in Nanoparticle CeO2–δ and Au-CeO2–δ during CO Oxidation," *J. Am. Chem. Soc.*, vol. 133, no. 33, pp. 12952–12955, Aug. 2011, doi: 10.1021/ja204479j.
- [230] S. As\ukrabić, R. Kostić, Z. Dohc\uević-Mitrović, and Z. V. Popović, "Raman scattering from low frequency phonons confined in CeO2nanoparticles," *J. Phys.: Conf. Ser.*, vol. 92, p. 012042, Dec. 2007, doi: 10.1088/1742-6596/92/1/012042.
- [231] J. E. Spanier, R. D. Robinson, F. Zhang, S.-W. Chan, and I. P. Herman, "Size-dependent properties of \${\mathrm{CeO}}_{2\ensuremath{-}}y}\$ nanoparticles as studied by Raman scattering," *Phys. Rev. B*, vol. 64, no. 24, p. 245407, Nov. 2001, doi: 10.1103/PhysRevB.64.245407.
- [232] H. Zhu *et al.*, "Charge transfer drives anomalous phase transition in ceria," *Nat Commun*, vol. 9, no. 1, pp. 1–8, Nov. 2018, doi: 10.1038/s41467-018-07526-x.
- [233] J. F. Lutsko, "How crystals form: A theory of nucleation pathways," *Sci. Adv.*, vol. 5, no. 4, p. eaav7399, Apr. 2019, doi: 10.1126/sciadv.aav7399.
- [234] M. A. Durán-Olivencia, P. Yatsyshin, S. Kalliadasis, and J. F. Lutsko, "General framework for nonclassical nucleation," *New J. Phys.*, vol. 20, no. 8, p. 083019, Aug. 2018, doi: 10.1088/1367-2630/aad170.
- [235] S. Karthika, T. K. Radhakrishnan, and P. Kalaichelvi, "A Review of Classical and Nonclassical Nucleation Theories," *Crystal Growth & Design*, vol. 16, no. 11, pp. 6663–6681, Nov. 2016, doi: 10.1021/acs.cgd.6b00794.
- [236] R. P. Sear, "The non-classical nucleation of crystals: microscopic mechanisms and applications to molecular crystals, ice and calcium carbonate," *International Materials Reviews*, vol. 57, no. 6, pp. 328–356, Nov. 2012, doi: 10.1179/1743280411Y.0000000015.
- [237] D. Gebauer and H. Cölfen, "Prenucleation clusters and non-classical nucleation," *Nano Today*, vol. 6, no. 6, pp. 564–584, Dec. 2011, doi: 10.1016/j.nantod.2011.10.005.

- [238] W. Kossel, "The theory of crystal growth. News from the Society of Sciences to Göttingen, Mathematical-Physical Class," News from the Society of Sciences to Göttingen, Mathematical-Physical Class, vol. 2, pp. 135–143, Jul. 1927.
- [239] H. Ham, N.-H. Park, S. S. Kim, and H. W. Kim, "Evidence of Ostwald ripening during evolution of micro-scale solid carbon spheres," *Sci Rep*, vol. 4, no. 1, p. 3579, May 2015, doi: 10.1038/srep03579.
- [240] M. Duer and A. Veis, "Water brings order," *Nature Mater*, vol. 12, no. 12, pp. 1081–1082, Dec. 2013, doi: 10.1038/nmat3822.
- [241] X. Lu *et al.*, "Redox cycles promoting photocatalytic hydrogen evolution of CeO2 nanorods," *J. Mater. Chem.*, vol. 21, no. 15, pp. 5569–5572, Mar. 2011, doi: 10.1039/C0JM04466K.
- [242] Z. Ji *et al.*, "Designed Synthesis of CeO2 Nanorods and Nanowires for Studying Toxicological Effects of High Aspect Ratio Nanomaterials," *ACS Nano*, vol. 6, no. 6, pp. 5366–5380, Jun. 2012, doi: 10.1021/nn3012114.
- [243] M. Duer and A. Veis, "Water brings order," *Nature Mater*, vol. 12, no. 12, pp. 1081–1082, Dec. 2013, doi: 10.1038/nmat3822.
- [244] Z. Liu, X. Li, M. Mayyas, P. Koshy, J. N. Hart, and C. C. Sorrell, "Growth mechanism of ceria nanorods by precipitation at room temperature and morphology-dependent photocatalytic performance," *CrystEngComm*, vol. 19, no. 32, pp. 4766–4776, Aug. 2017, doi: 10.1039/C7CE00922D.
- [245] Y. Yang *et al.*, "Redox enzyme-mimicking activities of CeO2 nanostructures: Intrinsic influence of exposed facets," *Sci Rep*, vol. 6, no. 1, p. 35344, Dec. 2016, doi: 10.1038/srep35344.
- [246] H.-Z. Zhu, Y.-M. Lu, F.-J. Fan, and S.-H. Yu, "Selective hydrogenation of nitroaromatics by ceria nanorods," *Nanoscale*, vol. 5, no. 16, pp. 7219–7223, Jul. 2013, doi: 10.1039/C3NR02662K.
- [247] A. Ahniyaz, Y. Sakamoto, and Lennart Bergström, "Tuning the Aspect Ratio of Ceria Nanorods and Nanodumbbells by a Face-Specific Growth and Dissolution Process," Crystal Growth & Design, vol. 8, no. 6, pp. 1798–1800, Jun. 2008, doi: 10.1021/cg800051s.

- [248] N. Du, H. Zhang, B. Chen, X. Ma, and D. Yang, "Ligand-free Self-Assembly of Ceria Nanocrystals into Nanorods by Oriented Attachment at Low Temperature," *J. Phys. Chem. C*, vol. 111, no. 34, pp. 12677–12680, Aug. 2007, doi: 10.1021/jp074011r.
- [249] H.-X. Mai *et al.*, "Shape-Selective Synthesis and Oxygen Storage Behavior of Ceria Nanopolyhedra, Nanorods, and Nanocubes," *J. Phys. Chem. B*, vol. 109, no. 51, pp. 24380–24385, Dec. 2005, doi: 10.1021/jp055584b.
- [250] Z. Wu, M. Li, D. R. Mullins, and S. H. Overbury, "Probing the Surface Sites of CeO2 Nanocrystals with Well-Defined Surface Planes via Methanol Adsorption and Desorption," *ACS Catal.*, vol. 2, no. 11, pp. 2224–2234, Nov. 2012, doi: 10.1021/cs300467p.
- [251] W. Huang, "Oxide Nanocrystal Model Catalysts," *Acc. Chem. Res.*, vol. 49, no. 3, pp. 520–527, Mar. 2016, doi: 10.1021/acs.accounts.5b00537.
- [252] M. Zhang, Y. Chen, C. Qiu, X. Fan, C. Chen, and Z. Wang, "Synthesis and atomic-scale characterization of CeO2 nano-octahedrons," *Physica E: Low-dimensional Systems and Nanostructures*, vol. 64, pp. 218–223, Nov. 2014, doi: 10.1016/j.physe.2014.08.002.
- [253] J. P. Y. Tan, H. R. Tan, C. Boothroyd, Y. L. Foo, C. B. He, and M. Lin, "Three-Dimensional Structure of CeO2 Nanocrystals," *J. Phys. Chem. C*, vol. 115, no. 9, pp. 3544–3551, Mar. 2011, doi: 10.1021/jp1122097.
- [254] Y. Wang, H.-J. Su, and S.-D. Wang, "Ceria nanocube with reactive {100} exposure planes: Simple and controllable synthesis under moderate conditions," *Ceramics International*, vol. 45, no. 12, pp. 15199–15204, Aug. 2019, doi: 10.1016/j.ceramint.2019.05.004.
- [255] Z. L. Wang and X. Feng, "Polyhedral Shapes of CeO2 Nanoparticles," *J. Phys. Chem. B*, vol. 107, no. 49, pp. 13563–13566, Dec. 2003, doi: 10.1021/jp036815m.
- [256] K. Siraj, M. Khaleeq-ur-Rahman, M. S. Rafique, and T. Nawaz, "Effect of 4MeV electron beam irradiation on carbon films," *Nuclear Instruments and Methods in Physics Research Section B: Beam Interactions with Materials and Atoms*, vol. 269, no. 1, pp. 53–56, Jan. 2011, doi: 10.1016/j.nimb.2010.09.022.
- [257] J. M. Yuk, M. Jeong, S. Y. Kim, H. K. Seo, J. Kim, and J. Y. Lee, "In situ atomic imaging of coalescence of Au nanoparticles on graphene: rotation and grain boundary

- migration," *Chem. Commun.*, vol. 49, no. 98, pp. 11479–11481, Nov. 2013, doi: 10.1039/C3CC46545D.
- [258] K. Zheng *et al.*, "Electron-beam-assisted superplastic shaping of nanoscale amorphous silica," *Nat Commun*, vol. 1, no. 1, p. 24, Dec. 2010, doi: 10.1038/ncomms1021.
- [259] Y. Ding, Y. Chen, K. C. Pradel, M. Liu, and Z. Lin Wang, "In-situ transmission electron microscopy study of oxygen vacancy ordering and dislocation annihilation in undoped and Sm-doped CeO ₂ ceramics during redox processes," *Journal of Applied Physics*, vol. 120, no. 21, p. 214302, Dec. 2016, doi: 10.1063/1.4971338.
- [260] J. Ghatak, W. Guan, and G. Möbus, "In situ TEM observation of lithium nanoparticle growth and morphological cycling," *Nanoscale*, vol. 4, no. 5, p. 1754, 2012, doi: 10.1039/c2nr11546h.
- [261] I.-T. Bae, Y. Zhang, W. J. Weber, M. Ishimaru, Y. Hirotsu, and M. Higuchi, "Temperature dependence of electron-beam induced effects in amorphous apatite," *Nuclear Instruments and Methods in Physics Research Section B: Beam Interactions with Materials and Atoms*, vol. 266, no. 12, pp. 3037–3042, Jun. 2008, doi: 10.1016/j.nimb.2008.03.160.
- [262] X. Z. Li, "JECP/PCED—a computer program for simulation of polycrystalline electron diffraction pattern and phase identification," *Ultramicroscopy*, vol. 99, no. 4, pp. 257–261, Jun. 2004, doi: 10.1016/j.ultramic.2004.01.006.
- [263] N. Jiang, "Electron beam damage in oxides: a review," Rep. Prog. Phys., vol. 79, no. 1, p. 016501, Jan. 2016, doi: 10.1088/0034-4885/79/1/016501.
- [264] K. Yasunaga, K. Yasuda, S. Matsumura, and T. Sonoda, "Nucleation and growth of defect clusters in CeO2 irradiated with electrons," *Nuclear Instruments and Methods in Physics Research Section B: Beam Interactions with Materials and Atoms*, vol. 250, no. 1–2, pp. 114–118, Sep. 2006, doi: 10.1016/j.nimb.2006.04.091.
- [265] C. Meis and A. Chartier, "Calculation of the threshold displacement energies in UO2 using ionic potentials," *Journal of Nuclear Materials*, vol. 341, no. 1, pp. 25–30, May 2005, doi: 10.1016/j.jnucmat.2005.01.001.
- [266] A. C. Johnston-Peck, J. S. DuChene, A. D. Roberts, W. D. Wei, and A. A. Herzing, "Dose-rate-dependent damage of cerium dioxide in the scanning transmission electron

- microscope," *Ultramicroscopy*, vol. 170, pp. 1–9, Nov. 2016, doi: 10.1016/j.ultramic.2016.07.002.
- [267] U. M. Bhatta, F. Karounis, A. Stringfellow, and G. Möbus, "Perforation and Carbon Ablation Experiments on Nano-Ceria by Electron Irradiation," *MRS Proc.*, vol. 1552, pp. 125–130, 2013, doi: 10.1557/opl.2013.714.
- [268] J. A. Aguiar *et al.*, "Linking Interfacial Step Structure and Chemistry with Locally Enhanced Radiation-Induced Amorphization at Oxide Heterointerfaces," *Adv. Mater. Interfaces*, vol. 1, no. 4, p. 1300142, Jul. 2014, doi: 10.1002/admi.201300142.
- [269] S. Gurbán *et al.*, "Electron irradiation induced amorphous SiO2 formation at metal oxide/Si interface at room temperature; electron beam writing on interfaces," *Sci Rep*, vol. 8, no. 1, p. 2124, Dec. 2018, doi: 10.1038/s41598-018-20537-4.
- [270] H. Y. Xiao, W. J. Weber, Y. Zhang, X. T. Zu, and S. Li, "Electronic excitation induced amorphization in titanate pyrochlores: an *ab initio* molecular dynamics study," *Scientific Reports*, vol. 5, p. 8265, Feb. 2015, doi: 10.1038/srep08265.
- [271] Z. Dang *et al., "In Situ* Transmission Electron Microscopy Study of Electron Beam-Induced Transformations in Colloidal Cesium Lead Halide Perovskite Nanocrystals," *ACS Nano*, vol. 11, no. 2, pp. 2124–2132, Feb. 2017, doi: 10.1021/acsnano.6b08324.
- [272] C. A. Taylor, T. M. Nenoff, S. H. Pratt, and K. Hattar, "Synthesis of complex rare earth nanostructures using in situ liquid cell transmission electron microscopy," *Nanoscale Adv.*, vol. 1, no. 6, pp. 2229–2239, Jun. 2019, doi: 10.1039/C9NA00197B.
- [273] M. Ishimaru, I.-T. Bae, and Y. Hirotsu, "Electron-beam-induced amorphization in SiC," *Phys. Rev. B*, vol. 68, no. 14, p. 144102, Oct. 2003, doi: 10.1103/PhysRevB.68.144102.
- [274] T.-T. Jiang *et al.*, "Progressive amorphization of GeSbTe phase-change material under electron beam irradiation," *APL Materials*, vol. 7, no. 8, p. 081121, Aug. 2019, doi: 10.1063/1.5102075.
- [275] Sören Selve and Dirk Berger, "Manufacturing and application of a 2 μm dark field aperture in TEM," in *In European Microscopy Congress 2016*, Weinheim, Germany, 2016, pp. 449–450, doi: DOI: 10.1002/9783527808465.EMC2016.6009.
- [276] G. V. Ramesh, M. D. Prasad, and T. P. Radhakrishnan, "Mercury Nanodrops and Nanocrystals," Chem. Mater., vol. 23, no. 23, pp. 5231–5236, Dec. 2011, doi: 10.1021/cm2022533.

- [277] X. Li, "Software Design for Simulation and Analysis of Electron Diffraction Patterns," Microscopy and Microanalysis, vol. 18, no. S2, pp. 1262–1263, Jul. 2012, doi: 10.1017/S1431927612008161.
- [278] H. E. M. Hussein *et al.*, "Tracking Metal Electrodeposition Dynamics from Nucleation and Growth of a Single Atom to a Crystalline Nanoparticle," *ACS Nano*, vol. 12, no. 7, pp. 7388–7396, Jul. 2018, doi: 10.1021/acsnano.8b04089.
- [279] U. M. Bhatta *et al.*, "Cationic Surface Reconstructions on Cerium Oxide Nanocrystals: An Aberration-Corrected HRTEM Study," *ACS Nano*, vol. 6, no. 1, pp. 421–430, Jan. 2012, doi: 10.1021/nn2037576.
- [280] W. Qin, T. Nagase, and Y. Umakoshi, "Electron irradiation-induced nanocrystallization of amorphous Fe85B15 alloy: Evidence for athermal nature," *Acta Materialia*, vol. 57, no. 4, pp. 1300–1307, Feb. 2009, doi: 10.1016/j.actamat.2008.11.009.
- [281] W. Qin, J. A. Szpunar, and Y. Umakoshi, "Electron or ion irradiation-induced phase-change mechanism between amorphous and crystalline state," *Acta Materialia*, vol. 59, no. 5, pp. 2221–2228, Mar. 2011, doi: 10.1016/j.actamat.2010.12.025.
- [282] J. Li *et al.*, "In Situ Atomic-Scale Study of Particle-Mediated Nucleation and Growth in Amorphous Bismuth to Nanocrystal Phase Transformation," *Adv. Sci.*, vol. 5, no. 6, p. 1700992, Jun. 2018, doi: 10.1002/advs.201700992.
- [283] F. Wang, V. N. Richards, S. P. Shields, and W. E. Buhro, "Kinetics and Mechanisms of Aggregative Nanocrystal Growth," *Chem. Mater.*, vol. 26, no. 1, pp. 5–21, Jan. 2014, doi: 10.1021/cm402139r.
- [284] M. Harada and E. Katagiri, "Mechanism of Silver Particle Formation during Photoreduction Using In Situ Time-Resolved SAXS Analysis," *Langmuir*, vol. 26, no. 23, pp. 17896–17905, Dec. 2010, doi: 10.1021/la102705h.
- [285] M. A. van Huis et al., "Low-Temperature Nanocrystal Unification through Rotations and Relaxations Probed by in Situ Transmission Electron Microscopy," Nano Lett., vol. 8, no. 11, pp. 3959–3963, Nov. 2008, doi: 10.1021/nl8024467.
- [286] N. T. K. Thanh, N. Maclean, and S. Mahiddine, "Mechanisms of Nucleation and Growth of Nanoparticles in Solution," *Chem. Rev.*, vol. 114, no. 15, pp. 7610–7630, Aug. 2014, doi: 10.1021/cr400544s.

- [287] K. Biswas, N. Varghese, and C. N. R. Rao, "Growth Kinetics of Gold Nanocrystals: A Combined Small-Angle X-Ray Scattering and Calorimetric Study," Small, vol. 4, no. 5, pp. 649–655, May 2008, doi: 10.1002/smll.200700937.
- [288] L. Wu *et al.*, "Interface Energies of Nanocrystalline Doped Ceria: Effects of Manganese Segregation," *J. Phys. Chem. C*, vol. 119, no. 49, pp. 27855–27864, Dec. 2015, doi: 10.1021/acs.jpcc.5b09255.
- [289] J. C. Ondry, M. R. Hauwiller, and A. P. Alivisatos, "Dynamics and Removal Pathway of Edge Dislocations in Imperfectly Attached PbTe Nanocrystal Pairs: Toward Design Rules for Oriented Attachment," ACS Nano, vol. 12, no. 4, pp. 3178–3189, Apr. 2018, doi: 10.1021/acsnano.8b00638.
- [290] Y. Yang, R. Scholz, H. J. Fan, D. Hesse, U. Gösele, and M. Zacharias, "Multitwinned Spinel Nanowires by Assembly of Nanobricks *via* Oriented Attachment: A Case Study of Zn ₂ TiO ₄," *ACS Nano*, vol. 3, no. 3, pp. 555–562, Mar. 2009, doi: 10.1021/nn800681q.
- [291] P. D. Edmondson, Y. Zhang, S. Moll, F. Namavar, and W. J. Weber, "Irradiation effects on microstructure change in nanocrystalline ceria Phase, lattice stress, grain size and boundaries," *Acta Materialia*, vol. 60, no. 15, pp. 5408–5416, Sep. 2012, doi: 10.1016/j.actamat.2012.07.010.
- [292] Y. Zhang *et al.*, "Structural modification of nanocrystalline ceria by ion beams," *Phys. Chem. Chem. Phys.*, vol. 13, no. 25, pp. 11946–11950, Jun. 2011, doi: 10.1039/C1CP21335K.
- [293] P. D. Edmondson, Y. Zhang, S. Moll, T. Varga, F. Namavar, and W. J. Weber, "Anomalous grain growth in the surface region of a nanocrystalline CeO 2 film under low-temperature heavy ion irradiation," *Phys. Rev. B*, vol. 85, no. 21, p. 214113, Jun. 2012, doi: 10.1103/PhysRevB.85.214113.
- [294] Y. Zhang *et al.*, "Grain growth and phase stability of nanocrystalline cubic zirconia under ion irradiation," *Phys. Rev. B*, vol. 82, no. 18, p. 184105, Nov. 2010, doi: 10.1103/PhysRevB.82.184105.
- [295] A. Guglielmetti *et al.*, "Atomistic simulation of point defects behavior in ceria,"

 Nuclear Instruments and Methods in Physics Research Section B: Beam Interactions

- with Materials and Atoms, vol. 266, no. 24, pp. 5120–5125, Dec. 2008, doi: 10.1016/j.nimb.2008.09.010.
- [296] K. Yasunaga, K. Yasuda, S. Matsumura, and T. Sonoda, "Nucleation and growth of defect clusters in CeO2 irradiated with electrons," *Nuclear Instruments and Methods in Physics Research Section B: Beam Interactions with Materials and Atoms*, vol. 250, no. 1–2, pp. 114–118, Sep. 2006, doi: 10.1016/j.nimb.2006.04.091.
- [297] A. C. Johnston-Peck, J. S. DuChene, A. D. Roberts, W. D. Wei, and A. A. Herzing, "Dose-rate-dependent damage of cerium dioxide in the scanning transmission electron microscope," *Ultramicroscopy*, vol. 170, p. 1, Nov. 2016, doi: 10.1016/j.ultramic.2016.07.002.
- [298] D. R. Mullins *et al.*, "Water Dissociation on CeO2(100) and CeO2(111) Thin Films," *J. Phys. Chem. C*, vol. 116, no. 36, pp. 19419–19428, Sep. 2012, doi: 10.1021/jp306444h.
- [299] P.-H. Huang and H.-Y. Lai, "Pressure-induced solid-state lattice mending of nanopores by pulse laser annealing," *Nanotechnology*, vol. 19, no. 25, p. 255701, May 2008, doi: 10.1088/0957-4484/19/25/255701.
- [300] P.-H. Huang and H.-Y. Lai, "Nucleation and propagation of dislocations during nanopore lattice mending by laser annealing: Modified continuum-atomistic modeling," *Phys. Rev. B*, vol. 77, no. 12, p. 125408, Mar. 2008, doi: 10.1103/PhysRevB.77.125408.
- [301] P.-H. Huang and H.-Y. Lai, "Atomistic modeling of lattice frame effects on laser-induced dislocation behaviors in nanopore mending processes," *Journal of Applied Physics*, vol. 108, no. 12, p. 123504, Dec. 2010, doi: 10.1063/1.3517788.
- [302] S.-Y. Chung and S.-J. L. Kang, "Effect of Dislocations on Grain Growth in Strontium Titanate," *Journal of the American Ceramic Society*, vol. 83, no. 11, pp. 2828–2832, 2000, doi: 10.1111/j.1151-2916.2000.tb01639.x.
- [303] D. A. Molodov and P. J. Konijnenberg, "Grain boundary dynamics and selective grain growth on non-ferromegnetic metals in high magnetic fields," *Zeitschrift für Metallkunde*, vol. 96, no. 10, pp. 1158–1165, 2005.
- [304] J. Monk and D. Farkas, "Strain-induced grain growth and rotation in nickel nanowires," *Phys. Rev. B*, vol. 75, no. 4, p. 045414, Jan. 2007, doi: 10.1103/PhysRevB.75.045414.

- [305] L. Ahmels, A. Kashiwar, T. Scherer, C. Kübel, and E. Bruder, "Grain growth mechanisms in ultrafine-grained steel: an electron backscatter diffraction and in situ TEM study," *J Mater Sci*, vol. 54, no. 14, pp. 10489–10505, Jul. 2019, doi: 10.1007/s10853-019-03611-8.
- [306] J. A. Haber and W. E. Buhro, "Kinetic Instability of Nanocrystalline Aluminum Prepared by Chemical Synthesis; Facile Room-Temperature Grain Growth," *J. Am. Chem. Soc.*, vol. 120, no. 42, pp. 10847–10855, Oct. 1998, doi: 10.1021/ja981972y.
- [307] M. J. Meziani *et al.*, "Formation and Properties of Stabilized Aluminum Nanoparticles," *ACS Appl. Mater. Interfaces*, vol. 1, no. 3, pp. 703–709, Mar. 2009, doi: 10.1021/am800209m.
- [308] M. J. McClain *et al.*, "Aluminum Nanocrystals," *Nano Lett.*, vol. 15, no. 4, pp. 2751–2755, Apr. 2015, doi: 10.1021/acs.nanolett.5b00614.
- [309] F. Langa, P. de la Cruz, A. de la Hoz, A. Díaz-Ortiz, and E. Díez-Barra, "Microwave irradiation: more than just a method for accelerating reactions," *Contemp. Org. Synth.*, vol. 4, no. 5, pp. 373–386, Jan. 1997, doi: 10.1039/CO9970400373.
- [310] R. Roy, "Accelerating the Kinetics of Low-Temperature Inorganic Syntheses," *Journal of Solid State Chemistry*, vol. 111, no. 1, pp. 11–17, Jul. 1994, doi: 10.1006/jssc.1994.1192.
- [311] K. A. S. Fernando, M. J. Smith, B. A. Harruff, W. K. Lewis, E. A. Guliants, and C. E. Bunker, "Sonochemically Assisted Thermal Decomposition of Alane N,N-Dimethylethylamine with Titanium (IV) Isopropoxide in the Presence of Oleic Acid to Yield Air-Stable and Size-Selective Aluminum Core-Shell Nanoparticles," *J. Phys. Chem. C*, vol. 113, no. 2, pp. 500–503, Jan. 2009, doi: 10.1021/jp809295e.
- [312] C. Mahendiran, R. Ganesan, and A. Gedanken, "Sonoelectrochemical Synthesis of Metallic Aluminum Nanoparticles," *European Journal of Inorganic Chemistry*, vol. 2009, no. 14, pp. 2050–2053, 2009, doi: 10.1002/ejic.200900097.
- [313] M. B. Pomfret, D. J. Brown, A. Epshteyn, A. P. Purdy, and J. C. Owrutsky, "Electrochemical Template Deposition of Aluminum Nanorods Using Ionic Liquids," *Chem. Mater.*, vol. 20, no. 19, pp. 5945–5947, Oct. 2008, doi: 10.1021/cm801983w.
- [314] S. Z. E. Abedin, E. M. Moustafa, R. Hempelmann, H. Natter, and F. Endres, "Electrodeposition of Nano- and Microcrystalline Aluminium in Three Different Air and

- Water Stable Ionic Liquids," *ChemPhysChem*, vol. 7, no. 7, pp. 1535–1543, 2006, doi: 10.1002/cphc.200600095.
- [315] S. R. Ghanta and K. Muralidharan, "Solution phase chemical synthesis of nano aluminium particles stabilized in poly(vinylpyrrolidone) and poly(methylmethacrylate) matrices," *Nanoscale*, vol. 2, no. 6, pp. 976–980, Jun. 2010, doi: 10.1039/B9NR00337A.
- [316] I. A. Safo, M. Werheid, C. Dosche, and M. Oezaslan, "The role of polyvinylpyrrolidone (PVP) as a capping and structure-directing agent in the formation of Pt nanocubes," *Nanoscale Advances*, vol. 1, no. 8, pp. 3095–3106, 2019, doi: 10.1039/C9NA00186G.
- [317] S. Zavyalov, "Formation and characterization of metal-polymer nanostructured composites," *Solid State Ionics*, vol. 147, no. 3–4, pp. 415–419, Apr. 2002, doi: 10.1016/S0167-2738(02)00038-3.
- [318] A. Das, S. Das, and A. K. Raychaudhuri, "Growth of two-dimensional arrays of uncapped gold nanoparticles on silicon substrates," *Bull Mater Sci*, vol. 31, no. 3, pp. 277–282, Jun. 2008, doi: 10.1007/s12034-008-0045-x.
- [319] P. Kumar, M. G. Krishna, A. K. Bhatnagar, and A. K. Bhattacharya, "Dynamic force microscopy study of the microstructural evolution of pulsed laser deposited ultrathin Ni and Ag films," J. Mater. Res., vol. 23, no. 7, pp. 1826–1839, Jul. 2008, doi: 10.1557/JMR.2008.0228.
- [320] P. R. Gogate, "Cavitational reactors for process intensification of chemical processing applications: A critical review," *Chemical Engineering and Processing: Process Intensification*, vol. 47, no. 4, pp. 515–527, Apr. 2008, doi: 10.1016/j.cep.2007.09.014.
- [321] P. R. Gogate, S. Mujumdar, and A. B. Pandit, "Large-scale sonochemical reactors for process intensification: design and experimental validation," *Journal of Chemical Technology*, vol. 78, no. 6, pp. 685–693, 2003, doi: 10.1002/jctb.697.
- [322] S. V. Sancheti and P. R. Gogate, "A review of engineering aspects of intensification of chemical synthesis using ultrasound," *Ultrasonics Sonochemistry*, vol. 36, pp. 527–543, May 2017, doi: 10.1016/j.ultsonch.2016.08.009.
- [323] D. Panda and S. Manickam, "Cavitation Technology—The Future of Greener Extraction Method: A Review on the Extraction of Natural Products and Process Intensification

- Mechanism and Perspectives," *Applied Sciences*, vol. 9, no. 4, p. 766, Jan. 2019, doi: 10.3390/app9040766.
- [324] Xu Wenlin, Ding Yuanqiong, Shao Qing, and Wang Yaqiong, "Application of Ultrasonic Intensification Technology in Chemical Engineering in China," *Chemical Engineering Transactions*, vol. 74, pp. 1351–1356, May 2019, doi: 10.3303/CET1974226.
- [325] R. R. Andrés, E. Riera, J. A. Gallego-Juárez, A. Mulet, J. V. García-Pérez, and J. A. Cárcel, "Airborne power ultrasound for drying process intensification at low temperatures: Use of a stepped-grooved plate transducer," *Drying Technology*, vol. 0, no. 0, pp. 1–14, Oct. 2019, doi: 10.1080/07373937.2019.1677704.
- [326] F. Vallespir, L. Crescenzo, Ó. Rodríguez, F. Marra, and S. Simal, "Intensification of Low-Temperature Drying of Mushroom by Means of Power Ultrasound: Effects on Drying Kinetics and Quality Parameters," *Food Bioprocess Technol*, vol. 12, no. 5, pp. 839–851, May 2019, doi: 10.1007/s11947-019-02263-5.
- [327] A. Chakravorty, "Process intensification by pulsation and vibration in miscible and immiscible two component systems," *Chemical Engineering and Processing Process Intensification*, vol. 133, pp. 90–105, Nov. 2018, doi: 10.1016/j.cep.2018.09.017.
- [328] Z. Wu, S. Tagliapietra, A. Giraudo, K. Martina, and G. Cravotto, "Harnessing cavitational effects for green process intensification," *Ultrasonics Sonochemistry*, vol. 52, pp. 530–546, Apr. 2019, doi: 10.1016/j.ultsonch.2018.12.032.
- [329] S. Bhoi, A. Das, J. Kumar, and D. Sarkar, "Sonofragmentation of two-dimensional plate-like crystals: Experiments and Monte Carlo simulations," *Chemical Engineering Science*, vol. 203, pp. 12–27, Aug. 2019, doi: 10.1016/j.ces.2019.03.070.
- [330] A. Klaue *et al.*, "Ziegler–Natta catalyst sonofragmentation for controlling size and size distribution of the produced polymer particles," *AIChE J*, vol. 65, no. 9, p. e16676, Sep. 2019, doi: 10.1002/aic.16676.
- [331] N. Edwin and P. Wilson, "Investigations on sonofragmentation of hydroxyapatite crystals as a function of strontium incorporation," *Ultrasonics Sonochemistry*, vol. 50, pp. 188–199, Jan. 2019, doi: 10.1016/j.ultsonch.2018.09.018.
- [332] X. Dong *et al.*, "Enhanced high-voltage cycling stability of Ni-rich cathode materials via the self-assembly of Mn-rich shells," *J. Mater. Chem. A*, vol. 7, no. 35, pp. 20262–20273, Sep. 2019, doi: 10.1039/C9TA07147D.

- [333] H. N. Kim and K. S. Suslick, "The Effects of Ultrasound on Crystals: Sonocrystallization and Sonofragmentation," *Crystals*, vol. 8, no. 7, p. 280, Jul. 2018, doi: 10.3390/cryst8070280.
- [334] H. N. Kim and K. S. Suslick, "Sonofragmentation of Ionic Crystals," *Chemistry A European Journal*, vol. 23, no. 12, pp. 2778–2782, 2017, doi: 10.1002/chem.201605857.
- [335] R. Gao, I. Gupta, and E. S. Boyden, "Sonofragmentation of Ultrathin 1D Nanomaterials," *Particle & Particle Systems Characterization*, vol. 34, no. 1, p. 1600339, 2017, doi: 10.1002/ppsc.201600339.
- [336] J. Jordens, T. Appermont, B. Gielen, T. Van Gerven, and L. Braeken, "Sonofragmentation: Effect of Ultrasound Frequency and Power on Particle Breakage," *Crystal Growth & Design*, vol. 16, no. 11, pp. 6167–6177, Nov. 2016, doi: 10.1021/acs.cgd.6b00088.
- [337] Y. Xi et al., "Sonocrystallization of conjugated polymers with ultrasound fields," Soft Matter, vol. 14, no. 24, pp. 4963–4976, Jun. 2018, doi: 10.1039/C8SM00905H.
- [338] S. Nalesso, M. J. Bussemaker, R. P. Sear, M. Hodnett, and J. Lee, "A review on possible mechanisms of sonocrystallisation in solution," *Ultrasonics Sonochemistry*, vol. 57, pp. 125–138, Oct. 2019, doi: 10.1016/j.ultsonch.2019.04.020.
- [339] J. Jordens *et al.*, "Sonocrystallisation: Observations, theories and guidelines," *Chemical Engineering and Processing Process Intensification*, vol. 139, pp. 130–154, May 2019, doi: 10.1016/j.cep.2019.03.017.
- [340] J. Lee, K. Yasui, M. Ashokkumar, and S. E. Kentish, "Quantification of Cavitation Activity by Sonoluminescence To Study the Sonocrystallization Process under Different Ultrasound Parameters," *Crystal Growth & Design*, vol. 18, no. 9, pp. 5108–5115, Sep. 2018, doi: 10.1021/acs.cgd.8b00547.
- [341] C. Backes *et al.*, "Guidelines for Exfoliation, Characterization and Processing of Layered Materials Produced by Liquid Exfoliation," *Chem. Mater.*, vol. 29, no. 1, pp. 243–255, Jan. 2017, doi: 10.1021/acs.chemmater.6b03335.
- [342] C. Gibaja *et al.*, "Few-Layer Antimonene by Liquid-Phase Exfoliation," *Angewandte Chemie International Edition*, vol. 55, no. 46, pp. 14345–14349, 2016, doi: 10.1002/anie.201605298.

- [343] J. T. Han *et al.*, "Extremely Efficient Liquid Exfoliation and Dispersion of Layered Materials by Unusual Acoustic Cavitation," *Scientific Reports*, vol. 4, no. 1, pp. 1–7, May 2014, doi: 10.1038/srep05133.
- [344] L. Lu *et al.*, "Few-layer Bismuthene: Sonochemical Exfoliation, Nonlinear Optics and Applications for Ultrafast Photonics with Enhanced Stability," *Laser & Photonics Reviews*, vol. 12, no. 1, p. 1700221, Jan. 2018, doi: 10.1002/lpor.201700221.
- [345] J. Shen *et al.*, "Liquid Phase Exfoliation of Two-Dimensional Materials by Directly Probing and Matching Surface Tension Components," *Nano Lett.*, vol. 15, no. 8, pp. 5449–5454, Aug. 2015, doi: 10.1021/acs.nanolett.5b01842.
- [346] H. Tao, Y. Zhang, Y. Gao, Z. Sun, C. Yan, and J. Texter, "Scalable exfoliation and dispersion of two-dimensional materials an update," *Phys. Chem. Chem. Phys.*, vol. 19, no. 2, pp. 921–960, Jan. 2017, doi: 10.1039/C6CP06813H.
- [347] P. Yasaei *et al.*, "High-Quality Black Phosphorus Atomic Layers by Liquid-Phase Exfoliation," *Adv. Mater.*, vol. 27, no. 11, pp. 1887–1892, Mar. 2015, doi: 10.1002/adma.201405150.
- [348] Damien Hanlon, "Liquid Phase Exfoliation of Novel 2D Nanomaterials," A thesis submitted for the degree of Doctor of philosophy in physics, Trinity College Dublin, Ireland, 2016.
- [349] S. Nalesso, M. J. Bussemaker, R. P. Sear, M. Hodnett, and J. Lee, "A review on possible mechanisms of sonocrystallisation in solution," *Ultrasonics Sonochemistry*, vol. 57, pp. 125–138, Oct. 2019, doi: 10.1016/j.ultsonch.2019.04.020.
- [350] K. S. Suslick, D. J. Casadonte, and S. J. Doktycz, "The effects of ultrasound on nickel and copper powders," *Solid State Ionics*, vol. 32–33, pp. 444–452, Feb. 1989, doi: 10.1016/0167-2738(89)90254-3.
- [351] K. S. Suslick, D. J. Casadonte, M. L. H. Green, and M. E. Thompson, "Effects of high intensity ultrasound on inorganic solids," *Ultrasonics*, vol. 25, no. 1, pp. 56–59, Jan. 1987, doi: 10.1016/0041-624X(87)90013-8.
- [352] K. S. Suslick, D. J. Casadonte, and S. J. Doktycz, "Ultrasonic irradiation of copper powder," *Chem. Mater.*, vol. 1, no. 1, pp. 6–8, Jan. 1989, doi: 10.1021/cm00001a003.
- [353] K. S. Suslick and S. J. Doktycz, "The sonochemistry of zinc powder," *J. Am. Chem. Soc.*, vol. 111, no. 6, pp. 2342–2344, Mar. 1989, doi: 10.1021/ja00188a081.

- [354] S. J. Doktycz and K. S. Suslick, "Interparticle collisions driven by ultrasound," *Science*, vol. 247, no. 4946, pp. 1067–1069, Mar. 1990, doi: 10.1126/science.2309118.
- [355] T. Prozorov, R. Prozorov, and K. S. Suslick, "High Velocity Interparticle Collisions Driven by Ultrasound," *J. Am. Chem. Soc.*, vol. 126, no. 43, pp. 13890–13891, Nov. 2004, doi: 10.1021/ja049493o.
- [356] K. Yasui and K. Kato, "Dipole–Dipole Interaction Model for Oriented Attachment of BaTiO3 Nanocrystals: A Route to Mesocrystal Formation," *J. Phys. Chem. C*, vol. 116, no. 1, pp. 319–324, Jan. 2012, doi: 10.1021/jp208848j.
- [357] F. Dang, K. Kato, H. Imai, S. Wada, H. Haneda, and M. Kuwabara, "A new effect of ultrasonication on the formation of BaTiO3 nanoparticles," *Ultrasonics Sonochemistry*, vol. 17, no. 2, pp. 310–314, Feb. 2010, doi: 10.1016/j.ultsonch.2009.08.006.
- [358] S. S. Berdonosov, I. V. Melikhov, and I. V. Znamenskaya, "Layered agglomeration of primary vaterite nanoparticles during ultrasonic stirring," *Inorg Mater*, vol. 41, no. 4, pp. 397–401, Apr. 2005, doi: 10.1007/s10789-005-0142-9.
- [359] C. Tang, L. Liu, Y. Li, and Z. Bian, "Aerosol spray assisted assembly of TiO2 mesocrystals into hierarchical hollow microspheres with enhanced photocatalytic performance," *Applied Catalysis B: Environmental*, vol. 201, pp. 41–47, Feb. 2017, doi: 10.1016/j.apcatb.2016.08.006.
- [360] F. Dang, K. Kato, H. Imai, S. Wada, H. Haneda, and M. Kuwabara, "Growth of BaTiO3 nanoparticles in ethanol—water mixture solvent under an ultrasound-assisted synthesis," *Chemical Engineering Journal*, vol. 170, no. 1, pp. 333–337, May 2011, doi: 10.1016/j.cej.2011.03.076.
- [361] J. P. Lorimer and T. J. Mason, "Sonochemistry. Part 1—The physical aspects," *Chem. Soc. Rev.*, vol. 16, no. 0, pp. 239–274, 1987, doi: 10.1039/CS9871600239.
- [362] C. U. Okoli *et al.*, "Solvent effect in sonochemical synthesis of metal-alloy nanoparticles for use as electrocatalysts," *Ultrasonics Sonochemistry*, vol. 41, pp. 427–434, Mar. 2018, doi: 10.1016/j.ultsonch.2017.09.049.
- [363] K. S. Suslick, J. J. Gawienowski, P. F. Schubert, and H. H. Wang, "Alkane sonochemistry," J. Phys. Chem., vol. 87, no. 13, pp. 2299–2301, Jun. 1983, doi: 10.1021/j100236a013.

- [364] Y. Chen *et al.*, "Solvent-dependent ultrasonic surface treatment on morphological reconstruction of CuO particles for copper electrodeposition," *Applied Surface Science*, vol. 491, pp. 206–215, Oct. 2019, doi: 10.1016/j.apsusc.2019.06.117.
- [365] S. R. Ghanta and K. Muralidharan, "Solution phase chemical synthesis of nano aluminium particles stabilized in poly(vinylpyrrolidone) and poly(methylmethacrylate) matrices," *Nanoscale*, vol. 2, no. 6, pp. 976–980, Jun. 2010, doi: 10.1039/B9NR00337A.
- [366] J. A. Haber and W. E. Buhro, "Kinetic Instability of Nanocrystalline Aluminum Prepared by Chemical Synthesis; Facile Room-Temperature Grain Growth," *J. Am. Chem. Soc.*, vol. 120, no. 42, pp. 10847–10855, Oct. 1998, doi: 10.1021/ja981972y.
- [367] T. Watanabe, K. Koyasu, and T. Tsukuda, "Density Functional Theory Study on Stabilization of the Al13 Superatom by Poly(vinylpyrrolidone)," *J. Phys. Chem. C*, vol. 119, no. 20, pp. 10904–10909, May 2015, doi: 10.1021/jp5107718.
- [368] D. A. Yatsenko and T. B. Medvedeva, "Estimating Crystality Index of Microcrystalline Cellulose Using Diffraction Methods," J Struct Chem, vol. 60, no. 9, pp. 1430–1436, Sep. 2019, doi: 10.1134/S0022476619090075.
- [369] D. Farlay, G. Panczer, C. Rey, P. Delmas, and G. Boivin, "Mineral maturity and crystallinity index are distinct characteristics of bone mineral," *J Bone Miner Metab*, vol. 28, no. 4, pp. 433–445, Jul. 2010, doi: 10.1007/s00774-009-0146-7.
- [370] L. Katz, "X-ray diffraction in crystals, imperfect crystals, and amorphous bodies (Guinier, A.)," *J. Chem. Educ.*, vol. 41, no. 5, p. 292, May 1964, doi: 10.1021/ed041p292.2.
- [371] J. S. O. Evans, "Advanced Input Files & Parametric Quantitative Analysis Using Topas," *MSF*, vol. 651, pp. 1–9, May 2010, doi: 10.4028/www.scientific.net/MSF.651.1.
- [372] L. Lutterotti, H. Pillière, C. Fontugne, P. Boullay, and D. Chateigner, "Full-profile search–match by the Rietveld method," *J Appl Cryst*, vol. 52, no. 3, pp. 587–598, Jun. 2019, doi: 10.1107/S160057671900342X.
- [373] M. Tamer, "Quantitative Phase Analysis Based on Rietveld Structure Refinement for Carbonate Rocks," vol. 2013, Aug. 2013, doi: 10.4236/jmp.2013.48154.

- [374] R. W. Cheary, A. A. Coelho, and J. P. Cline, "Fundamental Parameters Line Profile Fitting in Laboratory Diffractometers," *J Res Natl Inst Stand Technol*, vol. 109, no. 1, pp. 1–25, Feb. 2004, doi: 10.6028/jres.109.002.
- [375] S. Shabana *et al.*, "Improved synthesis of aluminium nanoparticles using ultrasound assisted approach and subsequent dispersion studies in di-octyl adipate," *Ultrasonics Sonochemistry*, vol. 36, pp. 59–69, May 2017, doi: 10.1016/j.ultsonch.2016.11.020.
- [376] M. Haneef, K. Yaqoob, M. Adeel Umer, and Z. Hussain, "A novel strategy for synthesis of Al powder comprising of Al nanoflakes via ultrasonication of Al foil," *Ultrasonics Sonochemistry*, vol. 61, p. 104838, Mar. 2020, doi: 10.1016/j.ultsonch.2019.104838.
- [377] X. Qian, J. Yin, S. Feng, S. Liu, and Z. Zhu, "Preparation and characterization of polyvinylpyrrolidone films containing silver sulfide nanoparticles," *J. Mater. Chem.*, vol. 11, no. 10, pp. 2504–2506, 2001, doi: 10.1039/b103708k.
- [378] X.-G. Li, I. Kresse, J. Springer, J. Nissen, and Y.-L. Yang, "Morphology and gas permselectivity of blend membranes of polyvinylpyridine with ethylcellulose," *Polymer*, vol. 42, no. 16, pp. 6859–6869, Jul. 2001, doi: 10.1016/S0032-3861(01)00057-X.
- [379] K. K. Kumar, M. Ravi, Y. Pavani, S. Bhavani, A. K. Sharma, and V. V. R. Narasimha Rao, "Investigations on PEO/PVP/NaBr complexed polymer blend electrolytes for electrochemical cell applications," *Journal of Membrane Science*, vol. 454, pp. 200–211, Mar. 2014, doi: 10.1016/j.memsci.2013.12.022.
- [380] E. M. Abdelrazek, A. M. Abdelghany, S. I. Badr, and M. A. Morsi, "Structural, optical, morphological and thermal properties of PEO/PVP blend containing different concentrations of biosynthesized Au nanoparticles," *Journal of Materials Research and Technology*, vol. 7, no. 4, pp. 419–431, Oct. 2018, doi: 10.1016/j.jmrt.2017.06.009.
- [381] P.-H. Huang and H.-Y. Lai, "Nucleation and propagation of dislocations during nanopore lattice mending by laser annealing: Modified continuum-atomistic modeling," *Phys. Rev. B*, vol. 77, no. 12, p. 125408, Mar. 2008, doi: 10.1103/PhysRevB.77.125408.
- [382] P.-H. Huang and H.-Y. Lai, "Pressure-induced solid-state lattice mending of nanopores by pulse laser annealing," *Nanotechnology*, vol. 19, no. 25, p. 255701, Jun. 2008, doi: 10.1088/0957-4484/19/25/255701.

- [383] P.-H. Huang and H.-Y. Lai, "Atomistic modeling of lattice frame effects on laser-induced dislocation behaviors in nanopore mending processes," *Journal of Applied Physics*, vol. 108, no. 12, p. 123504, Dec. 2010, doi: 10.1063/1.3517788.
- [384] B.-S. An, "Electron beam irradiation induced crystallization behavior of amorphous Ge2Sb2Te5 chalcogenide material," *Appl. Microsc.*, vol. 49, no. 1, p. 17, Dec. 2019, doi: 10.1186/s42649-019-0021-5.
- [385] I. Jenčič, M. W. Bench, I. M. Robertson, and M. A. Kirk, "Electron-beam-induced crystallization of isolated amorphous regions in Si, Ge, GaP, and GaAs," *Journal of Applied Physics*, vol. 78, no. 2, pp. 974–982, Jul. 1995, doi: 10.1063/1.360764.
- [386] B. J. Kooi, W. M. G. Groot, and J. Th. M. De Hosson, "In situ transmission electron microscopy study of the crystallization of Ge2Sb2Te5," Journal of Applied Physics, vol. 95, no. 3, pp. 924–932, Feb. 2004, doi: 10.1063/1.1636259.
- [387] Y. Zhang, J. Lian, C. M. Wang, W. Jiang, R. C. Ewing, and W. J. Weber, "Ion-induced damage accumulation and electron-beam-enhanced recrystallization in \$\mathrm{Sr}\mathrm{Ti}{\mathrm{O}}_{3}\$," *Phys. Rev. B*, vol. 72, no. 9, p. 094112, Sep. 2005, doi: 10.1103/PhysRevB.72.094112.
- [388] J. Murray, K. Song, W. Huebner, and M. O'Keefe, "Electron beam induced crystallization of sputter deposited amorphous alumina thin films," *Materials Letters*, vol. 74, pp. 12–15, May 2012, doi: 10.1016/j.matlet.2012.01.039.
- [389] Match! Phase Identification from Powder Diffraction, Kreuzherrenstr. 102, 53227 Bonn, Germany: Crystal Impact - Dr. H. Putz & Dr. K. Brandenburg GbR.
- [390] D. Huang *et al.*, "The synergistic effect of proton intercalation and electron transfer via electro-activated molybdenum disulfide/graphite felt toward hydrogen evolution reaction," *Journal of Catalysis*, vol. 381, pp. 175–185, Jan. 2020, doi: 10.1016/j.jcat.2019.11.003.
- [391] Y. Lei *et al.*, "Unveiling the influence of electrode/electrolyte interface on the capacity fading for typical graphite-based potassium-ion batteries," *Energy Storage Materials*, vol. 24, pp. 319–328, Jan. 2020, doi: 10.1016/j.ensm.2019.07.043.
- [392] T. Seita *et al.*, "Graphite–Lithium Sulfide Battery with a Single-Phase Sparingly Solvating Electrolyte," *ACS Energy Lett.*, vol. 5, no. 1, pp. 1–7, Jan. 2020, doi: 10.1021/acsenergylett.9b02347.

- [393] W. Li, Y. Li, and K. Xu, "Azidated Graphene: Direct Azidation from Monolayers, Click Chemistry, and Bulk Production from Graphite," *Nano Lett.*, vol. 20, no. 1, pp. 534–539, Jan. 2020, doi: 10.1021/acs.nanolett.9b04267.
- [394] F. Ma, L. Liu, X. Wang, M. Jing, W. Tan, and X. Hao, "Rapid production of few layer graphene for energy storage via dry exfoliation of expansible graphite," *Composites Science and Technology*, vol. 185, p. 107895, Jan. 2020, doi: 10.1016/j.compscitech.2019.107895.
- [395] T. Wang *et al.*, "Direct regeneration of spent LiFePO4via a graphite prelithiation strategy," *Chem. Commun.*, vol. 56, no. 2, pp. 245–248, Dec. 2019, doi: 10.1039/C9CC08155K.
- [396] Q. Wang, D. Zhou, Y. Chen, P. Eames, and Z. Wu, "Characterization and effects of thermal cycling on the properties of paraffin/expanded graphite composites," *Renewable Energy*, vol. 147, pp. 1131–1138, Mar. 2020, doi: 10.1016/j.renene.2019.09.091.
- [397] D Roylance, "Stress-strain curves," *Stress-strain curves. Massachusetts Institute of Technology study, Cambridge.*, 2001.
- [398] A. Jain *et al.*, "Commentary: The Materials Project: A materials genome approach to accelerating materials innovation," *APL Materials*, vol. 1, no. 1, p. 011002, Jul. 2013, doi: 10.1063/1.4812323.
- [399] E. M. C. Jones, Ö. Ö. Çapraz, S. R. White, and N. R. Sottos, "Reversible and Irreversible Deformation Mechanisms of Composite Graphite Electrodes in Lithium-Ion Batteries," *J. Electrochem. Soc.*, vol. 163, no. 9, pp. A1965–A1974, 2016, doi: 10.1149/2.0751609jes.
- [400] Y. Sui *et al.*, "Dual-ion batteries: The emerging alternative rechargeable batteries," *Energy Storage Materials*, vol. 25, pp. 1–32, Mar. 2020, doi: 10.1016/j.ensm.2019.11.003.
- [401] Y. Li, Y. Lu, P. Adelhelm, M.-M. Titirici, and Y.-S. Hu, "Intercalation chemistry of graphite: alkali metal ions and beyond," *Chem. Soc. Rev.*, vol. 48, no. 17, pp. 4655–4687, Aug. 2019, doi: 10.1039/C9CS00162J.
- [402] I. G. Gonzalez-Martinez *et al.*, "Electron-beam induced synthesis of nanostructures: a review," *Nanoscale*, vol. 8, no. 22, pp. 11340–11362, 2016, doi: 10.1039/C6NR01941B.

- [403] I. Jenčič, M. W. Bench, I. M. Robertson, and M. A. Kirk, "Electron-beam-induced crystallization of isolated amorphous regions in Si, Ge, GaP, and GaAs," *Journal of Applied Physics*, vol. 78, no. 2, pp. 974–982, Jul. 1995, doi: 10.1063/1.360764.
- [404] B. J. Kooi, W. M. G. Groot, and J. Th. M. De Hosson, "In situ transmission electron microscopy study of the crystallization of Ge2Sb2Te5," Journal of Applied Physics, vol. 95, no. 3, pp. 924–932, Feb. 2004, doi: 10.1063/1.1636259.
- [405] G. Lee et al., "Electron beam induced epitaxial crystallization in a conducting and insulating a-LaAlO 3 /SrTiO 3 system," RSC Advances, vol. 7, no. 64, pp. 40279–40285, 2017, doi: 10.1039/C7RA06353A.
- [406] O. Tengstrand *et al.*, "Beam-induced crystallization of amorphous Me–Si–C (Me = Nb or Zr) thin films during transmission electron microscopy," *MRS Communications*, vol. 3, no. 3, pp. 151–155, Sep. 2013, doi: 10.1557/mrc.2013.31.
- [407] G. Lulli, P. G. Merli, and M. V. Antisari, "Solid-phase epitaxy of amorphous silicon induced by electron irradiation at room temperature," *Phys. Rev. B*, vol. 36, no. 15, pp. 8038–8042, Nov. 1987, doi: 10.1103/PhysRevB.36.8038.
- [408] F. Corticelli, G. Lulli, and P. G. Merli, "Solid-phase epitaxy of implanted silicon at liquid nitrogen and room temperature induced by electron irradiation in the electron microscope," *Philosophical Magazine Letters*, vol. 61, no. 3, pp. 101–106, Mar. 1990, doi: 10.1080/09500839008206487.
- [409] T. Zhang, Z. Song, M. Sun, B. Liu, S. Feng, and B. Chen, "Investigation of electron beam induced phase change in Si2Sb2Te5 material," Appl. Phys. A, vol. 90, no. 3, pp. 451–455, Mar. 2008, doi: 10.1007/s00339-007-4302-4.
- [410] A. Meldrum, L. A. Boatner, and R. C. Ewing, "Electron-irradiation-induced nucleation and growth in amorphous LaPO4, ScPO4, and zircon," *Journal of Materials Research*, vol. 12, no. 7, pp. 1816–1827, Jul. 1997, doi: 10.1557/JMR.1997.0250.
- [411] M. O. Ruault, J. Chaumont, J. M. Penisson, and A. Bourret, "High resolution and in situ investigation of defects in Bi-irradiated Si," *Philosophical Magazine A*, vol. 50, no. 5, pp. 667–675, Nov. 1984, doi: 10.1080/01418618408237526.
- [412] R. Nakamura, M. Ishimaru, H. Yasuda, and H. Nakajima, "Atomic rearrangements in amorphous Al2O3 under electron-beam irradiation," *Journal of Applied Physics*, vol. 113, no. 6, p. 064312, Feb. 2013, doi: 10.1063/1.4790705.

- [413] X. Yang, R. Wang, H. Yan, and Z. Zhang, "Low energy electron-beam-induced recrystallization of continuous GaAs amorphous foils," *Materials Science and Engineering: B*, vol. 49, no. 1, pp. 5–13, Sep. 1997, doi: 10.1016/S0921-5107(97)00104-9.
- [414] F. Lu, Y. Shen, X. Sun, Z. Dong, R. C. Ewing, and J. Lian, "Size dependence of radiation-induced amorphization and recrystallization of synthetic nanostructured CePO4 monazite," Acta Materialia, vol. 61, no. 8, pp. 2984–2992, May 2013, doi: 10.1016/j.actamat.2013.01.058.
- [415] I.-T. Bae, Y. Zhang, W. J. Weber, M. Higuchi, and L. A. Giannuzzi, "Electron-beam induced recrystallization in amorphous apatite," *Appl. Phys. Lett.*, vol. 90, no. 2, p. 021912, Jan. 2007, doi: 10.1063/1.2430779.
- [416] W. Qin, T. Nagase, and Y. Umakoshi, "Electron irradiation-induced nanocrystallization of amorphous Fe85B15 alloy: Evidence for athermal nature," *Acta Materialia*, vol. 57, no. 4, pp. 1300–1307, Feb. 2009, doi: 10.1016/j.actamat.2008.11.009.
- [417] W. Qin, J. A. Szpunar, and Y. Umakoshi, "Electron or ion irradiation-induced phase-change mechanism between amorphous and crystalline state," *Acta Materialia*, vol. 59, no. 5, pp. 2221–2228, Mar. 2011, doi: 10.1016/j.actamat.2010.12.025.
- [418] W. G. Stratton, J. Hamann, J. H. Perepezko, and P. M. Voyles, "Electron beam induced crystallization of amorphous Al-based alloys in the TEM," *Intermetallics*, vol. 14, no. 8–9, pp. 1061–1065, Aug. 2006, doi: 10.1016/j.intermet.2006.01.025.
- [419] J. Hren, Ed., Introduction to Analytical Electron Microscopy. Springer US, 1979.
- [420] S. K. Padhi and M. G. Krishna, "Non-Classical Crystal Growth Recipe using nanocrystalline ceria a detailed review," arXiv:1911.07454 [cond-mat, physics:physics], Nov. 2019.
- [421] L. Ratke and P. W. Voorhees, *Growth and Coarsening: Ostwald Ripening in Material Processing*. Springer Science & Business Media, 2013.
- [422] J. Li *et al.*, "In Situ Atomic-Scale Study of Particle-Mediated Nucleation and Growth in Amorphous Bismuth to Nanocrystal Phase Transformation," *Advanced Science*, vol. 5, no. 6, p. 1700992, 2018, doi: 10.1002/advs.201700992.

- [423] B. Jia and L. Gao, "Growth of Well-Defined Cubic Hematite Single Crystals: Oriented Aggregation and Ostwald Ripening," *Crystal Growth & Design*, vol. 8, no. 4, pp. 1372–1376, Apr. 2008, doi: 10.1021/cg070300t.
- [424] S. Karthika, T. K. Radhakrishnan, and P. Kalaichelvi, "A Review of Classical and Nonclassical Nucleation Theories," *Crystal Growth & Design*, vol. 16, no. 11, pp. 6663–6681, Nov. 2016, doi: 10.1021/acs.cgd.6b00794.
- [425] S. Gottapu, S. K. Padhi, M. G. Krishna, and K. Muralidharan, "Poly(vinylpyrrolidone) stabilized aluminum nanoparticles obtained by the reaction of SiCl ₄ with LiAlH ₄," *New J. Chem.*, vol. 39, no. 7, pp. 5203–5207, 2015, doi: 10.1039/C5NJ00438A.
- [426] W. L. Perry *et al.*, "Nano-Scale Tungsten Oxides for Metastable Intermolecular Composites," *Propellants, Explosives, Pyrotechnics*, vol. 29, no. 2, pp. 99–105, 2004, doi: 10.1002/prep.200400037.
- [427] K. C. Walter, D. R. Pesiri, and D. E. Wilson, "Manufacturing and Performance of Nanometric Al/MoO3 Energetic Materials," *Journal of Propulsion and Power*, vol. 23, no. 4, pp. 645–650, 2007, doi: 10.2514/1.25461.
- [428] V. E. Sanders, B. W. Asay, T. J. Foley, B. C. Tappan, A. N. Pacheco, and S. F. Son, "Reaction Propagation of Four Nanoscale Energetic Composites (Al/MoO3, Al/WO3, Al/CuO, and B12O3)," *Journal of Propulsion and Power*, vol. 23, no. 4, pp. 707–714, Jul. 2007, doi: 10.2514/1.26089.
- [429] A. Prakash, A. V. McCormick, and M. R. Zachariah, "Synthesis and Reactivity of a Super-Reactive Metastable Intermolecular Composite Formulation of Al/KMnO4," *Adv. Mater.*, vol. 17, no. 7, pp. 900–903, Apr. 2005, doi: 10.1002/adma.200400853.
- [430] V. K. Tolpygo and D. R. Clarke, "Microstructural study of the theta-alpha transformation in alumina scales formed on nickel-aluminides," *Materials at High Temperatures*, vol. 17, no. 1, pp. 59–70, Jan. 2000, doi: 10.1179/mht.2000.011.
- [431] M. Boaro, M. Vicario, C. de Leitenburg, G. Dolcetti, and A. Trovarelli, "The use of temperature-programmed and dynamic/transient methods in catalysis: characterization of ceria-based, model three-way catalysts," *Catalysis Today*, vol. 77, no. 4, pp. 407–417, Jan. 2003, doi: 10.1016/S0920-5861(02)00383-8.

- [432] C. Aliotta *et al.*, "Ceria-based electrolytes prepared by solution combustion synthesis: The role of fuel on the materials properties," *Applied Catalysis B: Environmental*, vol. 197, pp. 14–22, Nov. 2016, doi: 10.1016/j.apcatb.2016.02.044.
- [433] H. Sohn *et al.*, "Oxygen Mobility in Pre-Reduced Nano- and Macro-Ceria with Co Loading: An AP-XPS, In-Situ DRIFTS and TPR Study," *Catal Lett*, vol. 147, no. 11, pp. 2863–2876, Nov. 2017, doi: 10.1007/s10562-017-2176-4.
- [434] T. S. Moraes *et al.*, "Effects of Ceria Morphology on Catalytic Performance of Ni/CeO2 Catalysts for Low Temperature Steam Reforming of Ethanol," *Top Catal*, vol. 58, no. 4–6, pp. 281–294, Apr. 2015, doi: 10.1007/s11244-015-0369-x.
- [435] Y. Wang, S. Liang, A. Cao, R. L. Thompson, and G. Veser, "Au-mixed lanthanum/cerium oxide catalysts for water gas shift," *Applied Catalysis B: Environmental*, vol. 99, no. 1–2, pp. 89–95, Aug. 2010, doi: 10.1016/j.apcatb.2010.06.004.
- [436] Z. Abdelouahab-Reddam, R. E. Mail, F. Coloma, and A. Sepúlveda-Escribano, "Platinum supported on highly-dispersed ceria on activated carbon for the total oxidation of VOCs," Applied Catalysis A: General, vol. 494, pp. 87–94, Mar. 2015, doi: 10.1016/j.apcata.2015.01.026.
- [437] A. Sossi *et al.*, "Non-isothermal oxidation of aluminum nanopowder coated by hydrocarbons and fluorohydrocarbons," *Applied Surface Science*, vol. 271, pp. 337–343, Apr. 2013, doi: 10.1016/j.apsusc.2013.01.197.
- [438] F. Noor, H. Zhang, T. Korakianitis, and D. Wen, "Oxidation and ignition of aluminum nanomaterials," *Phys. Chem. Chem. Phys.*, vol. 15, no. 46, p. 20176, 2013, doi: 10.1039/c3cp53171f.
- [439] S. C. Kettwich *et al.*, "Thermal investigations of nanoaluminum/perfluoropolyether core—shell impregnated composites for structural energetics," *Thermochimica Acta*, vol. 591, pp. 45–50, Sep. 2014, doi: 10.1016/j.tca.2014.07.016.
- [440] M. L. Pantoya and S. W. Dean, "The influence of alumina passivation on nano-Al/Teflon reactions," *Thermochimica Acta*, vol. 493, no. 1–2, pp. 109–110, Sep. 2009, doi: 10.1016/j.tca.2009.03.018.
- [441] M. Schoenitz, C.-M. Chen, and E. L. Dreizin, "Oxidation of Aluminum Particles in the Presence of Water," *J. Phys. Chem. B*, vol. 113, no. 15, pp. 5136–5140, Apr. 2009, doi: 10.1021/jp807801m.

- [442] X. Zhu, M. Schoenitz, and E. L. Dreizin, "Oxidation of Aluminum Particles in Mixed CO ₂ /H ₂ O Atmospheres," *J. Phys. Chem. C*, vol. 114, no. 44, pp. 18925–18930, Nov. 2010, doi: 10.1021/jp105363v.
- [443] "Zhang et al. 2010 Iodine Release, Oxidation, and Ignition of Mechani.pdf.".
- [444] A. Gromov, A. Ilyin, U. Förter-Barth, and U. Teipel, "Characterization of Aluminum Powders: II. Aluminum Nanopowders Passivated by Non-Inert Coatings," *Prop., Explos., Pyrotech.*, vol. 31, no. 5, pp. 401–409, Oct. 2006, doi: 10.1002/prep.200600055.
- [445] A. B. Vorozhtsov *et al.*, "Oxidation of nano-sized aluminum powders," *Thermochimica Acta*, vol. 636, pp. 48–56, Jul. 2016, doi: 10.1016/j.tca.2016.05.003.
- [446] H. Y. Jeong *et al.*, "Tailoring oxidation of Al particles morphologically controlled by carbon nanotubes," *Energy*, vol. 55, pp. 1143–1151, Jun. 2013, doi: 10.1016/j.energy.2013.04.039.
- [447] S. H. Kim and M. R. Zachariah, "Enhancing the Rate of Energy Release from NanoEnergetic Materials by Electrostatically Enhanced Assembly," *Adv. Mater.*, vol. 16, no. 20, pp. 1821–1825, Oct. 2004, doi: 10.1002/adma.200306436.
- [448] L. Shi *et al.*, "A high energy output and low onset temperature nanothermite based on three-dimensional ordered macroporous nano-NiFe ₂ O ₄," *RSC Adv.*, vol. 6, no. 96, pp. 93330–93334, 2016, doi: 10.1039/C6RA16429C.
- [449] M. G. Zaky, A. M. Abdalla, R. P. Sahu, I. K. Puri, M. Radwan, and S. Elbasuney, "Nanothermite colloids: A new prospective for enhanced performance," *Defence Technology*, vol. 15, no. 3, pp. 319–325, Jun. 2019, doi: 10.1016/j.dt.2018.08.016.
- [450] A. Shahravan, T. Desai, and T. Matsoukas, "Passivation of Aluminum Nanoparticles by Plasma-Enhanced Chemical Vapor Deposition for Energetic Nanomaterials," ACS Appl. Mater. Interfaces, vol. 6, no. 10, pp. 7942–7947, May 2014, doi: 10.1021/am5012707.
- [451] K. J. Huang and C. D. Tan, "Preparation and Exothermic Characterization of Dioctyl Sebacate (DOS)-Coated Aluminum Nanopowders," *AMM*, vol. 79, pp. 65–70, Jul. 2011, doi: 10.4028/www.scientific.net/AMM.79.65.
- [452] Q.-L. Yan, M. Gozin, F.-Q. Zhao, A. Cohen, and S.-P. Pang, "Highly energetic compositions based on functionalized carbon nanomaterials," *Nanoscale*, vol. 8, no. 9, pp. 4799–4851, 2016, doi: 10.1039/C5NR07855E.

- [453] A. Bach, P. Gibot, L. Vidal, R. Gadiou, and D. Spitzer, "Modulation of the Reactivity of a WO 3 /Al Energetic Material with Graphitized Carbon Black as Additive," *Journal of Energetic Materials*, vol. 33, no. 4, pp. 260–276, Oct. 2015, doi: 10.1080/07370652.2014.977979.
- [454] R. Thiruvengadathan *et al.*, "A Versatile Self-Assembly Approach toward High Performance Nanoenergetic Composite Using Functionalized Graphene," *Langmuir*, vol. 30, no. 22, pp. 6556–6564, Jun. 2014, doi: 10.1021/la500573e.
- [455] B. Siegert, M. Comet, O. Muller, G. Pourroy, and D. Spitzer, "Reduced-Sensitivity Nanothermites Containing Manganese Oxide Filled Carbon Nanofibers," *J. Phys. Chem. C*, vol. 114, no. 46, pp. 19562–19568, Nov. 2010, doi: 10.1021/jp1014737.
- [456] K. S. Martirosyan, L. Wang, and D. Luss, "Tuning the Gas Pressure Discharge of Nanoenergetic Materials by Boron and Carbon Nanotubes Additives," vol. 1, p. 4, 2011.